UC Berkeley
UC Berkeley Electronic Theses and Dissertations

Title
Micro-Columnated Loop Heat Pipe: The Future of Electronic Substrates

Permalink
https://escholarship.org/uc/item/7hg4396w

Author
Dhillon, Navdeep Singh

Publication Date
2012

Peer reviewed|Thesis/dissertation

eScholarship.org Powered by the California Digital Library
University of California

Micro-Columnated Loop Heat Pipe: The Future of Electronic Substrates

by

Navdeep Singh Dhillon

A dissertation submitted in partial satisfaction of the
requirements for the degree of
Doctor of Philosophy

in

Engineering – Mechanical Engineering

in the

GRADUATE DIVISION
of the
UNIVERSITY OF CALIFORNIA, BERKELEY

Committee in charge:

Professor Albert P. Pisano, Chair
Professor Liwei Lin
Professor Ömer Savaş
Professor Ali Javey

Spring 2012

Micro-Columnated Loop Heat Pipe: The Future of Electronic Substrates

Copyright 2012
by
Navdeep Singh Dhillon

Abstract

Micro-Columnated Loop Heat Pipe: The Future of Electronic Substrates

by

Navdeep Singh Dhillon
Doctor of Philosophy in Engineering – Mechanical Engineering

University of California, Berkeley

Professor Albert P. Pisano, Chair

The modern world is run by semiconductor-based electronic systems. Due to continuous improvements in semiconductor device fabrication, there is a clear trend in the market towards the development of electronic devices and components that not only deliver enhanced computing power, but are also more compact. Thermal management has emerged as the primary challenge in this scenario where heat flux dissipation of electronic chips is increasing exponentially, but conventional cooling solutions such as conduction and convection are no longer feasible. To keep device junction temperatures within the safe operating limit, there is an urgent requirement for ultra-high-conductivity thermal substrates that not only absorb and transport large heat fluxes, but can also provide localized cooling to thermal hotspots.

This dissertation describes the design, modeling, and fabrication of a phase change-based, planar, ultra-thin, passive thermal transport system that is inspired by the concept of loop heat pipes and capillary pumped loops. Fabricated on silicon and Pyrex wafers using microfabrication techniques, the micro-columnated loop heat pipe (μCLHP) can be integrated directly with densely packed or multiply-stacked electronic substrates, to provide localized high-heat-flux thermal management. The μCLHP employs a dual-scale coherent porous silicon(CPS)-based micro-columnated wicking structure, where the primary CPS wick provides large capillary forces for fluid transport, while a secondary surface-wick maximizes the rate of thin-film evaporation. To overcome the wick thickness limitation encountered in conventional loop heat pipes, strategies based on MEMS surface micromachining techniques were developed to reduce parasitic heat flow from the evaporator to the compensation chamber of the device. Finite element analysis was used to confirm this reduction in a planar evaporator design, thus enabling the generation of a large motive temperature head for continuous device operation. To predict the overall heat carrying capacity of the μCLHP in the capillary pumping limit, an analytical model was developed to account for a steady state pressure balance in the device flow loop. Based on this model, a design optimization study, employing monotonicity analysis and numerical optimization techniques, was undertaken. It was found that an optimized μCLHP device can

absorb heat fluxes as large as 1293 W/cm^2 when water is used as a working fluid. A finite volume method-based numerical model was also developed to compute the rates of thin-film evaporation from the patterned surface of the secondary wick. The numerical results indicated that, by properly optimizing the dual-scale wick topology, allowable evaporative heat fluxes can be made commensurate with the heat flux performance predicted by the capillary pumping limit.

The latter part of the dissertation deals with the fabrication, packaging, and experimental testing of several in-plane-wicking micro loop heat pipe (μLHP) prototypes. These devices were fabricated on silicon and Pyrex substrates and closely resemble the μCLHP design philosophy, with the exception that the CPS wick is substituted with an easier to fabricate in-plane wick. A novel thermal-flux method was developed for the degassing and fluid charging of the μLHP prototypes. Experiments were conducted to study the process of evaporation and dynamics of the liquid and vapor phases in the device flow loop. Using these results, the overall device and individual component topologies critical to the operation of the two-phase flow loop were identified. A continuous two-phase device flow loop was demonstrated for applied evaporator heat fluxes as high as 41 W/cm^2. The performance of these devices, currently found to be limited by the motive temperature head requirement, can be significantly improved by implementing the parasitic heat flow-reduction strategies developed in this work. The 3-D thin-film evaporation model, when integrated into the overall device modeling framework, will enable a design optimization of the micro-columnated wick for further device performance enhancements.

To my Family

Contents

List of Figures **vi**

List of Tables **xv**

I Overview 1

1 Introduction 2

1.1 Motivation 2
1.1.1 Thermal Management Demands of Electronic Devices 2
1.1.2 Thermal Management State of the Art 10
1.2 Review of Passive Phase Change Cooling Devices 16
1.2.1 Heat Pipes 16
1.2.2 Loop Heat Pipes 19
1.2.3 Capillary Pumped Loops 23
1.3 The Micro-Columnated Loop Heat Pipe 24
1.3.1 An Overview of the Device 25
1.3.2 Salient Device Performance Parameters 29
1.4 Dissertation Outline 31

II Modeling of Device Physics and Operation 32

2 Thermodynamic Analysis of Device Operation 33

2.1 Challenges to Miniaturization 33
2.1.1 Wick Thickness Limitation: 34
2.2 Device and Evaporator Thermodynamics 34
2.2.1 Device Theory of Operation 34
2.2.2 Thermodynamics of the Flow Loop 36
2.2.3 Device Operational Requirements 38
2.3 Planar Evaporator Design 40
2.3.1 Evaporator Thermal Modeling 41

2.3.2 Modeling Results . . . 42
2.4 Conclusions . . . 44

3 Device Optimization Based on Flow Loop Pressure Analysis 46
3.1 Device Theory and Theoretical Modeling . . . 46
3.1.1 Energy Balance in the Evaporator . . . 47
3.1.2 Pressure Balance in the Flow Loop . . . 48
3.1.3 Liquid Refilling of the Wicking Structure . . . 51
3.2 Design Optimization . . . 52
3.2.1 Monotonicity Analysis . . . 55
3.2.2 Numerical Optimization . . . 58
3.3 Conclusions . . . 63

4 Numerical Simulation of Phase Change in the Wick 64
4.1 Background . . . 64
4.2 Overview of Evaporation in the Micro-Columnated Wick . . . 65
4.3 Modeling of Thin-Film Evaporation . . . 67
4.3.1 Problem Statement . . . 67
4.3.2 Shape of the Liquid-Vapor Meniscus . . . 69
4.3.3 Evaporation at the Liquid-Vapor Interface . . . 72
4.4 Governing Equations and Boundary Conditions . . . 73
4.4.1 Governing Equations . . . 73
4.4.2 Boundary Conditions . . . 74
4.4.3 Numerical Solution . . . 75
4.5 Results and Discussion . . . 76
4.5.1 Fluid Flow and Heat Transfer Characteristics . . . 76
4.5.2 Effect of Wall Superheat on Heat Transfer . . . 78
4.5.3 Effect of Liquid Sub-cooling on Heat Transfer . . . 80
4.5.4 Application of the Results . . . 80
4.6 Conclusions . . . 80

III Device Fabrication and Experimental Testing 83

5 Device Design and Fabrication 84
5.1 Phase-I μLHP Prototype . . . 85
5.1.1 Device Design . . . 85
5.1.2 Device Fabrication Process Flow . . . 87
5.1.3 Fabrication Results . . . 89
5.2 Phase-II μLHP Prototype . . . 92
5.2.1 Device Design . . . 93
5.2.2 Device Fabrication . . . 95

5.3 Phase-III μLHP Prototype 99
5.3.1 Device Design 100
5.3.2 Device Fabrication 103

6 Device Filling and Packaging **105**
6.1 Statement of the Problem 105
6.2 Thermal Flux Degassing and Filling System 107
6.3 Device Packaging Techniques for Filling 108
6.3.1 Method I 109
6.3.2 Method II 112
6.3.3 Method III 113
6.4 A Standardized Packaging Solution 115
6.5 Hermetic Sealing of Device Prototypes 119
6.5.1 Noninvasive Hermetic Sealing Process 119
6.5.2 Experimental Verification 120
6.6 Conclusions 124

7 Experimental Testing of Devices **126**
7.1 Phase-I μLHP Prototype 126
7.1.1 Experimental Setup 127
7.1.2 Experimental Observations 129
7.1.3 Analysis of Results 131
7.2 Phase-II μLHP Prototype 134
7.2.1 Experimental Setup 134
7.2.2 Experimental Observations 136
7.2.3 Analysis of Results 138
7.3 Phase-III μLHP Prototype 138
7.3.1 Experimental Setup 139
7.3.2 Experimental Observations 139
7.3.3 Analysis of Results 139

8 A Detailed Study of Phase Change and Heat Transfer in the μLHP **143**
8.1 Experimental Setup 143
8.2 Onset of Evaporation in the Wick During Device Startup 149
8.3 Steady State Operation of the μLHP 151
8.4 Discussion of Results 155

IV Closure **157**

9 Summary and Conclusions **158**
9.1 Summary of Device Modeling Studies 158

9.2 Summary of Experimental Work 160
9.3 Conclusions and Future Work 162

Bibliography **164**

A Formal Rules of Monotonicity Analysis **174**

B Numerical Design Optimization Program **175**
B.1 Design Constants 175
B.2 Program Functions 179
B.3 Main Solver Program 185
B.4 Solving and Plotting Program 191

C Phase Change Simulation Program **195**
C.1 Overall Procedure 195
C.2 OpenFOAM Solver Program 195

List of Figures

1.1 Change in the maximum power dissipation of successive generations of Intel microprocessors [1]. 3
1.2 The available space inside a modern laptop for accommodating a thermal module (all dimensions in *mm*): (a) Top view; (b) Side view [2]. . 4
1.3 Stacked 3-D electronic packages: (a) A 3-D stacked die package, where the dies are electrically connected using through silicon vias (TSV) and solder connections [3]; (b) A larger scale 3-D package, where the printed circuit boards (PCBs) are stacked on top of each other [4]. . 5
1.4 High power light emitting diodes (LEDs): (a) A packaged single high-power LED chip with an air cooled heat sink [5, 6]; (b) A packaging assembly for a high power LED chip array, which can be interfaced with a heat sink [7]. 6
1.5 Electric batteries for automobiles: (a) Power components in an automobile [8]; (b) A lithium-ion (Li-ion) battery pack consisting of 48 cells connected in series [9]; (c) Panasonic Nickel Metal-Hydride (Ni-MH) battery module used in the 2001 Toyota Prius [10]. 8
1.6 Concentrating Photovoltaic (CPV) cells experience experience large incident solar intensities leading to large waste heat flux generation. (a) A photograph of a Fresnel lens CPV module [11]. (b) A schematic showing how a Fresnel lens concentrates the solar flux incident on a larger area onto the much smaller concentrator cell. Active liquid cooling is used to cool the cell [12]. 9
1.7 Cooling of a hot electronic chip by conduction and natural convection: (a) Schematic of the chip on the printed circuit board (PCB); (b) The thermal resistance network for the flow of heat from the chip to the ambient air. 11
1.8 A schematic showing the overall structure and theory of operation of a heat pipe [13]. 16
1.9 An inverted-meniscus wick design for a flat heat pipe evaporator [14]. The triangular grooves in the copper plate allow evaporation to take place, and the vapor to escape, from the surface of the wick in direct contact with the heat source. 18

1.10 A schematic outlining the basic structure and principle of operation of a loop heat pipe [15]. 19
1.11 Topologies of the evaporator section, compensation chamber, and wicking structure in loop heat pipes: (a) A cylindrical evaporator (dimension in mm) [16]; (b) A flat evaporator [2]. 21
1.12 Variation in the size and design topology of loop heat pipes (LHP) [15]: (a) A 21 m long cylindrical-evaporator LHP capable of carrying 1.7 kW of heat; (b) Flat-evaporator LHPs capable of carrying $\sim 100\ W$ of heat to a distance of 1 m; (c) Miniature LHPs with an evaporator diameter of not more than 6 mm, capable of carrying $\sim 90\ W$ of heat to a distance of 30 cm. 22
1.13 A schematic of the basic structure and principle of operation of a conventional capillary pumped loop (CPL) [17]. 23
1.14 A conceptualized view of a planar, ultra-thin, single-substrate micro-columnated Loop Heat Pipe (μCLHP) for localized high-heat flux cooling of integrated circuit (IC) electronics and packages. 25
1.15 A 3-D design schematic of a micro-columnated loop heat pipe (μCLHP) prototype: (a) Top view of the device showing the columnated coherent porous silicon (CPS) wicking structure and a built-in liquid-cooled heat sink for cooling the condenser section. The fill-holes in the top capping wafer connect to the fill-ports. (b) Bottom view of the device showing the liquid and vapor transport channels, the condenser section, and the compensation chamber. 27
1.16 Structure and principle of operation of the micro-columnated wicking structure. (a) The wick is composed of two components: a primary wick, which consists of vertical columns etched in the coherent porous silicon (CPS) base and a secondary wick, which consists of rectangular patterns etched into the top capping wafer. (b) Evaporation and fluid flow in the micro-columnated wicking structure: Incoming liquid is absorbed by the fine pores of the primary wick and conveyed for evaporation to the secondary wick. 28

2.1 A schematic of the liquid and vapor phase distributions, and fluid temperatures inside a planar micro-columnated loop heat pipe (μCLHP): (a) In steady state operation the vapor channel is completely, and the condenser section partially, liberated from the liquid phase. The compensation chamber can also contain pockets of vapor. (b) The dual scale wick in the evaporator section is supplied by the compensation chamber with liquid, which turns to vapor at the evaporator surface. 35

2.2 Phase change diagrams for the two-phase flow loop in the micro-columnated loop heat pipe (μCLHP): (a) P-T diagram obtained by modifying some elements of the conventional loop heat pipe analysis scheme[15]; (b) T-v diagram outlining the same process. 37
2.3 Phase change diagram illustrating potential device startup problems due to parasitic heat flow from the evaporator to the compensation chamber. 39
2.4 Evaporator design topology for minimizing parasitic heat flow to the compensation chamber. Thermal barriers are etched around the compensation chamber and a high thermal resistance channel is provided between the evaporator and the compensation chamber. 40
2.5 Low conductivity fluidic connection between the evaporator section and the compensation chamber: (a) Shallow cavity ($20 - 100\ \mu m$) beneath the wick; (b) A 200 μm wide connection channel; (c) Shallow cavity extended into the compensation chamber; (d) The compensation chamber. 41
2.6 Domain and boundary conditions for a coupled thermal-fluid simulation of the μCLHP evaporator and compensation chamber. 42
2.7 Transparent volume and sliced graphs showing the temperature distribution in the solution domain. The maximum domain temperature, at the surface of the silicon heater, is 373.15 K, while the minimum temperature, at 373.15 K, is the temperature of the incoming liquid. It is clear that the compensation chamber is kept comparatively cooler compared to the rest of the domain. 43
2.8 The temperature distribution of water in the compensation chamber and the evaporator, and of the surrounding silicon in the middle wafer. The temperature slice was taken at a depth of 50 μm from the bottom of the middle silicon wafer. 44

3.1 The micro-columated loop heat pipe (μCLHP): (a) Side view; (b) Top view. 47
3.2 The micro-columnated coherent porous silicon (CPS) wicking structure. 47
3.3 Plots of total latent heat carrying capacity of the μCLHP as a function of the wick pore diameter d_w, for different wick liquid wetting fractions $x_{w,liq}$. (a) The wick refilling limit is much larger than the pressure balance limit, and thus inactive. (b) The maximum heat flux decreases and the corresponding optimum wick pore diameter increases with decreasing wick liquid wetting fraction $x_{w,liq}$. 59
3.4 Plots of the different flow-loop pressure components of the μCLHP device in steady state operation, as a function of the wick pore diameter: (a) Wick liquid fraction, $x_{w,liq} = 0.95$; (b) Wick liquid fraction, $x_{w,liq} = 0.65$. 60

3.5 A comparison of the different pressure components in the wicking structure of the μCLHP device for a wick liquid fraction of $x_{w,liq} = 0.95$. . . 61
3.6 Plots of the total heat carrying capacity of the μCLHP as a function of the wick pore diameter, for different device lengths. 62

4.1 Coherent porous silicon (CPS)-based MEMS dual-scale wick. The dual-scale wick has a primary wick obtained by etching columns into a CPS substrate, and a secondary wick consisting of rectangular channels etched into the evaporating surface. The strong capillary action of the primary wick conveys the working liquid to the surface of the secondary wick, where it evaporates by absorbing heat from the heat source. Evaporation also occurs from the CPS pores of the primary wick exposed to the vapor region. 66
4.2 Proposed coherent porous silicon (CPS)-based wick topologies for integration into a micro-columnated loop heat pipe (μCLHP). The secondary wick is etched in the form of rectangular channels on the evaporating surface, while the primary wick consists of columns etched into the CPS base. (a) Uni-directional-channels wick topology consists of parallel channels in the secondary wick and continuous column walls in the primary wick. (b) Criss-crossing-channels wick topology consists of criss-crossing channels in the secondary wick and simple columns in the primary wick. 67
4.3 The model problem of thin-film evaporation in a rectangular microchannel of the secondary wick of the micro-columnated wicking structure. The liquid supply to the channel is from the CPS pores of the primary wick, and is specified as a liquid-inlet boundary condition. Evaporation occurs from the liquid meniscus exposed to the ambient vapor, while heat is transferred to the liquid from the solid walls of the microchannel. 68
4.4 Problem domain for the liquid-vapor meniscus generation in Surface Evolver. Face 1 is the liquid-vapor meniscus surface, which is iterated to minimize free energy; the other faces are used to define mesh surfaces and are not iterated. Geometrical constraints on the vertices and edges are used to define the channel and the liquid distribution in it. 69
4.5 Solution domain and boundary conditions for the numerical solution of the coupled fluid-thermal-evaporation problem. 73
4.6 Case I numerical simulation results: Heating of saturated incoming liquid with 5 K wall superheat. The inlet fluid is at a temperature of $T_i = 373.15\ K$, while the temperature of the channel wall is $T_w = 378.15\ K$. 77
4.7 A plot of the liquid velocity vectors inside the evaporating meniscus for different wall superheats. 78

4.8 Case II numerical simulation results: Heating of saturated incoming liquid with 10 K wall superheat. The inlet fluid is at a temperature of $T_i = 373.15\ K$, while the temperature of the channel wall is $T_w = 383.15\ K$. 79

4.9 Case III numerical simulation results: Heating of 5 K subcooled incoming liquid with 10 K wall superheat. The inlet fluid is at a temperature of $T_i = 368.15\ K$, while the temperature of the channel wall is $T_w = 383.15\ K$. 81

5.1 A design schematic of the phase-I μLHP device: (a) The top views of the device are drawn to scale; (b) Dimensioned cross-sectional view of individual device components. 86

5.2 Fabrication process flow for the Phase-I μLHP device. All of the device components are etched into the silicon wafer, while Pyrex is used as the capping wafer. 88

5.3 The fabricated phase-I μLHP prototype devices: (a) A picture showing one of the phase-I μLHP prototypes and its size comparison with a US quarter dollar. (b) A picture showing the different design variations obtained by varying the size of the in-plane wick and the number of vapor microchannels. 90

5.4 SEM images of the individual components of the phase-I μLHP device: (a-c) The evaporator section and the wicking structure; (d-f) Characteristics of the in-plane-wick microchannels. 91

5.5 A design schematic of the phase-II μLHP device: (a) The top views of the device are drawn to scale; (b) Dimensioned cross-sectional view of individual device components. 94

5.6 Fabrication process flow for the phase-II and phase-III μLHP devices. Device components are etched into the silicon wafer using DRIE and into the Pyrex wafer using HF wet etching. Anodic bonding is used to permanently bond the wafers. 96

5.7 Images of the fabricated phase-II μLHP device prototype. 99

5.8 A design schematic of the phase-III μLHP device: (a) The top views of the device are drawn to scale; (b) Dimensioned cross-sectional view of individual device components. 101

5.9 Images of the fabricated phase-III μLHP device prototype. 102

5.10 SEM images of the individual components of the phase-III μLHP device: (a-c) Topology of the evaporator section and the wick; (d) Monotonic variation of channel cross-section in the condenser section. . . . 103

6.1 Microscale loop heat pipe components susceptible to blockage due to the presence of non-condensible gases (NCGs) in the working fluid. Bubbles formed at the entrance to the rectangular wicking structure (region I) and at the end of the liquid supply channels can block the supply of liquid to the wick, causing immediate device failure. 106
6.2 A simple degassing and fluid-filling method employed in large-size cylindrical heat pipes. The working fluid should have a low boiling point, so that it readily vaporizes upon heating. 108
6.3 Thermal-flux based μLHP degassing and filling setup: (a) Superheated vapor, generated by heating the liquid in a flask, is used to purge NCGs from the μLHP. This also removes any dissolved gases from the liquid in the reservoir flask. (b) The flask is inverted and raised above the device; Using a valve the liquid is controllably bled into the device, taking advantage of pressure differential created by heating the flask. 109
6.4 Mechanically sealed plastic packaging (Method I): (a) The bottom polycarbonate (PC) plate has drilled holes containing O-rings, which align with the fill holes etched into the μLHP device. Steel microtubing is interference-fitted into these holes. A window in the bottom plate allows for the application of heat to the device evaporator section. (b) A top polycarbonate plate (with an observation window) is used to mechanically seal the package by applying pressure on the sandwiched μLHP device using screws. 110
6.5 Results for the packaging method I: (a) Implementation of the μLHP filling setup using the mechanically sealed plastic packaging; (b) Two phase flow is observed in the device during the initial stages of thermal-flux purging of the system (step 1); (c) With rise in the system temperature and pressure, pure vapor flow is observed in the device; (d) After the completion of the thermal-flux refilling step (step 2), no vapor bubbles are observed inside the device. 111
6.6 Aluminum double compression fitting assembly (DCFA) packaging (Method II): Copper tubing is mechanically placed on top of the μLHP fill holes using a machined aluminum setup. The tubing can be either epoxied or soldered onto the device. In the latter case, a thin metal film has to be deposited on the wafer. 113
6.7 Results for the packaging method II: (a) Implementation of the μLHP filling setup using the DCFA packaging; (b) The solder connections get compromised and leak water under high pressure, indicating the need for improving tube-to-chip soldering techniques. 114

6.8 Cold-welded plastic packaging (Method III): (a) A base is machined out of plastic, with cavities that can interface with the μLHP fill holes. The cavities lead to smaller holes, which are interference-fitted with copper microtubing. (b) A cold-weld epoxy is spread around the cavities, and the μLHP device is placed on top of the plastic base, making sure the device fill holes align with the base cavities. More epoxy is used on the top to increase the mechanical strength of the package. 115
6.9 Results for the packaging method III: (a) Implementation of μLHP filling setup using the cold-welded plastic packaging; (b) At low purge pressures, two-phase flow is observed through the device without any leaking; but at higher pressures, the epoxy seal is compromised at the inlet port by the superheated steam; (c) Additional high-temperature epoxy, employed to plug the possible leak, is also found to delaminate from the wafer surface. 116
6.10 A standardized packaging solution for degassing and liquid charging of arbitrarily spaced μLHP devices: (a) A schematic of the packaging approach; (b) A picture of the different components of the package; (c) A picture of the packaged phase-II μLHP device, with inlet and outlet copper tubing connected to steel values for controlling fluid flow into and out of the device. 117
6.11 Device degassing and fluid-charging results for the standardized packaging approach: (a) A picture of the degassing and filling setup; (b) A high speed image showing the movement of two-phase fluid (water) through the device during the thermal-flux purging process. 118
6.12 A hermetic sealing approach for sealing the μLHP device during the high-temperature degassing and fluid-filling process: (a) Pattern metal thin-film; (b) Place preformed solder ball; (c) Attach gasket-sealed filling-cavity, and degas and fill the device with water; (d) Boil off water from the vicinity of the fill-hole; (e) Inductively melt the solder to seal the hole. 120
6.13 Fabrication of holes in a silicon wafer for testing the inductive-soldering approach: (a) Fabrication process flow; (b) Wet-etched holes. 121
6.14 Experimental setup for implementing inductively-heated solder-sealing of holes in a silicon substrate: (a) Induction heating apparatus; (b) Solder-on-hole sample preparation. 122
6.15 Experimental results demonstrating inductively-heated solder sealing of holes: The key parameters are the initial mass of the solder preform and the induction heating time. (a) Soldering without flux is unsuccessful; (b-c) Low solder mass can be unstable; (d-e) Larger (optimum) solder mass ensures good sealing in a wider time window; (f) Soldering in water is successful. 123

7.1 Experimental setup for the operational testing of the phase-I μLHP device. A ceramic heater is used to heat the evaporator section of the packaged and filled μLHP device, while thermocouples are used to track the temperature of the heater. The condenser section of the device is cooled by ambient natural convection. 128
7.2 Liquid evaporation in the phase-I μLHP device connected to an external fluid reservoir (schematic representation of experimental observations): (a) Device completely filled with degassed water and connected to the external fluid reservoir via the inlet port; (b) Moderate heat-flux applied to the evaporator; (c) Larger heat-flux applied to the evaporator, expelling fluid from the device; (d) Fluid refilling the device as heater temperature is reduced; (e) Further cooling of the device. . . 129
7.3 Liquid evaporation in the phase-I μLHP device disconnected from the external fluid reservoir (schematic representation of experimental observations): (a-b) External fluid reservoir disconnected from the inlet port (open to ambient) of device completely filled with degassed water; (c) Inlet port closed after partially expelling water from the device. Unsteady boiling observed in the heated evaporator; (d) Working fluid rearrangement after device has cooled to room temperature. 130
7.4 Experimental setup for the operational testing of the phase-II μLHP device. A hot air gun is used to heat the evaporator section of the packaged and partially filled μLHP device, while the condenser section of the device is cooled by ambient natural convection. A high speed camera is used to observe the evaporator section of the device, which is illuminated by multiple light sources. 135
7.5 Liquid evaporation in a partially filled phase-II μLHP device. The images are taken using a high speed optical camera. 137
7.6 Experimental setup for the operational testing of the phase-III μLHP device. A hot air gun is used to heat the evaporator section of the packaged and partially filled μLHP device, while the condenser section of the device is cooled by ambient natural convection. A high speed camera is used to observe the evaporator section of the device, which is illuminated by multiple light sources. 140
7.7 Liquid evaporation in a partially filled phase-III μLHP device. The images are taken using a high speed optical camera. 141

8.1 A schematic of the experimental setup for measuring evaporation characteristics of the in-plane-wicking micro loop heat pipe (μLHP). The setup can be configured to obtain either visual data using a high speed optical camera or temperature data using an infrared (IR) camera. . 144

8.2 The experimental setup for studying evaporation in the phase-II μLHP using a high speed optical camera: (a) The overall setup; (b) The device test rig; (c) Close-up view of the device setup; (d) Computer showing image of device evaporator; (e) Liquid cooling system; (f) Heated external fluid reservoir. 146
8.3 The experimental setup for studying thermal characteristics of the μLHP during evaporation in the wicking structure: (a) Overall setup; (b) The device test rig; (c) Power source and thermocouple box; (d) Infrared (IR) camera. 147
8.4 Temperature of the saturated liquid-vapor system in the heated external fluid reservoir. The plate heater was set to a temperature of 260 ^oC, but the liquid and vapor temperatures in the glass flask were measured to be approximately 139 ^oC and 135.5 ^oC, respectively. . . 148
8.5 Evaporation characteristics of the μLHP in-plane wick during device startup, under an applied heat source of 12.63 W: (a) Device in OFF state; (b) Power to the ceramic heater turned on; (b-c) Vapor forms in the Pyrex evaporation cavity; (d-e) Thin-film evaporation occurs from the in-plane wick microchannels underneath the Pyrex evaporation cavity. 150
8.6 Effect of applied heat flux on steady-state evaporation in the in-plane wicking structure. Q is the thermal power output of the ceramic heater, Q" is the applied heat flux per unit area, and Δt is the time elapsed after the heater voltage is increased. 152
8.7 The surface temperature profile of the phase-II μLHP at different values of applied evaporator heat flux. Q is the thermal power output of the ceramic heater, Q" is the applied heat flux per unit area, T_{ch} is the temperature of the ceramic heater, and T_{hs} is the temperature of the heat sink. 153

List of Tables

3.1 Design constants of the μCLHP 50
3.2 Parameters of the μCLHP design optimization problem 52
3.3 Objective function and equality constraints for the μCLHP design optimization problem 53
3.4 Inequality constraints for the μCLHP design optimization problem . . 53
3.5 Initial Monotonicity table 54
3.6 Monotonicity table (Case I) 55
3.7 Monotonicity table (Case II) 56
3.8 Objective function and constraints for the pre-optimized μCLHP design optimization problem 58

4.1 Vertex, edge, and face constraints for meniscus shape definition . . . 70

Acknowledgments

First, I would like to thank my adviser Prof. Albert P. Pisano for both his professional and personal help and support during my doctoral years the University of California, Berkeley. I have not only acquired a lot of engineering and management skills from him, but also learned how to be an ambitious and a kind person at the same time.

I am also grateful to my postdoctoral research specialists Dr. Matthew Hopcroft and Dr. Jim Cheng for their valuable guidance and support in the early and later years of my Ph.D., respectively. My thanks are also due to all my fellow researchers in the Berkeley Micromechanical Engineering and Design (BMAD) lab, who helped to provide a stimulating and collaborative environment for the generation and exchange of novel and innovative ideas. I would also like to thank staff of the Berkeley Sensor and Actuator Center and the Berkeley Microfabrication Laboratory for their direct and indirect help and assistance in furthering my research efforts.

Last but not the least, I want to express my deepest gratitude to my family for their love and support during all these years. My mother has always been a source of inspiration for me and she, as a science teacher, was the one who started me on the path leading to this point. I also want to thank my wife Anurit for her unwavering support and patience during my graduate years. Without you, this would not have been possible.

Part I

Overview

Chapter 1

Introduction

1.1 Motivation

The electronics industry is currently in dire need of new thermal management solutions. Due to market pressures and technology advancements, the heat dissipated per unit area of an electronic chip is increasing continuously. Further, electronic systems and subsystems are becoming more densely packed, which is making the task of cooling them more difficult. Conventional thermal management solutions, which include solid conduction at the chip level and convection air cooling at the package level, are no longer sufficient for cooling contemporary electronic devices and systems. Silicon-based chip-scale electronics can operate reliably only below a given safe temperature limit, which is typically quoted to be 120^oC. In addition to this, many system components are susceptible to thermal stress damage. In this section, we will provide motivation for the present work by first looking at the thermal management demands of a host of different electronic devices. Following this, we will take a look at the cooling capabilities of various thermal management technologies currently in the market and also those that are being actively researched.

1.1.1 Thermal Management Demands of Electronic Devices

Computers and Laptops

Computers and laptops occupy a big share of the consumer electronics market. Today's devices are much more powerful, compact, and lightweight compared to their counterparts from only a decade ago [2]. This has been possible in-part due to the tremendous advances in the microprocessor or integrated chipset (IC) industry. The primary sources of heat inside a computer are the Central Processing Unit (CPU) (which contains the high-speed microprocessor) and the associated electronics (hard drive, graphics card, memory card etc.) [2].

The number of transistors per unit are of the microprocessor chip has been in-

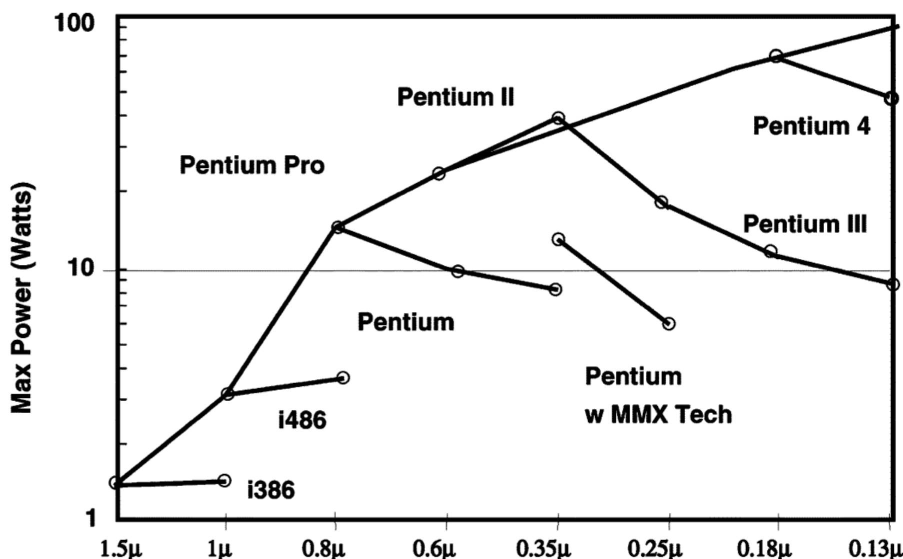

Figure 1.1: Change in the maximum power dissipation of successive generations of Intel microprocessors [1].

creasing steadily with each new generation—according to Moore's law they double every 18 months [1]—while the size of the individual transistor and that of the chip itself has decreased. While this has improved overall circuit performance and reduced the cost of an individual transistor component, it has also led to an increase in the heat dissipated per unit are of the chip surface. Figure 1.1 shows how the maximum power dissipated by Intel microprocessors has increased exponentially with each new generation.

The dominant component of power dissipation in circuits is the *switching power*—power dissipated due to the charging and discharging of the capacitive load. However, *leakage power*, which is the other main component, is also increasing at an exponential rate due to sub-threshold and gate oxide tunneling [1]. Another major problem arises due to chip thermal hotspots, which can be as large as eight times the average power density.

Laptops are now becoming popular and commonplace due to their slim cabinets, increased processing power, and enhanced graphics capabilities [2]. The waste heat output of current laptops is estimated to be about 25 to 50 W. These devices pose an even larger thermal management problem. Due to the compact structure of laptops, thermal control devices have to contend with limited space availability, in addition to the high heat flux densities [2]. In Figure 1.2 is shown the amount of space that is available inside a modern laptop for accommodating thermal management components. The microprocessor chip generating the heat is just 10 $mm \times 10$ mm in size, and it usually lies somewhere near the center of the laptop. The heat generated

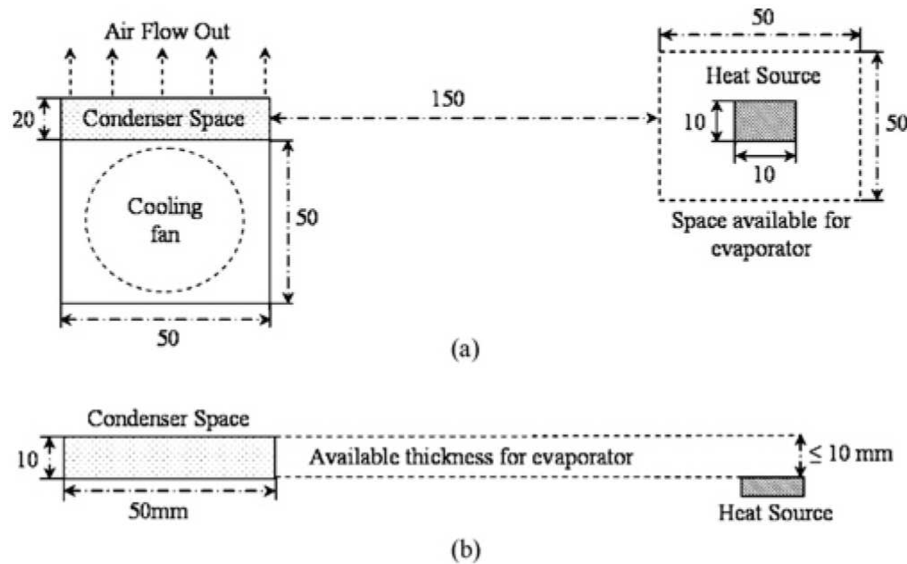

Figure 1.2: The available space inside a modern laptop for accommodating a thermal module (all dimensions in mm): (a) Top view; (b) Side view [2].

by the chip has to be carried to a heat sink (usually a cooling fan) at the periphery of the cabinet. Due to the compact nature of laptops, the thickness of the cooling device usually cannot exceed 10 mm, and in many recent thinner versions this value is required to be less than 3 mm. This means that the cooling module not just has to provide a large thermal conductivity value, but also has to have a slim cross-section in order to fit inside the laptop.

Power Amplifiers

Radio frequency (RF) solid-state power amplifiers (SSPA) are employed in a number of portable communication systems, the best examples of which are the modern cell phones and smart phones. Due to recent industry trends towards higher operating frequencies (> 5 GHz for personal communications service), packaging and thermal management of these devices is becoming more and more difficult [18]. This is because, irrespective of whether the technology uses field-effect or bipolar transistors, there is a drop in efficiency at higher operating frequencies, which essentially implies larger heat dissipation per chip. Chip heat flux densities have reached values as high as 1 kW/cm^2 in some applications [18].

The use of multi-chip modules (MCM) in RF products for wireless applications allows for mixed signal computing and higher integration, which means portable electronic products can offer more features for enhanced communication. But this multi-chip topology also creates significant thermal management problems [19]. A low thermal resistance path has to be provided from the heat source to the system card.

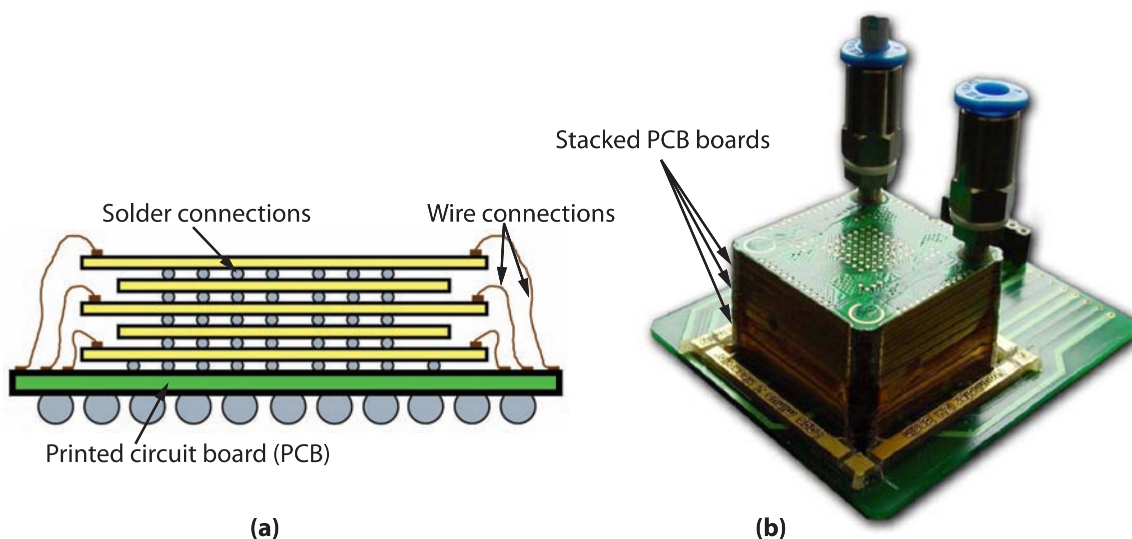

Figure 1.3: Stacked 3-D electronic packages: (a) A 3-D stacked die package, where the dies are electrically connected using through silicon vias (TSV) and solder connections [3]; (b) A larger scale 3-D package, where the printed circuit boards (PCBs) are stacked on top of each other [4].

However, due to the topology of MCMs, conventional conduction-based heat removal paths are insufficient, especially during high duty cycles and for higher output powers.

Stacked Electronics Packages

A new trend that has emerged in the development of advanced microsystems is the use of three dimensional integrated circuits. This means that instead of having all the electronic chips distributed on a single flat printed circuit board (PCB), either the chips are stacked on top of each other [20, 3] or the individual PCB modules containing electronic chips are arranged on top of each other to make full use of the third dimension [4]. This is called die level and package level stacking respectively. In Figure 1.3(a) is shown a schematic of a 3-D stacked die package, where the different layers are electrically connected to each other using through silicon via (TSV) technology and individually wired to the PCB substrate. In Figure 1.3(b) is shown a 3-D package where PCBs are stacked on top of each other. Three dimensional packages offer the following two major advantages over single chip packages: 1) improved electrical performance due to shorter interconnect distances between devices [3], and 2) a large reduction in size, which makes them the package of choice when real estate on the board is a premium [21].

Despite all their advantages, current die and package level stacking is limited to low power applications, such as memory, base band, and logic devices [21]. In fact, thermal management is one of the biggest performance bottlenecks for stacked 3-D packages, especially when the package size is small and power dissipation is high [22].

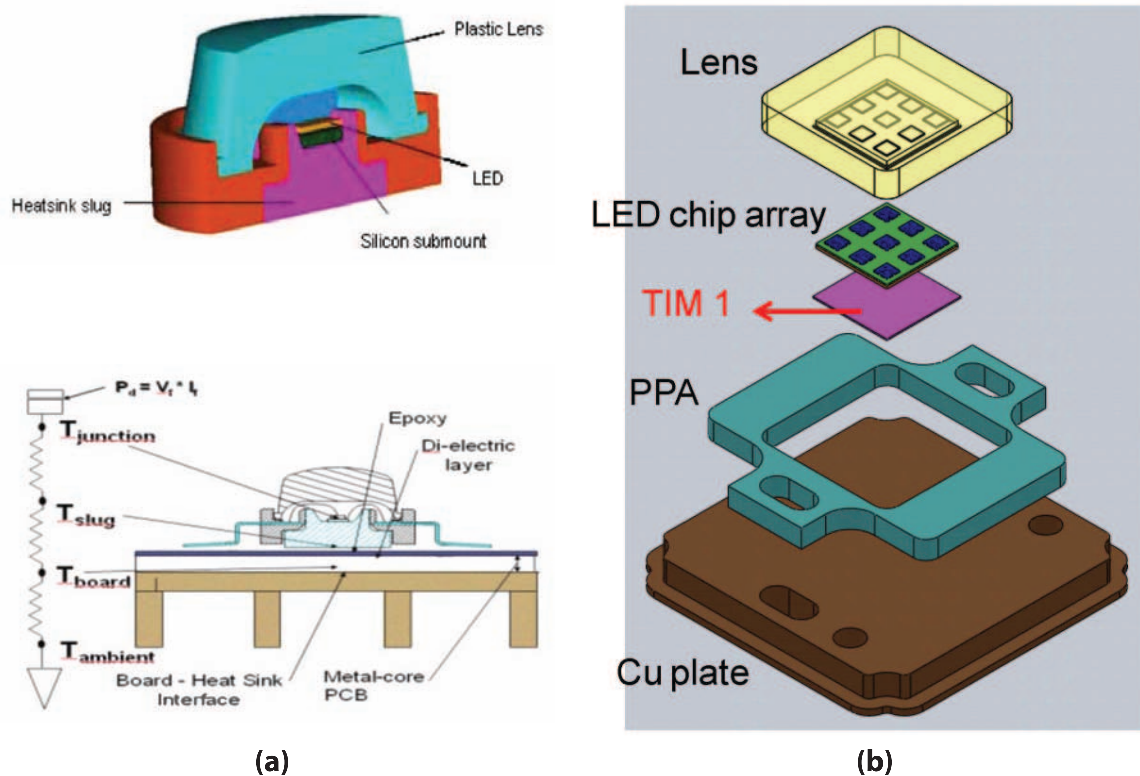

Figure 1.4: High power light emitting diodes (LEDs): (a) A packaged single high-power LED chip with an air cooled heat sink [5, 6]; (b) A packaging assembly for a high power LED chip array, which can be interfaced with a heat sink [7].

In the case of single-chip packages, heat generated by the chip can readily flow to the PCB metalization layer. On the other hand, in 3-D stacked packages the heat has to travel a much longer distance, across many interfaces, to reach the cooling solution exterior to the package [20]. The resulting large conduction thermal resistance in these packages can significantly increase the junction temperatures, resulting in performance degradation and even device failure.

High Power LEDs

High-power light emitting diodes (LEDs) are another application area where thermal management will have a big role to play in the coming years. The LEDs initially developed in the 1960s primarily produced white and monochromatic light in the milliwatt range, for indicators and small displays [5]. However, by the 1990s LEDs had evolved into a fascinating, multifaceted, watt-level light source technology [5]. Compared to conventional incandescent and fluorescent light sources, LEDs exhibit a number of favorable characteristics, such as high flux efficiency and reliability, low power consumption, long life, and reduced environmental impact [23]. Today, LEDs

are used in a number of applications, such as liquid crystal displays (LCD), mobile projectors, interior and exterior automotive lighting, large signs and displays, traffic signals, street lighting, and general lighting [23, 24].

The optical conversion efficiency of high power LEDs, however, is only about 15–30%, which means that 70–85% of the input power is converted to heat [25, 24, 26]. This heat, if not properly dissipated, increases the junction temperature of the LED, which has an adverse effect on the optical efficiency, the spectrum, the reliability, and the life of the LED [23, 7, 24]. In Figure 1.4 is shown the design and packaging characteristics of single chip and multi-chip-array high power LED systems. These devices come in different packaging configurations, a primary design objective of which is to remove the waste heat from the LED. Due to the market demand for high-luminosity LED lighting systems, densely packed LED chip arrays are being developed and the power dissipated by individual LED chips is also on the rise. Chip heat fluxes have already reached values in excess of 80 W/cm^2 according to one source [26]. Although most of the initial LED thermal management systems employed air cooled heat sinks [7], active liquid cooling approaches are now being seriously pursued [5, 27, 26, 28].

Automobile Electric Batteries

Due to the increasing price of oil and in an effort to address the challenge of pollution from gas emissions, the automobile industry, worldwide, is trying to move away from conventional internal combustion engines (ICE), and towards the development of electric and hybrid electric vehicles [29, 30]. Electric vehicles (EVs) are still a long distance away from large scale commercial production, mainly due to the large cost associated with batteries. However, hybrid electric vehicle (HEV) technology has already been successful in increasing the mileage of cars, and plug-in HEVs look promising in the near future [29].

Battery technology is the main stumbling block in the success of EVs and HEVs. Batteries for automobiles need to have a high efficiency, high energy and power densities, and a long life in order to successfully compete in the market, which is still mostly driven by liquid fuels. The battery technologies that are in this competition include Lead acid (VRLA), Nickel Cadmium (Ni-Cd), Nickel Metal Hydride (Ni-MH), and Lithium Ion (Li-ion) [29]. Batteries and power electronics for a typical electric automobile are shown in Figure 1.5. Li-ion and Ni-MH batteries, due to their high energy densities, are showing the most promise for future application in electric vehicles. However, thermal management and accurate temperature control are major concerns for both these battery technologies that still need to be addressed in a comprehensive manner.

A large amount of heat is generated in batteries due to the high currents flowing to and from the battery during the rapid charging (when the battery is plugged into an outlet) and discharging (during large vehicle accelerations) events, respectively.

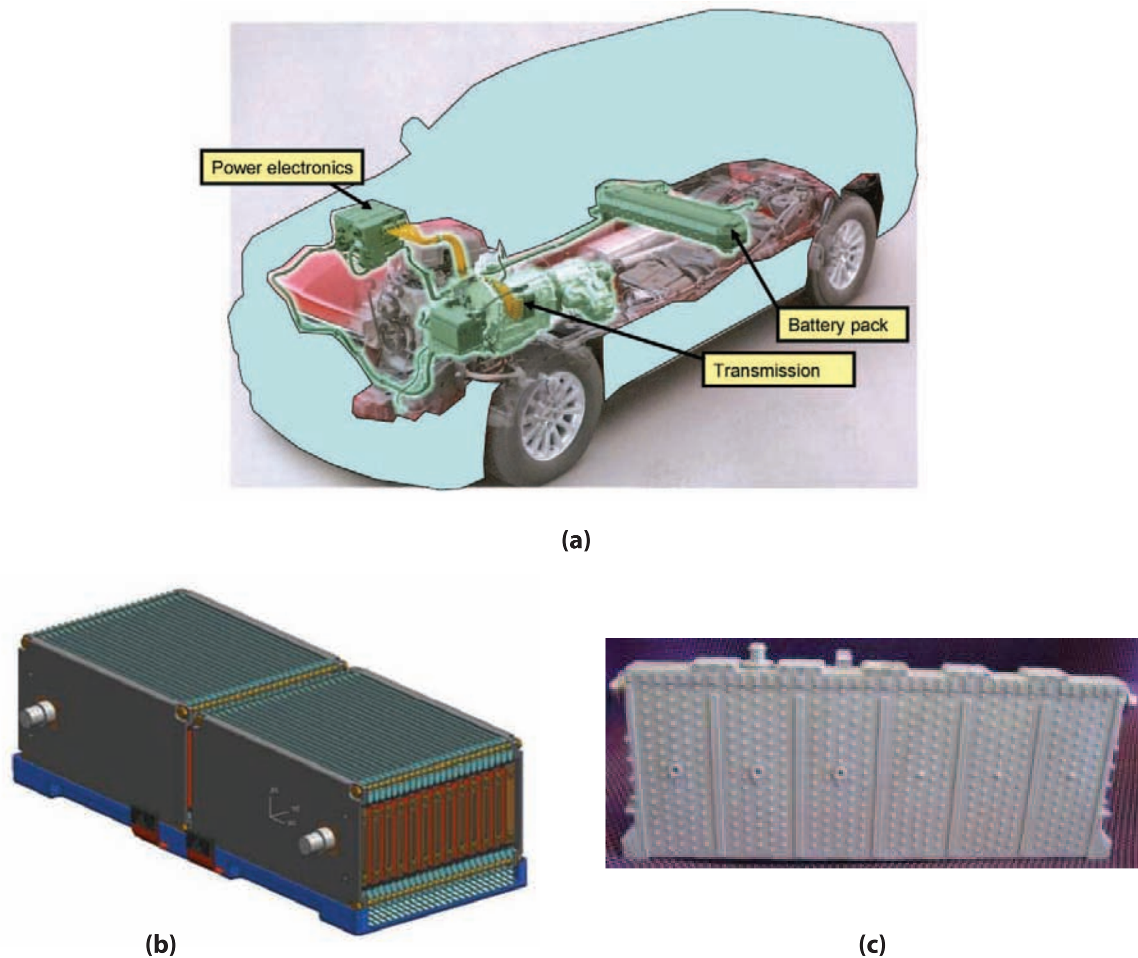

Figure 1.5: Electric batteries for automobiles: (a) Power components in an automobile [8]; (b) A lithium-ion (Li-ion) battery pack consisting of 48 cells connected in series [9]; (c) Panasonic Nickel Metal-Hydride (Ni-MH) battery module used in the 2001 Toyota Prius [10].

This impacts battery characteristics, such as capacity, power, and self-discharge, and reduces the total life of the battery [29]. All batteries have a given temperature range for optimum performance. Further, any non-uniformity in temperature distribution in the battery pack also leads to performance degradation [8, 30]. For example, the best operating temperature range for Li-ion batteries is from $-10\ ^oC$ to $50\ ^oC$ [9]. These batteries are also prone to explosion due to overheating [29]. Thermal management solutions will therefore have to be incorporated into the design of future electric vehicle batteries, to make them efficient, safe, and reliable. Potential cooling solutions should be able to deal with the large heat fluxes that are generated during rapid charging and discharging of batteries. The thermal management should also be localized in order to ensure minimum temperature variation inside the battery pack.

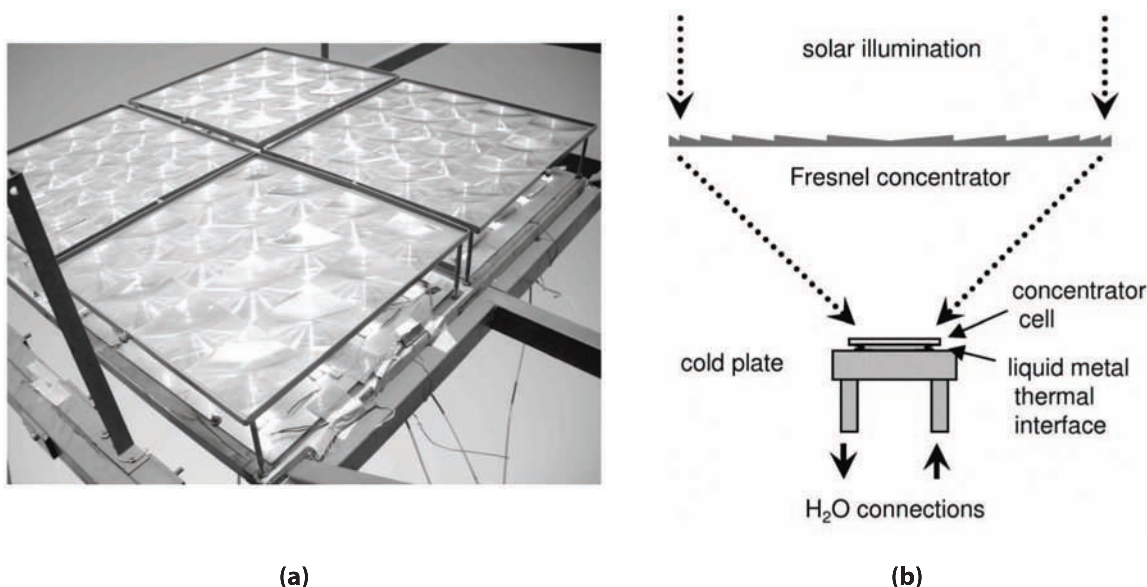

Figure 1.6: Concentrating Photovoltaic (CPV) cells experience experience large incident solar intensities leading to large waste heat flux generation. (a) A photograph of a Fresnel lens CPV module [11]. (b) A schematic showing how a Fresnel lens concentrates the solar flux incident on a larger area onto the much smaller concentrator cell. Active liquid cooling is used to cool the cell [12].

Solar Cells

Solar Photovoltaic (PV) cells or solar cells are one of the most promising sources of renewable energy, which is the key to a sustainable future for the human race [11]. A number of different solar cell technologies are currently in development, and they fall into three basic groups: organic, semiconductor, and thin film material [31]. Semiconductor-based solar cells are fabricated out of both silicon and III-V semiconductors, and currently constitute the most mature segment of the photovoltaics market [32]. In order to succeed in the market and replace conventional non-renewable energy sources, solar cells need to make substantial progress on the following fronts: 1) increasing the efficiency of incident-to-output energy conversion, 2) decreasing the capital investment required for PV installations, and 3) reducing the continuing output energy cost [31]. As we will see, efficient thermal management has emerged as one of the most important design requirements in enabling competitive solar cell energy generation systems.

The energy conversion efficiency of currently available solar cells lies somewhere between 10–30% [31, 32]. This means that only 10–30% of the solar energy incident on the cell surface is converted to electricity, while the rest is converted to heat. This waste heat increases the temperature of the material and has to be dissipated by providing appropriate thermal pathways, because the energy efficiency of semiconductor junction solar cells decreases with an increase in temperature [11, 33]. At higher tem-

peratures, the equilibrium population of electrons increases, resulting in a larger dark saturation current density. This decreases the output voltage and thus the output electrical power of the cell [31, 34], leading to reduced cell efficiency. Now, cooling of conventional PV cells is not a big problem due to the fact that the incident solar power per unit surface area on these cells is only one sun, which corresponds to a value of only about 1000 W/m^2 [31]. But in this case the entire surface of the PV system is covered with solar cells, which leads to inherently high costs due to the fact that silicon and III-V semiconductors are expensive materials [31].

To reduce material costs, the semiconductor solar cell industry is moving towards concentrating photovoltaic (CPV) systems, where low cost concentrating technologies such as parabolic dish reflectors, trough reflectors, disc-shaped reflectors, and Fresnel lens solar collectors are used to project solar intensities from 200–2000 *suns* on multi-junction solar cells [35, 11, 12]. In Figure 1.6 is shown a CPV system where relatively cheap Fresnel lenses are used to concentrate the incident solar flux onto the much smaller concentrator solar cells placed directly underneath them. The concentrator cells (and the Fresnel lenses) are arranged in arrays to absorb the solar flux from a very large surface area, without having to cover that entire area with solar cells. Although this approach provides the additional advantage of significantly enhanced energy conversion efficiencies (at the same temperature) [32, 35], it leads to substantial thermal challenges. Depending on the value of concentrated solar intensity, the waste heat flux that must be removed from the chip can be anywhere from 10–140 W/cm^2 [31, 35, 12]. In the absence of appropriate cooling mechanisms, the temperature of the solar cell can rise significantly, leading to not just short term efficiency losses but also long term irreversible damage to the system [34]. In fact, thermal issues associated with high solar flux in CPV systems are a major hurdle in the proper implementation of these systems. For example, in Figure 1.6 each concentrator cell is being individually cooled by forced liquid convection [12]. This requires additional power and makes the system much more inefficient and complex. Better thermal management strategies need to be developed in order to enable the large scale profitable implementation of these vital renewable energy generation systems.

1.1.2 Thermal Management State of the Art

In this section is found a brief overview of the currently available thermal management technologies and their salient characteristics. All thermal management systems can be broadly divided into two categories: 1) active cooling systems, which are mechanically assisted and require external power for operation, and 2) passive cooling systems, which are self-sustaining [36]. Examples of active cooling include forced air convection, forced liquid convection in microchannels (both single and two-phase), jet impingement cooling, spray cooling, thermoelectric coolers, and refrigeration systems. Passive cooling solutions include heat spreading by conduction, heat sinks cooled by natural convection, solid phase change materials for energy storage, and liquid phase

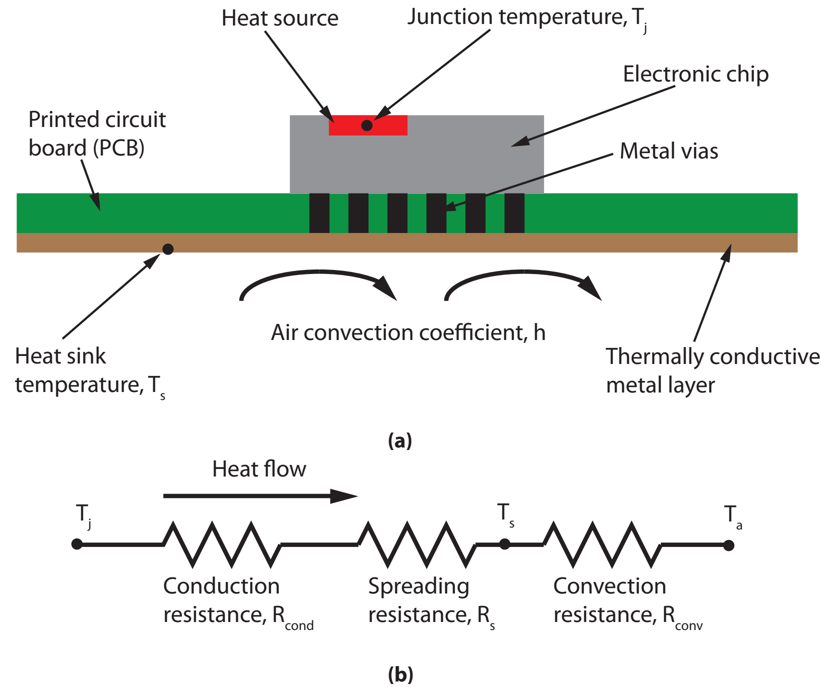

Figure 1.7: Cooling of a hot electronic chip by conduction and natural convection: (a) Schematic of the chip on the printed circuit board (PCB); (b) The thermal resistance network for the flow of heat from the chip to the ambient air.

change-based passive heat transport systems (heat pipes, loop heat pipes, and capillary pumped loops).

Conduction / Natural Convection

Heat transfer by conduction is one of the simplest and earliest techniques employed by the electronics industry for getting rid of waste heat and keeping device junction temperatures within the safe operating limit. In Figure 1.7, it is shown how simple conduction can be used to reject heat from a hot electronic chip to the ambient air. The chip is mounted onto a printed circuit board (PCB) for packaging and for establishing electrical connections. By coating the backside of the PCB with a thermally conductive metal layer (such as copper) and providing metal vias from the chip to this layer, the heat can be effectively dissipated to the ambient. The heat conducts to and spreads over of the copper layer, which provides a large surface area for heat dissipation by natural convection. The device junction temperature is given by

$$\begin{aligned} T_j &= T_a + \dot{Q}\left[\left(\frac{t_{chip}}{A_{chip}k_{chip}} + \frac{t_{vias}}{A_{vias}k_{vias}}\right) + R_s + \left(\frac{1}{hA_s}\right)\right] \\ &= T_a + \dot{Q}\left[(R_{cond}) + R_s + (R_{conv})\right] \end{aligned} \tag{1.1}$$

where T_a is the ambient air temperature and $\dot{Q}$ is the thermal power dissipated by the chip. The junction temperature rises with increases in heat dissipation ($\dot{Q}$) as well as the conduction (R_{cond}), spreading (R_s), and convection (R_{conv}) resistances.

Early electronic devices were large ($A_{chip} \uparrow$, $A_{vias} \uparrow$) and generated low waste heats ($\dot{Q} \downarrow$). As a result, moderate values of thermal conductivities (k_{chip}, k_{vias}, k_{metal}) and convection coefficients (h) were enough for keeping the junction temperatures within the allowable limit. However, due to increasing electronic thermal budgets ($\dot{Q} \uparrow$) and constant device miniaturization trends ($A_{chip} \downarrow$, $A_{vias} \downarrow$), conventional conduction and convection cooling technologies are no longer sufficient. Ultra high thermal conductivity materials, such as diamond, are being looked into to reduce the conduction resistance from the heat source to the heat sink, and the heat sinks are themselves being modified to reduce the thermal resistance component associated with convective heat transfer. Finned heat sinks are widely being used for reducing the spreading resistance (R_S) and increasing the heat sink area (A_s) available for convection heat transfer. However, natural convection is only known to effectively handle electronic heat fluxes in the range of 0.0155–0.155 W/cm^2 [36]. This is clearly not enough for most modern high-heat-flux electronics.

Forced Convection Air Cooling

Forced convection air cooling is employed in situations where natural convection is not sufficient, or the module containing the heat generating component can not be properly ventilated. It is used in a variety of electronics systems, both portable devices as wells as large business systems. It can involve the use of a fan, pump, or a jet of air to increase the convective heat transfer coefficient, and is usually accompanied by the use of extended surfaces such as finned heat sinks to increase the total area available for convective heat transfer. The range of electronic heat fluxes that can be handled by forced convection lies between 0.08–1.6 W/cm^2 [36].

Zhang *et al.* [7] has numerically demonstrated the use of forced air convection in the cooling of a LED lighting module. A piezoelectric fan blowing air at 2 mm/sec into a 12 fin heat sink can reduce the temperature of the 10 W LED luminaire by almost 35 ^oC. Grimes *et al.* [37] has shown that, for a constant surface temperature, the power dissipation by a cell phone can be increased 50–75% by using a miniature cooling fan inside the package. Despite these novel applications, as we move towards electronic heat fluxes in excess of 1 W/cm^2, the heat transfer coefficients afforded by convective air cooling become insufficient [38].

Liquid microchannel cooling

Liquid cooling is the preferred approach for cooling high power electronics, since it can provide much larger convective heat transfer coefficients than air cooling. Liquid microchannel cooling is one of the many different variations in which liquid cooling

can be implemented. The range of heat fluxes that can be absorbed by conventional single-phase and two-phase liquid convective cooling are 1.1–93 W/cm^2 and 1.55–140 W/cm^2, respectively [36]. However, microchannel coolers have been shown to absorb heat fluxes as large as 1430 W/cm^2 [38]. In this approach, using external pumping, liquid is flown through a series of microchannels that are interfaced with the heat source. The liquid absorbs the heat conducted to the channel walls either by single phase convection or by additionally undergoing boiling in the channels. There are many challenges, however, to the implementation of microchannel cooling in electronic systems, such as 1) electrical and corrosion problems arising from liquid leakage, 2) large pressure drops in the microchannels, which necessitate the use of large and powerful pumping solutions, and 3) temperature non-uniformity in the channels [38, 36]. The external pumping requirement can be reduced by using moderate boiling point fluids (e.g. R-113, Flourinert^{TM}, and Novec^{TM}), which can absorb larger heat fluxes at smaller mass flow rates due to the boiling latent heat. However, compared to water, these fluids have lower thermal conductivities and latent heats, which adversely affects their cooling performance [36].

Kim *et al.* [5] studied the two-phase thermo-fluid characteristics of a dielectric liquid, FC-72, for the purpose of two-phase microchannel cooling of an LED array. For a 500 μm deep, 10 mm wide, and 37 mm long channel, the area-averaged heat transfer coefficient was measured to be 0.75 W/cm^2K. For a wall superheat of 60 K, this can dissipate a heat flux of about 45 W/cm^2 from the LED array. Calame *et al.* [39] conducted experimental investigations to examine the impact of the number of branching levels on the performance of a hierarchically-branched water microchannel cooler. Optimum performance was achieved using a three-channel-size configuration, with effective heat transfer coefficients of approximately 13 W/cm^2K at a water flow rate of 275 mL/min. Kermani *et al.* [40] achieved a heat transfer coefficient of 6.5 W/cm^2K, at a water flow rate of 1.1 gm/sec, using a novel manifold heat sink. Lee *et al.* [41] demonstrated that a microchannel heat sink (using HFE7100 as the working fluid) integrated into an indirect refrigeration cooling system can dissipate heat fluxes as high as 840 W/cm^2 without incurring the critical heat flux.

Liquid Jet Impingement Cooling

Jet impingement is another active liquid cooling technique that can successfully remove high heat fluxes from electronic components. In this approach, a jet of liquid capable of providing high convective heat transfer coefficients is directed at the heat source, which leads to high heat transfer rates near the stagnation point [36]. The jets can be generated by nozzles, orifices, or slots, and can be either free surface jets or submerged jets [38]. Also, depending on the fluid properties, the fluid temperature, and the temperature of the surface being cooled, the cooling can be either single phase or two phase [36]. A maximum heat flux absorption rate of 2000 W/cm^2 has been reported in the literature [38]. The main drawbacks of this approach are 1) the

large pumping power requirement for maintaining the liquid jet and cycling back the spent liquid, 2) the large weight and volume footprint associated with such a pumping system, and 3) the need to protect the electronic circuitry from the working fluid.

Luo *et al.* [42] demonstrated a microjet-based cooling system for the thermal management of high-power light-emitting diodes (LEDs). Using this system, the temperature of a 4 $cm \times 4$ cm LED array containing 64 chips and generating 220 W of thermal power can be maintained under a temperature of 70 ^oC. Michna *et al.* [43] investigated the impingement heat transfer performance of a water jet, using a device with orifices fabricated using MEMS microfabrication techniques. The microjet was able to absorb a heat flux of 400 W/cm^2 with a 50 ^oC temperature difference. Elsewhere, heat removal rates as high as 2000 W/cm^2 have been reported using a jet that employs a eutectic alloy of Gallium and Indium as the working fluid [38].

Liquid Spray Cooling

Another liquid cooling technique, which bears some resemblance to jet impingement, is spray cooling. In this approach, a spray of the cooling liquid, injected from a nozzle or orifice, is aimed directly at the surface of the heat source [38, 36]. The spray droplets that hit the hot surface can evaporate individually or form a thin liquid film that affords high rates of evaporation. Cooling happens due to both single phase convection as well as the evaporation of the thin liquid film. The hot liquid and vapor cools in a container before it is pumped back to repeat the cycle [36]. Spray cooling is advantageous in the sense that direct spraying of the coolant liquid on hot electronics eliminates contact and conduction thermal resistances, and ,further, the ratio of the pumping power to the heat removed is smaller compared to microchannel cooling and jet impingement [36]. The main disadvantage of this technique is that protective coatings are required to prevent electronic short circuits in case the working liquid has a low dielectric strength. Alternative working fluids such as Flourinert^{TM}, FC-72, and R-134a can help avoid these problems, although they don't provide the same level of performance as water [36].

Mudawar *et al.* [44] has shown that spray cooling using HFE-7100 as the working fluid can extract heat fluxes as high as 200 W/cm^2 from hybrid vehicle electronics, while maintaining surface temperatures below 125 ^oC. Cotler *et al.* [18] has demonstrated a spray cooling system for the thermal management of a 500 MHz RF power amplifier. The junction temperature was reduced from 214 ^oC to 115 ^oC, with a spray-induced heat flux absorption rate of 162 W/cm^2. Heat flux removal rates as high as 1200 W/cm^2 have been achieved using spray cooling, according to published literature [38].

Thermoelectric Cooling

Thermoelectric coolers are solid state devices that use Peltier, Seebeck, and Thomson effects to implement cooling [36]. In semiconductor materials, both phonons and electrons/holes can transport heat. Whereas phonons only travel under an applied temperature gradient, electrons and holes are charged particles and can be manipulated using an applied electric potential. Taking advantage of this property of electrons/holes, an applied voltage can be used to transport heat from one end of a semiconductor to the other end, even under an adverse temperature gradient. Thermoelectric cooling is used in applications where temperature stabilization or cooling below ambient are required. It has been considered for the integrated cooling of opto-electronic devices such as semiconductor lasers and detectors, which require a low temperature for maintaining device performance [36]. The advantage of thermoelectric cooling lies in the fact that it involves no moving parts. However, it requires significant amount of external power for operation. Further, its main action of lowering the temperature of the heat source is thwarted by the fundamental material challenge of coming up with semiconductor materials that are both bad thermal conductors and good electrical conductors at the same time. Most of the current research in thermoelectrics is aimed at engineering materials with such properties.

Cheng *et al.* [45] used a silicon-based thermoelectric device between a high power LED and an aluminum sink to reduce the effective thermal resistance seen by the LED by 13.72 $^oC/W$. By supplying a current of 0.27 A to the thermoelectric device, a temperature drop of 24.9 ^oC could be achieved across the thermoelectric device. Alaoui *et al.* [46] implemented a thermoelectric pump-based thermal unit for the thermal management of electric and hybrid vehicles.

Solid Phase Change Materials (PCMs)

Solid phase change materials (PCMs) can absorb large amounts of heat due to the latent heat of fusion. A passive cooling approach based on these materials is suitable for managing transient power dissipation by electronics and for cooling IC packages that work in a boolean manner [36]. Because these materials have a high thermal resistance, they are usually embedded in other heat spreaders. They can therefore absorb sudden large heat fluxes, which are then dissipated to the environment over time as the melted material re-solidifies. Fok *et al.* [47] experimentally demonstrated the cooling of a 3–5 W portable handheld electronic device, using eicosane as the phase change material placed inside heat sinks with and without internal fins. The viability of the PCM-based heat sinks with internal fins was confirmed subject to the optimization of the amount of PCM used and the number of fins employed, depending on the power level of the heat source and the usage mode of the device.

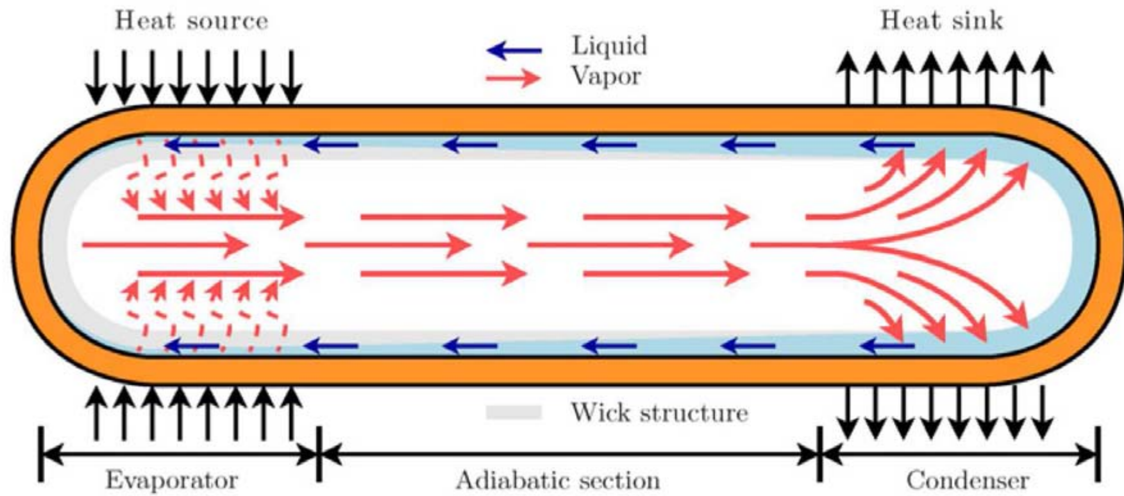

Figure 1.8: A schematic showing the overall structure and theory of operation of a heat pipe [13].

Heat Pipes / Loop Heat Pipes / Capillary Pumped Loops

Heat pipes are passive liquid phase change-based devices that can transport large amounts of heat from a heat source to an external heat sink, while incurring minimal temperature drops. They operate on the principle of surface tension-based capillary pressures and do not require any external power for operation. Loop heat pipes and capillary pumped loops are improved versions of heat pipes, all of which have found widespread use in the field of electronic thermal management. In the next section, these systems are discussed in further detail.

1.2 Review of Passive Phase Change Cooling Devices

1.2.1 Heat Pipes

Heat pipes are passively-operated two-phase heat transfer devices than can transport large quantities of heat using the latent heat of evaporation of a working fluid, while incurring minimal temperature drops between the heat source and the heat sink. In Figure 1.8 is illustrated the overall structure and theory of operation of this device [13], whose name originated from the fact that original versions were fabricated using metal pipes. The inner surface of the heat pipe is covered with a capillary wicking material [48], such as metal screens, fiber or felt metals, and powdered metals [14]. The device is completely evacuated, filled with enough working liquid to saturate the wick, and then hermetically sealed [48]. The working liquid should be hydrophilic

and, ideally, should have a large surface tension and latent heat of evaporation. From the operational perspective, the heat pipe is divided into three distinct regions: the evaporator, the adiabatic section, and the condenser. In the evaporator, the liquid saturating the wick evaporates upon the application of a heat source. The vapor formed as a result diffuses into the empty interior of the heat pipe. Since the middle of the heat pipe is nearly adiabatic, the vapor continues to travel until it reaches the condenser, where is condenses and releases the heat to an external heat sink that is interfaced with the heat pipe. Due to the capillary pressure generated across the evaporating liquid-vapor meniscus, the condensed liquid travels through the surface wick back to the evaporator. Since the liquid in the entire device is saturated, the temperature of the heat pipe is nearly isothermal [48]. There is only a small temperature drop going from the evaporator to the condenser, due to the pressure variations associated with the two-phase fluid flow loop. As a result, the heat pipe essentially behaves like a very high thermal conductivity material.

When initially invented in the 1940s, heat pipes were the first true capillary-driven passive liquid phase change transport systems [49]. The predecessor to the heat pipe was the Perkin tube [50], which was basically a wickless gravity-assisted heat pipe patented by Jacob Perkins in 1836. Gaugler [51] arguably conceived the first heat pipe in 1944, using sintered iron as the wick [49]. Trefethen [52] suggested the use of heat pipes in the space program, and Grover [53, 54] fabricated several prototypes using water and sodium as the working fluids. The first significant theoretical analysis of the heat pipe by Cotter [55] in 1965 led to the recognition of the heat pipe as a reliable thermal device [49]. Faghri *et al.* [56] proposed a concentric annular heat pipe, which is made of two concentric pipes of unequal diameters that create an annular vapor space. Due to the larger surface area available for evaporation and the increase in cross-sectional area of the wick, which could now be placed on two surfaces, the heat carrying capacity was significantly improved compared to conventional heat pipes. The annular heat pipe was predicted to perform 82% better than the conventional heat pipe.

Gillot *et al.* [48] demonstrated the use of a flat miniature heat pipe with microcapillary grooves for the purpose of spreading heat flux across a heat sink. The device did not contain a wicking material, but instead used rectangular grooves etched on its inner surface to provide the capillary wicking action. Although compact in nature, the device was unable to handle high heat fluxes, with a brass/water prototype only able to absorb around 13 W/cm^2. A silicon prototype based on MEMS microfabrication techniques was also proposed. Kimura *et al.* [57] experimentally tested a slim-profiled flat micro heat pipe that employed a braided-wire wick. The device was 1 mm thick and 16 cm long, and transported thermal energies on the order of 10 W. Anderson *et al.* [35] demonstrated the feasibility of cooling concentrating photovoltaic cells using a copper/water heat pipe. An input heat flux of 40 W/cm^2 was rejected by the heat pipe to the ambient using natural convection, while incurring a $\Delta T = T_{cell} - T_{ambient}$ of only 40 ^oC. For comparison, a copper block system, under the same conditions,

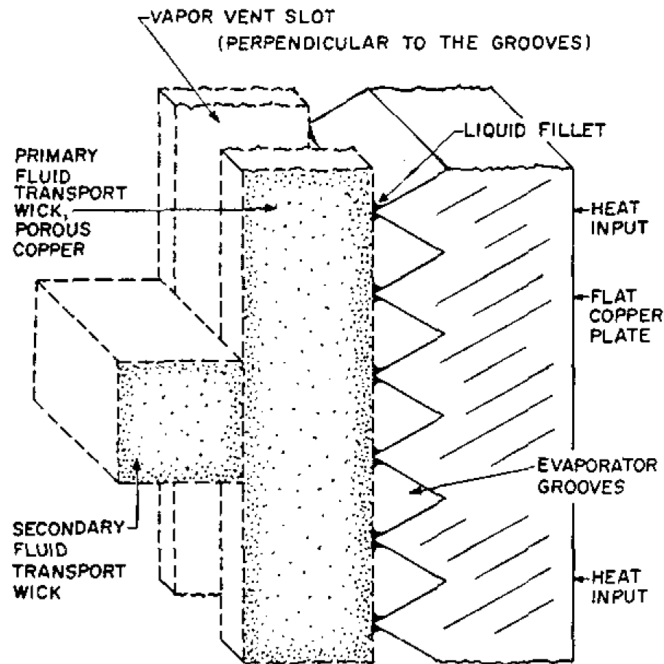

Figure 1.9: An inverted-meniscus wick design for a flat heat pipe evaporator [14]. The triangular grooves in the copper plate allow evaporation to take place, and the vapor to escape, from the surface of the wick in direct contact with the heat source.

would have a ΔT of 210 ^oC. Wits *et al.* [13] fabricated and experimentally tested a flat miniature heat pipe that was integrated inside the laminated structure of a printed circuit board (PCB). With a measured equivalent thermal conductivity seven times than of copper, the concept is a promising thermal management solution for PCB electronics.

Feldman Jr. *et al.* [14] had earlier invented a flat heat pipe evaporator for cooling laser mirrors using a heat pipe. It employed an *inverted meniscus* design, where the liquid-vapor meniscus could form on the side of the wick in contact with the heat source (see Figure 1.9). This led to a higher heat flux capability compared to conventional heat pipe wicks, where the heat has to travel through the entire wick material—not a very good thermal conductor due to its porous nature—before it reaches the evaporating meniscus. This inverted meniscus wick topology was similar to the wicks that would eventually find use in loop heat pipes and capillary pumped loops, since it provided for a separate pathway for the vapor to escape after evaporation.

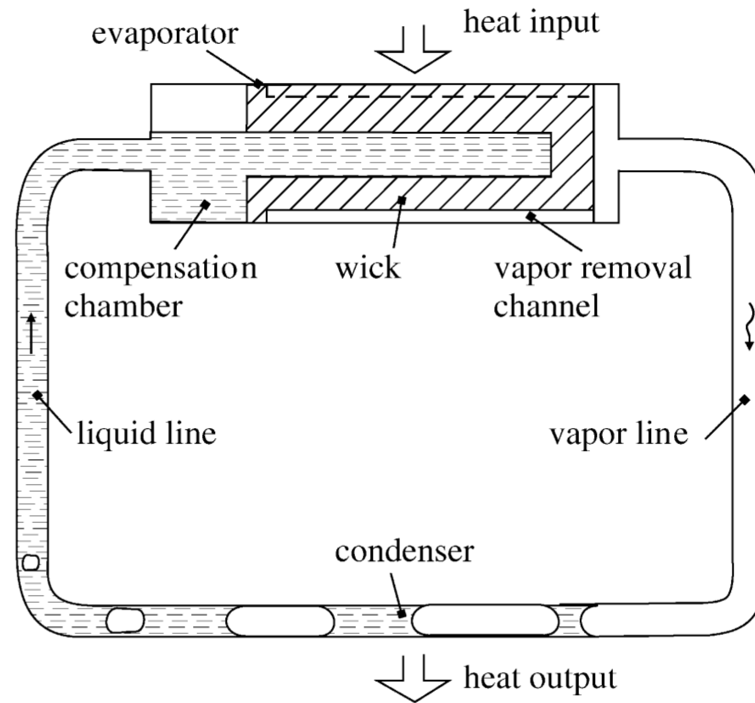

Figure 1.10: A schematic outlining the basic structure and principle of operation of a loop heat pipe [15].

1.2.2 Loop Heat Pipes

Despite their large heat carrying capacities, heat pipes have the following two limitations: 1) they cannot transport heat efficiently over large distances, and 2) their performance suffers when the evaporator section is below the condenser section in the presence of a gravitational field [15, 49]. The reason behind both these limitations is that the capillary wicking material in a heat pipe extends along the entire length of the device. This is necessary in order to bring the condensed liquid back to the evaporator. When the length of the heat pipe is increased, the capillary wicking pressure remains the same but the pressure drop due to liquid flow in the wick increases proportional to the length of the device. As a result, the maximum heat carrying capacity of the heat pipe decreases drastically with an increase in its length. Regarding the second limitation, when the evaporator lies below the condenser in a gravity field, extra capillary pumping pressure is required to overcome the liquid gravitational pressure head. This could have been provided by decreasing the pore size of the wick, but it in turn results in a larger liquid-flow pressure drop in the long wick—the primary reason why pores in a heat pipe cannot be made too small in the first place. The two inherent design limitations of heat pipes are overcome by loop heat pipes and capillary pumped loops.

Maydanik and Gerasimov developed and tested the first loop heat pipe (LHP) in 1972 at the Ural Polytechnical Institute in Russia [58, 59, 15], using water as the working fluid. The incentive was to create a heat transfer device for aerospace applications that provided the same advantages as a heat pipe but was less sensitive to orientation in a gravity field [15]. The basic structure and principle of operation of the LHP is illustrated in Figure 1.10. It incorporates the following main principles that distinguish it from the heat pipe [15]:

1. There are separate transport lines for the vapor and liquid phases.
2. Distinct evaporator and condenser sections are designed to provide for effective heat exchange during evaporation and condensation.
3. The distance of liquid motion in the wick is minimized by restricting it to the evaporator region of the device.
4. A partially-filled liquid compensation chamber is attached to the evaporator, to regulate the liquid distribution in the device.

The liquid evaporates in the evaporator section and the vapor preferentially travels towards the vapor transport line, which carries it to a condenser section. The condensed liquid travels, via the liquid transport line, back to the compensation chamber, which feeds it to the evaporator section. Since the liquid and vapor phases are now separated, there are no counter-flow frictional losses that negatively effect device performance in the case of a heat pipe. Also, since there is no wicking material in the transport channels connecting the evaporator and condenser sections, these channels can be made extremely long without any significant increase in frictional pressure drops, which have a negative effect on device performance. Further, since the wick is confined to the evaporator, the length of the liquid flow path in the wick is quite small. As a result, the capillary pumping pressure can be significantly increased by reducing the wick pore size, without resulting in large frictional flow pressure drops in the wick. This dominance of capillary pressure over liquid gravitational pressure head is what makes the LHP performance independent of device orientation in a gravitational field.

The evaporator section of a LHP is designed in order to ensure separation of the liquid and vapor phases during evaporation. Shown in Figure 1.11 are the key design features of both cylindrical as well as flat LHP evaporators [16, 2]. The idea is to partition the evaporator using a thick fine-pored wick: On one side of the wick is the compensation chamber partially filled with liquid. The other side of the wick is in contact with the heated surface and has vapor channels that lead to the vapor line. Since the latter side of the wick is at a higher temperature, it experiences evaporation, and the vapor diffuses from the vapor removal channels into the vapor transport line. Some heat also conducts through the wick into the compensation chamber, but it

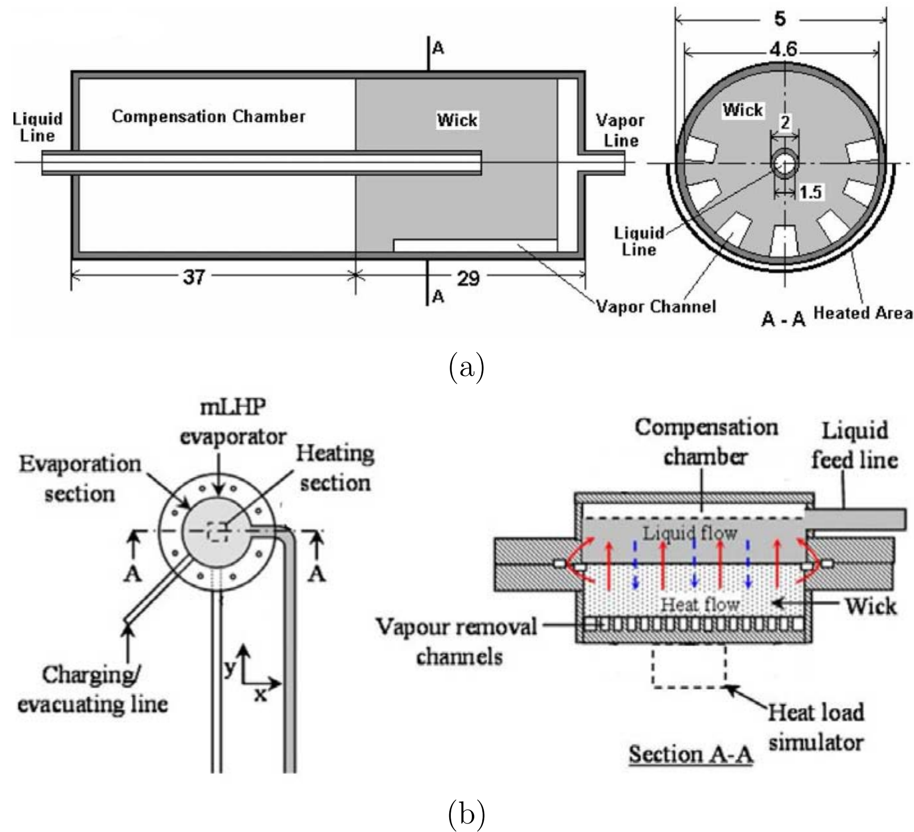

Figure 1.11: Topologies of the evaporator section, compensation chamber, and wicking structure in loop heat pipes: (a) A cylindrical evaporator (dimension in mm) [16]; (b) A flat evaporator [2].

does not lead to evaporation due to the constant supply of subcooled liquid from the liquid line.

The main structural materials for metal-based loop heat pipes include stainless steel, aluminum, and copper [15]. Stainless steel is strong and amenable to vacuum welding, with low thermal conductivity being its only drawback. Aluminum is more conductive but less durable than copper, which has emerged as the most promising option [15]. Sintered nickel and titanium powders are the most commonly used wick materials (due to their compatibility with low temperature working fluids), with other successful cheaper options being polymeric, ceramic, copper, and stainless steel porous materials [15]. The most efficient LHP working fluids include ammonia ($-20\ ^oC$ to $80\ ^oC$) and water ($100\ ^oC$ to $150\ ^oC$), with some other working fluids being neon, oxygen, nitrogen, ethane, propane, propylene, freon152A, freon11, n-pentane, acetone, and toluene [15].

Maydanik *et al.* [15] provides an extensive overview of the general theory and different design variations of loop heat pipes. In Figure 1.12 is shown the variation in size and design topology of loop heat pipes fabricated for different cooling appli-

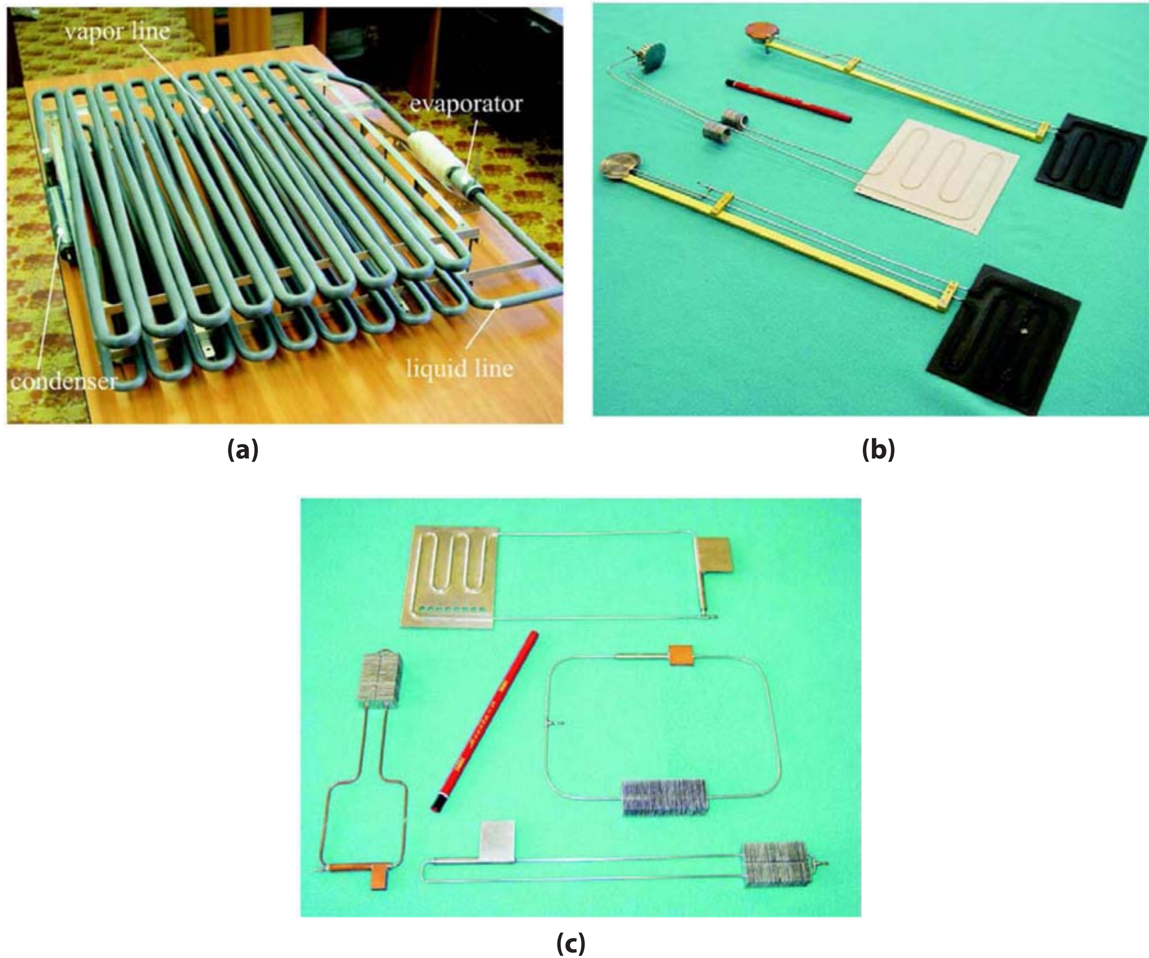

Figure 1.12: Variation in the size and design topology of loop heat pipes (LHP) [15]: (a) A 21 m long cylindrical-evaporator LHP capable of carrying 1.7 kW of heat; (b) Flat-evaporator LHPs capable of carrying $\sim$ 100 W of heat to a distance of 1 m; (c) Miniature LHPs with an evaporator diameter of not more than 6 mm, capable of carrying $\sim$ 90 W of heat to a distance of 30 cm.

cations. They range from large LHPs capable of carrying more than 1.7 kW of heat over a distance of 21 m, to miniature LHPs with an overall thickness not more than 6 mm. Pastukhov *et al.* [60] fabricated and tested a miniature loop heat pipe for electronics cooling. The device had a cylindrical evaporator 5–6 mm in diameter, was 25 cm long, and could transfer a maximum heat flux of 80 W at a thermal resistance of 0.3–0.5 $^oC/W$. Ammonia and acetone were employed as the working fluids, with the former yielding better performance. Maydanik *et al.* [61] designed an innovative asymmetric evaporation chamber for miniature loop heat pipes, in order to enable a decrease in the minimum allowable size of both cylindrical and flat evaporators. Zuo *et al.* [62] implemented a large-scale hybrid-loop cooling system for high heat flux components. It employed a pump-driven excess-liquid loop inside a standard LHP

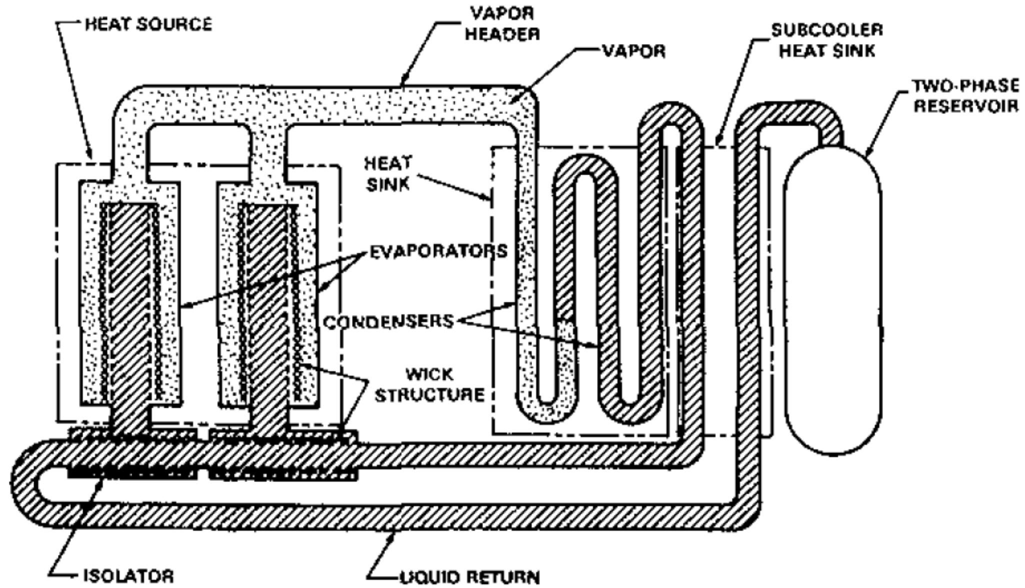

Figure 1.13: A schematic of the basic structure and principle of operation of a conventional capillary pumped loop (CPL) [17].

two-phase flow loop. The 4 cm^2 device evaporator was able to absorb heat fluxes as high as 350 W/cm^2 and transport the resulting heat load of 1400 W to a distance of 1 m. Maydanik *et al.* [63] presents several miniaturized LHP designs for cooling compact electronic systems. Ghajar *et al.* [64] proposed and mathematically modeled a MEMS loop heat pipe for electronics cooling applications.

1.2.3 Capillary Pumped Loops

A capillary pumped loop (CPL) is a two-phase thermal transport system [65], which is quite similar to a loop heat pipe (LHP) in terms of device structure and operation. In Figure 1.13 is shown a schematic of a conventional CPL design outlining its main components and the overall principle of operation. The main CPL components are as follows: 1) a capillary evaporator, 2) a condenser, 3) a two-phase reservoir, and 4) liquid and vapor transport lines [66]. The distinction between the CPL and the LHP lies in the placement and thermodynamic conditions of the two-phase reservoir, also called a compensation chamber in the case of a LHP. Whereas the compensation chamber of a LHP is directly attached to the evaporator section and fed by the liquid transport line, the two-phase reservoir of a CPL is completely separated from the evaporator and only connected to it by a connecting line. Prior to operating the CPL, the temperature of the two-phase reservoir has to be increased and set to a fixed value, in order to start the *loop pressure priming*. When heat is applied to the

capillary evaporator, it results in initial sensible heating of the liquid. Evaporation starts only when the liquid reaches the temperature set at the liquid reservoir [66]. In other words, the temperature of the evaporator can be actively controlled in a CPL, something that in a LHP only depends on the temperature of the condenser and the ambient temperature. The rest of the mechanism of operation of the CPL is exactly similar to that of the LHP, as discussed in detail in the previous section. Another important feature of the CPL, which can also be seen in Figure 1.13, is that multiple evaporators can be used as part of the same flow loop. This is possible due to the fact that the single heated two-phase reservoir, by pressure-priming the flow loop, ensures liquid supply to all the individual evaporators. Such an arrangement is difficult in a LHP, where a separate compensation chamber would be required next to each and every evaporator. The structural materials and working fluids for CPLs are the same as for LHPs.

Dickey *et al.* [65] conducted an experimental study of a CPL and developed a numerical model to predict device performance. Riehl *et al.* [66] conducted experimental investigations of a CPL for application in a scientific micro-satellite. The CPL, capable of transporting 50 W of heat, used ultra high molecular weight (UHMW) polyethylene as the wicking material and anhydrous ammonia as the working fluid. Bazzo *et al.* [67] studied the operational characteristics of a small-scale CPL fabricated from stainless steel tubing and capable of absorbing 50 W of heat.

In recent years, many attempts have been made to implement micro capillary pumped loops on silicon wafers using MEMS microfabrication techniques. Kirshberg *et al.* [68] proposed a micro-cooler for chip level temperature control, based on the working principle of a CPL. The device was fabricated by etching and then bonding together silicon and Quartz wafers. Kirshberg *et al.* [69] presented the experimental testing results for the above device, using a borofloat wafer instead of the more expensive quartz wafer. The device evaporator was heated with a CO_2 laser but results were largely inconclusive. Kirshberg *et al.* [70] could only demonstrate a 7 ^oC cooling of the backside of the wafer that contained the above device. Liepmann *et al.* [71] gave an overview of the work done in an effort to implement MEMS-based CPL devices. Many challenges to the MEMS-scale miniaturization of CPLs and LHPs were cited, including the need for an effective integrated wicking structure and uncertainties associated with the dynamic behavior of evaporation/boiling at small length scales. Yerkes *et al.* [72] fabricated and tested a planar, silicon-based mini-CPL by etching and fusion-bonding three silicon wafers. A 15 ^oC cooling of a 3–10 W heat source was observed, when compared to conduction cooling using a solid silicon substrate.

1.3 The Micro-Columnated Loop Heat Pipe

Microscale loop heat pipes, fabricated completely on silicon and silicon carbide wafers, have been proposed by several researchers in order to integrate the cooling

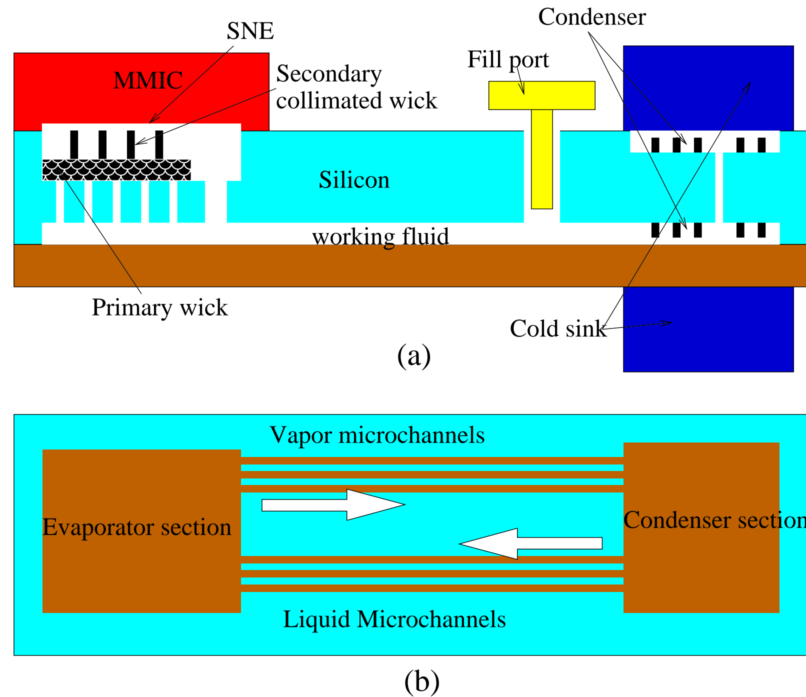

Figure 1.14: A conceptualized view of a planar, ultra-thin, single-substrate micro-columnated Loop Heat Pipe (μCLHP) for localized high-heat flux cooling of integrated circuit (IC) electronics and packages.

system directly with hot electronic chips. These devices employ a planar wicking structure, which can be fabricated by either isotropically etching channels in a Pyrex wafer [68, 69, 70, 73, 74, 75] or by an-isotropically etching rectangular channels in a silicon wafer using deep reactive ion etching (DRIE) [72]. Although such an in-plane wicking structure is easy to fabricate, it will exhibit limited performance due to the fact that the liquid has to flow in a direction perpendicular to the incoming heat flux. This leads to non-uniform evaporation in the wick, and wick dry-out is observed at fairly low heat flux values [70]. Even though past work in this field has demonstrated the viability of microscale loop heat pipes, many device physics issues still need to be addressed for the successful implementation of a MEMS-based loop heat pipe.

1.3.1 An Overview of the Device

I propose a planar, ultra-thin, wafer-level heat transporting device to address the issue of localized cooling of high-power, high-density electronics. In Figure 1.14 is shown a conceptualized view of the proposed micro-columnated loop heat pipe (μCLHP). The device will be fabricated on a silicon wafer and will employ a number of novel features designed to address issues related to the performance and reliability of microscale phase change thermal transport devices. Broadly, the device consists

of evaporator and condenser sections connected by liquid and vapor microchannels. The evaporator section, interfaced with the heat producing chip, converts the liquid to vapor, which is then conveyed to the condenser by the vapor microchannels. It contains the micro-columnated coherent porous silicon (MCPS) wicking structure, which is specially designed to prevent catastrophic wick dryout and improve device performance. The condenser section, interfaced with a heat sink, condenses the vapor back to liquid. The liquid is then pumped back into the evaporator due to the suction force generated by the capillary wicking structure.

In Figure 1.15 is shown a 3-D design schematic of a micro-columnated loop heat pipe (μCLHP) prototype. The device is designed for fabrication on a three-layer wafer stack. Most of the device components can be fabricated on both sides of the middle silicon wafer (layer 2) which is about 675 μm thick. It is capped on the top by a silicon wafer and on the bottom by a Pyrex wafer. The middle silicon wafer will have coherent porous silicon (CPS) pre-patterned on it to serve as the base for the vertically wicking micro-columnated wicking structure. As shown in Figure 1.15a, the columns of the columnated primary wick face upward and interface with the secondary evaporator wick patterned on the top silicon capping wafer. The vapor and liquid transport channels and the condenser section are etched on the bottom of the middle silicon wafer, as shown in Figure 1.15b. The vapor generated in the evaporator, at the top, will enter the vapor channel via a vapor through-hole and travel to the condenser, which is cooled by an in-built liquid-cooled heat sink patterned above it. The condensed liquid will travel, via the liquid channel, back to the evaporator, where it will feed into the bottom of the primary CPS wick via a liquid feed-cavity. Fill-ports, for degassing and filling the device with a working fluid, can be accessed via fill-holes in the top capping wafer. The connecting channels from the inlet and outlet fill-ports end up on the two sides of the micro-columnated wick, to enable proper purging of the wick during a thermal-flux purging of the device for removing non-condensible gases.

The CPS-based micro-columnated wicking structure has two main design features: (a) it is designed to be fabricated completely out of silicon and (b) it operates by wicking the liquid vertically onto the evaporating surface. Since there is no way to conveniently handle conventional wicking materials such as wire meshes or sintered metal powders in microfabrication processes, being able to fabricate the wick completely out of silicon is very important from the viewpoint of device integration. Also, due to the ultra-thin topology of MEMS-based loop heat pipes, the planar in-plane wicking structures that have been employed until now [68, 69, 70, 73, 74, 75, 72] are extremely inefficient and prone to failure due to wick dryout at relatively moderate heat flux values. By wicking the liquid vertically, it can be spread more evenly over the evaporating surface. This has the potential of both increasing the total amount of thin-film evaporative heat transfer and also making it more uniform over the entire heated surface.

In Figure 1.16a is shown a 3-D design schematic of the micro-columnated wicking

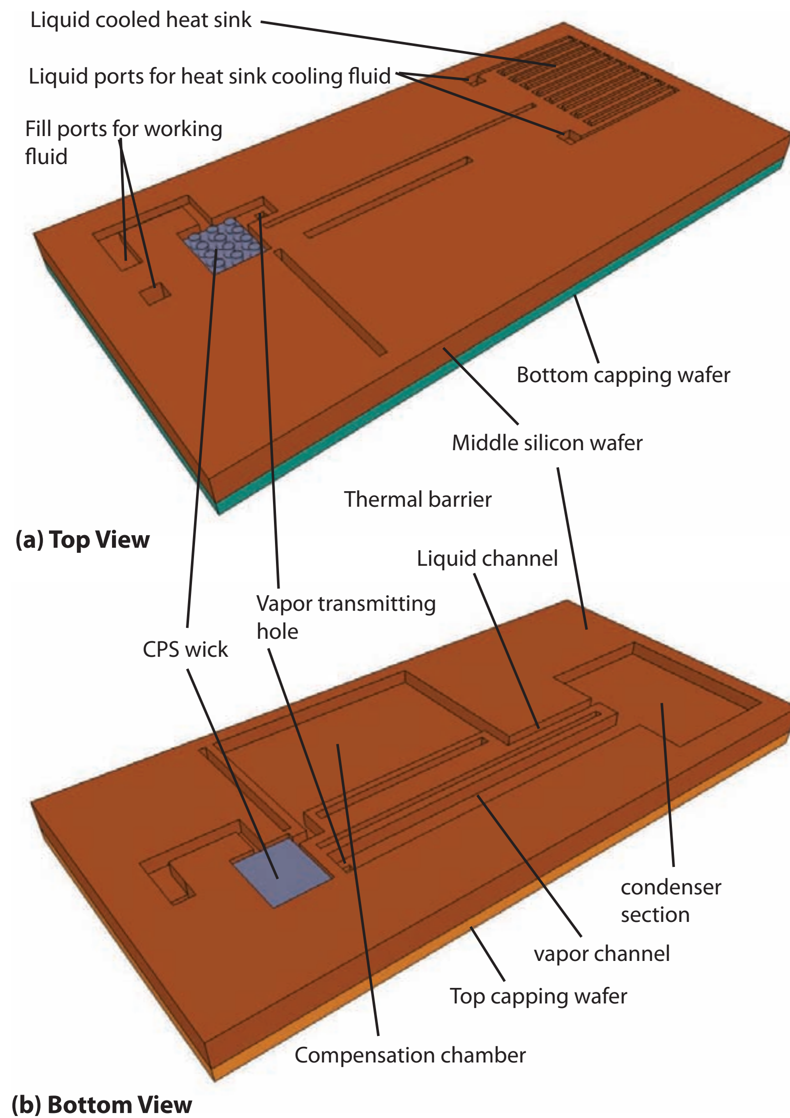

Figure 1.15: A 3-D design schematic of a micro-columnated loop heat pipe (μCLHP) prototype: (a) Top view of the device showing the columnated coherent porous silicon (CPS) wicking structure and a built-in liquid-cooled heat sink for cooling the condenser section. The fill-holes in the top capping wafer connect to the fill-ports. (b) Bottom view of the device showing the liquid and vapor transport channels, the condenser section, and the compensation chamber.

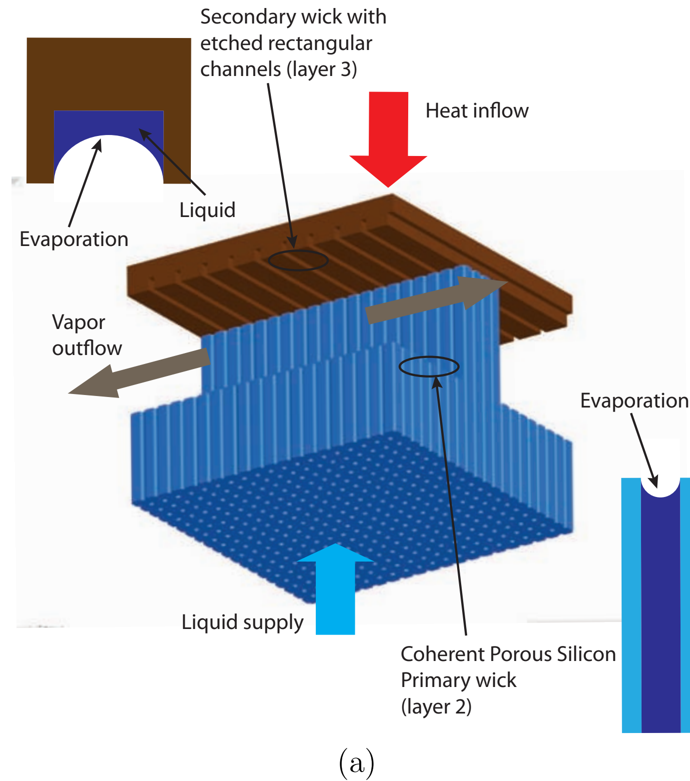

(a)

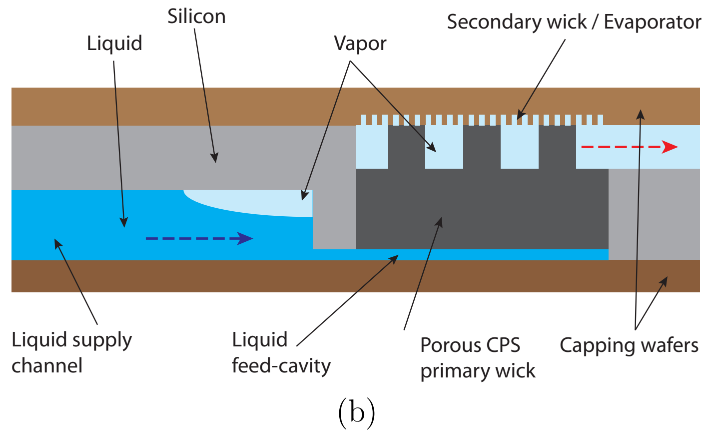

(b)

Figure 1.16: Structure and principle of operation of the micro-columnated wicking structure. (a) The wick is composed of two components: a primary wick, which consists of vertical columns etched in the coherent porous silicon (CPS) base and a secondary wick, which consists of rectangular patterns etched into the top capping wafer. (b) Evaporation and fluid flow in the micro-columnated wicking structure: Incoming liquid is absorbed by the fine pores of the primary wick and conveyed for evaporation to the secondary wick.

structure. It is a dual-scale design composed of a coherent porous silicon primary wick, which lies in the main silicon wafer (layer 2), and a secondary wick, which straddles the top silicon capping wafer. The primary wick consists of vertical columns etched into the coherent porous silicon base. These columns interface with the secondary wick, which consists of rectangular channels etched into the top capping wafer. With its much smaller pore size (on the order of a *micron* or less), the primary wick can generate a large capillary pressure across the liquid vapor meniscus, given by

$$\Delta P_c = \frac{2\cos\theta}{r}\sigma \tag{1.2}$$

where r is the radius of the wick pores, σ is the surface tension of the liquid, and θ is the liquid-solid contact angle. As shown in Figure 1.16b, the main purpose of the primary wick is to use these large capillary pressures to absorb the liquid from the liquid supply side and transport it to the surface of the secondary wick for evaporation. It also prevents the superheated vapor in the vapor chamber from bursting through the wick and into the liquid supply. Although some amount of evaporation also occurs from the liquid-vapor interface in the primary-wick pores, most of it takes place on the evaporator surface, where the wicking micro-patterned channels are optimized to maximize phase change heat transfer.

1.3.2 Salient Device Performance Parameters

The main objectives of the μCLHP are 1) to carry large amounts of heat from one point to another without incurring significant temperature drops across those points, 2) to be able to transport heat over large distances without experiencing any significant drop in performance, and 3) to have a very small thickness so as to fit inside densely packed or stacked electronic substrates.

The following performance parameters can be defined in order to characterize planar microscale loop heat pipes that aim to achieve these goals:

1. *Maximum heat carrying capacity, $\dot{Q}_{max}$:* This is the maximum amount of heat per unit time that the device can transport from the evaporator to the condenser. If the heat input into the evaporator exceeds this value, it will result in a failure of the two-phase flow loop due to catastrophic wick dryout. The exact value of $\dot{Q}_{max}$ will, of course, depend on device operating conditions, such as the condenser temperature and ambient heat transfer processes. The operating conditions are a function of the particular situation in which the device is being used and will have to be specified in any effort to characterize $\dot{Q}_{max}$.

2. *Maximum evaporator heat flux, $\dot{q}_{max}$:* This is the maximum amount of input thermal power than can be absorbed per unit area of the evaporator surface. It

is related to the maximum heat carrying capacity $\dot{Q}_{max}$ as follows:

$$\dot{q}_{max} = \frac{\dot{Q}_{max}}{A_e} \tag{1.3}$$

where A_e is the area of the device evaporator in contact with the heat source. The importance of $\dot{q}_{max}$ lies in the fact that a high-heat-flux thermal management system should not only be able to transport large amounts of heat, but also have the ability to absorb this heat from the extremely small surface areas that characterize modern electronic substrates. A small value of $\dot{q}_{max}$ forces the use of intermediary thermal spreaders between the surface of the heat source and the LHP evaporator surface. This introduces a spreading resistance component into the overall thermal circuit and also precludes the localized cooling of thermal hotspots on an electronic chip. A planar μCLHP device with a high value of $\dot{q}_{max}$ can be interfaced directly with high-heat-flux electronic components. Increasing the value of $\dot{q}_{max}$ will require the use of highly efficient wick and evaporator configurations, in addition to the other techniques that help to ensure a large $\dot{Q}_{max}$.

3. *Distance of heat throw, d_{throw}:* The μCLHP transports heat from one point to another. How far this heat can be carried depends on the total length of the device, which is roughly equal to d_{throw} if the device is linear in shape. The constraints on d_{throw} can come from aspects of device fabrication as well as the physics of the flow loop. Microscale loop heat pipes fabricated completely on silicon wafers cannot be bigger than the diameter of the largest available wafer sizes. From the operational perspective, a larger value of d_{throw} implies longer liquid and vapor transport channels, which increases the frictional pressure drops in the two-phase flow loop. Although, as discussed previously, this is less of a concern in loop heat pipes compared to heat pipes, the phenomena involved might play out differently in MEMS-based LHPs where the smallest dimension of the liquid-vapor transport channel is only a few hundred *microns*.

4. *Device thickness, t*: The most innovative feature of planar MEMS-based loop heat pipes, as compared to conventional pipe-based designs, is the very small thickness of these wafer-scale devices. The thickness of most wafers used in microfabrication lies anywhere between 500 μm and 1 mm, and therefore the thickness of the μCLHP devices can be kept in the sub-millimeter range. This, in addition to their planar topology, is critical to integrating these thermal management devices into stacked electronic substrates and in general using these devices as thermal ground planes on top of which electronic components can be mounted directly.

1.4 Dissertation Outline

This dissertation is divided into two main parts. The first part, which includes chapters 2–4, deals with the theoretical aspects of micro-columnated loop heat pipe (μCLHP) design and operation. In this regard, chapter 2 provides a detailed thermodynamic analysis of device operation, identifies challenges to the miniaturization of loop heat pipes, and suggests possible design solutions for overcoming these challenges. A finite element method-based coupled thermo-fluid modeling study is conducted to demonstrate the efficacy of these planar design topologies. In chapter 3 is presented a design optimization study that employs a flow loop pressure balance analysis to calculate the maximum heat transport capability of the μCLHP device. Monotonicity analysis and numerical design optimization are used to arrive at optimum values for the device design parameters, to maximize device performance. Chapter 4 looks at a numerical approach for computing the rates of thin-film evaporation from a stationary liquid-vapor meniscus in the three-dimensional micro-columnated wick. A surface free energy-minimizing algorithm is used to arrive at the shape of the liquid-vapor meniscus, while a finite volume discretization approach is used to numerically solve the thermo-fluid and phase change governing equations.

The second part of the dissertation, which includes chapters 5-8, deals with the design, fabrication, packaging, and experimental testing of in-plane-wicking micro loop heat pipes (μLHP). In chapter 5 is presented the design aspects and microfabrication process flows for three different μLHP prototypes. These devices are fabricated on silicon and Pyrex wafers and, due to its ease of fabrication, use an in-plane wicking structure instead of the dual-scale micro-columnated wick. Chapter 6 deals with the various methods and techniques employed for degassing and filling the μLHP devices with a working fluid. A novel thermal-flux degassing and filling approach is introduced, and high temperature-compatible device packaging techniques are developed to implement it. Device hermetic sealing approaches are also discussed. Experimental results demonstrating the operational characteristics of each of the three different μLHP prototypes are presented in chapter 7. Based on these results, the optimum structure and design topologies of components most critical to the proper operation of these devices are characterized. A more detailed experimental study of the process of evaporation in the in-plane wicking structure of the μLHP device is presented in chapter 8. The nature of thin-film evaporation in these microscale structures is characterized using a high-speed optical camera and a thermal infrared camera. Chapter 9 concludes the dissertation by summarizing the main results and providing ideas and directions for future work in this field.

Part II

Modeling of Device Physics and Operation

Chapter 2

Thermodynamic Analysis of Device Operation

The primary challenge to the miniaturization of loop heat pipes to wafer-based devices is the identification of appropriate planar device components and their thermodynamic behavior during device operation [68]. The objective of this chapter is to address these issues, by taking a look at the thermodynamic processes governing microscale loop heat pipe operation, and highlighting the main issues that arise due to device miniaturization. Component-wise design topologies that best address these device physics related challenges are explored and identified.

2.1 Challenges to Miniaturization

The following issues arise when scaling down the overall size of a loop heat pipe to enable millimeter-thin wafer-based devices:

1. Due to the small overall device size, large temperature gradients are to be expected along the length of the device. As will be shown in the following section, this only slightly modifies the thermodynamic characteristics of the flow loop, and has little or no bearing on device operation.

2. Surface tension-related geometrical effects, which do not show up in macroscale geometries, begin to influence the behavior of the liquid-vapor meniscus in a planar small-scale LHP device.

3. In a planar MEMS-based loop heat pipe, the maximum thickness of the evaporator section (and therefore the wicking structure) is constrained by the thickness of the process wafer and available wick microfabrication techniques. This can lead to problems, discussed in the following sections, that arise due to the thermodynamic principles underlying device operation.

2.1.1 Wick Thickness Limitation:

In conventional loop heat pipes employed for space applications, the diameter of the cylindrical evaporator typically ranges from 12 to 28 mm. Attempts have been made to miniaturize such devices for electronics applications [60]. However, in doing so, it is seen that an evaporator diameter below 4–8 mm leads to problems for LHP operation, which have been attributed to a minimum required wick thickness between its absorbing and evaporating surfaces [61]. This minimum wick thickness is necessary for two reasons: a) to prevent the vapor from penetrating through the wick, and b) to avoid excessive parasitic heat flow into the compensation chamber, which can compromise device startup and also limit device performance. Some modest design variations have been proposed to enable a reduction in the diameter of the cylindrical LHP evaporator [61]. These solutions, however, do not promise reductions in wick size that are required for millimeter-thin wafer-based loop heat pipes, where the maximum achievable wick thickness is approximately 500 μm.

On the other hand, wafer-based LHPs also have several design advantages, which can be harnessed to overcome limitations associated with thinner wicks. First, much smaller wick pore diameters are possible using coherent porous silicon based wicking structures. The resulting larger capillary forces can prevent vapor penetration through the wick. Second, microfabrication techniques allow for innovative evaporator design topologies that are not possible in the cylindrical LHPs.

2.2 Device and Evaporator Thermodynamics

In this section, we will look at the thermodynamic principles that can be used to describe the process of two-phase thermal transport in a planar wafer-based loop heat pipe.

2.2.1 Device Theory of Operation

Based on conventional loop heat pipe theory [15, 76], the expected behavior of the two-phase working fluid inside a planar wafer-based micro-columnated loop heat pipe (μCLHP) during steady state operation is shown in Figure 2.1. Figure 2.1(b) shows a detailed cross-section of the evaporator section and the compensation chamber of the μCLHP. The liquid absorbed by the porous CPS wick from the compensation chamber is carried by capillary forces to the surface of the evaporator/secondary wick for evaporation. In the absence of any heat flux applied to the evaporator, or in the so called OFF state, the liquid in the device occupies portions of the device that minimize the overall free energy of the system. Usually, this implies that the wick and transport channels (both liquid and vapor), which provide more liquid wetting area per unit volume, are completely filled with liquid, while the condenser and compen-

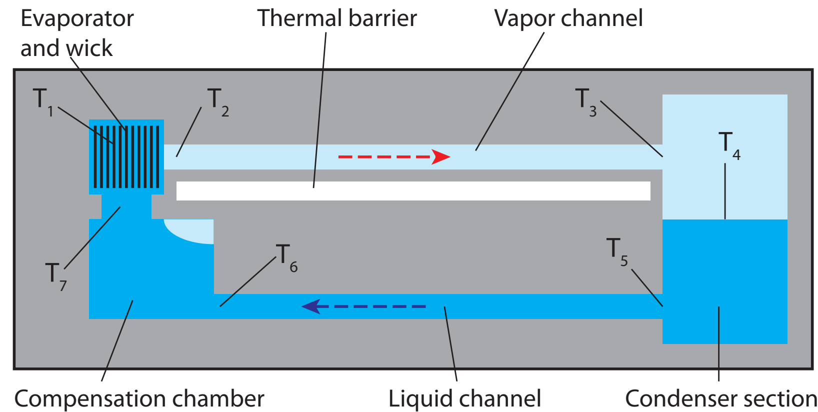

(a) Overall Device

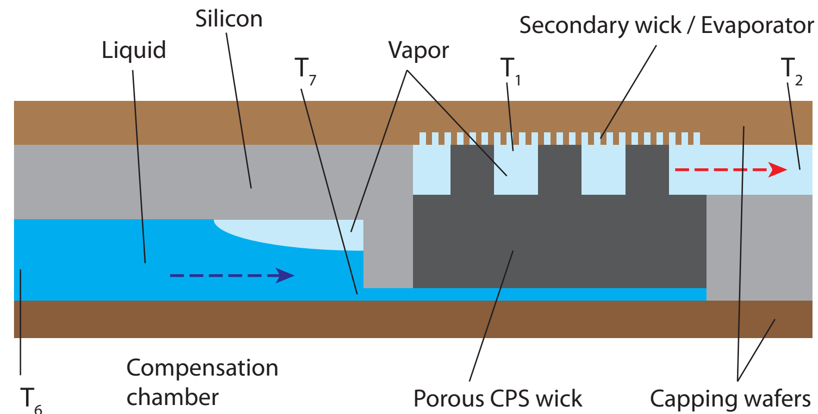

(b) Evaporator section

Figure 2.1: A schematic of the liquid and vapor phase distributions, and fluid temperatures inside a planar micro-columnated loop heat pipe (μCLHP): (a) In steady state operation the vapor channel is completely, and the condenser section partially, liberated from the liquid phase. The compensation chamber can also contain pockets of vapor. (b) The dual scale wick in the evaporator section is supplied by the compensation chamber with liquid, which turns to vapor at the evaporator surface.

sation chamber are partially filled. As heat is applied to the evaporator, the following processes occur:

1. The liquid in the evaporator as well as the compensation chamber, which is thermally adjacent to it, begins to evaporate.

2. Because of the finite conduction thermal resistance of the wicking material, the liquid (assumed saturated) in the evaporator, which is directly exposed to the heat flux, has a temperature and pressure (T_1, P_1) higher than the liquid in the compensation chamber (T_7, P_7). Therefore, the higher vapor pressure in the

evaporator is able to expel the liquid out from the vapor line, into the condenser section, and finally back to the compensation chamber. This phenomenon, resulting from the thermal resistance of the wick, is referred to as its *thermal locking* behavior [15].

3. The capillary pressure across the liquid-vapor meniscus in the tiny pores of the wick prevents the high pressure vapor in the evaporator from pushing through the wick, into the compensation chamber. The wick in this case is said to serve as a *hydraulic lock* [15].

4. The vapor moves out from the evaporator, into the vapor channel, and finally into the condenser section, where it condenses back to liquid. Given a finite value of the condensation coefficient, the rate of condensation in the condenser section is proportional to its surface area that is exposed to the condensing vapor. Due to this, as the evaporator heat flux is increased, more liquid is pushed out of the condenser section and into the compensation chamber.

2.2.2 Thermodynamics of the Flow Loop

Shown in Figure 2.2 are the thermodynamic phase change diagrams for the micro-columnated loop heat pipe (μCLHP) flow loop. These diagrams were developed by modifying some elements of an analytical scheme originally developed for conventional cylindrical loop heat pipes [15]. The working fluid temperatures and pressures used in the graphical analysis correspond to specific positions in the device flow loop, as depicted in the μCLHP flow schematic shown in Figure 2.1.

As seen in Figure 2.2, the vapor just above the liquid-vapor meniscus in the evaporator is at the saturation temperature T_1 and saturation pressure P_1. As it moves through the vapor collection channels, on its way out of the evaporator, the vapor undergoes a small pressure drop due to flow friction, and superheats further by absorbing some more heat from the evaporator surface (T_2, P_2). The vapor pressure drops considerably due to flow friction as the vapor travels along the length of the device, via the vapor channel (2-3), to reach the condenser inlet (3). Whereas in conventional loop heat pipes this would be an adiabatic process, in planar MEMS-based devices T_3 can be noticeably less than T_2 due to the large material temperature gradients along the length of the device. Once in the condenser section, the vapor condenses (3-4) into the liquid state, and then subcools (4-5) by releasing more heat to the condenser.

The subcooled liquid travels back to the compensation chamber inlet through the liquid line (5-6), again incurring a modest pressure and a small temperature drop in the process. Traveling across the compensation chamber, the liquid temperature increases (6-7) due to the parasitic heat leaking from the evaporator section. The liquid becomes saturated by the time it reaches the wick inlet (7), and is in a metastable

Figure 2.2: Phase change diagrams for the two-phase flow loop in the micro-columnated loop heat pipe (μCLHP): (a) P-T diagram obtained by modifying some elements of the conventional loop heat pipe analysis scheme[15]; (b) T-v diagram outlining the same process.

state (7-8) as it travels through the wick to the evaporating liquid-vapor meniscus. In this metastable state, the liquid can be superheated for a very short time duration [15], but does not undergo boiling due to the surface tension-related boiling retardation, which is further aided by spatial confinement in the micron-sized pores of the wick.

2.2.3 Device Operational Requirements

From the above thermodynamic analysis, we can arrive at the following three relations that characterize the startup and steady-state operation of the micro-columnated loop heat pipe (μCLHP):

Capillary pumping requirement. This states that the maximum capillary pressure across the liquid vapor meniscus in the wicking structure should be greater that or equal to the sum of all pressure losses in the LHP flow loop.

$$\Delta P_c \geq \Delta P_{wl} + \Delta P_{ev} + \Delta P_v + \Delta P_l + \Delta P_g \tag{2.1}$$

where ΔP_c is the capillary pressure in the wick, $\Delta P_{wl} = P_7 - P_8$ (see Figure 2.2a) is the liquid frictional pressure drop in the wick, $\Delta P_{ev} = P_1 - P_2$ is the vapor pressure drop in the evaporator vapor collection channels, $\Delta P_v = P_2 - P_3$ is the vapor pressure drop in the vapor transport channel, $\Delta P_l = P_5 - P_6$ is the pressure drop in the liquid transport channel, and ΔP_g is the gravitational pressure drop, which is usually small for microscale loop heat pipes.

Motive temperature head requirement. From the saturation line in Figure 2.2a, we can see that, under steady state operation, the temperature difference between the wick evaporator surface and the compensation chamber also dictates the amount of pressure head that can be created between them—something that drives the flow loop. This pressure head must equal ΔP_{EX}, the viscous flow related pressure losses in all of the device components except the wick, and is given by [15]

$$\Delta P_{EX} = \left[\frac{\partial P}{\partial T}\right]_{\bar{T_a}} \Delta T_{1-7} \tag{2.2}$$

where $\bar{T_a}$ is the average of T_1 and T_7, and ΔT_{1-7} is the temperature difference between the wick evaporator surface and the compensation chamber, appropriately called the motive temperature head [15]. An increase in the parasitic heat flow from the evaporator to the compensation chamber can increase T_7, which can both increase the evaporator temperature T_1 and reduce the motive temperature head, thereby reducing device performance.

Another very important scenario, which is affected by this limit, is the process of device startup. As illustrated by the phase change diagram in Figure 2.3, during

Figure 2.3: Phase change diagram illustrating potential device startup problems due to parasitic heat flow from the evaporator to the compensation chamber.

startup the compensation chamber inlet temperature T_6 is very close to the ambient temperature $T_{ambient}$, which is usually higher than the condenser temperature. As a result, the required motive temperature head can result in higher device operating temperatures, i.e., T_1 is higher during startup than during normal device operation. This effect is worse in devices with lower wick thermal resistances, where large parasitic heat flows into the compensation chamber can result in wick dry out due to vapor formation in the compensation chamber.

Liquid subcooling requirement. The liquid in the condenser section needs to be sufficiently subcooled, in order to prevent boiling in the liquid line as a result of the viscous pressure losses during the liquid flow from the condenser to the compensation chamber. This requirement can be summarized using the following equation [15]

$$\left[\frac{\partial P}{\partial T}\right]_{\bar{T}_b} \Delta T_{4-6} \geq \Delta P_{5-6} \tag{2.3}$$

where $\bar{T}_b$ is the average of T_4 and T_6 (see Figure 2.2). In terms of the μCLHP evaporator-side design process, this condition is affected by the non-adiabatic nature of the liquid channel. Efforts should be made to minimize any parasitic heat flow from the evaporator to the liquid channel.

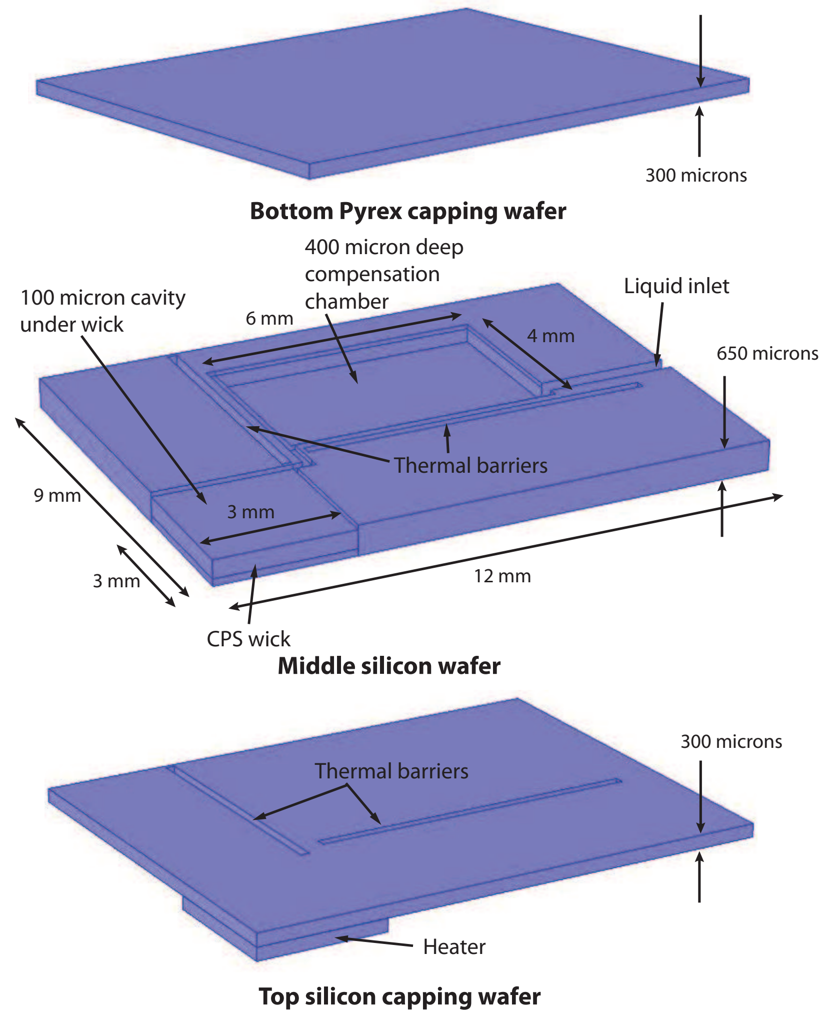

Figure 2.4: Evaporator design topology for minimizing parasitic heat flow to the compensation chamber. Thermal barriers are etched around the compensation chamber and a high thermal resistance channel is provided between the evaporator and the compensation chamber.

2.3 Planar Evaporator Design

In order to enable a microscale loop heat pipe with wick thicknesses less than half a *millimeter*, we need to come up with evaporator design topologies that minimize the amount of parasitic heat flow to the compensation chamber. This will help to improve device performance and also prevent wick dryout during startup.

In Figure 2.4 is shown one such design topology, which uses in-plane conduction barriers to minimize heating of the liquid in the compensation chamber. The evaporator section, which contains the wick, and the compensation chamber are etched into the bottom of the middle silicon wafer and sealed by a plain Pyrex wafer. At

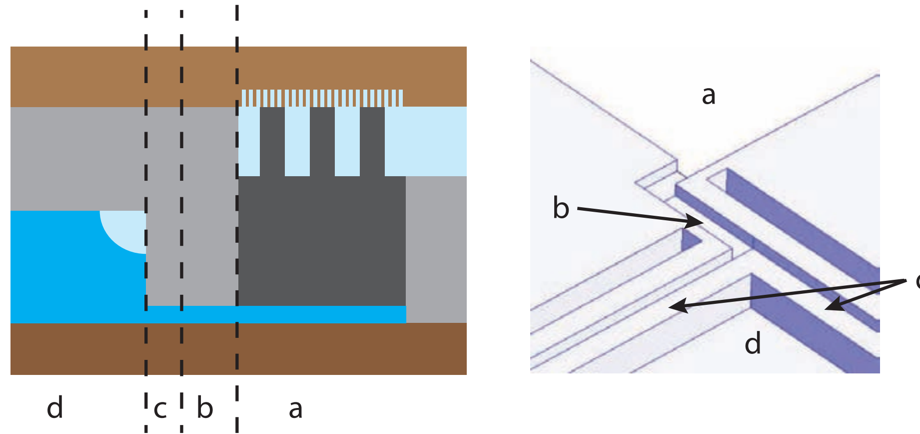

Figure 2.5: Low conductivity fluidic connection between the evaporator section and the compensation chamber: (a) Shallow cavity ($20-100$ μm) beneath the wick; (b) A 200 μm wide connection channel; (c) Shallow cavity extended into the compensation chamber; (d) The compensation chamber.

the top, the wicking structure is capped by a silicon wafer. The evaporator section is heated by a heater interfaced with the top capping wafer. Thermal barriers are etched into the middle silicon wafer and the top silicon capping wafer, to prevent parasitic heat flow to the compensation chamber via conduction. The liquid conduit between the evaporator and the compensation chamber is designed to maximize conduction thermal resistance between the two.

In Figure 2.5 is illustrated how a shallow cavity (20–100 μm deep) beneath the wicking structure, in the evaporator section, is extended into the compensation chamber, to serve as a liquid conduit between them. The purpose of this cavity is to serve as an extension of the coherent porous silicon wick into the compensation chamber, and prevent bubble formation in this region. The narrow, 200 μm wide, channel connecting the evaporator section to the compensation chamber ensures a high thermal resistance path between them.

2.3.1 Evaporator Thermal Modeling

In order to evaluate the thermal performance of the evaporator design topology discussed above, and shown in Figure 2.4, a coupled fluid-thermal solver was implemented using the finite element method in COMSOL. Laminar, incompressible, non-isothermal steady state flow equations were solved in the liquid domain, while steady state conduction equations were solved in the solid domain. The problem domain and boundary conditions are shown in Figure 2.6. Only the region of the μCLHP containing the evaporation section and the compensation chamber is modeled. The boundary conditions are set according to the expected behavior of the overall device. The heater interfaced with the evaporator section is set to a temper-

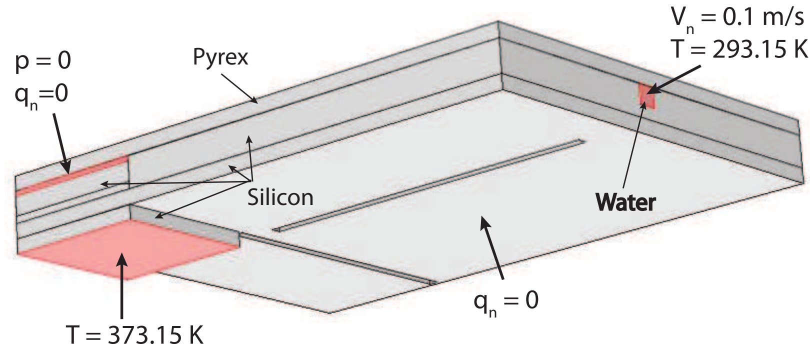

Figure 2.6: Domain and boundary conditions for a coupled thermal-fluid simulation of the μCLHP evaporator and compensation chamber.

ature of 373.15 K, while all the other solid boundaries are set to zero heat flux. A small amount of heat that can leak via conduction along the length of the device is ignored. An inlet velocity of 0.1 m/s is set for the liquid entering the liquid line that feeds the compensation chamber, while its temperature is set to 293.15 K. A zero pressure, zero heat flux liquid outlet boundary conditions is applied to the two faces of the cavity underneath the wick, in order to virtually simulate the absorption of the liquid into the CPS wick.

2.3.2 Modeling Results

The temperature distribution in the three-layer stack containing the evaporator section, compensation chamber, and the working fluid (water) is shown in Figure 2.7. We can see that the compensation chamber temperatures are significantly lower compared to the rest of the domain. This is a direct result of the fact that the thermal barriers around the compensation chamber, which are through-etched in the top and middle silicon wafers, prevent the flow of heat into the compensation chamber via conduction. The Pyrex wafer has a very low thermal conductivity and does not contribute much to in-plane thermal conduction. Due to these combined factors, most of the parasitic heat flow from the evaporator to the compensation chamber occurs via fluid and solid conduction through the narrow channel connecting the two. Due to the low thermal conductivity of water as well as the small cross section of the connecting channel, heat flow into the compensation chamber is inhibited.

The point is more clearly illustrated in Figure 2.8, where temperature distribution is plotted in a horizontal plane going through the liquid in the compensation chamber as well as the evaporator. This plane lies midway through the height of the shallow cavity that connects the evaporator to the compensation chamber. First, we notice clearly that region B, containing the compensation chamber, has the lowest temperatures in the domain. The cold water flowing into the compensation chamber

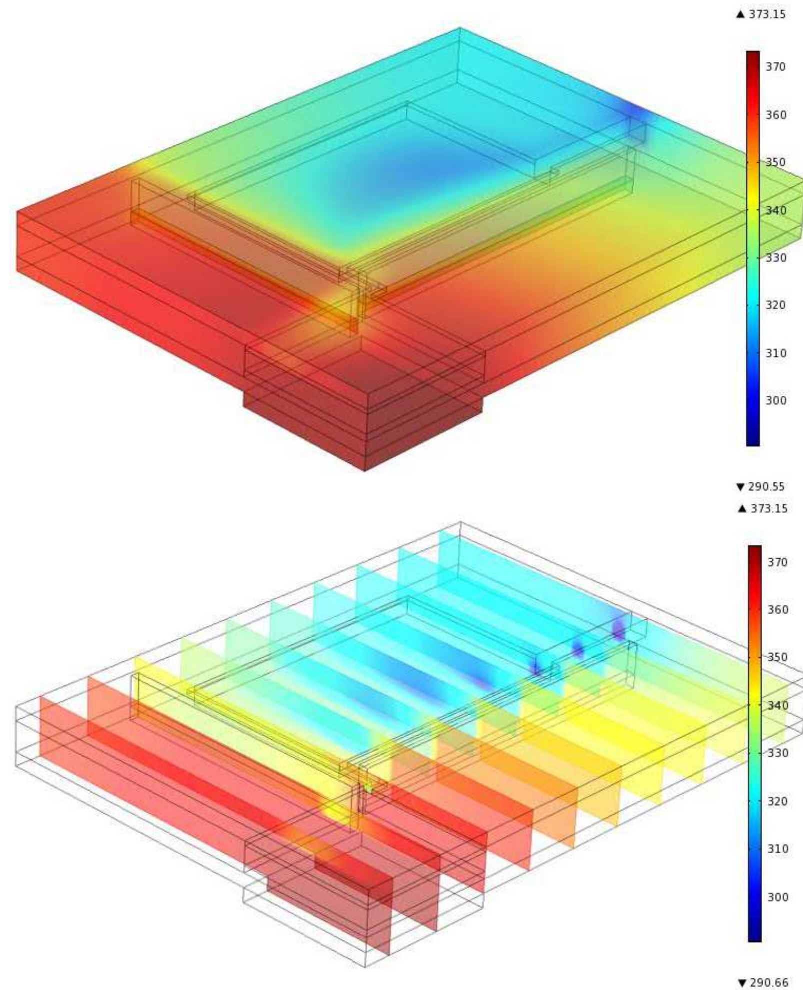

Figure 2.7: Transparent volume and sliced graphs showing the temperature distribution in the solution domain. The maximum domain temperature, at the surface of the silicon heater, is 373.15 K, while the minimum temperature, at 373.15 K, is the temperature of the incoming liquid. It is clear that the compensation chamber is kept comparatively cooler compared to the rest of the domain.

absorbs heat from the surrounding silicon, thereby reducing its temperature. The water temperature in the compensation chamber rises as it absorbs the parasitic heat leaking from the evaporator section. Since water is a bad thermal conductor, most of the heat it absorbs is by conduction from the compensation chamber walls. Now, we can see that the silicon temperatures in region B are much less than those in regions C and D. This is due to the thermal conduction barriers, which increase the thermal resistance of the conduction path from the heat source to the compensation chamber. As a result, the liquid temperatures do not rise significantly until they have reached the evaporator section.

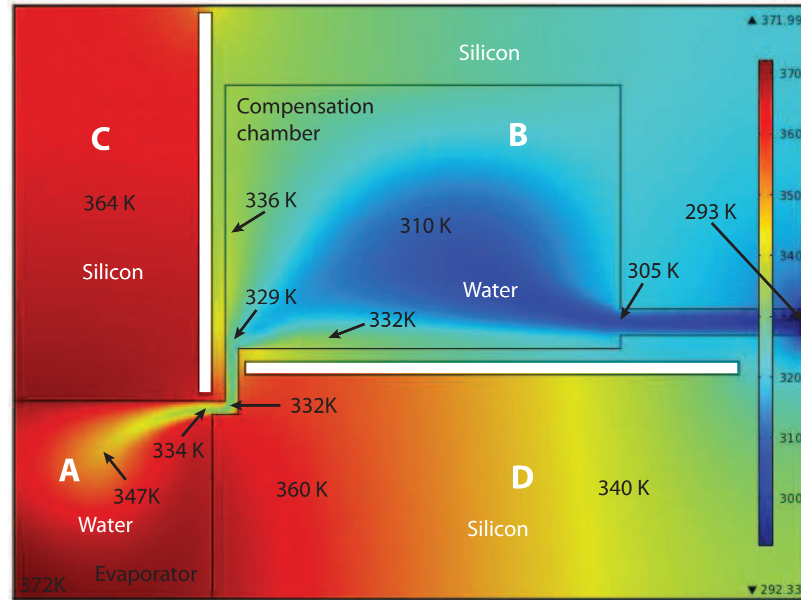

Figure 2.8: The temperature distribution of water in the compensation chamber and the evaporator, and of the surrounding silicon in the middle wafer. The temperature slice was taken at a depth of 50 μm from the bottom of the middle silicon wafer.

This analysis leads to the prediction that the compensation chamber temperatures can be reduced significantly by designing appropriate in-plane thermal conduction barriers in a microscale loop heat pipe. As a result, a sufficient motive temperature head can be generated during device startup, and the associated steady state performance of the device can also be improved. Such conduction barriers can also be helpful in other parts of the device. For example, a conduction path can be established between the condenser and the liquid line in order to promote subcooling and prevent boiling in the transport line. Similarly, conduction barriers can be used to insulate the vapor line from the condenser cold sink, to avoid vapor condensation in it.

2.4 Conclusions

A planar evaporator/compensation chamber design topology was proposed and analyzed numerically in order to satisfy thermodynamic operational requirements related to the minimum allowed wick thickness in a wafer-based loop heat pipe. A three-dimensional finite element thermal-fluid solver was implemented to study solid and liquid temperature distributions in the vicinity of the evaporator section of a planar vertically-wicking micro-columnated loop heat pipe (μCLHP). Using in-plane thermal-conduction barriers and a thermally-resistive fluidic connection, it was

demonstrated that an adequate temperature difference can be maintained between the evaporator section and the compensation chamber of a planar wafer-based loop heat pipe, even for a coherent porous silicon-based wick only several hundred *microns* thick. These techniques will help ensure a sufficient motive temperature head between the evaporator section and the compensation chamber, in order to improve performance and alleviate startup problems in these devices.

Chapter 3

Device Optimization Based on Flow Loop Pressure Analysis

In this chapter is performed a design optimization study on the micro-columnated loop heat pipe (μCLHP), assuming that the overall device performance is limited by the capillary pumping requirement discussed in section 2.2.3. An optimization problem is setup in terms of the various μCLHP design parameters, and the use of monotonicity analysis, a pre-optimization technique, is demonstrated. The simplified cases derived using monotonicity analysis are solved numerically to determine the influence of various design parameters on device performance. For a particular μCLHP design, the optimum values of these parameters are calculated.

3.1 Device Theory and Theoretical Modeling

A proper appreciation of the device physics and accurate theoretical modeling of heat transfer and fluid flow phenomena at the microscale are critical to predicting the performance of the μCLHP. Models have been developed for predicting the operation of macroscale loop heat pipes which agree very well with experimental studies [65]. An overall energy balance and a pressure balance of the fluid flow loop are used to predict the steady state operation of the loop heat pipe. Since the basic thermodynamic principles are expected to remain unchanged as the device is scaled down in size, a similar overall approach towards modeling a microscale loop heat pipe is justified [77, 78]. Nevertheless, the heat transfer and fluid flow equations that work well at the macroscale are not guaranteed to give accurate results in the microscale regime [79]. Hence, theoretical models developed using recent studies in heat transfer and fluid flow in minichannels and microchannels [80, 81, 82, 83] have been employed in this study.

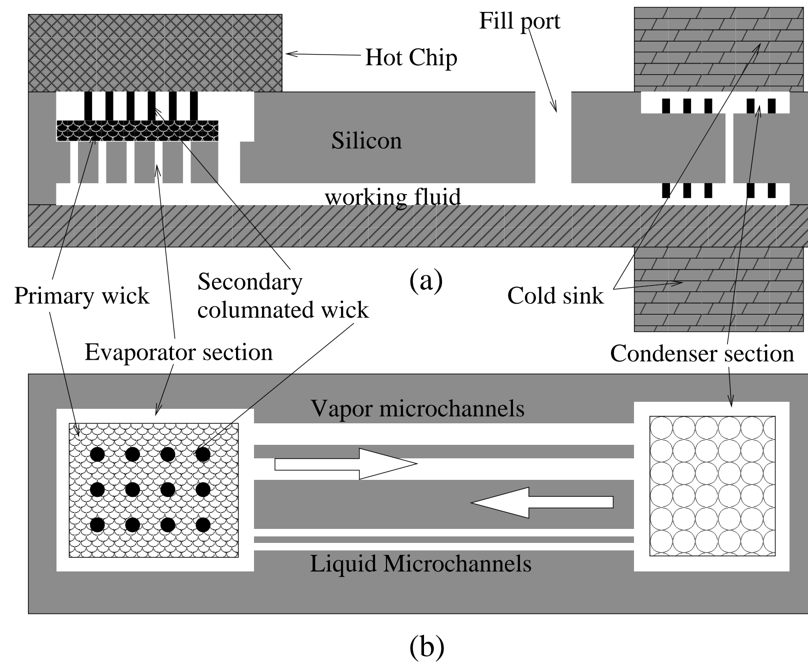

Figure 3.1: The micro-columated loop heat pipe (μCLHP): (a) Side view; (b) Top view.

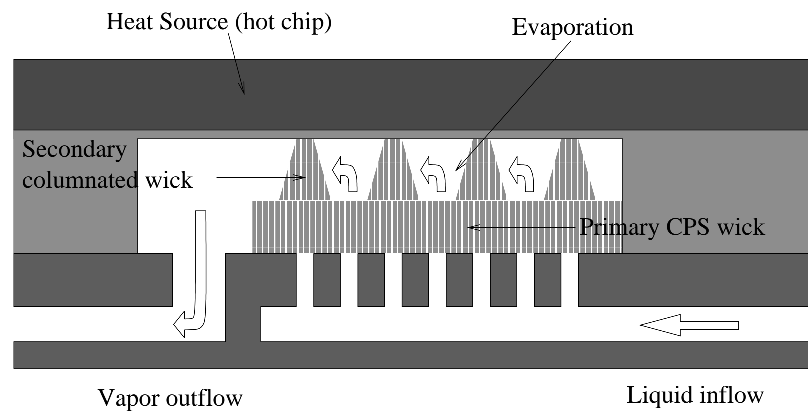

Figure 3.2: The micro-columnated coherent porous silicon (CPS) wicking structure.

3.1.1 Energy Balance in the Evaporator

Performing an overall every balance on the evaporator section of the μCLHP gives [65]:

$$Q_t = Q_{h_{fg}} + Q_{C_p \Delta T, liq} + Q_{C_p \Delta T, vap} \tag{3.1}$$

where Q_t is the total amount of heat entering the evaporator, $Q_{h_{fg}}$ is the latent heat of evaporation, and $Q_{C_p\Delta T,liq}$ and $Q_{C_p\Delta T,vap}$ are the sensible heats of the liquid and vapor respectively. These quantities are related to the mass flow rate through the evaporator, $\dot{m}$, as follows:

$$Q_{h_{fg}} = \dot{m}h_{fg} \tag{3.2}$$

$$Q_{C_p\Delta T,liq} = \dot{m}C_p(T_s - T_l) \tag{3.3}$$

$$Q_{C_p\Delta T,vap} = \dot{m}C_p(T_v - T_s) \tag{3.4}$$

where h_{fg} is the fluid latent heat capacity and T_s the saturation temperature of the working fluid. T_l is the temperature of the subcooled liquid entering the reservoir and T_v is the temperature of the superheated vapor leaving the evaporator.

3.1.2 Pressure Balance in the Flow Loop

As shown in Figure 3.1(b), the working fluid moves in a loop during normal operation of the μCLHP. The capillary pressure developed across the liquid/vapor interface in the wick provides the pumping action for this motion. For proper device operation, the capillary pressure must balance the viscous pressure drops due to fluid flow in the wick and connecting microchannels. In steady state operation, a pressure balance around the flow loop should satisfy the following equation:

$$\Delta P_c \geq \Delta P_w + \Delta P_l + \Delta P_v \tag{3.5}$$

where ΔP_c is the capillary pressure gain across the vapor/liquid interface in the wick, ΔP_w is the viscous liquid pressure drop in the wick, and ΔP_l and ΔP_v are the viscous liquid and vapor pressure drops in the liquid and vapor microchannels respectively.

Capillary pressure gain

The capillary pressure gain across the liquid/vapor interface in the circular pores of the wick is given by the Young-Laplace equation [65, 78]:

$$\Delta P_c = \frac{2\sigma_l}{r} cos\theta \tag{3.6}$$

where σ_l is the surface tension of the working fluid, r the wick pore radius, and θ the contact angle of the meniscus. The contact angle is close to zero for hydrophilic solids and wetting liquids [78].

Liquid and vapor microchannel pressure drop

The liquid and vapor microchannels, which connect the evaporator and condenser sections, are rectangular in shape. The frictional pressure drop due to laminar flow

of a viscous fluid in a rectangular microchannel is given by [80, 81]:

$$\Delta P_{fluid} = \frac{2\,(fRe)\,\mu u_m x}{{D_h}^2} + K_\infty \frac{\rho u_m^2}{2} \tag{3.7}$$

$$\begin{aligned} fRe = \quad & 24(1 - 1.3553\alpha_c + 1.9467{\alpha_c}^2 \\ & -1.7012{\alpha_c}^3 + 0.9564{\alpha_c}^4 - 0.2537{\alpha_c}^5) \end{aligned} \tag{3.8}$$

$$\begin{aligned} K_\infty = \quad & 0.0697 + 1.2197\alpha_c + 3.3089{\alpha_c}^2 \\ & -9.5921{\alpha_c}^3 + 8.9089{\alpha_c}^4 - 2.9959{\alpha_c}^5 \end{aligned} \tag{3.9}$$

$$D_h = \frac{4A_c}{P} \tag{3.10}$$

$$\alpha_c = \frac{a}{b} \tag{3.11}$$

Here f is the friction factor, Re is the Reynold's number, μ is the dynamic viscosity of the fluid, u_m is the mean fluid flow velocity, ρ is the fluid density, and K_∞ is the Hagenbach's factor for rectangular channels. Also D_h is the hydraulic diameter, and A_c and P are the area of cross section and perimeter of the rectangular channel, where a and b are the short and long sides of the channel respectively.

Wick pressure drop

The pressure drop in the wick is associated with the process of phase change and the two-phase flow characteristics in the micron-sized circular pores of the cohorent porous silicon wicking structure. The pressure drop in the circular pores of the wicking structure, ΔP_w, is a sum of the following components [80]:

$$\Delta P_w = \Delta p_c + \Delta p_{f,1-ph} + \Delta p_{f,tp} + \Delta p_e \tag{3.12}$$

where Δp_c is the contraction pressure drop at the wick entrance, $\Delta p_{f,1-ph}$ is the liquid pressure drop in the wick, $\Delta p_{f,tp}$ is the two phase pressure drop in the wick, and Δp_e is the expansion pressure drop at the wick exit.

The contraction pressure drop due to sudden contraction of the liquid entering the wick is given by [80, 84]

$$\Delta p_c = \frac{G^2}{2\rho_l}\left[\left(\frac{1}{C_o} - 1\right)^2 + 1 - \frac{1}{\sigma_c^2}\right]\psi_h \tag{3.13}$$

where G is the mass flux, σ_c is the area contraction ratio, and C_o is the contraction coefficient given by

$$C_o = \frac{1}{0.639(1 - 1/\sigma_c)^{0.5} + 1} \tag{3.14}$$

Table 3.1: Design constants of the μCLHP

Shape related constants			
A_e	$10.44\ mm^2$	A_c	$79.21\ mm^2$
n_l	4	n_v	2
h_l	$150\ \mu m$	h_v	$150\ \mu m$
$L_{l,min}$	$4.6\ cm$	$L_{v,min}$	$4.6\ cm$
$L_{l,max}$	$10\ cm$	$L_{v,max}$	$10\ cm$
$w_{l,min}$	$2\ \mu m$	$w_{v,min}$	$2\ \mu m$
$w_{l,max}$	$150\ \mu m$	$w_{v,max}$	$2000\ \mu m$
$d_{w,min}$	$1\ nm$	$d_{w,max}$	$1.8\ mm$
$t_{w,min}$	$200\ \mu m$	$t_{w,max}$	$400\ \mu m$
$p_{w,max}$	0.349		
Properties of the working fluid (water)			
T_s	$373.15K$	C_p	$4217\ J/kgK$
h_{fg}	$2256.3\ kJ/kg$	C_p	$4217\ J/kgK$
ρ_l	$958\ kg/m^3$	ρ_v	$0.5974\ kg/m^3$
μ_l	$281.8\ \mu Pa\ s$	μ_v	$13.3\ \mu Pa\ s$
σ_l	$0.05885\ N/m$	θ	29°

The two-phase homogeneous flow multiplier, ψ_h, is given by

$$\psi_h = \left[1 + x\left(\frac{\rho_l}{\rho_v} - 1\right)\right] \tag{3.15}$$

where x is the local vapor quality.

The expansion pressure drop at the wick exit is given by

$$\Delta p_e = \frac{G^2}{\rho_l}\sigma_e(1 - \sigma_e)\psi_s \tag{3.16}$$

where σ_e is the expansion ratio from the wick to the vapor area and ψ_s is the separated flow multiplier, given by

$$\psi_s = 1 + \left(\frac{\rho_l}{\rho_v} - 1\right)\left[0.25x(1 - x) + x^2\right] \tag{3.17}$$

In part of the wick where there is no nucleation, fluid flow pressure drop is modeled by considering developing laminar viscous flow of liquid through circular microchannels as follows [80, 82, 83]:

$$\Delta p_{f,1-ph} = \frac{2\,(fRe)\,\mu_l u_{m,l} x_{w,liq} t_w}{{D_h}^2} + K_\infty \frac{\rho_l u_{m,l}^2}{2} \tag{3.18}$$

$$fRe = 16 \tag{3.19}$$

$$K_\infty = 1.28 \tag{3.20}$$

where t_w is the total wick thickness, while $x_{w,liq}$ is the fractional length of the wick completely wetted by the liquid phase.

The two-phase pressure drop in the wick is given by

$$\Delta p_{f,tp} = \frac{2\,(fRe)\,\mu_l u_{m,l}(1 - x_{w,liq})t_w}{{D_h}^2}\phi_L^2 \tag{3.21}$$

$$fRe = 16 \tag{3.22}$$

where the two-phase multiplier ϕ_L^2 is given by

$$\phi_L^2 = 1 + \frac{C(1 - e^{-319D_h})}{X} + \frac{1}{X^2} \tag{3.23}$$

and the Martinelli parameter X is given by

$$X^2 = \left(\frac{dp_F}{dz}\right)_L \Big/ \left(\frac{dp_F}{dz}\right)_V = \frac{\mu_l \rho_v}{\mu_v \rho_l} = \frac{\nu_l}{\nu_v} \tag{3.24}$$

3.1.3 Liquid Refilling of the Wicking Structure

A hydrophilic liquid would take a finite amount of time to refill an empty capillary wicking structure. The liquid penetration rate into a cylindrical capillary tube of radius r is given by [85]

$$\frac{dl}{dt} = \frac{\Sigma P(r^2 + 4\epsilon r)}{8\eta l} \tag{3.25}$$

where ΣP is the total driving pressure, ϵ is the coefficient of slip, and η is the dynamic viscosity of the fluid. Integrating the above equation in time results in the following expression for the distance penetrated by a liquid flowing under capillary pressure alone [85]:

$$l = \sqrt{\frac{\sigma_l r t \cos\theta}{2\eta}} \tag{3.26}$$

where σ_l is the liquid surface tension coefficient and θ is the contact angle. The above result implies a limit on the liquid mass flow rate through the capillary wicking structure, where the individual pores are constantly being dried out and refilled. For a CPS wick of thickness $t_w \equiv l$ and pore diameter $d_w \equiv 2r$, an equivalent average fluid velocity through the wick is given by

$$v_{eq} = \frac{l}{t} = \frac{t_w}{t} = \frac{\sigma_l d_w \cos\theta}{4\eta t_w} \tag{3.27}$$

Table 3.2: Parameters of the μCLHP design optimization problem

Design Parameters	
d_w	Wick pore diameter
t_w	Wick thickness
p_w	Wick porosity
L_l	Length of liquid microchannels
L_v	Length of vapor microchannels
w_l	Width of liquid microchannels
w_v	Width of vapor microchannels
Non-design Parameters	
$\dot{m}$	Mass flow rate
ΔP_c	Capillary Pressure gain
ΔP_w	Wick pressure drop
ΔP_l	Liquid flow pressure drop
ΔP_v	Vapor flow pressure drop

The mass flow rate in the wicking structure can therefore never exceed a particular value ($\dot{m}_R$), irrespective of the overall flow dynamics of the μCLHP. This limit is given by

$$\dot{m} \leq \dot{m}_R = \frac{\rho\sigma_l \cos\theta}{4\eta}\left(\frac{p_w d_w A_e}{t_w}\right) \tag{3.28}$$

This directly correlates to the maximum amount of heat flux that can be applied to the wick before it starts to dry out due to the liquid evaporation rate exceeding the wick refilling rate, and is given by

$$\begin{aligned} Q_R = Q_{max,refill} &= h_{fg}\dot{m}_R = \rho h_{fg} v_{eq} A_e p_w \\ &= \frac{\rho h_{fg}\sigma_l \cos\theta}{4\eta}\left(\frac{p_w d_w A_e}{t_w}\right) \end{aligned} \tag{3.29}$$

where ρ is the density of the liquid, h_{fg} is the latent heat of evaporation of the liquid, A_e is the area of the evaporator, and p_w is the wick porosity.

3.2 Design Optimization

Designing an optimal μCLHP involves optimization of a number of design parameters, to maximize the heat flux carrying capacity of the system, while satisfying the necessary design criteria and constraints. Design parameters are variables related to the shape, size, fabrication, and other characteristics of the μCLHP. Initial design decisions, related to such aspects as fabrication of the device and the choice of a working fluid, fix the value of some of these design parameters. They are listed in Table 3.1

Table 3.3: Objective function and equality constraints for the μCLHP design optimization problem

Objective Function		
$Obj:$	$Q_{h_{fg}} = \dot{m}h_{fg}$	Latent heat flux carrying capacity of μCLHP
Equality Constraints		
$H_1:$	$\Delta P_c - f_c(d_w) = 0$	Capillary pressure gain (Equation 3.6)
$H_2:$	$\Delta P_w - f_w(\dot{m}, d_w, t_w, p_w) = 0$	Wick pressure drop (Equation 3.12)
$H_3:$	$\Delta P_l - f_l(\dot{m}, L_l, w_l) = 0$	Liquid pressure drop (Equation 3.7)
$H_4:$	$\Delta P_v - f_v(\dot{m}, L_v, w_v) = 0$	Liquid pressure drop (Equation 3.7)

Table 3.4: Inequality constraints for the μCLHP design optimization problem

Inequality Constraints		
$G_1:$	$\dot{m} \geq 0$	Mass flow rate is positive
$G_2:$	$d_w - d_{w,min} \geq 0$	Wick pore fabrication limit
$G_3:$	$d_{w,max} - d_w \geq 0$	Wick pore fabrication limit
$G_4:$	$t_w - t_{w,min} \geq 0$	Lower limit of wick thickness
$G_5:$	$t_{w,max} - t_w \geq 0$	Upper limit of wick thickness
$G_6:$	$p_w \geq 0$	Lower limit on porosity
$G_7:$	$p_{w,max} - p_w \geq 0$	Upper limit for circular pores
$G_8:$	$L_l - L_{l,min} \geq 0$	Heat transport distance
$G_9:$	$L_{l,max} - L_l \geq 0$	Design considerations
$G_{10}:$	$L_v - L_{v,min} \geq 0$	Heat transport distance
$G_{11}:$	$L_{v,max} - L_v \geq 0$	Design considerations
$G_{12}:$	$w_l - w_{l,min} \geq 0$	Fabrication limit
$G_{13}:$	$w_{l,max} - w_l \geq 0$	Design considerations
$G_{14}:$	$w_v - w_{v,min} \geq 0$	Fabrication limit
$G_{15}:$	$w_{v,max} - w_v \geq 0$	Design considerations
$G_{16}:$	$\Delta P_c - \Delta P_w - \Delta P_l - \Delta P_v \geq 0$	Pressure balance (Equation 3.5)
$G_{17}:$	$\dot{m}_R - \dot{m} \geq 0$	Wick refilling limit (Equation 3.28)

and will henceforth be referred to as design constants. Determining an optimum value for the rest of the design parameters is the primary concern of the design optimization problem. Non-design parameters are variables that, although not directly related to device design, appear in the mathematical formulation of the optimization problem. All of these unknown parameters are listed in Table 3.2.

The overall design optimization problem is formulated in Table 3.3 and Table 3.4. Given in Table 3.3 are the objective function and the equality constraints. The ob-

Table 3.5: Initial Monotonicity table

	$\dot{m}$	d_w	t_w	p_w	L_l	L_v	w_l	w_v	ΔP_c	ΔP_w	ΔP_l	ΔP_v	Act
Obj	+												
G_1	+												
G_2		+											
G_3		-											
G_4			+										
G_5			-										
G_6				+									
G_7				-									
G_8					+								
G_9					-								
G_{10}						+							
G_{11}						-							
G_{12}							+						
G_{13}							-						
G_{14}								+					
G_{15}								-					
G_{16}									+	-	-	-	
G_{17}	-	+	-	+									
H_1		?							?				
H_2	?	?	?	?						?			
H_3	?				?		?				?		
H_4	?					?		?				?	

jective function, to be maximized, is the latent heat carrying capacity of the μCLHP (Equation 3.2). The sensible heat components of the total heat carried by the μCLHP (Equation 3.1) are relatively small and can be neglected. The equality constraints correspond to the definitions of the various pressure terms involved in the pressure balance equation (Equation 3.5). The inequality constraints on the design parameters are given in Table 3.4. They arise from user defined limits on the design parameters, as well as from the pressure balance (Equation 3.5) and wick-liquid-refilling (Equation 3.28) requirements. An optimum μCLHP design would maximize the objective function subject to the given equality and inequality constraints. A pre-optimization tool called Monotonicity analysis is used to narrow down the optimization problem to simpler cases, which can then be solved either analytically or numerically.

Table 3.6: Monotonicity table (Case I)

	$\dot{m}$	d_w	t_w	p_w	L_l	L_v	w_l	w_v	ΔP_c	ΔP_w	ΔP_l	ΔP_v	Act
Obj	+												
G_1	+												
G_2		+											
G_3		-											Ac
G_4			+										Ac
G_5			-										
G_6				+									
G_7				-									Ac
G_8					+								
G_9					-								
G_{10}						+							
G_{11}						-							
G_{12}							+						
G_{13}							-						
G_{14}								+					
G_{15}								-					
G_{16}									+	-	-	-	
G_{17}	-	+	-	+									Ac
H_1		?							?				
H_2	?	?	?	?						?			
H_3	?				?		?				?		
H_4	?					?		?				?	

3.2.1 Monotonicity Analysis

Monotonicity analysis is a pre-optimization tool used to simplify large constrained optimization problems [86]. It helps to reduce the number of possible cases leading to an optimum solution by characterizing the different constraints relevant to the problem. A numerical solution of these simplified cases will indeed still capture all the relevant optima—but with much less numerical effort and ambiguity. Inequality constraints can be active or inactive depending upon the location of the optimum solution in the feasible domain. An inequality constraint is considered active if the optimum solution lies on a domain boundary defined by that particular constraint and inactive otherwise. Similarly, a relevant equality constraint would affect the position of the optimum solution in the feasible domain, whereas the optimum solution would remain unaffected in the event an irrelevant equality constraint is discarded.

The rules governing monotonicity analysis are given in Appendix A. A monotonicity table is constructed by arranging the problem parameters along the columns

Table 3.7: Monotonicity table (Case II)

	$\dot{m}$	d_w	t_w	p_w	L_l	L_v	w_l	w_v	ΔP_c	ΔP_w	ΔP_l	ΔP_v	Act
Obj	+												
G_1	+												
G_2		+											
G_3		-											
G_4			+										Ac
G_5			-										
G_6				+									
G_7				-									Ac
G_8					+								Ac
G_9					-								
G_{10}						+							Ac
G_{11}						-							
G_{12}							+						
G_{13}							-						Ac
G_{14}								+					
G_{15}								-					Ac
G_{16}									+	-	-	-	Ac
G_{17}	-	+	-	+									
H_1		-							-				Re
H_2	-	+	-	+						+			Re
H_3	-				-		+				+		Re
H_4	-					-		+				+	Re

and the constraints along the rows. In Table 3.5 is shown the initial monotonicity table obtained as follows: The partial derivatives of the objective function Obj and inequality constraints G_i, given in Table 3.3 and Table 3.4, are calculated using rule 2 and represented in the monotonicity table using "+" and "-" signs. While some of these partial derivatives can be deduced analytically, others have to be determined numerically. The signs of partial derivatives of the equality constraints would be marked temporarily with a "?" sign. Now, either the inequality constraint G_{17} has to be active or one of the equality constraints H_2, H_3, H_4 has to be relevent due to parameter $\dot{m}$ by rule 8. This leads to the following two cases:

Case I: Wick refilling limited (G_{17} active)

Assume that the constraint G_{17} is active. Constraint G_3 is then made active due to parameter d_w and constraint G_{17} by rule 9. G_4 is made active due to t_w and G_{17} by rule 9. G_7 is made active due to p_w and G_{17} by rule 9. The final result is shown

in Table 3.6.

This particular case corresponds to the situation when the device heat flux carrying capacity is limited by wick dry out caused by insufficient liquid refilling of the wick. The active inequality constraints in the monotonicity table (Table 3.6) lead to the following optimum values for these design parameters:

$$\begin{aligned} d_w &= d_{w,max} \\ t_w &= t_{w,min} \\ p_w &= p_{w,max} \end{aligned} \tag{3.30}$$

This is a logical result, since having a smaller wick thickness, and larger wick porosity and wick pore diameter lead to faster refilling of the wick. The rest of the design parameters L_l, L_v, w_l, and w_v do not have any effect on the result in this case, since they do not have an active or relevant constraint of opposite monotonicity (see rule 9 in Appendix A).

Case II: Pressure balance limited (G_{17} inactive)

Since G_{17} is assumed to be inactive, either H_2, H_3, or H_4 has to be relevant due to parameter $\dot{m}$ by rule 8. As a first sub-case, assume H_2 to be active.

The inequality constraint G_4 is made active due to parameter t_w and constraint H_2 by rule 9. G_7 is made active due to p_w and H_2 by rule 9. G_{16} is made active due to ΔP_w and H_2 by rule 9. H_1 is made relevant due to ΔP_c and G_{16} by rule 9. H_3 is made relevant due to ΔP_l and G_{16} by rule 9. H_4 is made relevant due to ΔP_v and G_{16} by rule 9. G_8 is made active due to L_l and H_3 by rule 9. G_{10} is made active due to L_v and H_4 by rule 9. G_{13} is made active due to w_l and H_3 by rule 9. G_{15} is made active due to w_v and H_4 by rule 9.

The final monotonicity table for this case is shown in Table 3.7. All equality constraints are found to be relevant, while the inequality constraints G_4, G_7, G_8, G_{10}, G_{13},G_{15} and G_{16} are active. No more sub-cases need be considered since those would only involve making H_1, H_3, and H_4 relevant, which they are in this case. From the active inequality constraints in Table 3.7, the following optimum values of the design parameters are obtained:

$$\begin{aligned} t_w &= t_{w,min} \\ p_w &= p_{w,max} \\ L_l &= L_{l,min} \\ L_v &= L_{v,min} \\ w_l &= w_{l,max} \\ w_v &= w_{v,max} \end{aligned} \tag{3.31}$$

The wick pore diameter d_w, however, will assume a value that maximizes the objective function (latent heat flux capacity) subject to the active constraint G_{16}, which

Table 3.8: Objective function and constraints for the pre-optimized μCLHP design optimization problem

Problem Parameters		
	$\dot{m}$	Mass flow rate
	d_w	Wick pore diameter
	ΔP_c	Capillary Pressure gain
	ΔP_w	Wick pressure drop
	ΔP_l	Liquid flow pressure drop
	ΔP_v	Vapor flow pressure drop
Objective Function		
$Obj:$	$Q_{h_{fg}} = \dot{m}h_{fg}$	Latent heat flux carrying capacity of μCLHP
Equality Constraints		
$h_1:$	$\Delta P_c - \Delta P_w - \Delta P_l - \Delta P_v = 0$	Pressure balance (Equation 3.5)
$h_2:$	$\Delta P_c - f_c(d_w) = 0$	Capillary pressure gain (Equation 3.6)
$h_3:$	$\Delta P_w - f_w(\dot{m}, d_w) = 0$	Wick pressure drop (Equation 3.12)
$h_4:$	$\Delta P_l - f_l(\dot{m}) = 0$	Liquid pressure drop (Equation 3.7)
$h_5:$	$\Delta P_v - f_v(\dot{m}) = 0$	Liquid pressure drop (Equation 3.7)
Inequality Constraints		
$g_1:$	$\dot{m} \geq 0$	Mass flow rate is positive
$g_2:$	$d_w - d_{w,min} \geq 0$	Wick pore fabrication limit
$g_3:$	$d_{w,max} - d_w \geq 0$	Wick pore fabrication limit
$g_4:$	$\dot{m}_R - \dot{m} \geq 0$	Wick refilling limit (Equation 3.28)

corresponds to the pressure balance in Equation 3.5. This optimum value will have to be determined numerically.

3.2.2 Numerical Optimization

The μCLHP device optimization problem, considerably simplified by monotonicity analysis, can now be solved numerically. In Table 3.8 is listed the updated optimization problem, which now involves fewer parameters and constraints. Cases I and II discussed above had lead to analytical solutions for all of the design parameters except the wick pore diameter d_w for Case II. The objective is to numerically maximize the device latent heat carrying capacity $Q_{h_{fg}}$, while satisfying the steady state pressure balance requirement. Indeed, monotonicity analysis yielded a one-dimensional problem that was considerably much simpler to solve. To obtain a numerical solution for the optimum value of d_w, the actual numerical values of the design constants (Ta-

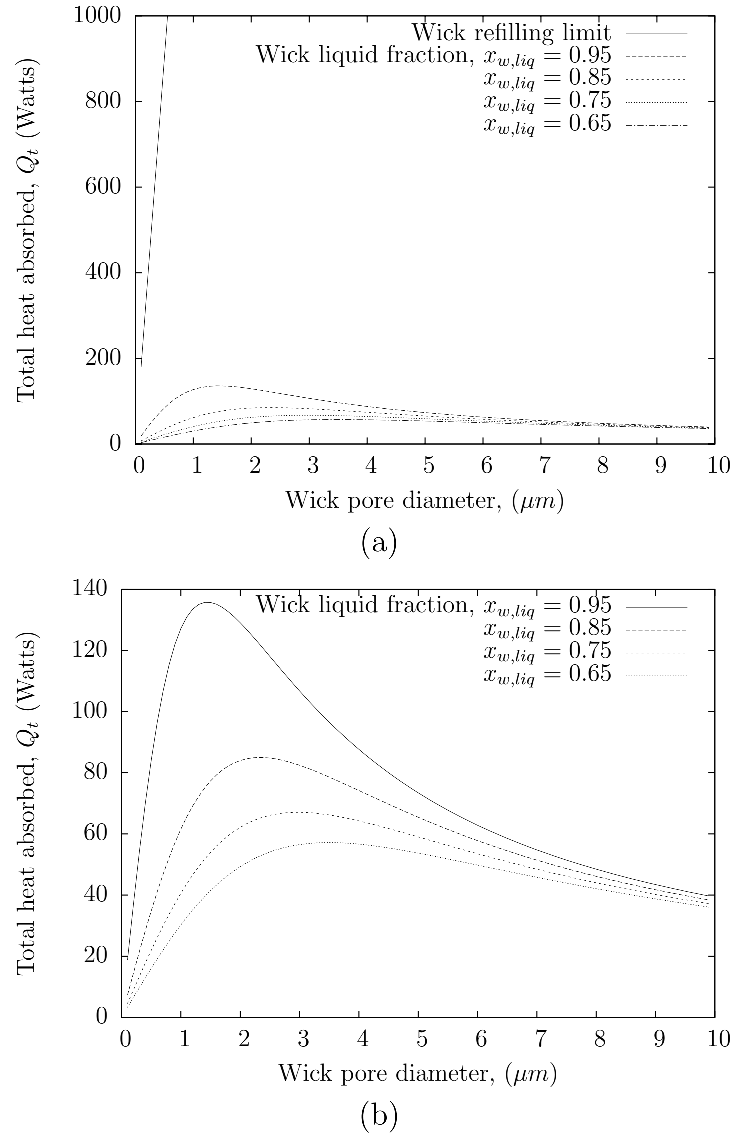

Figure 3.3: Plots of total latent heat carrying capacity of the μCLHP as a function of the wick pore diameter d_w, for different wick liquid wetting fractions $x_{w,liq}$. (a) The wick refilling limit is much larger than the pressure balance limit, and thus inactive. (b) The maximum heat flux decreases and the corresponding optimum wick pore diameter increases with decreasing wick liquid wetting fraction $x_{w,liq}$.

ble 3.1) have to be employed. This assigns fixed numerical values to the rest of the design parameters, which were previously optimized using monotonicity analysis. For a given arbitrary value of d_w, the non-linear system of algebraic equations given in Table 3.8 can be solved numerically to get the corresponding heat flux capacity $Q_{h_{fg}}$. By plotting $Q_{h_{fg}}$ against d_w, the value of the wick pore diameter that maximises the

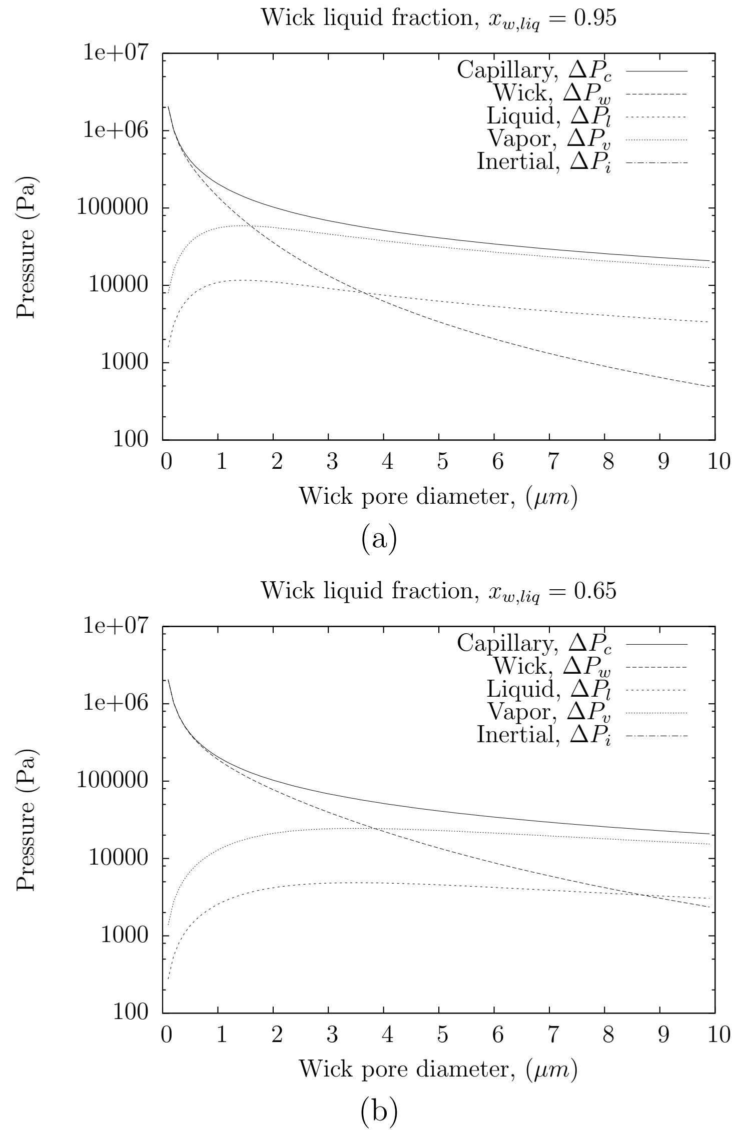

Figure 3.4: Plots of the different flow-loop pressure components of the μCLHP device in steady state operation, as a function of the wick pore diameter: (a) Wick liquid fraction, $x_{w,liq} = 0.95$; (b) Wick liquid fraction, $x_{w,liq} = 0.65$.

heat flux capacity can be obtained.

In Figure 3.3 is shown the numerically calculated total heat carrying capacity of the μCLHP as a function of the wick pore diameter, for different wick liquid wetting fractions. The wick refilling limit on Q_t is plotted in Figure 3.3(a) and is seen to be irrelevant for this particular numerical choice of the design constants. This implies that case II from the monotonicity analysis is active.

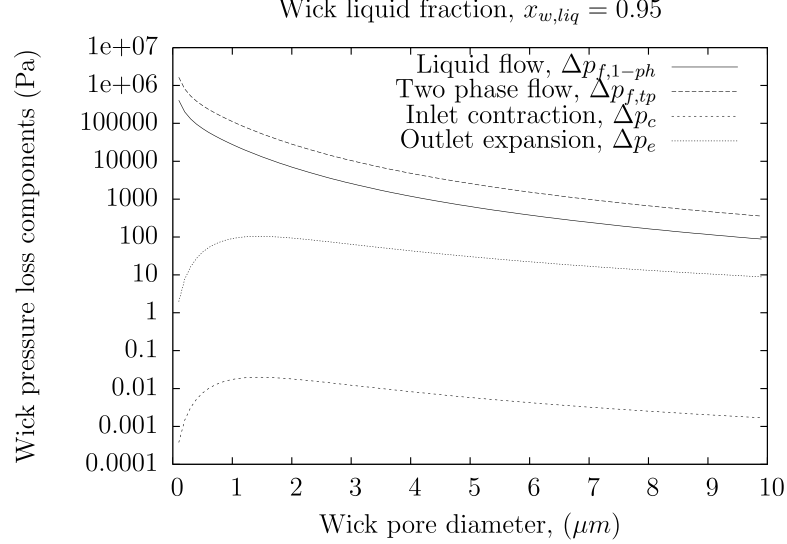

Figure 3.5: A comparison of the different pressure components in the wicking structure of the μCLHP device for a wick liquid fraction of $x_{w,liq} = 0.95$.

The general trend of Q_t in Figure 3.3(b) can be explained as follows: For very low values of the wick pore diameter d_w, the wick pressure drop term ΔP_w in Equation 3.5 becomes extremely large, which reduces the mass flow rate and hence Q_t. Conversely, for very high values of d_w, the capillary pressure term ΔP_c becomes extremely small, thus reducing Q_t. In between these extremities lies an optimum value of the wick pore diameter that maximizes the heat carrying capacity Q_t.

The wick liquid fraction $x_{w,liq}$ is an empirical parameter that will depend on the details of the micro-columnated wick design and its microscale boiling characteristics. A smaller value of $x_{w,liq}$ implies that, when averaged over time, a larger volume is occupied by vapor in the thin-film evaporation that happens in the wick. For $x_{w,liq} = 0.95$, the maximum value of Q_t is found to be 135 W, at an optimum wick pore diameter of $d_w = 1.3$ μm. This corresponds to an input heat flux of 1293 W/cm^2 per unit are of the device evaporator. For smaller values of $x_{w,liq}$, the maximum value of Q_t decreases, while the optimum wick pore diameter increases. Both of these results can be attributed to the two-phase-flow pressure drop in the wick $\Delta p_{f,tp}$, given by Equation 3.21. With decreasing $x_{w,liq}$, there is an increase in $\Delta p_{f,tp}$, which opposes the fluid flow in the wick thereby reducing the overall heat transport capacity of the μCLHP. An increase in the wick pore diameter $d_w = D_h$ helps to slightly alleviate this negative effect, and hence the increase in optimum wick pore diameter with decreasing wick liquid fraction.

In Figure 3.4 we can see the different pressure components in the device as a function of the wick pore diameter, for two different wick wetting fractions. In Fig-

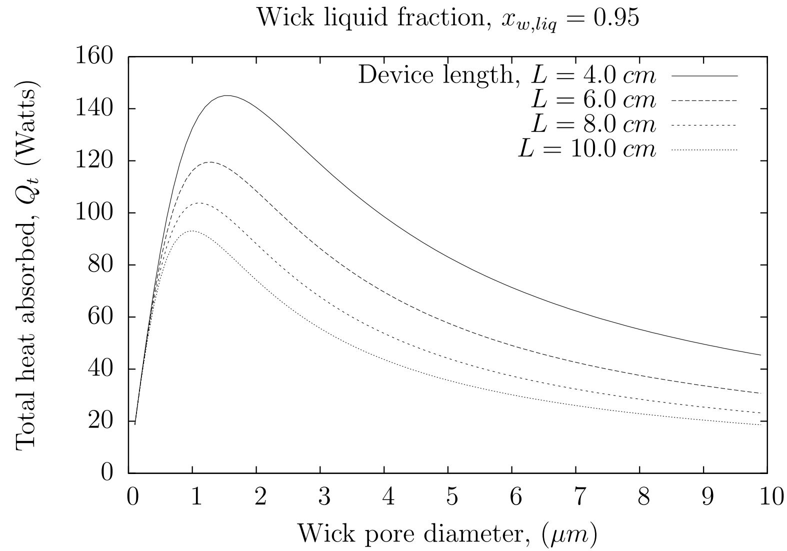

Figure 3.6: Plots of the total heat carrying capacity of the μCLHP as a function of the wick pore diameter, for different device lengths.

ure 3.3 it is seen that the optimum wick pore diameters for the two wick liquid wetting fractions $x_{w,liq} = 0.95$ and $x_{w,liq} = 0.65$ are $d_w = 1.3\ \mu m$ and $d_w = 3.5\ \mu m$, respectively. Figure 3.4 helps to explain this result. In steady state operation, the capillary pressure gain in the wick is balanced by the wick, liquid microchannel, and vapor microchannel pressure drops. From Figure 3.4 it is clear that for larger wick pore diameters the vapor microchannel pressure drop is the primary component balancing the capillary pressure gain in the wick. But as the wick pore diameter approaches its optimum value, the wick fluid flow pressure drop component becomes dominant. Below the optimum wick pore diameter, the wick fluid flow pressure loss increases at a rate higher than the capillary pressure gain. As a result, the mass flow rate, and hence the liquid and vapor microchannel pressure drops, decrease when going below the optimum wick pore diameter.

In Figure 3.5 can be seen the various pressure loss components in the micro-columnated coherent porous silicon wicking structure as a function of the wick pore diameter, for a wick liquid wetting fraction of $x_{w,liq} = 0.95$. The two-phase-flow pressure drop $\Delta p_{f,tp}$ appears to be the major contributor to the overall wick pressure drop, while the liquid flow pressure drop is a smaller fraction. The inlet and outlet pressure drops due to flow contraction and expansion are found to be negligible.

The analytical results from monotonicity analysis can also be verified by numerically plotting the variation of heat carrying capacity Q_t with some of the concerned design parameters. In Figure 3.6 can be seen the heat carrying capacity as a function of the wick pore diameter, for different device lengths. predicts that minimizing L_l

and L_v will maximize Q_t, which is clearly demonstrated by Figure 3.6. The plot of Q_t vs d_w monotonically decreases as the device length ($L = L_l = L_v$) is increased from 4 *cm* to 10 *cm*. It is also worthwhile to note that although the device length scales the overall heat carrying capacity of the device, it does not change the optimum wick pore diameter by a large amount. This can be explained by the fact that the device length only affects the liquid and vapor microchannel pressure drops, which are dominated by the wick pressure drop near the optimum wick pore diameter.

3.3 Conclusions

A design optimization study was performed to determine the values of μCLHP design parameters that maximize device performance. The heat carrying capacity of the device was modeled by performing a pressure balance around the flow loop, along with taking into account any possible limitations imposed by wick-refilling requirements due to possible vapor bubble formation in the pores of the wicking structure. Monotonicity analysis and numerical optimization were performed to maximize the heat carrying capacity of the device. Monotonicity analysis yielded analytical solutions for most of the design parameters, such as the lengths and widths of the microchannels, and the thickness and porosity of the wicking structure. For the set of design constants chosen, the wick-refilling limit was found to be inactive. The monotonicity analysis reduced the optimization problem to a 1 DOF nonlinear system. The optimum wick pore diameter was calculated numerically by solving the non-linear pressure balance equations over a range of values of the wick pore diameter. The maximum heat carrying capacity also depends on the wick liquid wetting fraction and is found to be approximately 135 W for a wick wetting fraction of 0.95. This corresponds to an input heat flux of 1293 W/cm^2 per unit area of the evaporator. The wick pressure drop and the vapor microchannel pressure drop are comparable near the optimum wick pore diameter.

Chapter 4

Numerical Simulation of Phase Change in the Wick

The rate of evaporation in the wicking structure is one of the critical operating parameters of the micro-columnated loop heat pipe (μCLHP). Although the upper limit on the heat transfer carrying capacity of the μCLHP can be calculated by performing a pressure balance on the device flow loop, the actual heat transported by the device is limited by the rate of evaporation from the liquid-vapor meniscus in the wicking structure. In order to optimize evaporator wick design, we need a way to predict evaporation rates from the different wick topologies that can be fabricated using standard MEMS microfabrication techniques. In this chapter is described a numerical model that was developed to compute the rates of thin-film evaporation from a steady-state stationary meniscus in an arbitrarily shaped wick microstructure.

4.1 Background

Wayner *et al.* [87] developed a theoretical model to calculate the evaporative heat transfer coefficient of the interline region in a wetting liquid film. Xu and Carey [88] developed an analytical model to predict heat transfer characteristics of film evaporation on a microgroove surface, and compared their results with experiments. They concluded that the disjoining pressure plays an important role in determining the rate of evaporation. Ma and Peterson [89] developed a mathematical model to predict the rate of evaporation and temperature distribution along the axial direction of a groove plate. They accounted for surface tension and disjoining pressure effects, and showed that the apparent contact angle, and hence the rate of heat transfer through the micro region, increases in the axial direction, and that temperature induced surface tension changes can be neglected in the micro region. Wang *et al.* [90] developed a numerical model, using the complete expression for the kinetic theory-based mass transport equation, to study heat transfer aspects of the liquid-vapor meniscus in a

two-dimensional microchannel. Beyond a channel width of a few microns, the rate of heat transfer in the thin film region is found to be relatively insensitive to channel size. Conversely, heat transfer in the intrinsic meniscus has a significant dependence on channel size. For the channel sizes considered, thin film accounts for only a small portion of the overall heat transfer, while most of it happens in a micro-region defined to be within a one micron thick meniscus. Morris [91, 92] analyzed the stationary meniscus of an evaporating perfectly wetting system to show that the apparent contact angle is dictated by a small scale flow (driven by evaporation near the contact line), which does not contribute much to the overall heat transfer. The apparent contact angle depends on material properties and wall superheat, and can be calculated separately in order to simplify the meniscus heat transfer problem, which can now be posed without worrying about the disjoining pressure and other nanometer scale effects. Ranjan *et al.* [93] developed a finite volume based 3-D numerical model to predict evaporative heat transfer rates for the different wick materials used in heat pipes. They were able to characterize the effects of wick geometry, wick porosity, and liquid superheating on heat transfer from the liquid-vapor interface.

4.2 Overview of Evaporation in the Micro-Columnated Wick

In Figure 4.1 is shown the structure and operation of coherent porous silicon (CPS)-based MEMS dual-scale wicking structure used in the micro-columnated loop heat pipe (μCLHP). The micro-columnated wick consists of two separate wick components: The primary wick is fabricated by etching vertical columns into a CPS base (patterned on a silicon wafer) using deep reactive ion etching (DRIE). The secondary wick is fabricated by etching rectangular microchannels into a silicon capping wafer, which is in contact with the heat source. The two wafer substrates are then bonded together, whereby the primary wick is connected to the secondary wick.

The base of the primary wick is in contact with the liquid coming in from the liquid microchannels and the compensation chamber. Using the strong capillary forces across the liquid-vapor menisci in the CPS pores, the primary wick transports this liquid to the rectangular microchannels of the secondary wick. Here, the liquid spreads over the entire area of the hot surface, and evaporation occurs across the liquid vapor meniscus in the rectangular microchannels. Some amount of evaporation also occurs from the liquid-vapor menisci in the CPS pores of the primary wick, but most of it happens from the secondary wick surface due to the larger surface superheat temperatures that exist close to the heat source. The primary wick, with its smaller pores, also acts as a buffer by preventing total wick dry out during sudden spikes in heat flux.

Shown in Figure 4.2 are two different wick topologies that can be fabricated using MEMS microfabrication techniques. A uni-directional-channel wick topology has par-

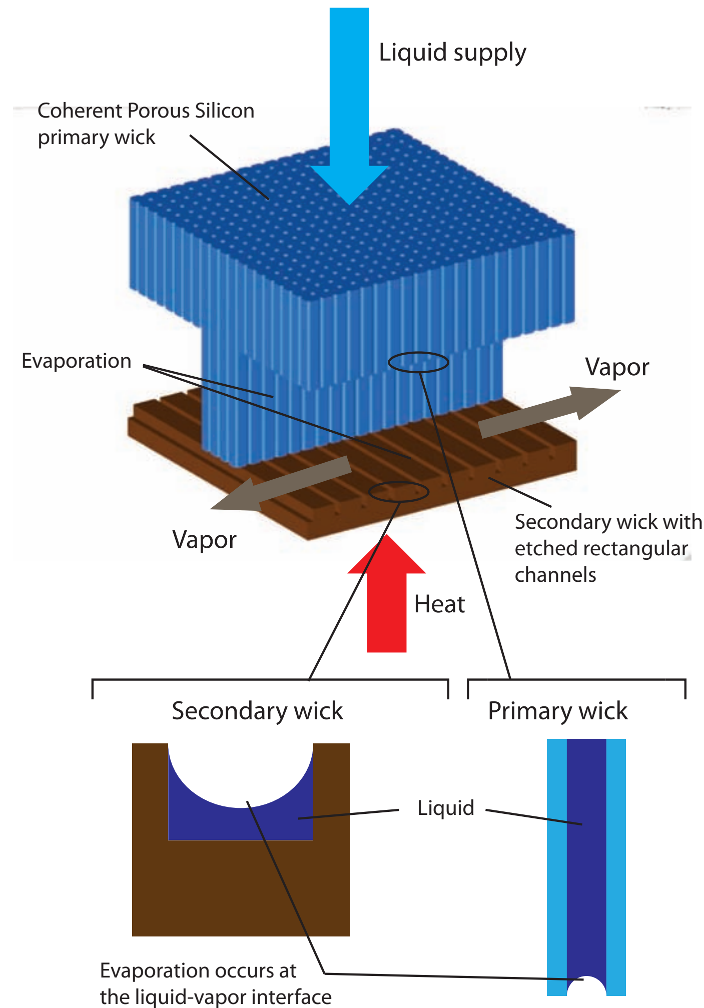

Figure 4.1: Coherent porous silicon (CPS)-based MEMS dual-scale wick. The dual-scale wick has a primary wick obtained by etching columns into a CPS substrate, and a secondary wick consisting of rectangular channels etched into the evaporating surface. The strong capillary action of the primary wick conveys the working liquid to the surface of the secondary wick, where it evaporates by absorbing heat from the heat source. Evaporation also occurs from the CPS pores of the primary wick exposed to the vapor region.

allel microchannels in the secondary wick and continuous column walls in the primary wick. The vapor formed due to evaporation has to travel along the column walls on its way out to the vapor line. In another wick topology, criss-crossing channels can be etched to form the secondary wick and cubical columns used to wick the liquid from the primary wick to the evaporating surface in the secondary wick.

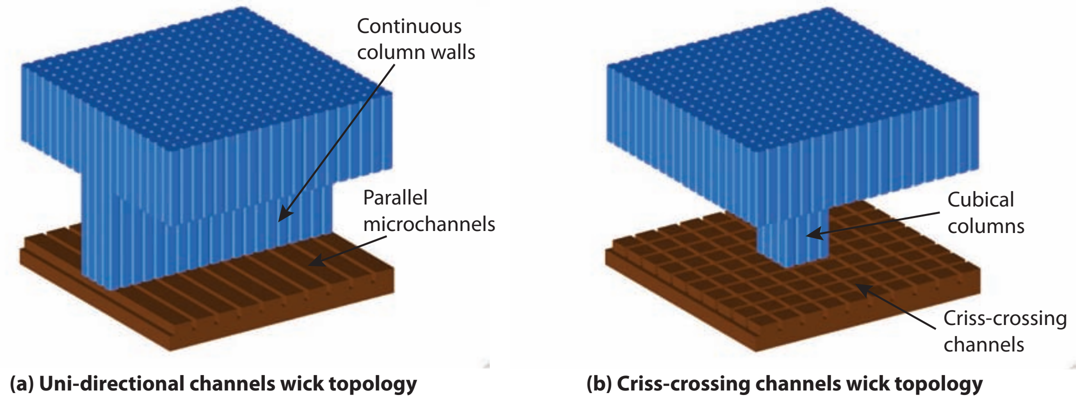

(a) Uni-directional channels wick topology **(b) Criss-crossing channels wick topology**

Figure 4.2: Proposed coherent porous silicon (CPS)-based wick topologies for integration into a micro-columnated loop heat pipe (μCLHP). The secondary wick is etched in the form of rectangular channels on the evaporating surface, while the primary wick consists of columns etched into the CPS base. (a) Uni-directional-channels wick topology consists of parallel channels in the secondary wick and continuous column walls in the primary wick. (b) Criss-crossing-channels wick topology consists of criss-crossing channels in the secondary wick and simple columns in the primary wick.

4.3 Modeling of Thin-Film Evaporation

As discussed above, most of the evaporation is expected to occur from the liquid-vapor menisci in the rectangular microchannels of the secondary wick, which is in direct contact with the heat source. During normal device operation, the function of the primary wicking structure is mainly to convey the liquid to the secondary wick for evaporation. It does this by using the capillary force developed across the liquid-vapor menisci in its tiny CPS pores. Once the liquid reaches the evaporating surface, it is pulled into the rectangular microchannels of the secondary wick, which again is due to the capillary pressure across the menisci formed in the channels. If no heat is applied to the secondary wick—and gravitational forces are neglected compared to those due to surface tension, due to the small length scale of the problem—the rectangular channels should be completely filled with the working liquid. In the presence of a heat source, the liquid supply to the secondary wick is balanced by the evaporation from the channels. The rate of evaporation will depend on wall superheat and the shape of the liquid-vapor meniscus in the channel, which in turn will depend on the rate of liquid supply from the CPS pores of the primary wick.

4.3.1 Problem Statement

The thin-film evaporation problem to be solved is shown in Figure 4.3. It consists of a rectangular microchannel on the surface of the secondary wick, which obtains it liquid supply (at the liquid inlet boundary) from the CPS pores of the primary

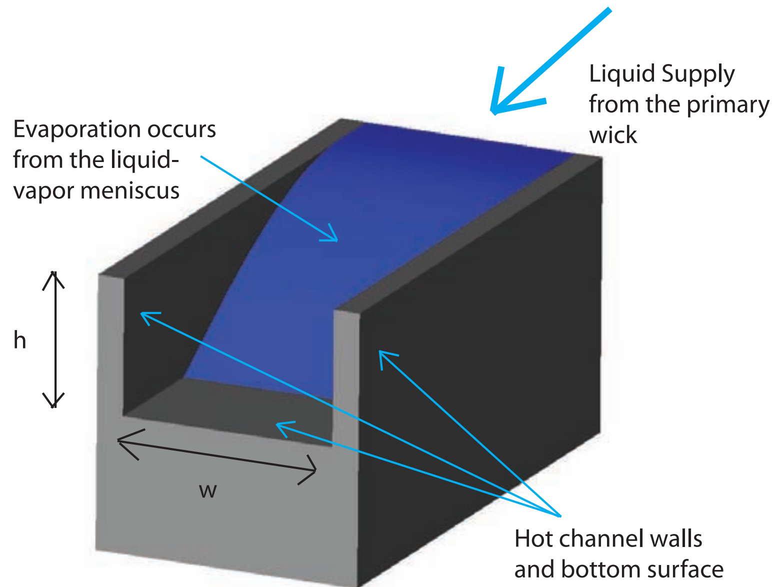

Figure 4.3: The model problem of thin-film evaporation in a rectangular microchannel of the secondary wick of the micro-columnated wicking structure. The liquid supply to the channel is from the CPS pores of the primary wick, and is specified as a liquid-inlet boundary condition. Evaporation occurs from the liquid meniscus exposed to the ambient vapor, while heat is transferred to the liquid from the solid walls of the microchannel.

wick. The liquid, which wets the channel material, is pulled into the channel by the surface tension-related capillary forces. The heat, supplied to the liquid by the hot channel walls, causes evaporation of liquid at the liquid-vapor interface. In steady state, the liquid supply to the channel is balanced by the rate of evaporation of the liquid, which results in a stationary evaporating meniscus.

The amount of liquid in the wick microchannel will depend on a complex interrelationship between the surface superheat, which dictates the rate of evaporation, and the thermodynamics of the flow loop, which involves a balance between the capillary pressure across the liquid-vapor meniscus in the wick microchannel and the pressure drop due to fluid flow in the rest of the μCLHP device.

In order to pose the problem of steady-state thin-film evaporation in a secondary wick microchannel, we will assume that the amount of liquid in the channel is dictated by extraneous parameters that can be modeled separately. As will be shown in the next section, given a fixed value for the amount of liquid in the channel, we can compute the shape of the liquid meniscus in the channel. A thermal-fluid solver, coupled with a kinetic theory-based evaporation boundary condition at the liquid-vapor meniscus, will then be implemented in the liquid domain.

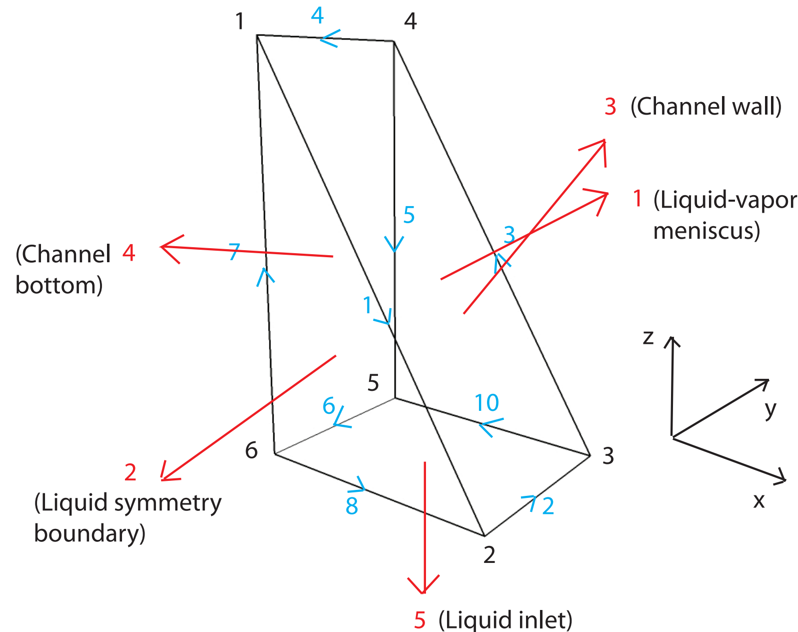

Figure 4.4: Problem domain for the liquid-vapor meniscus generation in Surface Evolver. Face 1 is the liquid-vapor meniscus surface, which is iterated to minimize free energy; the other faces are used to define mesh surfaces and are not iterated. Geometrical constraints on the vertices and edges are used to define the channel and the liquid distribution in it.

4.3.2 Shape of the Liquid-Vapor Meniscus

The shape of a non-evaporating, static liquid-vapor meniscus can be obtained by solving the Young-Laplace equation for a given solid-liquid contact angle. This contact angle only depends on the solid, liquid, and vapor present at the contact line. For a perfectly wetting system, the contact angle is equal to zero. On the other hand, the stationary meniscus of an evaporating perfectly wetting system exhibits a non-zero *apparent contact angle*; This contact angle vanishes as the wall heat source, responsible for evaporation, is turned off [91]. Using a scaling analysis, Morris [91] has shown that the theory of evaporation at the liquid-vapor interface can be divided into two distinct theories of an inner and outer structure. The nanometer-scale inner structure near the contact line determines the apparent contact angle; however, it contributes only a small fraction to the total evaporation heat transfer. Most of the heat transfer happens in the larger scale outer region, which subtends an apparent contact angle on the wall. By assuming a given value for the apparent contact angle, the problem of heat flow computation can be decoupled from the nanoscale physics governing the apparent contact angle.

The shape of the liquid-vapor meniscus is calculated using a numerical surface energy minimizer called Surface Evolver [94]. In this method, the surface is imple-

Table 4.1: Vertex, edge, and face constraints for meniscus shape definition

Index	Constraint	Vertices	Edges	Faces
0	Fixed	2, 3	2	
1	$x = 0$	1, 4	4	
2	$y = 0$	1	1	
3	$y = w$	4	3	
4	$x \leq h$	1, 4	1, 3	
5	$x \geq 0$	1, 4	1, 3	1

mented as a union of triangles, where free energy can be attributed to the surface and its edges. The surface is iterated upon to minimize the free energy of a collection of surfaces, subject to geometrical constraints on vertex positions as well as constraints on integral quantities such as volume. During the iteration procedure, the surface mesh can be tuned using procedures such as equi-angulation, vertex averaging and mesh refinement [95].

The problem domain for the generation of the liquid-vapor meniscus in Surface Evolver is shown in Figure 4.4. Vertices, edges, and faces are used to define the liquid in the open rectangular microchannel shown in Figure 4.3. Due to symmetry, only half of the liquid in the channel is modeled. Geometrical constraints on the vertices and edges are used to define the channel wall and the bottom surface. Similarly, constraints are applied on the liquid-vapor meniscus surface and edges to keep the liquid within the channel (see Table 4.1).

Surface Free Energy

In order to obtain the shape of the stationary meniscus, Surface Evolver needs to minimize the surface tension-related free energy associated with the liquid-vapor, liquid-solid, and solid-vapor interfaces. Since the solid-vapor interface is not defined in the problem domain (Figure 4.4), a virtual surface tension is instead assigned to the liquid-solid interface. This virtual surface tension depends on the liquid-vapor surface tension γ and the liquid-solid contact angle θ as follows:

$$\gamma_{virtual} = -\gamma \cos(\theta) \tag{4.1}$$

However, assigning surface tension values to all surfaces in this way leads to evolution problems for vertices that are located on flat faces. The solution is to use Green's theorem to convert surface free energy integrals to line integrals over the edges bounding the surface. Using this method, only the liquid-vapor surface needs to be iterated upon to minimize the free energy of the system. Edge surface tension-related free energies for the different faces can be calculated as follows:

Channel bottom. The following energy term is applied to edge 4, through constraint 1

$$E_1 = \iint_{face\,4} (-\gamma \cos\theta_b)(-\hat{\imath}).d\vec{A} = \oint_{edge\,4} z\gamma\cos\theta_b \hat{\jmath}.d\vec{s} + c \tag{4.2}$$

Liquid symmetry boundary. Since this boundary lies inside the liquid, it has no associated free energy.

Channel wall. The following energy term is applied to edge 3, through constraint 3

$$E_3 = \iint_{face\,3} (-\gamma \cos\theta_w)\hat{\jmath}.d\vec{A} = \oint_{edge\,3} z\gamma\cos\theta_w \hat{\imath}.d\vec{s} + c \tag{4.3}$$

Fluid inlet. Since this boundary lies inside the liquid, it has no associated free energy.

Liquid-vapor meniscus. A surface energy term is applied to the liquid-vapor meniscus by specifying the value of liquid-vapor surface tension γ for face 1.

Volume of the Liquid

To constrain the amount of liquid inside the meniscus, Gauss's theorem is used to express volume as a surface integral as follows:

$$V = \iiint_V dV = \oiint_A \vec{F}.d\vec{A} \quad \text{where} \quad \nabla\vec{F} = 1 \tag{4.4}$$

By default, Surface Evolver specifies $\vec{F} = z\hat{k}$. The volume of the liquid is a sum of the surface integral of $\vec{F}$ over all the liquid faces. This integral can be calculated for the individual faces as follows:

Channel bottom. The surface integral on face 4 is given by

$$\iint_{face\,4} \vec{F}.d\vec{A} = \iint_{face\,4} z\hat{k}.d\vec{A} = 0 \text{ since } \hat{k}\perp d\vec{A} \tag{4.5}$$

Liquid symmetry boundary. The surface integral on face 2 is given by

$$\iint_{face\,2} \vec{F}.d\vec{A} = \iint_{face\,2} z\hat{k}.d\vec{A} = 0 \text{ since } \hat{k}\perp d\vec{A} \tag{4.6}$$

Channel wall. The surface integral on face 3 is given by

$$\iint_{face\,3} \vec{F}.d\vec{A} = \iint_{face\,3} z\hat{k}.d\vec{A} = 0 \text{ since } \hat{k} \perp d\vec{A} \tag{4.7}$$

Fluid inlet. The surface integral on face 5 is given by

$$\iint_{face\,5} \vec{F}.d\vec{A} = \iint_{face\,5} z\hat{k}.d\vec{A} = 0 \text{ since } z = 0 \tag{4.8}$$

Liquid-vapor meniscus. Surface Evolver calculates the surface integral of $\vec{F}$ automatically.

In this study, to calculate the shape of the meniscus, a contact angle of 29° is assumed for both the channel bottom and walls. The volume of the half-meniscus is assumed to be 50 μm × 50 μm × 100 μm.

4.3.3 Evaporation at the Liquid-Vapor Interface

Mass flux due to evaporation at the liquid-vapor interface is given by [93, 90]

$$\dot{m}" = \frac{2\hat{\sigma}}{2-\hat{\sigma}} \left(\frac{\bar{M}}{2\pi\bar{R}}\right)^{1/2} \left(\frac{p_{\nu,equ}(T_{lv})}{T_{lv}^{1/2}} - \frac{p_v}{T_v^{1/2}}\right) \tag{4.9}$$

where $\bar{M}$ is the molecular weight of the fluid in $kg/kmol$, $\hat{\sigma}$ is the accommodation coefficient, $\bar{R}$ is the universal gas constant in $J/molK$, $p_{\nu,equ}$ is the equilibrium vapor pressure, and T_{lv} is the temperature at the liquid-vapor interface. The value of the accommodation coefficient for non-polar liquids is usually equal to one, but its value for water is a matter of much debate [96]. In this study we will assume $\hat{\sigma} = 1$. The equilibrium vapor pressure, i.e., the pressure at which the vapor is in equilibrium with the liquid, is given by

$$p_{\nu,equ}(T_{lv}) = p_{sat}(p_{lv}) \exp\left[\frac{p_{\nu,equ} - p_{sat}(T_{lv}) - (p_d + p_c)}{\rho_l T_{lv} \bar{R}/\bar{M}}\right] \tag{4.10}$$

where ρ_l is the density of the liquid, p_d is the disjoining pressure, p_c is the capillary pressure, and p_{sat} is the saturation pressure of the liquid. In the absence of capillary and disjoining pressures, the equilibrium vapor pressure is given by

$$p_{\nu,equ} = p_{sat}(T_{lv}) \tag{4.11}$$

The saturation pressure of the liquid p_{sat} is a function of temperature, and can be found at the vapor-liquid interface as follows:

$$p_{sat}(T_{lv}) = p_{sat,ref}(T_{sat,ref}) \exp\left[\frac{\bar{M}h_{fg}}{\bar{R}}\left(\frac{1}{T_{sat,ref}} - \frac{1}{T_{lv}}\right)\right] \tag{4.12}$$

where $T_{sat,ref}$ and $p_{sat,ref}$ are the reference saturation temperature and pressure respectively.

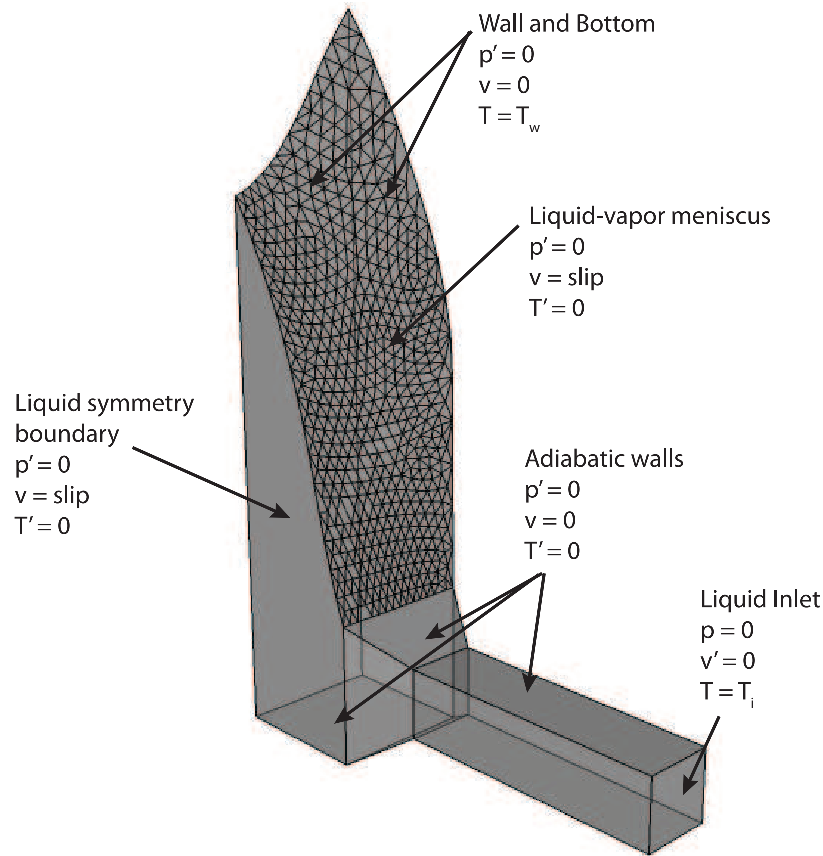

Figure 4.5: Solution domain and boundary conditions for the numerical solution of the coupled fluid-thermal-evaporation problem.

4.4 Governing Equations and Boundary Conditions

4.4.1 Governing Equations

Non-isothermal, incompressible, laminar, and unsteady mass, momentum, and energy equations are solved in the liquid domain. The vapor is assumed to be saturated, with a given vapor temperature. The effects of disjoining and capillary pressures are not modeled explicitly; Instead, disjoining pressure related flow dynamics can be accounted for by assuming a Capillary number-dependent apparent contact angle [91, 92] for the evaporating meniscus. Capillary pressure-related heat transfer suppression effects are negligible for high superheat values [90], and can be accounted for at low superheat by offsetting the value of the vapor pressure (using Young's Laplace equation) in the numerical solution. The governing equations are as follows:

Mass conservation. For incompressible flow with a mass source term, the mass conservation equation reduces to

$$\nabla.\vec{u} = \frac{S_m}{\rho} \tag{4.13}$$

where ρ is the liquid density and S_m is a mass source term applied to the cells adjacent to the liquid-vapor interface boundary, to simulate evaporation at this interface. The mass source term is negative and is given by:

$$S_m = -\frac{\dot{m}"A_f}{V_{cell}} \tag{4.14}$$

where $\dot{m}$" is the evaporative mass flux at the interface (see Equation 4.9), A_f is the area of the cell face adjacent to the liquid-vapor interface, and V_{cell} is the volume of the corresponding cell.

Momentum conservation. The incompressible momentum conservation equation is given by

$$\frac{\partial \vec{u}}{\partial t} + \vec{u}(\nabla \vec{u}) = -\frac{\nabla p}{\rho} + \nabla.(\nu \nabla \vec{u}) \tag{4.15}$$

where $\vec{u}$ is the liquid velocity, p is the pressure, and ν is the liquid kinematic viscosity.

Energy conservation. The energy equation for incompressible fluid flow is given by

$$\frac{\partial T}{\partial t} + \nabla.(\vec{u}T) - (\nabla.\vec{u})T = \nabla.(\alpha \nabla T) \tag{4.16}$$

where T is the liquid temperature and α is the liquid thermal diffusivity. Using Equation 4.13, we can write this as

$$\frac{\partial T}{\partial t} + \nabla.(\vec{u}T) = \nabla.(\alpha T) + \left(\frac{S_m}{\rho}\right) T \tag{4.17}$$

where the last term on the R.H.S. is a heat source term, which appears due to the evaporative mass flux in the cells adjacent to the liquid-vapor meniscus.

4.4.2 Boundary Conditions

Shown in Figure 4.5 are the problem domain and boundary conditions on which the numerical solution is implemented. The domain consists of the stationary liquid-vapor meniscus in an open rectangular channel that is 100 μm wide and 50 μm deep. This channel is supplied with liquid by an orthogonally connected 25 $\mu m \times 25$ μm rectangular channel.

Liquid-vapor meniscus. The evaporative mass and heat fluxes through the meniscus are taken care of by incorporating appropriate source terms in the mass and energy conservation equations. Therefore, the normal velocity and temperature gradient is set to zero at this boundary. A zero-gradient pressure boundary conditions is also applied.

$$\frac{\partial p}{\partial \hat{n}} = p' = 0; \qquad \vec{u}.\hat{n} = u_n = 0; \qquad \frac{\partial T}{\partial \hat{n}} = T' = 0 \tag{4.18}$$

Liquid inlet. At the liquid inlet, a zero-gradient pressure and velocity boundary condition is applied. The temperature of the incoming liquid is set to T_i.

$$\frac{\partial p}{\partial \hat{n}} = 0; \qquad \frac{\partial \vec{u}}{\partial \hat{n}} = 0; \qquad T = T_i \tag{4.19}$$

Wall and bottom. A no-slip velocity boundary condition and a zero-gradient pressure boundary condition is applied at the wall and bottom. The temperature of the wall and bottom is set to T_w.

$$\frac{\partial p}{\partial \hat{n}} = 0; \qquad \vec{u} = 0; \qquad T = T_w \tag{4.20}$$

Adiabatic walls. A no-slip velocity boundary condition and a zero-gradient pressure boundary condition is applied at the adiabatic walls. The normal temperature gradient is set to zero.

$$\frac{\partial p}{\partial \hat{n}} = 0; \qquad \vec{u} = 0; \qquad \frac{\partial T}{\partial \vec{n}} = 0 \tag{4.21}$$

Liquid symmetry boundary. Since only half of the channel is modeled, a symmetric boundary condition is applied at the face that aligns with the middle of the channel.

4.4.3 Numerical Solution

The above governing equations and boundary conditions are solved using OpenFOAM, an open source CFD toolbox. The solution domain is discretized with a hexahedral mesh, using the blockMesh and snappyHexMesh utilities in OpenFOAM. Since there are mass source terms in the solution domain, mass and momentum equations are first solved for a given uniform liquid temperature $T = T_w$, in order to obtain a divergence-less velocity field. This is accomplished by solving the steady form of these equations using a SIMPLE algorithm, which uses under-relaxation. Using this result as a starting point, the complete set of equations is now solved in time using the PISO loop, until a steady state is reached. The time step during the solution procedure is limited by the maximum Courant number in the domain.

4.5 Results and Discussion

Thin film evaporation of water in a rectangular channel of the secondary wick was studied for different values of wall superheat and liquid-inlet-subcooling temperatures. The temperature T_v and pressure p_v of the saturated vapor were, in all cases, set to $373.15\ K$ and $1.013 \times 10^5\ Pa$ respectively.

In case I, the incoming liquid is assumed to be saturated with a temperature of $T_i = 373.15\ K$, while a wall superheat of $T_w - T_i = 5\ K$ is applied at the channel walls. The effect of increase in wall superheat is studied in case II, where a wall superheat of $10\ K$ is applied to the saturated incoming liquid. In case III, a wall superheat of $10\ K$ is applied to the channel walls, while the inlet liquid is subcooled by $T_v - T_i = 5\ K$.

4.5.1 Fluid Flow and Heat Transfer Characteristics

In Figure 4.6 can be seen the numerical simulation results for case I, where the incoming liquid is saturated at $T_i = 373.15\ K$, while the channel wall, at $T_w = 378.15\ K$, is $5\ K$ above the liquid temperature. From Figure 4.6a, we can see that the liquid enters the domain from the liquid inlet and flows towards the liquid-vapor meniscus, where it undergoes evaporation to the vapor phase. We note that the maximum velocity in the domain is $0.448\ m/s$, with comparatively larger values existing in the adiabatic supply channel due to its smaller cross-section. The total pressure drop in the domain, from the liquid inlet to the evaporating meniscus, is approximately $336\ Pa$ (see Figure 4.6b).

The temperature distribution in the domain is plotted in Figure 4.6c. The first thing that we readily see is that most of the liquid in the supply channel is close to the inlet temperature T_i. This is easily explained, since the supply channel walls are adiabatic and water has a low coefficient of thermal conductivity. We can also see that water close to the heated channel walls is at a higher temperature, and this high temperature front moves further into the liquid as it travels along the channel. As we get close to the end of the meniscus in the channel corner, we see that most of the liquid has become superheated. This is because 1) the meniscus is getting thinner and 2) it is receiving heat from both the side and bottom channel walls.

In Figure 4.6d can be seen a plot of the evaporation heat flux from the surface of the meniscus. We can easily correlate the heat flux distribution to the liquid surface temperature by comparing Figure 4.6c and Figure 4.6d. This dependence is a direct consequence of Equation 4.9, the kinetic-theory based expression for evaporation mass flux. The heat flux varies from zero, at the center of the liquid coming into the channel, to a maximum value of $8.0 \times 10^7\ W/cm^2$ near the channel walls. Most of the evaporation from the meniscus occurs near the channel walls, especially in its elongated part near the channel corners. Integrating the heat flux over the entire meniscus surface, we find that the average heat flux is equal to $4.72 \times 10^7\ W/m^2$ and

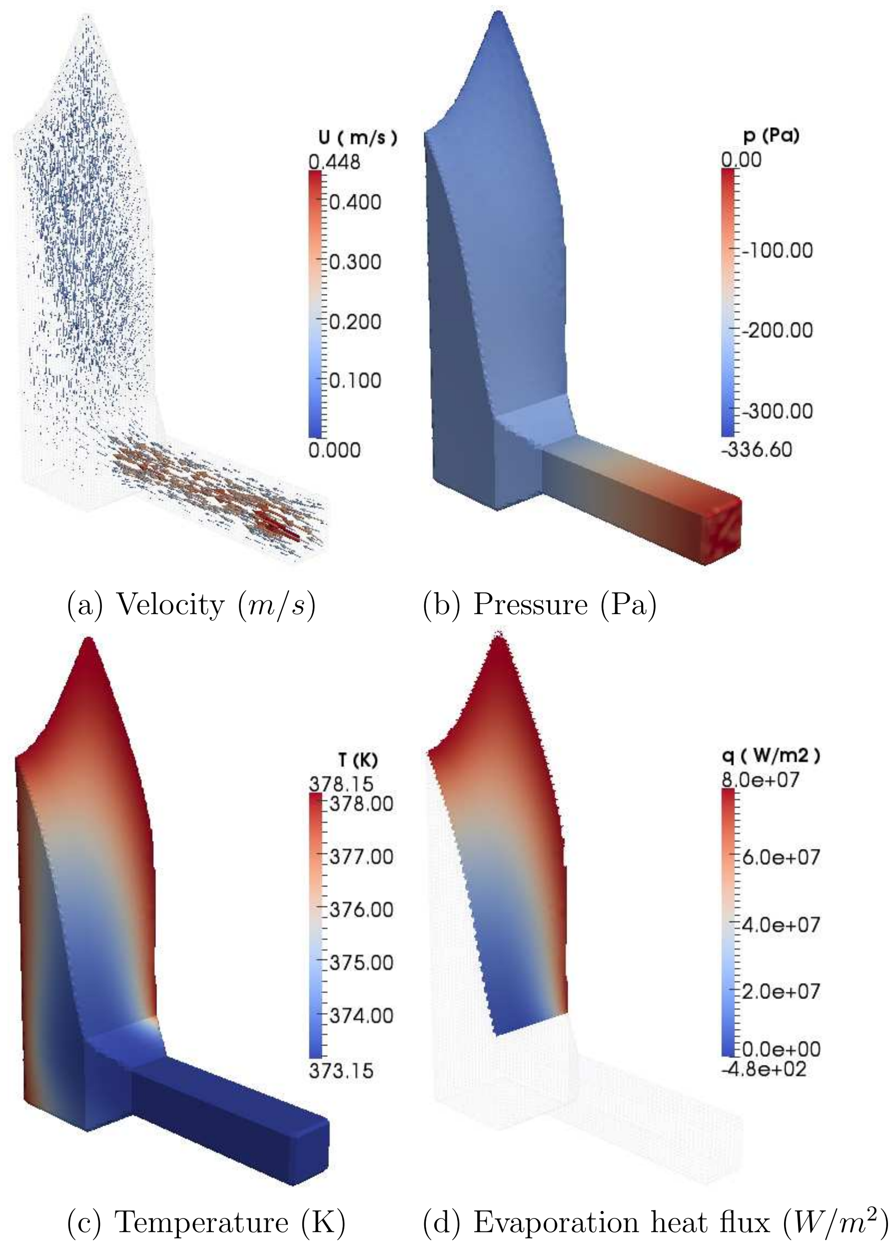

(a) Velocity (m/s) (b) Pressure (Pa)

(c) Temperature (K) (d) Evaporation heat flux (W/m^2)

Figure 4.6: Case I numerical simulation results: Heating of saturated incoming liquid with 5 K wall superheat. The inlet fluid is at a temperature of $T_i = 373.15\ K$, while the temperature of the channel wall is $T_w = 378.15\ K$.

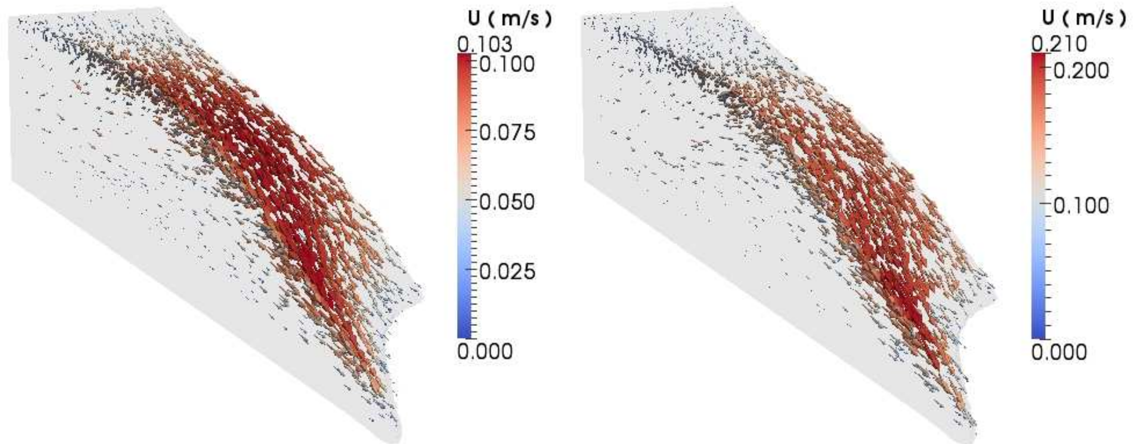

(a) Velocity field for 5 K wall superheat (b) Velocity field for 10 K wall superheat

Figure 4.7: A plot of the liquid velocity vectors inside the evaporating meniscus for different wall superheats.

the total rate of heat loss due to evaporation from the meniscus is 0.42 W.

In Figure 4.7 can be seen a plot of the velocity vectors inside the evaporating meniscus for two different values of the wall superheat (5 K and 10 K). In both the cases, we can see that the bulk of liquid transport is occurring near the surface of the meniscus. This can be attributed to the fact that 1) there is a no-slip condition at the channel walls, as opposed to the free slip boundary condition on the meniscus, and 2) the meniscus surface acts as an evaporative mass sink. We also see that the fluid velocities are larger near the channels walls and this asymmetry in velocity distribution is enhanced by an increase in the wall superheat. For a larger superheat value, the peak velocities in the evaporating meniscus tend to move towards the meniscus in the channel corners.

4.5.2 Effect of Wall Superheat on Heat Transfer

In Figure 4.8 can be seen the numerical simulation results for case II, where a higher wall superheat of 10 K has been applied to the incoming saturated liquid. The liquid inlet temperature is still kept at 373.15 K, while the wall temperature is increased to 383.15 K. Compared to case I, overall, we see an increase in all the relevant field quantities such as velocity, pressure drop across the domain, and evaporation heat flux values. This is just a consequence of the fact that there is more fluid evaporation across the meniscus as a result of the increased fluid temperatures, brought about by a higher wall superheat. The average heat flux over the entire meniscus increases to 8.35×10^7 W/m^2, a little less than double the value obtained for case I. The total rate of heat loss due to evaporation is now 0.75 W.

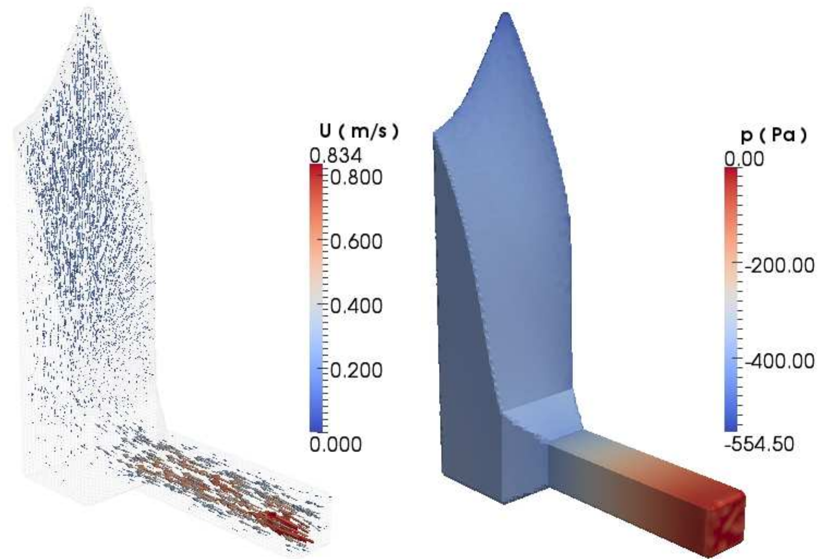

(a) Velocity (m/s) (b) Pressure (Pa)

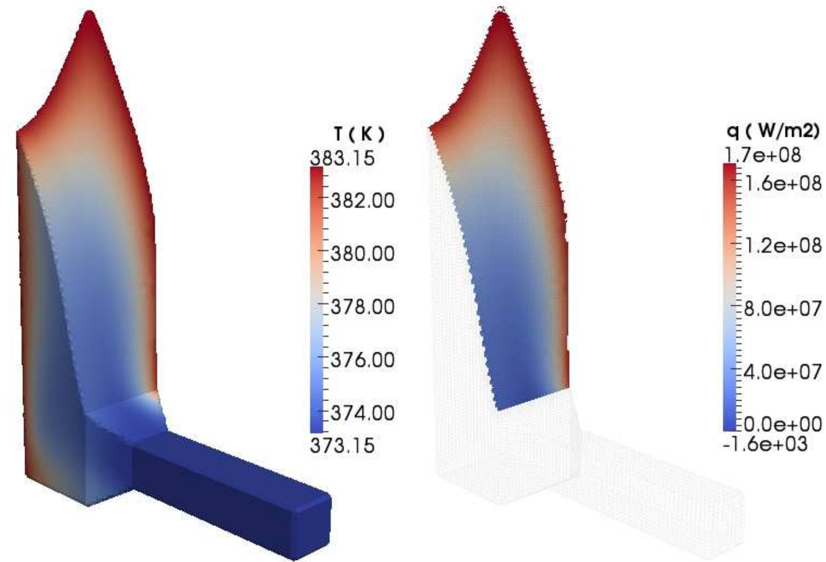

(c) Temperature (K) (d) Evaporation heat flux (W/m^2)

Figure 4.8: Case II numerical simulation results: Heating of saturated incoming liquid with 10 K wall superheat. The inlet fluid is at a temperature of $T_i = 373.15\ K$, while the temperature of the channel wall is $T_w = 383.15\ K$.

4.5.3 Effect of Liquid Sub-cooling on Heat Transfer

In Figure 4.9 can be seen the numerical simulation results for case III, where the wall superheat is maintained at 10 K, while the inlet liquid is subcooled by 5 K compared to the saturated vapor. The wall temperature in this case is 383.15 K, while the liquid inlet temperature is 368.15 K. Interestingly, there is a large drop in the overall rate of evaporation compared to case II, and this is reflected in the lower values of fluid velocity and pressures gradients as well. As to why this is the case, we look at Figure 4.9d and note that although the maximum evaporative heat flux in the domain ($1.7 \times 10^8\ W/m^2$) is the same as in case II, now we also have a considerable amount of condensation in parts of the incoming liquid that are subcooled. The average evaporation heat flux and the total rate of evaporative heat loss, at $4.63 \times 10^7\ W/m^2$ and 0.42 W respectively, are even less than the corresponding values for case I.

4.5.4 Application of the Results

The numerical results presented above need to be interpreted in the context of thin-film evaporation in the micro-columnated wick. It should be kept in mind that the channel size for the secondary wick needs to be optimized, to adequately promote its wetting and maximize the evaporative heat transfer. This can be done by integrating the above evaporation model with a broader flow-loop model for the micro-columnated loop heat pipe.

Decreasing the secondary wick channel size promotes wetting by increasing capillary forces, which draw more liquid into the microchannel. This will lead to a larger fluid volume in the microchannels, and hence a large surface area for evaporation. On the other hand, the evaporative heat flux, per unit area of the meniscus, will decrease due to capillary suppression effects. As a result, more liquid superheat will be required in order to maintain the rate of evaporation; this can lead to wick dry out due to spontaneous homogeneous bubble nucleation.

Large secondary wick channels, despite promising higher thin-film evaporation rates due to lower capillary suppression effects, will be susceptible to dry out due to insufficient liquid wetting of the wick. An optimum channel size should be chosen to provide a high rate of evaporation, while maintaining the capillary pressures necessary for device operation.

4.6 Conclusions

A numerical model was implemented to solve for the rate of evaporative heat transfer from the surface of a stationary liquid-vapor meniscus. The aim of the model is to study the process of microscale thin-film evaporation inside a dual-scale micro-columnated coherent porous silicon wicking structure. The shape of the meniscus inside a rectangular channel, on the surface of the secondary wick, is obtained

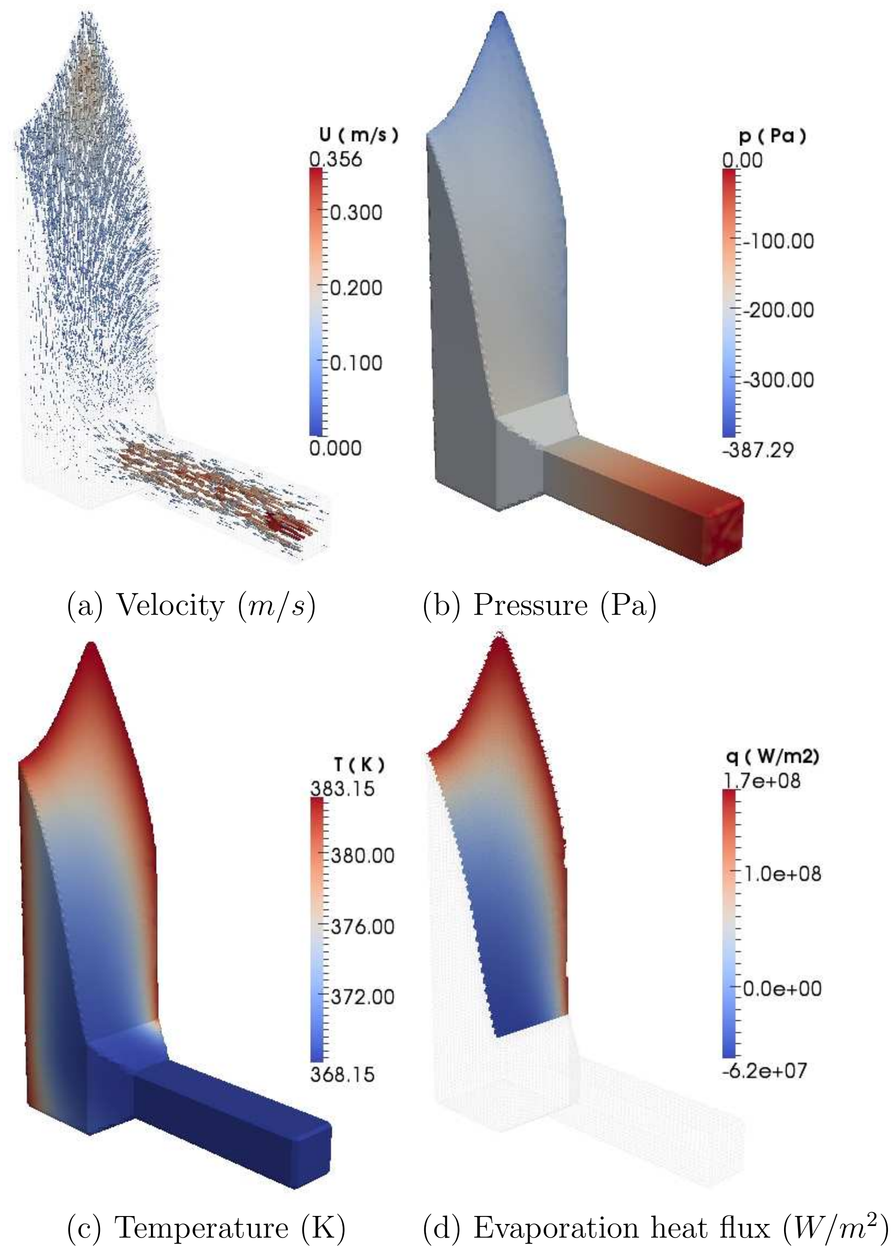

(a) Velocity (m/s) (b) Pressure (Pa)

(c) Temperature (K) (d) Evaporation heat flux (W/m^2)

Figure 4.9: Case III numerical simulation results: Heating of 5 K subcooled incoming liquid with 10 K wall superheat. The inlet fluid is at a temperature of $T_i = 368.15\ K$, while the temperature of the channel wall is $T_w = 383.15\ K$.

by solving the Young-Laplace equation using a surface energy minimizing algorithm called Surface Evolver. This approach ignores the effect of actual flow mechanics on the shape of the meniscus. Mass, momentum, and energy equations, containing source terms to account for evaporation from the meniscus surface, are discretized and solved using the finite volume approach. Numerical simulation results show that most of the evaporative heat transfer from the meniscus happens near the channel walls. Increasing wall superheat increases the overall rate of evaporation, whereas subcooling the inlet liquid decreases the same.

Part III

Device Fabrication and Experimental Testing

Chapter 5

Device Design and Fabrication

In order to implement the vision of a micro-columnated loop heat pipe (μCLHP) fabricated completely on wafer substrates, a number of different design and fabrication goals have to be achieved. The μCLHP consists of a number of individual components, such as the micro-columnated wicking structure, the evaporator section, the condenser section, the fluid transport channels, the thermal barriers, and the liquid fill-ports. The micro-columnated coherent porous silicon (CPS)-based vertical wicking structure has a topology that is expressly different from the rest of the device components. As a result, its fabrication procedure will also involve the use of processes and technologies that are superfluous for the purpose of fabricating a microscale loop heat pipe without the use of a vertical wick. The micro-columnated wick is the only μCLHP component that requires the use of coherent porous silicon (CPS), which is obtained by illumination-enhanced electrochemical etching—a non-standard microfabrication process.

The micro-columnated wicking structure, although beneficial from the point of view of enhanced evaporation, is not an absolute necessity for the operation of the μCLHP device. A simpler wicking structure, the fabrication of which conforms to the fabrication procedure for the rest of the device components, can also be used for the purpose of experimentally studying overall device operation. A two-fold approach for studying the μCLHP has, therefore, been adopted. The task of fabrication and experimental testing of overall μCLHP device topologies has been decoupled from the complexities of the wicking structure, by replacing the vertically-wicking micro-columnated wick with a horizontally-wicking in-plane wick. In-plane-wicking micro loop heat pipe (μCLHP) prototypes are fabricated for the purpose of experimentally studying the topological behavior of the overall device design. Information on a design and fabrication approach for the complete μCLHP device, which includes the electrochemical etching of coherent porous silicon (CPS) and its integration into the standard microfabrication process flow, can be found elsewhere in a M.S. report by the author [97]. A detailed experimental study of different vertically-wicking micro-columnated wick topologies can be found elsewhere in the Ph.D. dissertation

of Christopher Hogue [98].

In this chapter are presented the design and fabrication details of a number of in-plane-wicking μLHP prototypes. These devices use an in-plane or horizontal wick, which consists of extremely narrow (16–32 μm) parallel rectangular channels. The advantage of using an in-plane wick is that the wick channels can be etched at the same time as the rest of the device features, which considerably simplifies the fabrication process flow.

5.1 Phase-I μLHP Prototype

5.1.1 Device Design

The phase-I μLHP prototype uses an in-plane wicking structure fabricated exclusively on the silicon wafer, with the Pyrex wafer employed only as a capping wafer. The design details of this device are shown in Figure 5.1. The top views of the device are drawn to scale, whereas the cross-sections serve to illustrate the salient features of the different components of the device. The device is designed using a two wafer stack. The silicon wafer has all the device features etched into it and the Pyrex wafer serves as the capping wafer.

The device is approximately 5.9 cm long, 1.4 cm wide, and 1 mm thick. It has rectangular evaporator and condenser sections, connected by liquid and vapor microchannels. The evaporator section contains an in-plane wick 4 mm long and 3.8 mm wide, which consists of parallel rectangular channels 32 μm wide and 150–200 μm deep. While the wick channel width can be designed, its depth, as we will see in the following sections, is proportional to the etch depth of the rest of the device components. The condenser section in this prototype is an empty 8.9 $mm \times 8.9$ mm silicon cavity, which is slightly larger than the evaporator section. In general, the condenser section should be large in order to facilitate condensation. The condenser section is connected to the wick inlet (Section A-A') using 150 μm wide liquid channels (4 in all). The wick outlet (Section C-C') is connected to the condenser section using 450 μm wide vapor microchannels (10 in all). The idea behind making the vapor microchannels larger is to reduce flow loop frictional pressure losses. This is further achieved by having multiple channels, which reduces the mass flow rate through a single microchannel.

A thermal barrier is positioned between the liquid and vapor microchannels. This is a 400 μm wide rectangular cavity that is etched through to the bottom of the silicon wafer all the way from the evaporator to the condenser. It prevents parasitic heat flow to the incoming liquid in the liquid microchannels. A compensation chamber is also attached to the wick inlet to provide reserve liquid for keeping the wick wetted. Inlet and outlet working-fluid fill-ports are situated in the compensation chamber and the condenser section, respectively. As shown in section E-E', these fill-ports are 0.7 mm

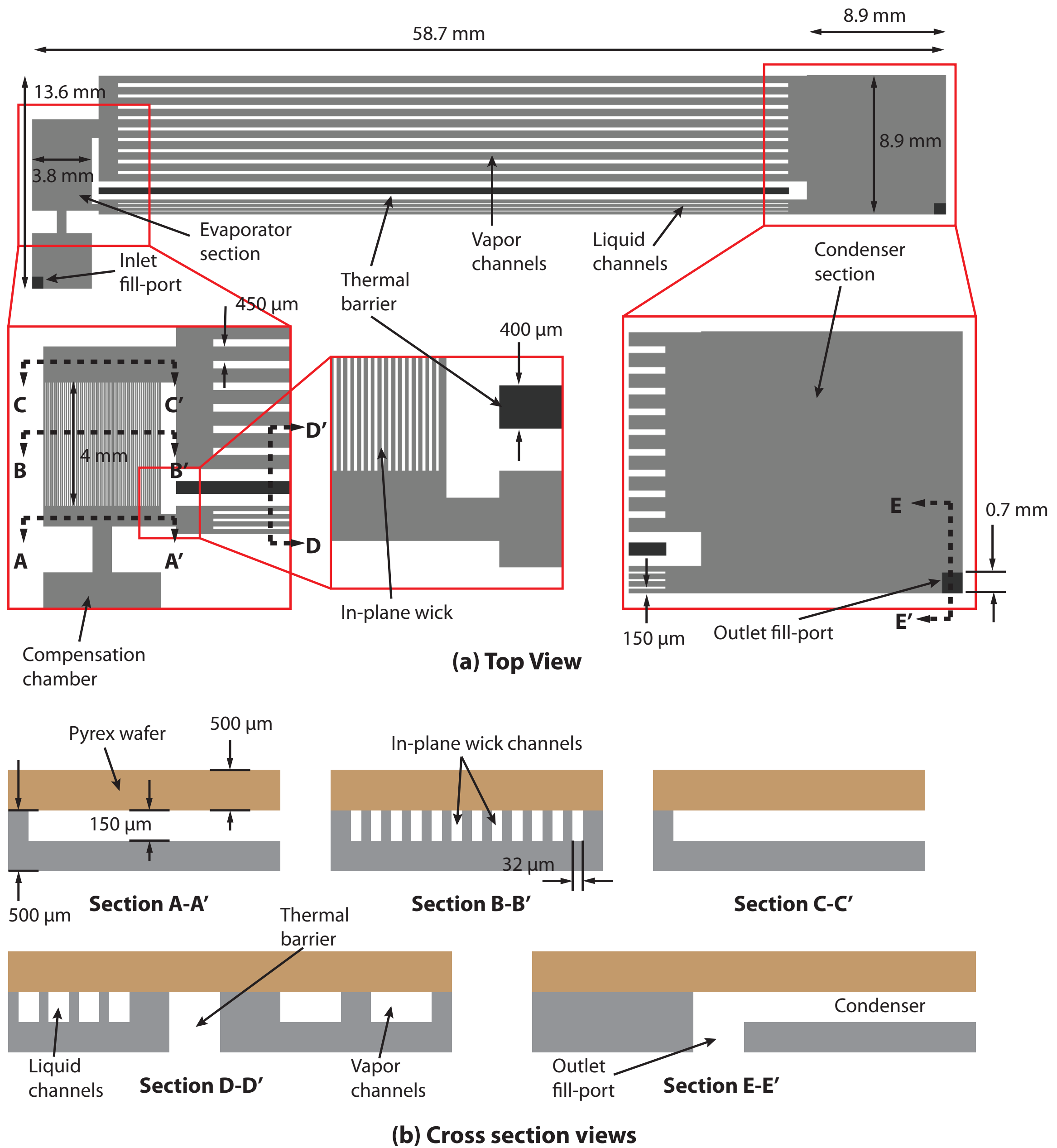

Figure 5.1: A design schematic of the phase-I μLHP device: (a) The top views of the device are drawn to scale; (b) Dimensioned cross-sectional view of individual device components.

square holes etched through to the bottom of the silicon wafer.

Taking a look at the cross-sectional views of the evaporator section in Figure 5.1(b), we can understand the principle of operation of the in-plane wicking structure in the phase-I μLHP prototypes (The topology of the in-plane wick will be slightly different in the phase-II μLHP prototypes). The liquid from the liquid microchannels, as it reaches the evaporator, is first fed to a cavity between the compensation chamber and the wick (section A-A'). The wick microchannels (section B-B') will absorb this liquid due to capillary action. The liquid will fill the channels completely but should not exit to the vapor side, since it will be stopped by another cavity (section C-C') that has a smaller wetting surface area compared to the wick microchannels. Once the hot liquid in the wick microchannels forms vapor, it can escape to the vapor microchannels.

5.1.2 Device Fabrication Process Flow

The phase-I μLHP prototype was fabricated in the Berkeley microfabrication laboratory using standard MEMS microfabrication techniques. In Figure 5.2 is shown the detailed fabrication process flow of the device. The process starts with a bare 4-inch <100>-oriented silicon wafer. The wafer can be either n-type or p-type, since doping does not affect any of the process parameters and neither does it have any influence on the operation of the final product. First, the wafer is cleaned using standard piranha clean and a 2 μm-thick silicon dioxide layer is deposited in a thermal furnace using a low pressure chemical vapor deposition (LPCVD) process. A low temperature phosphorous-doped recipe is employed, which yields phospho-silicate glass (PSG) or doped low temperature oxide (LTO) with good reflow properties. The oxide layer is annealed in a thermal furnace at 1050 ^oC for a few hours to achieve better oxide thickness uniformity across the surface of the wafer.

Following this, the wafer is piranha-cleaned and a HMDS (Hexamethyldisilazane) monolayer is deposited on the wafer prior to depositing 2.6 μm of G-line positive photoresist. HMDS serves as an adhesion layer for the photoresist. The wafer is exposed to UV light using the first chrome mask, and the photoresist is developed and hardbaked in a 120 ^oC oven for about 12 hours. This step patterns into the photoresist most of the μLHP components such as the wicking structure, the liquid and vapor transport channels, the compensation chamber, and the evaporator and condenser sections.

This photoresist mask is used to dry-etch the underlying oxide layer using a plasma etcher. The hardbaked photoresist is removed by immersing the wafers in a photoresist stripper (PRS-3000) for 12–24 hours. The wafers are piranha-cleaned and the oxide layer on the backside of the wafers is removed using plasma etching. This is supposed to help in the subsequent Deep Reactive Ion Etching (DRIE) step, where backside cooling of the wafer could be inhibited by the low thermal conductivity of silicon dioxide, leading to grass formation. Nevertheless, it has been observed in some

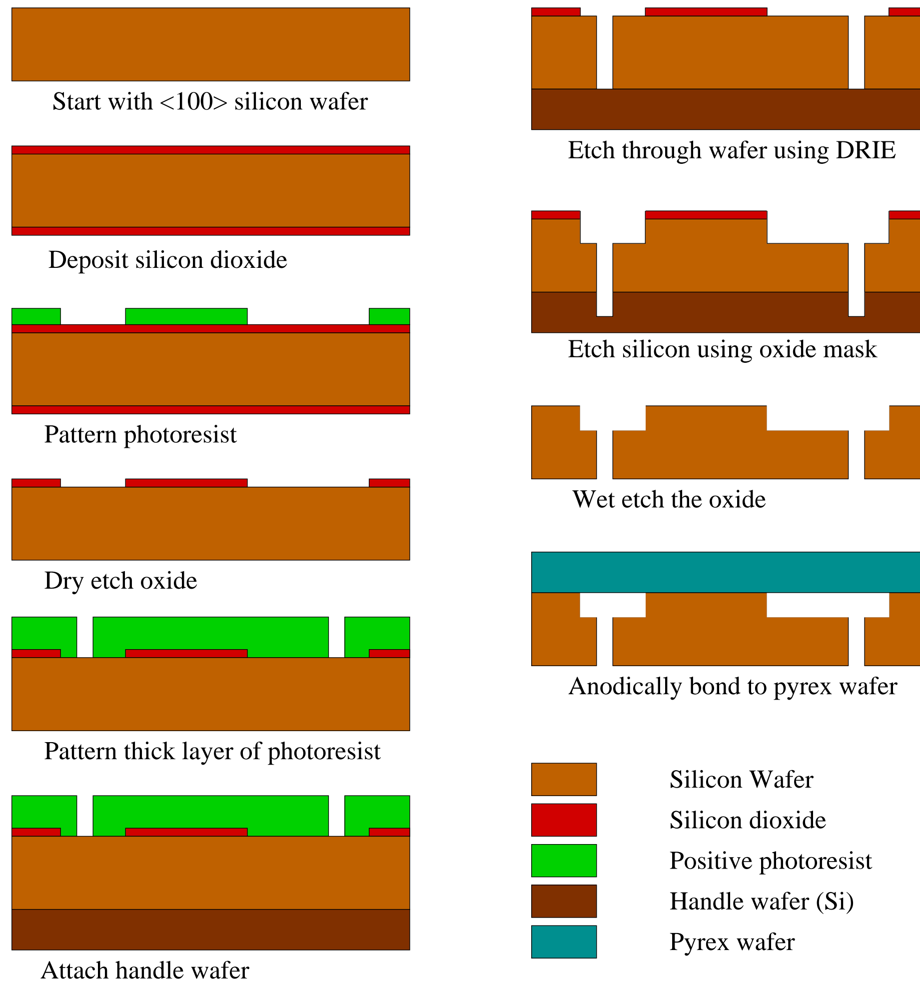

Figure 5.2: Fabrication process flow for the Phase-I μLHP device. All of the device components are etched into the silicon wafer, while Pyrex is used as the capping wafer.

of the fabrication runs that keeping this backside oxide layer did not have any adverse impact on the DRIE process.

The wafers are then cleaned in piranha and a 10 μm thick layer of photoresist is deposited on the silicon wafer. The photoresist is exposed using the second chrome mask, developed, and hardbaked. This patterns the through-holes and the thermal barrier features onto the photoresist. A silicon handle wafer (with a 1 μm thick silicon dioxide layer) is attached to the backside of the device wafer, for protecting the chuck from damage during through-etching of the device wafer in the DRIE etcher. Cool grease is used to bond the device wafer to the handle wafer because of it high thermal conductivity.

The Bosch deep reactive ion etching (DRIE) process is used to through-etch the

silicon wafer, using the thick photoresist as the etch mask. The photoresist is then removed by plasma etching to expose the underlying silicon dioxide mask. Using this oxide as the etch mask, the silicon wafer is further etched to a depth of 150 μm using DRIE. In the previous step, the alternative to the plasma etching of the photoresist requires the removal of the handle wafer, photoresist stripping in PRS-3000, wafer cleaning, and re-attachment of the handle wafer—all of which add up to a lengthy tedious process.

The handle wafer is then carefully separated from the device wafer by immersing in acetone for a few hours. The oxide layer is removed from the silicon wafer by dipping it in concentrated hydrofluoric (HF) acid for a few minutes. A Pyrex wafer is then permanently bonded to the top side of the silicon wafer, to seal all the microfluidic components. This is accomplished using the anodic bonding process at a temperature of 450 ^{o}C and a voltage bias of 1000 V. The bonded wafer are then diced to obtain the individual μLHP devices.

5.1.3 Fabrication Results

The fabricated and diced phase-I μLHP device prototypes are shown in Figure 5.3. From Figure 5.3(a) we can get a sense of the size and overall topology of these devices; Here, the device is placed next to a US quarter dollar. At an overall length of approximately 6 cm and a thickness of exactly 1 mm, the device is extremely compact compared to conventional loop heat pipes, and is completely planar. We can also see that the reflectance properties of the etched region of silicon are quite different from that of the non-etched part (both of which are covered by the transparent Pyrex wafer). As a result, we can clearly see the main device components such as the evaporator and condenser sections and the transport microchannels. The through-etched thermal barrier (between the liquid and vapor microchannels) and the inlet and outlet fluid fill-ports (in the compensation chamber and the condenser section respectively) are also visible.

As is clear from looking at the condenser section, there are some etching defects that result from the last DRIE step in the fabrication process. This is a direct result of the fact that prior to this etching step the photoresist was removed by plasma etching and the wafer could not be piranha-cleaned because of the attached handle wafer. This problem has been addressed in the fabrication of the phase-II μLHP device by appropriately modifying the fabrication process. Another important aspect of device fabrication is the proper dicing of the individual devices on the wafer. The fluid fill-ports (more importantly the inlet fill-port in this particular design) should be sufficiently removed from the edge of the diced device in order to avoid any potential problems during the degassing and filling of these devices.

From the phase-I μLHP design, a number of different prototypes were fabricated with slight variation in the attributes of two of its components: the in-plane wick and the vapor microchannels. Since evaporation in the wicking structure is one of the

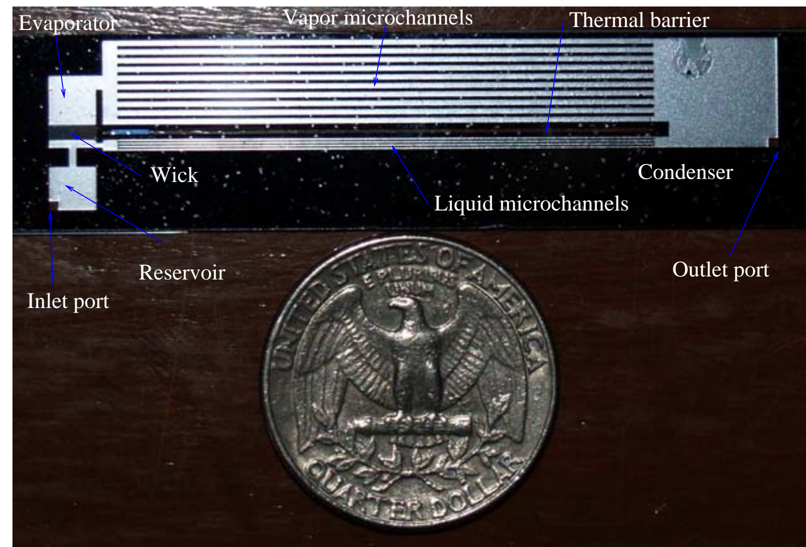

(a)

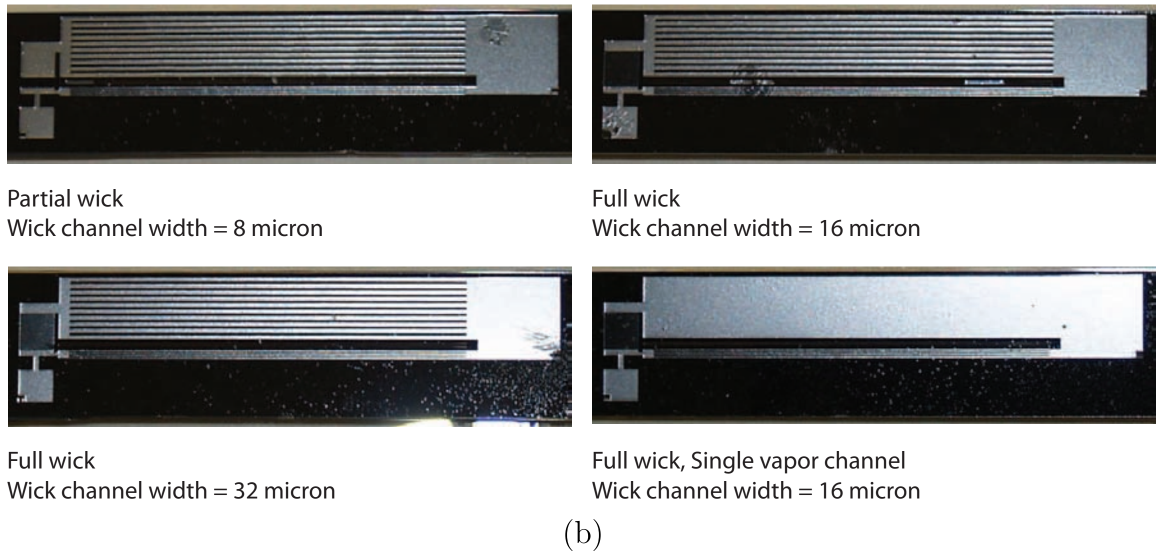

(b)

Figure 5.3: The fabricated phase-I μLHP prototype devices: (a) A picture showing one of the phase-I μLHP prototypes and its size comparison with a US quarter dollar. (b) A picture showing the different design variations obtained by varying the size of the in-plane wick and the number of vapor microchannels.

most important physical phenomena affecting device operation, it is worthwhile to see how the extent and size of the in-plane wick microchannels affect liquid evaporation in the evaporator section. Accordingly, in one instance the wick was limited to the entrance region of the evaporator (partial wick), while in the other instances it was designed to occupy most of the heated evaporator region (full wick). The width of

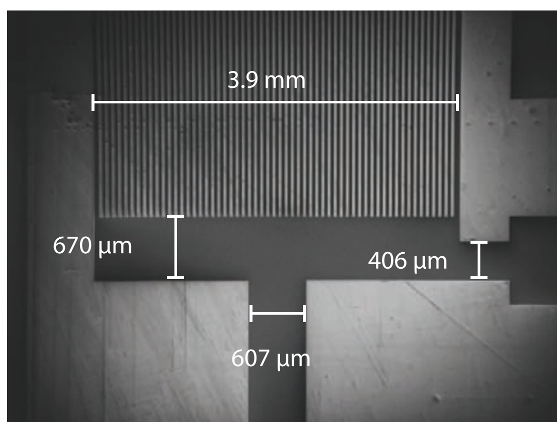

(a) In-plane wick with rectanular channels

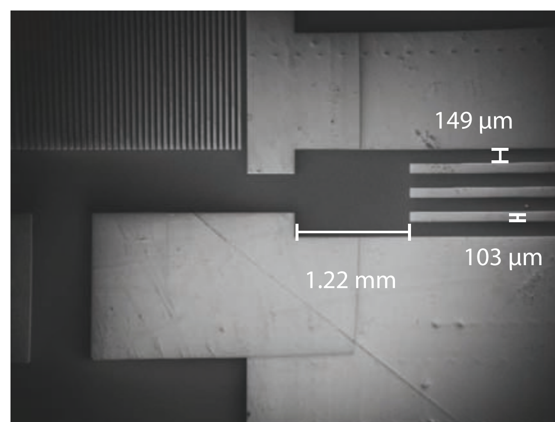

(b) Liquid channels feeding the wick

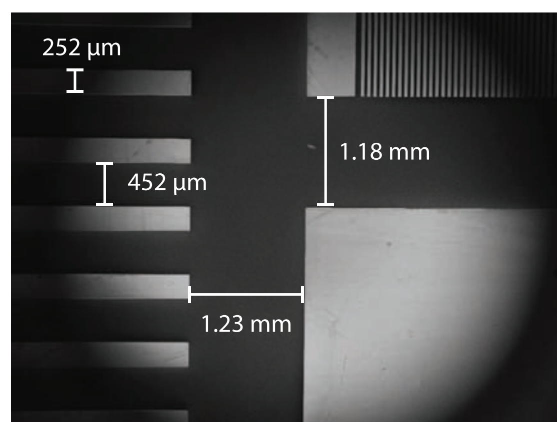

(c) Vapor channels emerging from wick

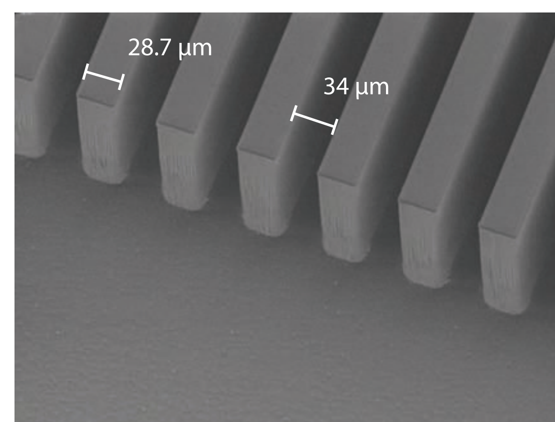

(d) Rectangular wick channels

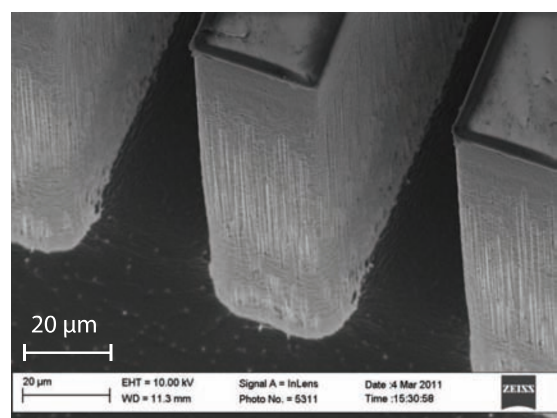

(e) Vertical nature of wick channels

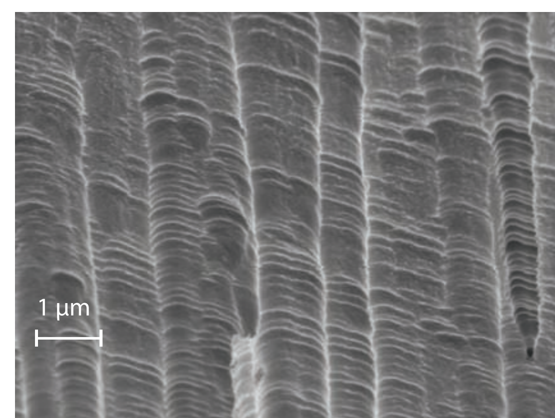

(f) Corrugated surface from DRIE etching

Figure 5.4: SEM images of the individual components of the phase-I μLHP device: (a-c) The evaporator section and the wicking structure; (d-f) Characteristics of the in-plane-wick microchannels.

the wick microchannels (or the wick pore size) was also varied between 8 μm, 16 μm, and 32 μm. As discussed previously, compared to the liquid microchannels, the vapor microchannels are made wider and more numerous in order to reduce the frictional vapor pressure drop (which dominates the liquid frictional pressure drop component). The preference for multiple vapor microchannels, instead of one large vapor channel, originated from the following two considerations: 1) A narrow channel can withstand larger pressures and is therefore more robust against fracture; 2) Liquid drops condensed in a very large aspect ratio vapor channel might not be easily dislodged, due to ample flow pathways around it. Nevertheless, it was also important to compare the dynamics of the liquid-vapor meniscus in both of these configurations. Therefore, one of the prototypes was fabricated with a single large vapor channel, instead of the multiple microchannels.

In Figure 5.4 can be seen some SEM images of the phase-I μLHP device components etched onto the silicon wafer, before it is anodically bonded to the Pyrex wafer. These images provide significant information about the structure, sidewall shape, and surface quality of the features etched using DRIE, which is a process known for its high aspect ratio anisotropic etching behavior. Figure 5.4(a) and Figure 5.4(b) show the evaporator section and in-plane wicking structure. The evaporator section cavity, which contains the extremely thin wick microchannels, is connected to the compensation chamber and the liquid microchannels. Figure 5.4(c) shows the interface between the vapor microchannels and the wick. Figure 5.4(d) takes a look at the wick microchannels from an angle. These microchannels are approximately 32 μm wide and about 150 μm deep. Taking a closer look at the sidewalls of the wick microchannels (Figure 5.4(e)), it is clear that the sidewalls are fairly straight. In fact, DRIE is known to yield almost perfectly vertical straight sidewalls with measured angles of $90^o \pm 2^o$ [99]. The maximum channel aspect ratio that can be achieved using this technique is approximately $20:1$ (depth : width).

The channel sidewalls appear slightly rough and this is confirmed by Figure 5.4(f). The scalloped sidewalls that we see in this high resolution image are a characteristic feature of DRIE, which is a cyclic process consisting of alternate passivation and etching steps. During the passivation step, a polymer compound is deposited to protect the feature sidewalls. The anisotropic etch step preferentially etches downwards, thereby etching the polymer and silicon from the floor, while leaving the sidewalls unaffected. These alternating steps typically being only a few seconds long, the process leaves repeating nanoscale patterns on the sidewall.

5.2 Phase-II μLHP Prototype

As it will become clear in the next two chapters, the phase-I μLHP device suffers from a few design shortcomings that lead to the following two problems: 1) Device packaging for the purpose of degassing and liquid-charging of the device is extremely

inconvenient; 2) The wick topology inhibits thin-film evaporation and only allows for nucleate boiling at high values of wall superheat temperatures.

5.2.1 Device Design

In order to overcome these design limitations associated with the phase-I μLHP device, a phase-II μLHP prototype was designed and fabricated. A detailed design schematic of the phase-II μLHP device is shown in Figure 5.5. The top view of the device is drawn to scale, while the cross-sectional views are not to scale. Taking a look at the top view of the entire device, we can see that the overall topology of the device is quite similar to that of the phase-I μLHP. There are evaporator and condenser sections that are connected by liquid and vapor microchannels. A thermal barrier separates the liquid and vapor microchannels. However, there are in fact two major changes that have been incorporated into this improved phase-II μLHP design.

The first design change in this prototype is amply clear from the top view of the entire device (Figure 5.5(a)). The reader may recall that in the phase-I μLHP prototype the inlet fluid fill-port was located inside the compensation chamber, while the outlet fill port was located inside the condenser section. In the next chapter, we will see that this arrangement of the device fill-ports is not conducive to the development of standardized device packaging techniques, for degassing and filling these devices with a working fluid. For example, a change in the linear dimensions of many of the individual device components will lead to a shift in the position of the fill ports. As a result, the external package that works for one device prototype might not work for another. In order to solve this problem in the phase-II μLHP design, the individual geometry and the relative positioning of the fill-ports have been standardized. The fill-ports have been moved away from the actual device and are now connected to the device using channels. Each fill port is 1 $mm \times 1$ mm and they are always maintained at a distance of 10 mm from each other. In the next chapter, it will be shown how this simplifies device packaging by 1) allowing a single external packaging to be used for the degassing and filling of arbitrarily shaped device prototypes, and 2) making the μLHP prototypes more accessible to the experimentation equipment, by confining the packaging components to the region containing the fill-ports.

The second design improvement in the phase-II μLHP concerns the in-plane wicking structure and the evaporator section, as shown in Figure 5.5(b). As discussed previously, the in-plane wicking structure consists of extremely narrow and high aspect ratio rectangular channels, which are approximately 150 μm deep. Due to the small channel width, there is a large capillary pressure difference across the liquid-vapor menisci in these channels, which is given by

$$\Delta P_c = 2\sigma \cos\theta_c \left(\frac{1}{w} + \frac{1}{h}\right) \approx \frac{2\sigma \cos\theta_c}{w} \qquad \text{(since } w << h\text{)} \tag{5.1}$$

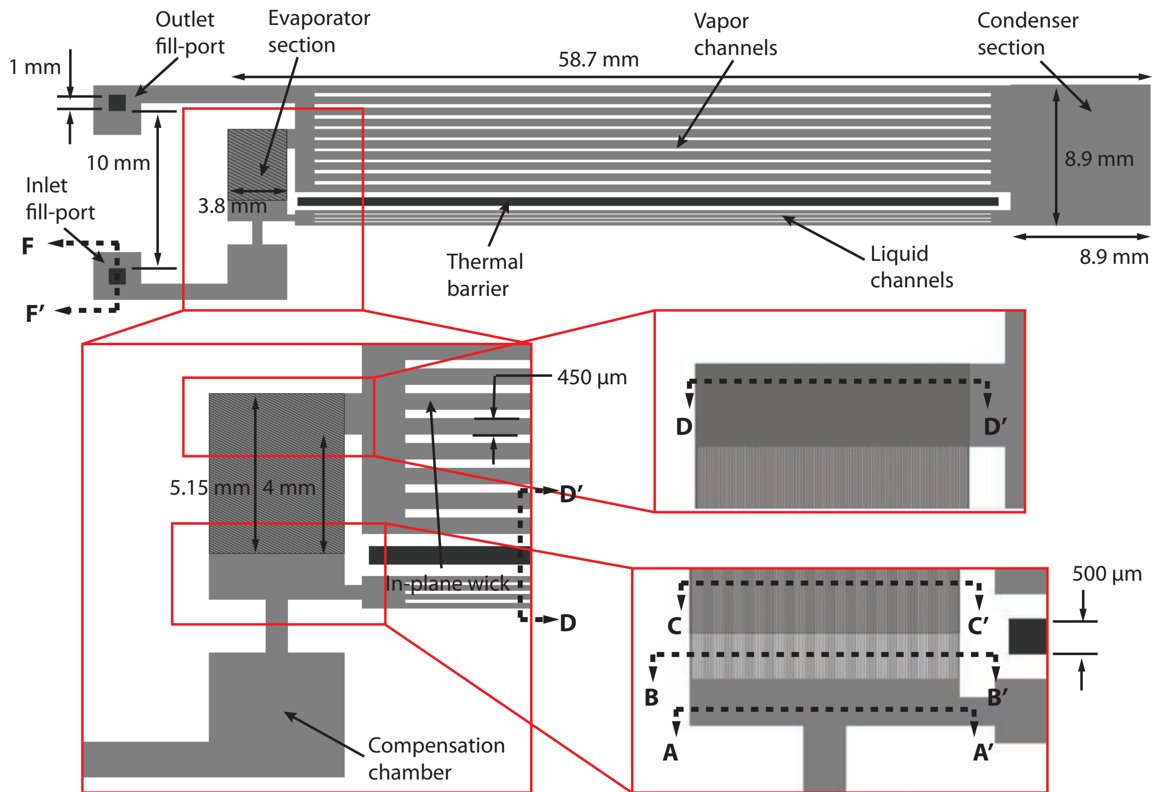

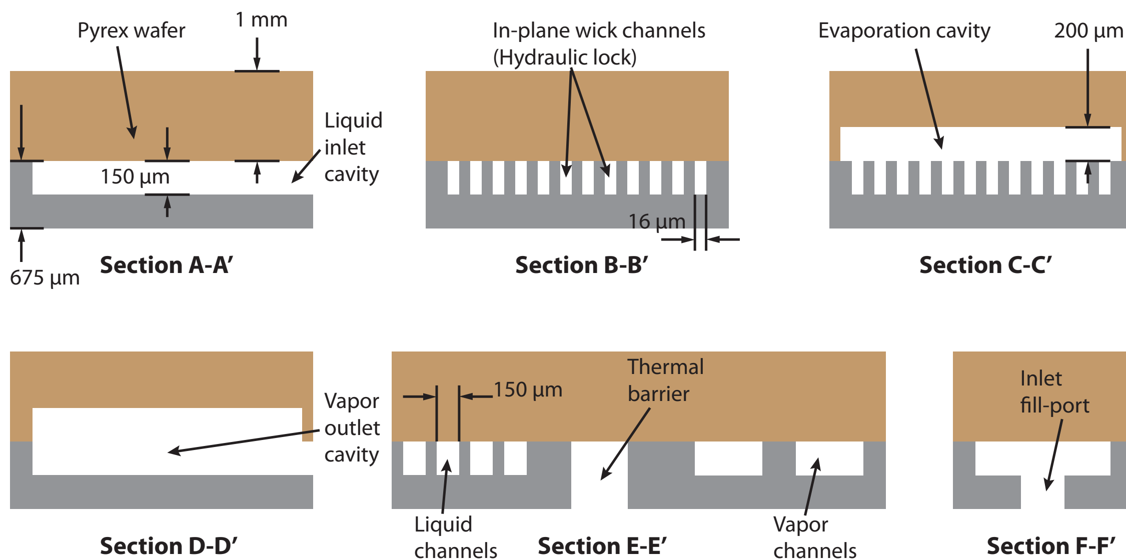

Figure 5.5: A design schematic of the phase-II μLHP device: (a) The top views of the device are drawn to scale; (b) Dimensioned cross-sectional view of individual device components.

where σ is the liquid surface tension, θ_c is the liquid-solid contact angle, h is the height, and w is the width of an individual rectangular wick microchannel. This capillary pressure helps the wick to drive the liquid from the liquid inlet cavity (section A-A' in Figure 5.5(b)) into the evaporator section, where evaporation is to take place. In the phase-I μLHP, the wick microchannels were bounded from all side (as in section B-B') in the entire heated region. This allowed for the formation of a liquid-vapor meniscus only at the very end of the wick microchannels. Since thin-film evaporation takes place at the surface of a meniscus, it is crucial to extend the liquid-vapor meniscus over the entire heated surface, without compromising the capillary wicking action of the in-plane wick.

In the phase-II μLHP design, an evaporation cavity (section C-C') is etched into the Pyrex wafer, above the in-plane wick in the heated region of the evaporator section. A relatively small part of the wick (section B-B') close to the liquid inlet cavity is kept sealed by the non-etched part of the Pyrex wafer. The principle of operation of this wick design topology is as follows: The liquid microchannels and the compensation chamber supply the liquid to the liquid inlet cavity (section A-A'), which is adjacent to the in-plane wick. The capped in-plane-wick microchannels (section B-B') absorb this liquid and transport it to the evaporation cavity (section C-C') using the capillary surface tension forces. They also serve as a hydraulic lock, by preventing the vapor formed in the evaporation cavity from intruding back into the liquid inlet cavity. This functionality is attributed to the fact that, compared to the exposed wick microchannels in the evaporation cavity, the covered microchannels in the hydraulic lock cannot sustain any significant amount of thin-film evaporation. Further, nucleate boiling in these microchannels can only occur at larger values of wall superheat, since it is inhibited by the small channel sizes.

The liquid in the heated part of the in-plane wick can undergo thin-film evaporation from a much larger liquid-vapor meniscus area, compared to what would be available in the phase-I μLHP design. After the liquid in the Pyrex evaporation cavity has turned to vapor, a horizontal meniscus should form in the wick microchannels underneath it. Since the wick has a porosity of 0.5, the total area of this meniscus should be approximately half the area of the heat region, provided there is no partial dry out in the wick microchannels. Note that the evaporation cavity extends further into the rest of the evaporator region, after the wick microchannels have ended (section D-D'). This provides a pathway for the vapor formed above the wick microchannels to travel to the vapor outlet cavity, and from there into the vapor transport channels.

5.2.2 Device Fabrication

The phase-II μLHP device was fabricated in Berkeley's Marvell nanofabrication laboratory. Since most of the machinery in this lab is dedicated to 6-inch wafer processing, phase-II and phase-III μLHP devices were fabricated using 6-inch silicon and Pyrex wafers, as opposed the phase-I device, which was fabricated on 4-inch

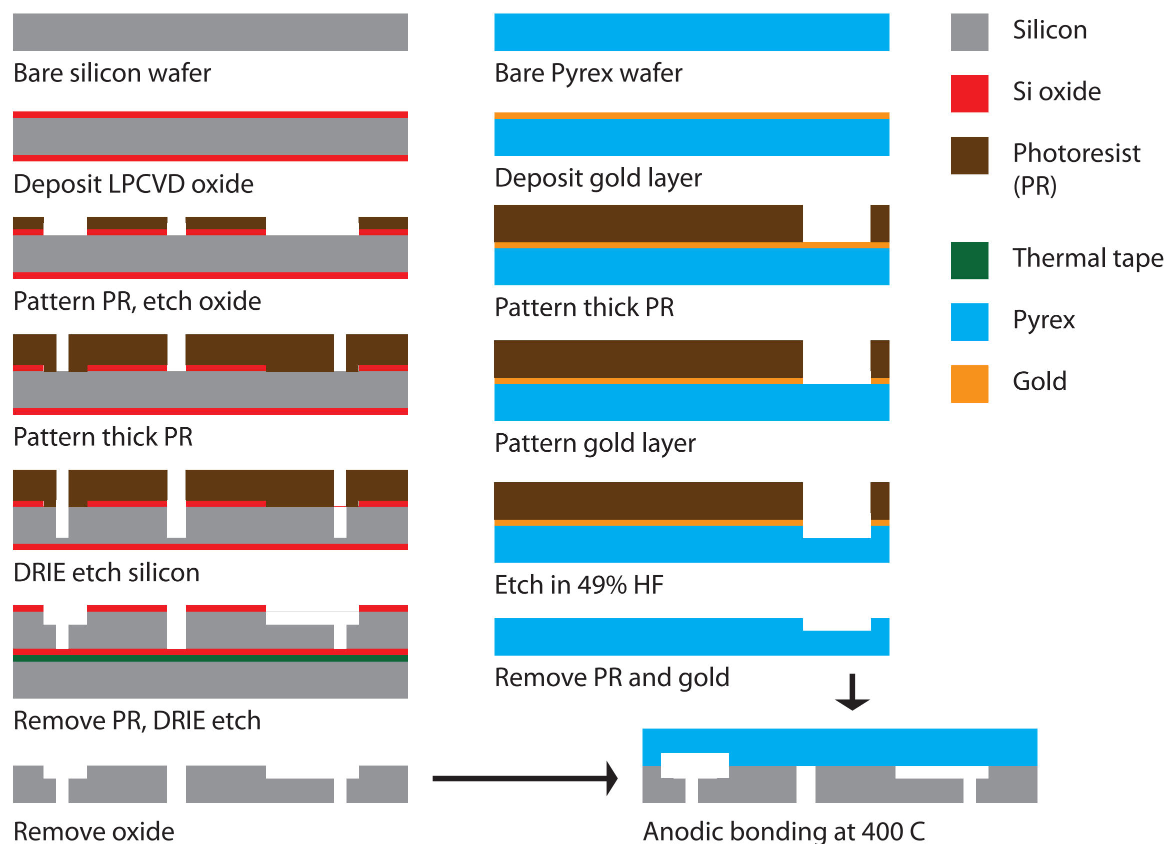

Figure 5.6: Fabrication process flow for the phase-II and phase-III μLHP devices. Device components are etched into the silicon wafer using DRIE and into the Pyrex wafer using HF wet etching. Anodic bonding is used to permanently bond the wafers.

wafers. The device fabrication process flow, which applies to both phase-II and phase-III devices, is shown in Figure 5.6. This process flow is different from the phase-I μLHP process flow in the following two respects: 1) Both the silicon and Pyrex wafers have to be micro-machined, unlike the previous process where Pyrex was used only as a capping wafer; 2) The process steps for the etching of the silicon wafer have been modified to avoid issues associated with the use of the handle wafer during DRIE etching, as mentioned in the previous section.

The silicon and Pyrex wafers were processed separately until the last step, when they were bonded together to yield the final device. The process steps for the silicon and Pyrex wafers are given next.

Silicon wafer processing

The fabrication process starts with a 6-inch <100> n-type silicon wafer. The wafer is piranha-cleaned to remove organic impurities and dipped in HF to remove the native

oxide layer. A low pressure chemical vapor deposition (LPCVD) process is used to deposit 2 μm silicon dioxide layer in a 450 ^oC thermal furnace. A phosphorous-doped low temperature oxide (LTO) recipe is employed and therefore the oxide layer formed is also called phospho-silicate glass (PSG). The silicon wafer is annealed in a 1000 ^oC thermal furnace for 5 hours to reduce stress in the oxide layer and make the oxide thickness uniform across the surface of the wafer.

Following this, the wafer is piranha-cleaned, treated with HMDS for better photoresist adhesion, and deposited with a 2.6 μm thick layer of G-line positive photoresist. The wafer is then exposed to UV light using the first chrome mask. This mask patterns all of the silicon device features, including the thermal barrier and the fill-ports, onto the photoresist. Although the thermal barrier and the fill-ports will be etched using a subsequent thick photoresist mask, it is necessary to remove the oxide layer from those areas in this current step. The exposed photoresist is developed and hardbaked in a 120 ^oC oven for 2 hours. Using the patterned photoresist as an etch mask, the underlying oxide layer is etched in a plasma etching system. The hardbaked photoresist is then removed by dipping the wafer in a hot photoresist stripping solution (PRS-3000) for 12–24 hours.

The wafer is once again cleaned in a piranha solution and treated with HMDS. A 10 μm thick G-line photoresist layer is deposited and exposed to UV light using the second chrome mask, which patterns the thermal barrier and the fill-ports. After development and hardbaking, this thick photoresist layer is used as an etch mask for the deep reactive ion etching (DRIE) of silicon, to obtain the thermal barrier and the fluid fill-ports. Unlike the process flow for the phase-I μLHP device, a backside handle wafer is not employed in this etch step. Instead of through-etching the features, the silicon wafer is etched to a depth that is approximately 100 μm less than the total wafer thickness. The thick photoresist is then removed by dipping the wafer in hot PRS-3000 for 12–24 hours, and is wafer is subsequently cleaned in a piranha solution.

A silicon handle wafer, with a 2 μm thick oxide layer, is attached to the backside of the device silicon wafer using a thermal tape. Using the previously patterned oxide layer as an etch mask, the silicon wafer is etched using DRIE to a depth of 150 μm. This not only etches the device components such as the evaporator/condenser sections and the fluid transport channels, but also completes the through-etching of the previously etched thermal barrier and fluid fill-ports. The usage of the thermal tape makes the removal of the handle wafer much easier; the device wafer can be separated from the handle wafer by simply placing them on a 230 ^oC hot plate for a few seconds.

Pyrex wafer processing

The μLHP device components that need to be etched into the Pyrex wafer include the evaporation cavity and a condensation cavity (for the condenser section of the phase-III device). While a host of dry and wet etching techniques are available for both anisotropic and isotropic etching of silicon, the options are extremely limited

when it comes to Pyrex etching. Hydrofluoric (HF) acid is well know to isotropically etch glass substrates and, since the required feature size is relatively large, in this case it is a viable option. However, HF is known to be very reactive towards most conventional masking materials, which tend to delaminate from the wafer before a considerable etch depth is achieved. For example, hardbaked photoresist in concentrated HF comes off the wafer surface within a few minutes. The measured etch rate of Pyrex in 48% HF is approximately 6.5 $\mu m/min$. In order to etch to a depth of 200 μm, the masking layer should be able to hold for at least 31 *mins*. A gold/photoresist dual mask has been shown to be durable enough for this purpose [100].

The process steps employed for the wet etching of Pyrex are shown in Figure 5.6. The bare Pyrex wafer is first cleaned in piranha solution. A 50 nm/400 nm Cr:Au layer is then deposited on the wafer using electron-beam evaporation. The chromium acts as an adhesion layer for gold, which does not stick very well to Pyrex on its own. After this, a 20 μm layer of the SPR-220 thick positive photoresist is deposited onto the wafer. The wafer is soft-baked on a 90 ^oC hot plate for 5–10 *mins*, while taking care to avoid any thermal shock, which can lead to cracks in the photoresist. Following this, the wafer is left standing for about 12 hours. The photoresist is then exposed to UV light using the third chrome mask. The exposed wafer is left standing for 30 mins so that the UV-initiated chemical reactions can take place. The wafer is then developed in the M-26A developer solution. Following this, the wafer is hardbaked on a 90 ^oC hot plate for 3 hours, taking care to avoid any thermal shock.

Using the photoresist layer as an etch mask, the exposed gold and chromium layers are etched using liquid gold (GOLD ETCH - TYPE TFA) and chromium (CR-7) etchants, respectively. After the wafer has been rinsed in water and dried, a blue adhesive tape is applied to its backside. This tape is resistant to HF and protects the Pyrex wafer backside during HF etching. The Pyrex wafer is then etched in 48% HF at room temperature for 31 *mins* to obtain the necessary device components. Following this, the blue tape is removed manually, the hardbaked photoresist is stripped in hot PRS-3000, and the gold and chromium layers are dissolved off in their respective liquid etchants.

Wafer bonding

After both the silicon and Pyrex wafers are ready, they are cleaned in hot piranha solution. This not only cleans the wafers but also hydroxylates their surfaces, which helps in the formation of the temporary Van der Waals bond before anodic bonding. When aligning the two wafers for anodic bonding, it should be ensured that there are no residual dust particles between them, since this can prevent the wafers from coming into proper contact for bonding. The wafers are permanently bonded together using anodic bonding at 350 ^oC and 1000 V. The bonded wafers are then diced to obtain the individual μLHP devices.

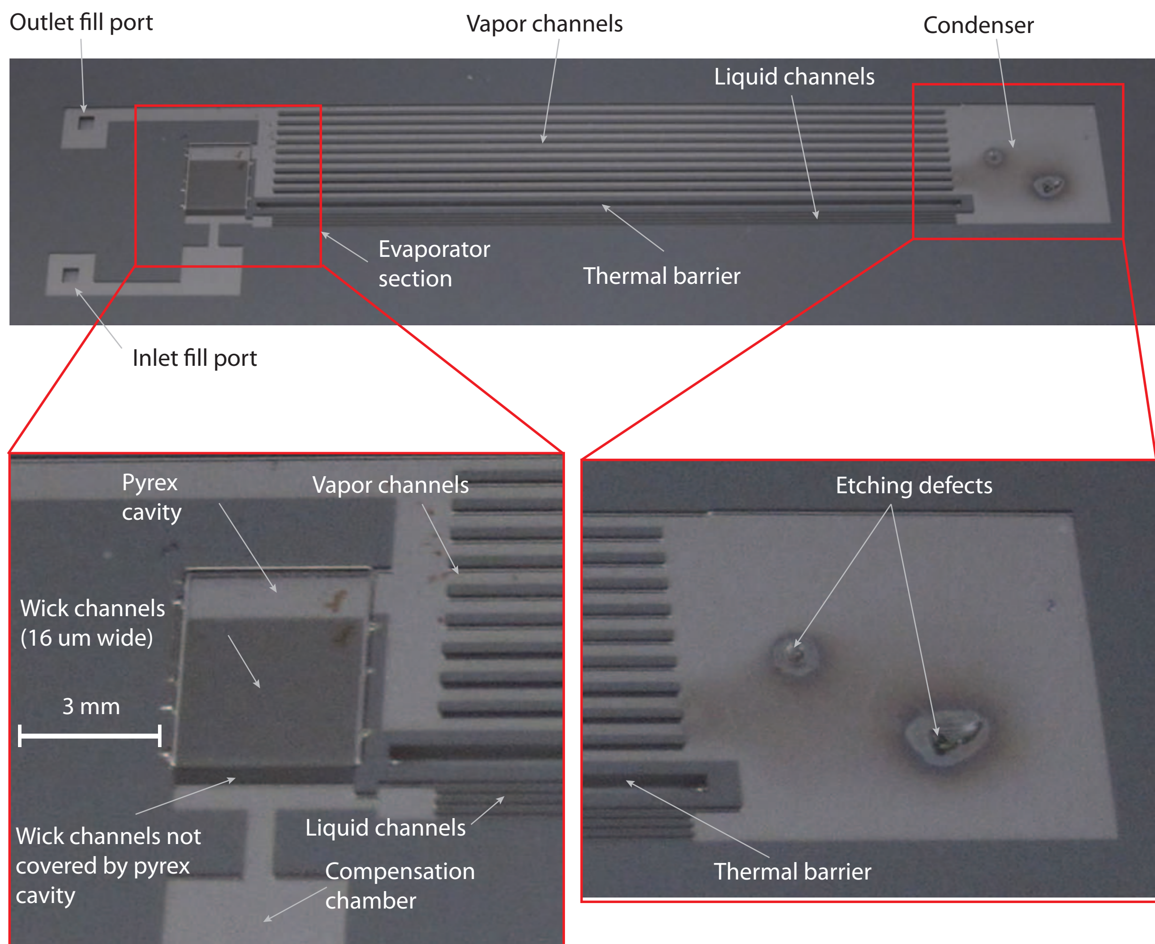

Figure 5.7: Images of the fabricated phase-II μLHP device prototype.

Figure 5.7 shows the fabricated phase-II μLHP device. We can see that the silicon etching is fairly clean except for a few defects in the condenser section. The thermal barrier between the liquid and vapor microchannels has successfully etched through the entire wafer. The Pyrex evaporation cavity above the in-plane wick is also clearly visible.

5.3 Phase-III μLHP Prototype

The primary objective behind the design of the phase-III μLHP device is to implement the concept of *geometric control* of the fluid transport meniscus in these devices. As we will see later in chapter 7, the dynamics of the two-phase liquid-vapor meniscus in microchannels is substantially influenced by surface tension forces, due

to the small meniscus radius of curvature. This means that, unlike macroscale loop heat pipes, the thermodynamic condition of the two-phase working fluid is not the sole determining factor in the distribution of liquid and vapor phases in the flow loop. The relative size of the microchannels and cavities also determines how the liquid is distributed in the device.

5.3.1 Device Design

In Figure 5.8 is shown the design schematic of the phase-III μLHP device. The top view of the device (Figure 5.8(a)) is drawn to scale and shows the overall device topology as well as close-up views of the evaporator and condenser sections. The cross-sectional views (Figure 5.8(b)) are not drawn to scale but are accurate representations of the features etched into the silicon and Pyrex wafers. First, take a look at Figure 5.8(a). The overall device topology, except the inlet and outlet fill ports, is quite different from the phase-I and phase-II μLHP devices. The main design principles of the phase-III μLHP are as follows:

1. The hydrophilic wetting surface area available per unit volume of the working fluid increases as we go from the vapor channels to the condenser, from the condenser to the liquid channels, and finally from the liquid channels to the in-plane wick channels.

2. The wetting area per unit liquid volume increases monotonically when transitioning between the above device components, i.e., there is no local minimum.

The idea is to control the location of the working liquid, in a partially filled device, by geometrically designing some components to have lower surface-wetting free energies compared to others. As a result, in the absence of other thermophysical factors, the liquid in the device should rearrange itself to preferentially occupy certain components, while leaving the vapor to occupy the rest of the device. In a partially filled μLHP, the device startup time can be minimized by ensuring the absence of liquid in the vapor microchannels even in the device OFF state. Further, the liquid microchannels should be occupied by liquid at all times in order to avoid wick dry out, especially during device startup. The liquid in the condenser should preferentially move into the liquid microchannels. The phase-III μLHP design satisfies all of these three requirements.

The liquid-surface-wetting free energy of a microchannel per unit liquid volume decreases in proportion to the ratio of the channel surface area to the channel volume.

$$\frac{A_c}{V_c} = \frac{2(w+h)l}{whl} = 2\left(\frac{1}{h} + \frac{1}{w}\right) \tag{5.2}$$

where w, h, and l are the width, height, and length of the microchannel, respectively. For a channel of constant height, the wetting free energy per unit liquid volume

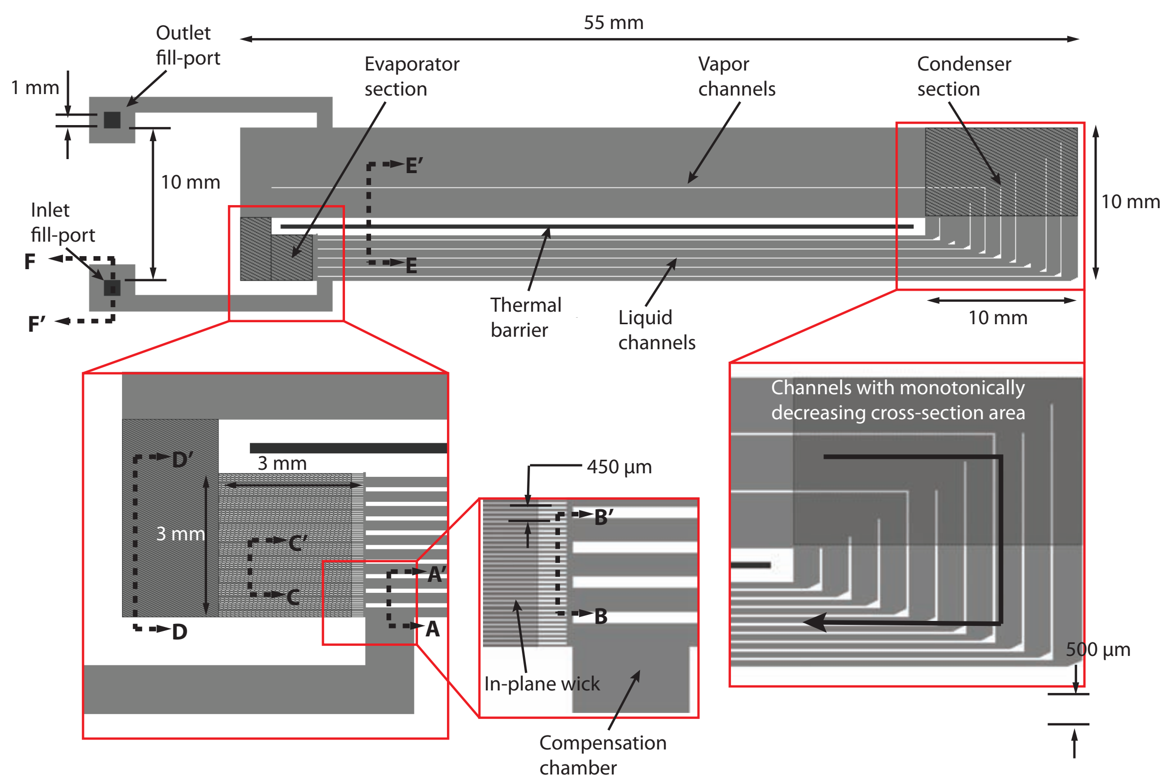

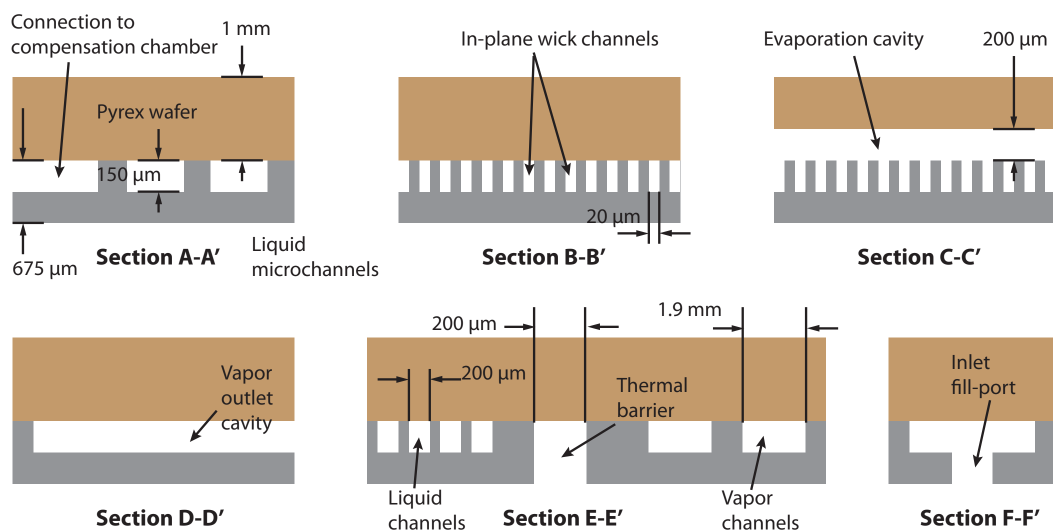

Figure 5.8: A design schematic of the phase-III μLHP device: (a) The top views of the device are drawn to scale; (b) Dimensioned cross-sectional view of individual device components.

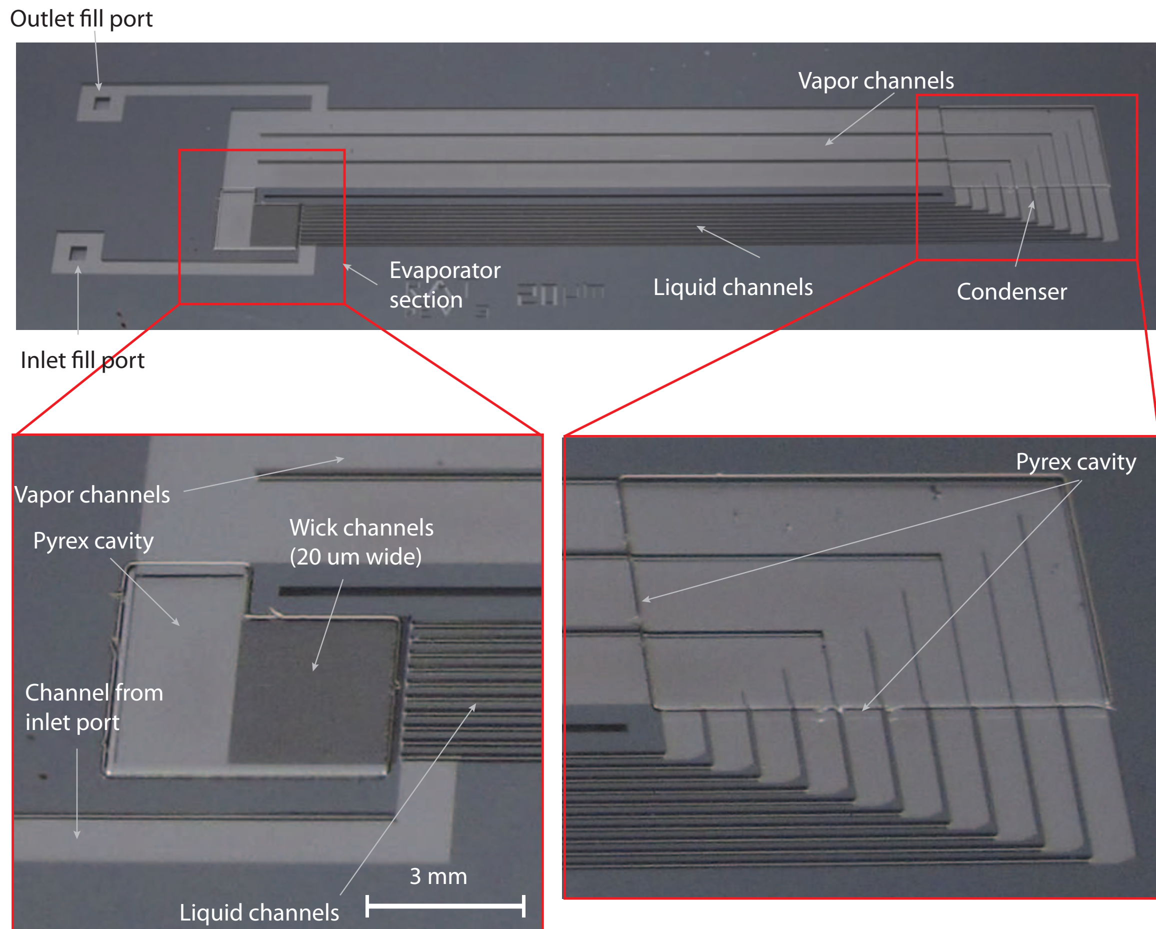

Figure 5.9: Images of the fabricated phase-III μLHP device prototype.

decreases with a decrease in the width of the microchannel. Since physical systems tend to minimize their free energies in equilibrium, liquid from a wider channel will automatically move into an adjacent narrower channel, provided there is a monotonic decrease in channel width from the wider channel to the narrower channel. The monotonicity is to ensure that the system does not encounter a local maximum in wetting free energy as the liquid-vapor meniscus travels across the interface between the two channels. In the phase-III μLHP, the liquid channels are narrower than the condenser channels, which in turn are narrower than the vapor channels.

Unlike the phase-II μLHP evaporator design, a large cavity is not provided between the liquid microchannels and the extremely narrow in-plane wick microchannels. The objective, again, is to provide a monotonically decreasing channel width, going from the liquid microchannels to the wick microchannels. An extremely small cavity (only 50 μm long), however, is provided in order to avoid a situation where many of the wick

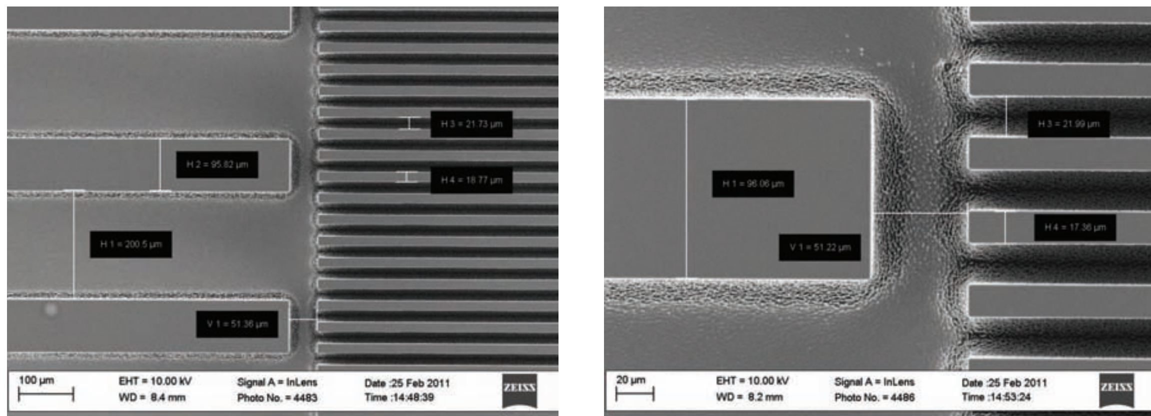

(a) Liquid channels feeding the wick

(b) Close-up view of wick inlet

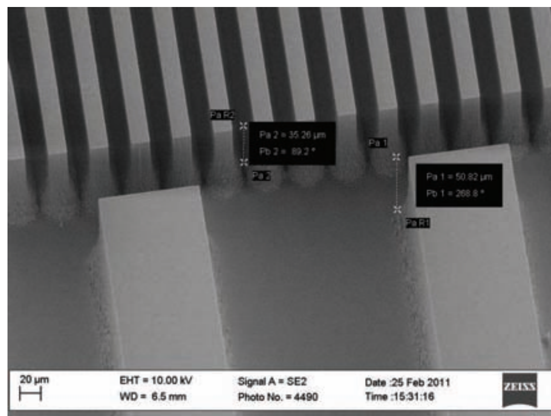

(c) 3-D view of the wick evaporator/wick

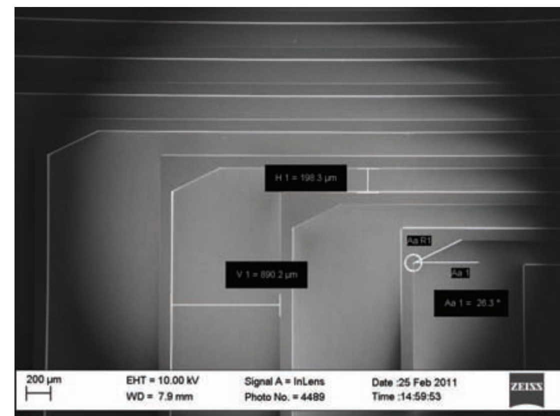

(d) Monotonically varying cross-sections of channels in the condenser section

Figure 5.10: SEM images of the individual components of the phase-III μLHP device: (a-c) Topology of the evaporator section and the wick; (d) Monotonic variation of channel cross-section in the condenser section.

microchannels would end up being completely blocked by the liquid microchannel walls. Looking at Figure 5.8(b), we see that the in-plane wick topology is almost identical to that of the phase-II μLHP, except for the fact that there is no large liquid supply cavity preceding the hydraulic lock (section B-B'). Instead, liquid is supplied directly by the liquid microchannels and a larger channel from the liquid inlet port, which sort of acts like a liquid reservoir.

5.3.2 Device Fabrication

The fabrication process flow for the phase-III μLHP device is identical to the phase-II μLHP fabrication process flow and is given in section 5.2.2. The fabricated

phase-III μLHP device is shown in Figure 5.9. The features etched into the silicon wafer are clearly defined and no etching defects are visible. The Pyrex evaporation cavity above the in-plane wick and a Pyrex condensation cavity above part of the condenser are also clearly visible. Although it is not clear from the figure, it was observed that the 200 μm wide thermal barrier between the liquid and vapor microchannels did not manage to go through the entire silicon wafer. This might have to do with a reduction in DRIE etch rate associated with the smaller feature width, when compared to the 500 μm wide phase-II μLHP thermal barrier, which etched fine. Nevertheless, with most of the silicon removed, the thermal resistance of the barrier should still be relatively good.

In Figure 5.10 can be seen close-up SEM images of the evaporator and condenser features etched into the silicon wafer. As discussed previously, the liquid microchannels feed the liquid directly to the wick, without any intermediate liquid cavity. The separation between the liquid microchannels and wick is only about 50 μm (see Figure 5.10(b)), which is less than half the depth of the channels. Figure 5.10(d) illustrates how the width of the microchannels decreases monotonically while going from the condenser to the liquid microchannels.

Chapter 6

Device Filling and Packaging

Degassing and controlled fluid charging is one of the major challenges to the successful operation of microscale loop heat pipes (μLHP). The working fluid can be chosen according to the desired device operating temperatures—water, ammonia, acetone, methanol, toluene, freon-11, freon-152A are among the many available options [15, 66]. Water was used as the μLHP working fluid in this work due to its good wetting properties, high latent heat value, and good efficiency in the 100–150 ^oC temperature range [15]. Anhydrous ammonia and acetone are also very good candidates for the μLHP working fluid due to good heat transfer efficiencies in the 50–100 ^oC temperature range [60]. The μLHP needs to be completely degassed to remove all non-condensible gases (NCGs), before it is filled with the working fluid. This is essential, because the presence of NCGs can lead to flow blockages due to the formation of bubbles in the wick structure as well as the transport microchannels. This affects device performance and can also lead to a general failure of the capillary evaporator. In this chapter are presented high-temperature-compatible MEMS device packaging techniques for implementing a novel two-port degassing and fluid filling setup for microscale loop heat pipes.

6.1 Statement of the Problem

Figure 6.1 illustrates why degassing is so important in loop heat pipes, and especially so in its MEMS versions. It provides a close-up view of the entrance region to the capillary wicking structure in the phase-I μLHP prototype. The wicking structure consists of very narrow (10–20 μm wide) rectangular channels, where the liquid to vapor phase change happens. The wick is supplied with liquid by the liquid supply channels and a reservoir supply channel. Due to the presence of non-condensible gases in the working fluid, we can see bubbles both at the entrance to the wicking structure (Region I) and at the end of the liquid supply channels (Region II). These bubbles can prevent the supply of liquid to the wick for evaporation during device operation,

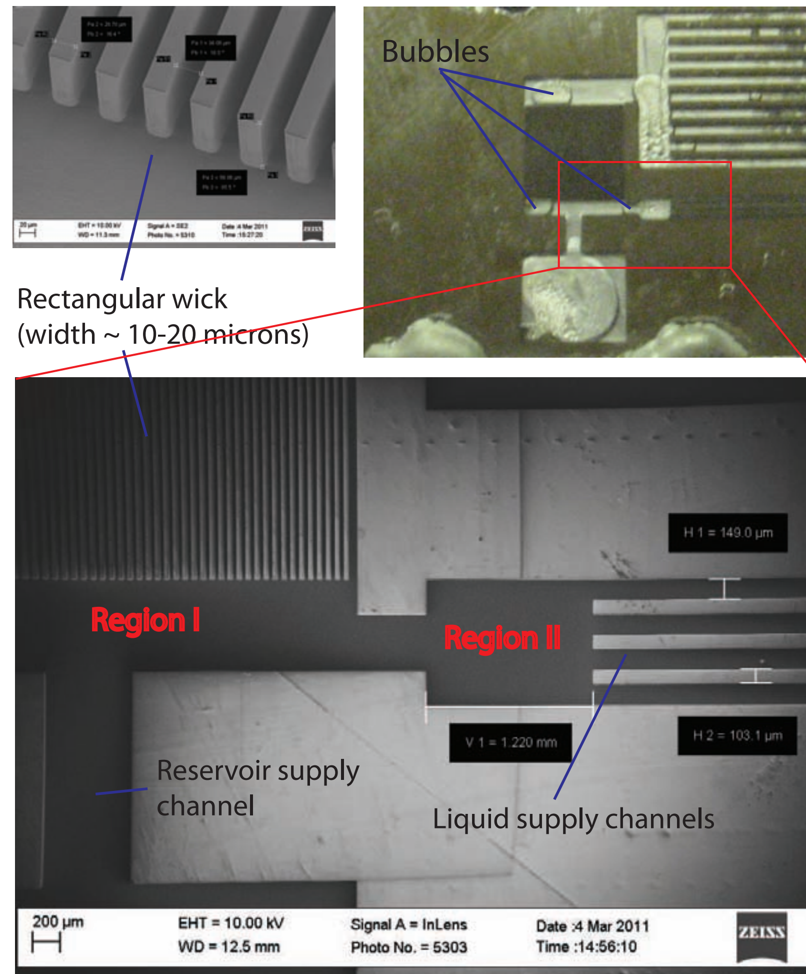

Figure 6.1: Microscale loop heat pipe components susceptible to blockage due to the presence of non-condensible gases (NCGs) in the working fluid. Bubbles formed at the entrance to the rectangular wicking structure (region I) and at the end of the liquid supply channels can block the supply of liquid to the wick, causing immediate device failure.

causing wick dry out and subsequent device failure.

In macroscale pipe-based designs, the loop heat pipes are first evacuated by establishing a secure connection to an external vacuum pump, and then the working fluid is introduced into the device in a controlled manner. Vacuum levels as low as 5×10^{-6} $Torr$ are required to minimize the presence of non-condensible gases in the device [67]. The amount of the liquid in the device needs to be strictly controlled, since the device can only be partially filled; the volume of liquid in the device is dictated by the size of the compensation chamber and that of the device itself [64].

Similarly, in the design and fabrication of the μLHP prototypes, the degassing and filling issues are deferred until after the fabrication of the entire device. This

is currently the only option, since the available microfabrication equipments do not allow for in-situ liquid filling of MEMS devices. Since the last step in μLHP device fabrication is the anodic bonding of silicon and pyrex wafers—at only moderately high temperatures (∼350–400 ^oC) in a Karl Suss anodic bonder—opportunities exist for the industrial level modification of this equipment to enable injection of a degassed liquid into the device before the bonding process. But this will require significant capital investment and substantial modifications to the current MEMS anodic-bonding technology.

The remaining alternative, which we have pursued, is to provide fill-holes in the fabricated μLHP devices, which are connected to an external degassing and filling system. This requires high-vacuum-grade tube-to-chip connections and connecting tubing, and an ultra-high-vacuum pumping system that can provide vacuum levels as low as 10^{-6} $Torr$. This will, in practice, be a large system with a big pump, and is extremely impractical when evacuating devices whose internal volumes are on the order of microliters. In the following section is presented a novel thermal flux-based degassing and fluid-filling system that does not require a vacuum pump. Device packaging techniques that were implemented in order to interface the μLHP device with the external filling system are also introduced.

6.2 Thermal Flux Degassing and Filling System

In contrast to the vacuum-pump based system for degassing cylindrical loop heat pipes, as described in the previous section, there is an alternative approach that is commonly employed for heat pipes (HP) when the working fluid has a low boiling point, for example acetone. As shown in Figure 6.2, a small amount of liquid is introduced through the open end of the cylindrical heat pipe. The liquid settles at the bottom of the heat pipe, which is then heated with a flame to cause evaporation. The vapor rises through the pipe, and in the process purges the air from the pipe. When the pipe is completely saturated with vapor, its open end is sealed shut using soldering or brazing. This method works best for heat pipes as they require only a small amount of working fluid for operation, with most of the space occupied by vapor. On the other hand, loop heat pipes are mostly filled with liquid. Moreover, the MEMS versions have large capillary forces, which prevent air bubbles from escaping the device.

The above concept was extended to design a two-step, thermal flux-based degassing and fluid filling process, using water as a working fluid, as outlined in Figure 6.3. The inlet port of the μLHP device is connected, using steel capillary tubing, to an external reservoir flask containing water, which has been previously boiled to remove dissolved air. The outlet port of the μLHP is open to the ambient. The operating procedure is as follows: In step 1, the water in the flask is boiled vigorously using a digital heater. This extracts any dissolved gases from the water, and

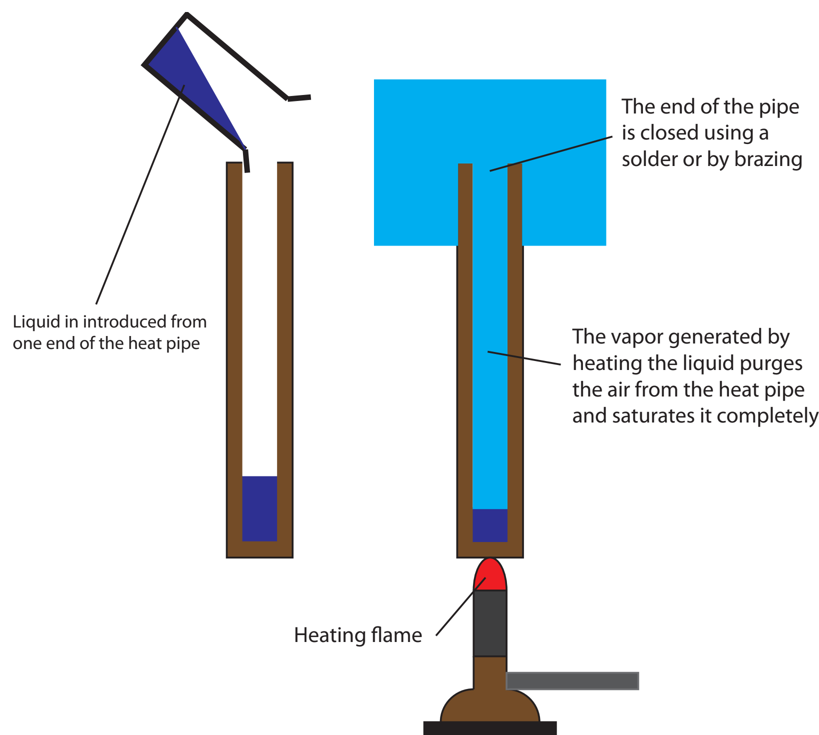

Figure 6.2: A simple degassing and fluid-filling method employed in large-size cylindrical heat pipes. The working fluid should have a low boiling point, so that it readily vaporizes upon heating.

further, the steam generated in the process creates a high pressure inside the flask. The pressure gradient between the flask and ambient drives the steam through the capillary tubing, into the μLHP device, and then out to the ambient through the exit tubing connected to the outlet port. All gases except water vapor are removed from the system due to convection. In step 2, the outlet port tube exit is closed, and the reservoir flask is inverted to let water into the connecting steel tubing. A valve is used to control the flow of liquid into the device, the liquid being pushed into the device by thermally pressurizing the reservoir flask. In this way, the μLHP can be partially filled with a working fluid that is devoid of all non-condensible gases.

6.3 Device Packaging Techniques for Filling

In order to implement the above system for degassing and filling individual micro loop heat pipes, we need high-temperature compatible, high-vacuum grade chip-to-tube interconnects. Currently, only epoxy-based plastic microfluidic interconnects are available in the market, and there are no commercial solutions for reliably connecting metal microtubing to MEMS wafer-scale devices. Further, any microfluidic connec-

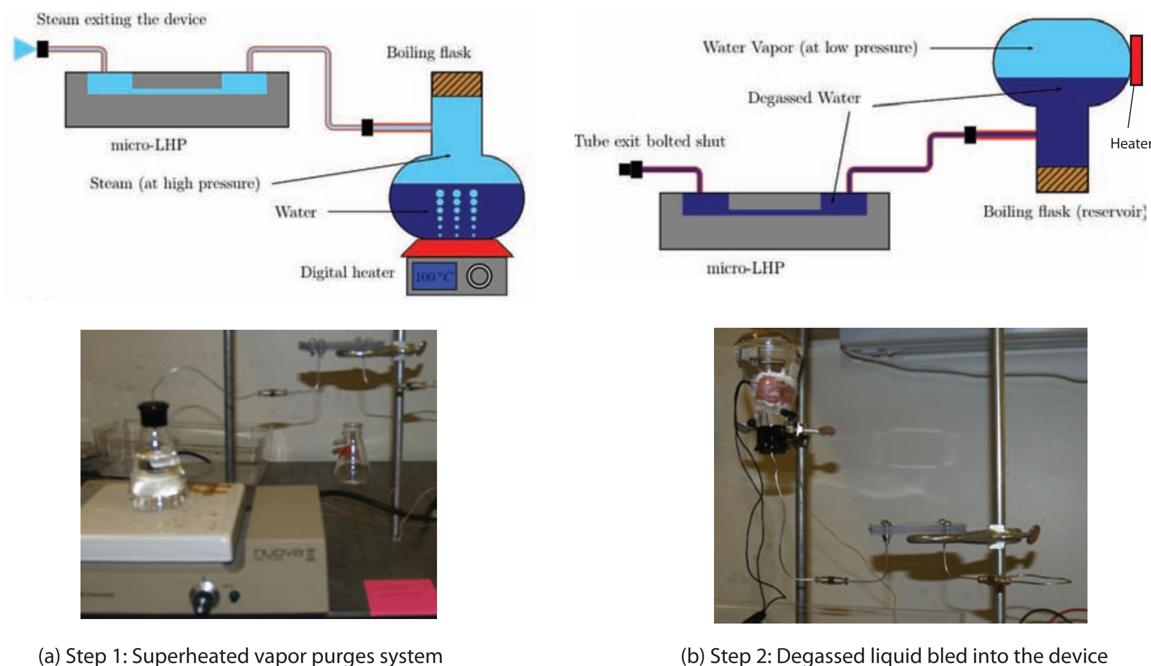

(a) Step 1: Superheated vapor purges system

(b) Step 2: Degassed liquid bled into the device

Figure 6.3: Thermal-flux based μLHP degassing and filling setup: (a) Superheated vapor, generated by heating the liquid in a flask, is used to purge NCGs from the μLHP. This also removes any dissolved gases from the liquid in the reservoir flask. (b) The flask is inverted and raised above the device; Using a valve the liquid is controllably bled into the device, taking advantage of pressure differential created by heating the flask.

tions to the μLHP device must be able to withstand the stresses that can propagate through the stiff metal tubing. In this section are presented three different preliminary device packaging techniques that were implemented in order to degas and fill μLHP devices using the thermal flux method. A more robust standardized packaging method, which builds upon the cumulative knowledge obtained from these initial studies, is presented in section 6.4.

6.3.1 Method I: Mechanically Sealed Plastic Package with O-rings and Interference-fitted Microtubing

In Figure 6.4 is shown a packaging technique that employs a mechanically sealed polycarbonate (PC) package to establish a vacuum-grade, high-temperature-resistant connection between the phase-I μLHP device and 1/16 inch-OD steel microtubing. The package consists of a bottom polycarbonate plate, which has 3/64 inch diameter holes drilled into it. The steel tubing is interference fitted into these holes to provide a leak proof and mechanically stable connection. At the top of the holes, nylon O-rings are placed inside a slightly bigger cavity, half as deep as the thickness of the O-rings.

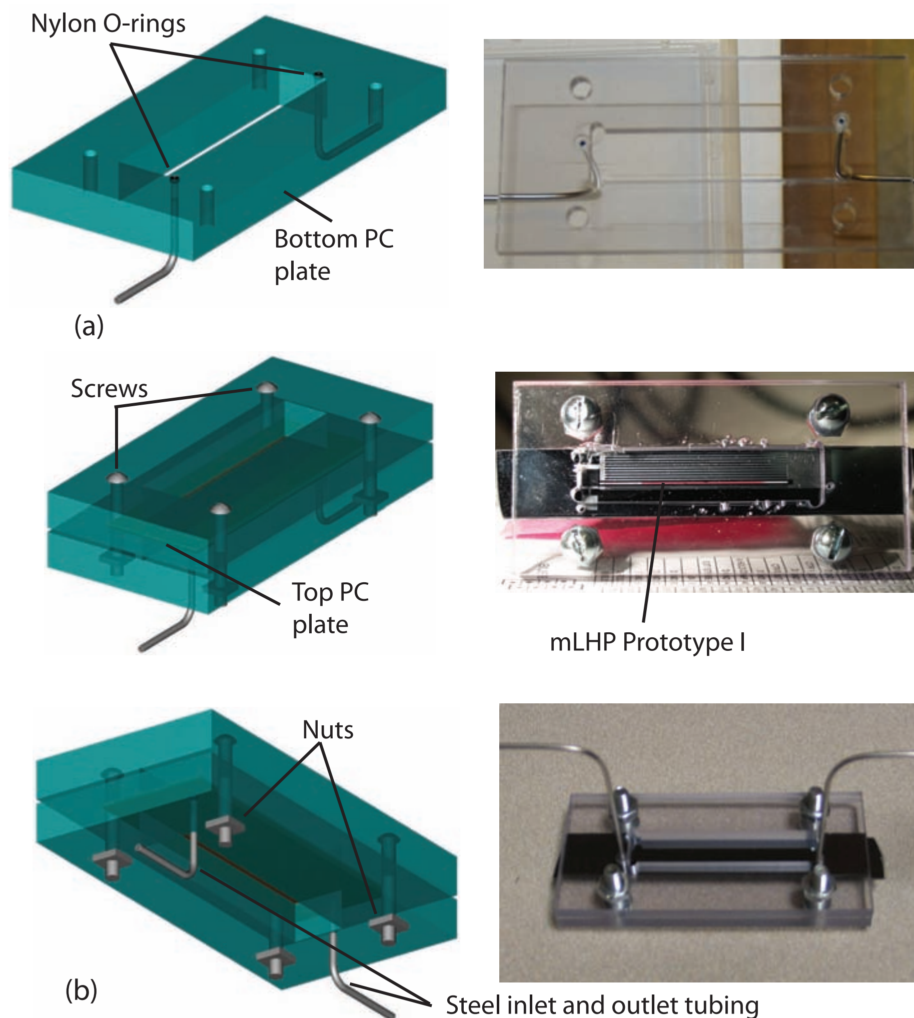

Figure 6.4: Mechanically sealed plastic packaging (Method I): (a) The bottom polycarbonate (PC) plate has drilled holes containing O-rings, which align with the fill holes etched into the μLHP device. Steel microtubing is interference-fitted into these holes. A window in the bottom plate allows for the application of heat to the device evaporator section. (b) A top polycarbonate plate (with an observation window) is used to mechanically seal the package by applying pressure on the sandwiched μLHP device using screws.

The μLHP device, with two $1\ mm \times 1\ mm$ square holes on its bottom side, is aligned with the O-rings. A top polycarbonate plate, forced down with screws attached to both plates, sandwiches the μLHP device, and establishes a secure connection between the device fill holes and the steel tubing. Observation windows are also machined in the top and bottom plates for visual data collection and for heating/cooling of the device components. This packaging approach is a good way to enable the experimental testing of μLHP devices in the lab. The package is reusable and can be easily

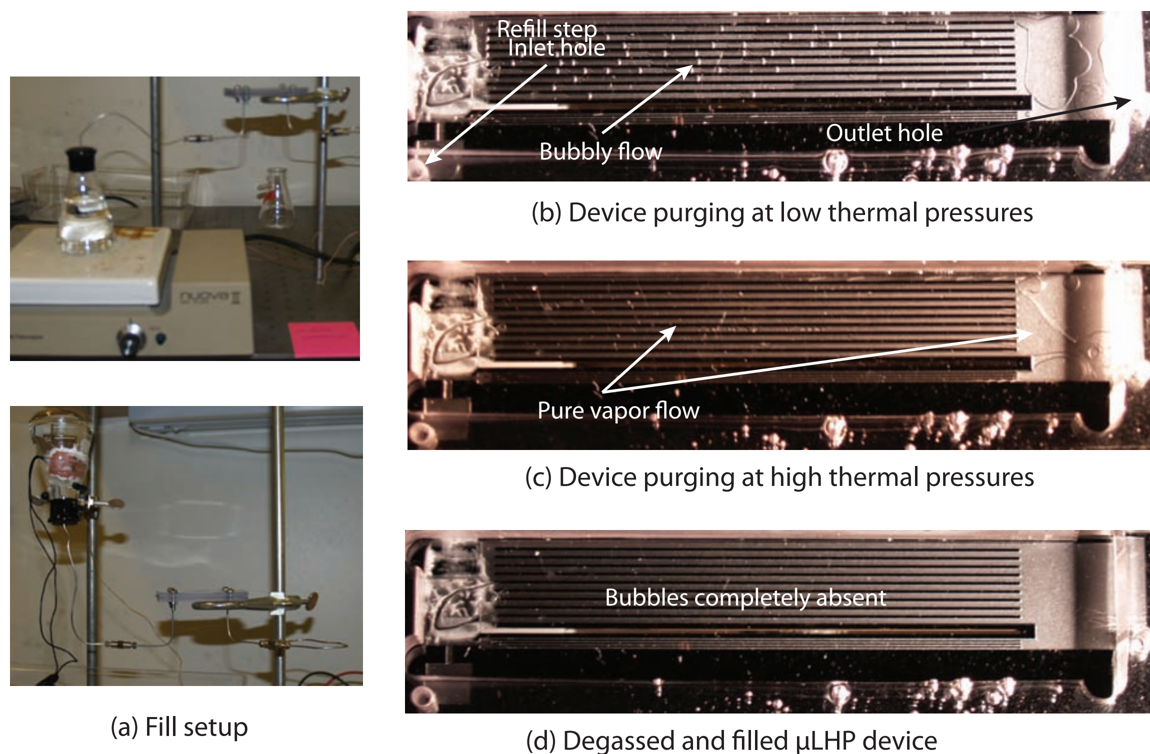

(a) Fill setup

(b) Device purging at low thermal pressures

(c) Device purging at high thermal pressures

(d) Degassed and filled µLHP device

Figure 6.5: Results for the packaging method I: (a) Implementation of the μLHP filling setup using the mechanically sealed plastic packaging; (b) Two phase flow is observed in the device during the initial stages of thermal-flux purging of the system (step 1); (c) With rise in the system temperature and pressure, pure vapor flow is observed in the device; (d) After the completion of the thermal-flux refilling step (step 2), no vapor bubbles are observed inside the device.

assembled/disassembled to accommodate different device prototypes, with the only limitation being size and placement of fill holes on the devices.

In Figure 6.5 can be seen the degassing and filling results obtained using the mechanically sealed plastic packaging (Method I). During the thermal-flux purging step (step 1), water in the flask was boiled and the vapor forced through the device. During the initial stages of this process, a two-phase flow was observed in the device (see Figure 6.5b). This happened because the vapor, as it traveled from the hot flask to the device, partially condensed in the steel tubing. As the temperature and pressure in the flask was further increased, pure vapor flow was observed in the device (see Figure 6.5c). During this process, however, parts of the device still remained occupied with water due to the large capillary forces in the device. But this water, hopefully, is already degassed due to its high temperature. In Figure 6.5d we see that the device got completely filled with water after the thermal-flux refilling step (step 2), and no bubbles were observed in any part of the device. This proves that the thermal-flux technique is successful in completely removing all non-condensible and

dissolved gases, both from the external fluid reservoir as well as the μLHP device. As the external fluid reservoir is cooled down to room temperature, over several days, small air bubbles begin to enter the reservoir through the steel tubing. This indicates that some part of the system, either the compression-fitted microtubing connections or the μLHP package itself, is leaking air into the system.

6.3.2 Method II: Aluminum Double Compression Fitting Assembly (DCFA) employing Solder connections

In Figure 6.6 is shown a different packaging approach that relies on a double compression fitting technique for the relative mechanical positioning of the μLHP device and the metal tubing, while employing solder or epoxy-based sealing solutions to create a hermetic connection between them. The package is machined out of three different aluminum blocks, which are connected to each other with the help of screws. The μLHP device is fixed in place by sandwiching it between the middle and the bottom blocks. The top and the middle blocks grip the 1/4 inch-OD inlet and outlet copper tubing, thus helping to position it over the device fill holes. They also provide mechanical protection for the chip-tube connections by neutralizing any external system stresses that can migrate through the stiff copper tubing. The connection between the tubing and the μLHP fill-holes can be established either by using a high-temperature-compatible epoxy paste, or by soldering the copper tube to a thin metal film that has been sputtered onto the device. The DCFA package is entirely reusable and, unlike in the previous approach, the positioning of fill holes on the device is not critical, due to the available flexibility in positioning of copper tubing. Some manual labor, however, is expended in shaping the copper tubing, to interface it correctly with the device fill holes. Moreover, this has to be done for every new device that is to be filled and tested.

As is illustrated in Figure 6.7, the DCFA packaging (Method II) needs some more work before it can be successfully implemented for the filling setup. Although the epoxy sealing method showed no signs of leakage during the thermal-flux purging step, no flow was observed through the μLHP prototype due to a device design flaw, leading to the possible blockage of the microchannels in the device. The solder-based connection, implemented by sputtering a gold layer on the device, underwent failure at high system pressures, as shown in Figure 6.7b. Soldering experiments need to be conducted to characterize the sputtered metal thin film requirements and the allowable soldering temperatures.

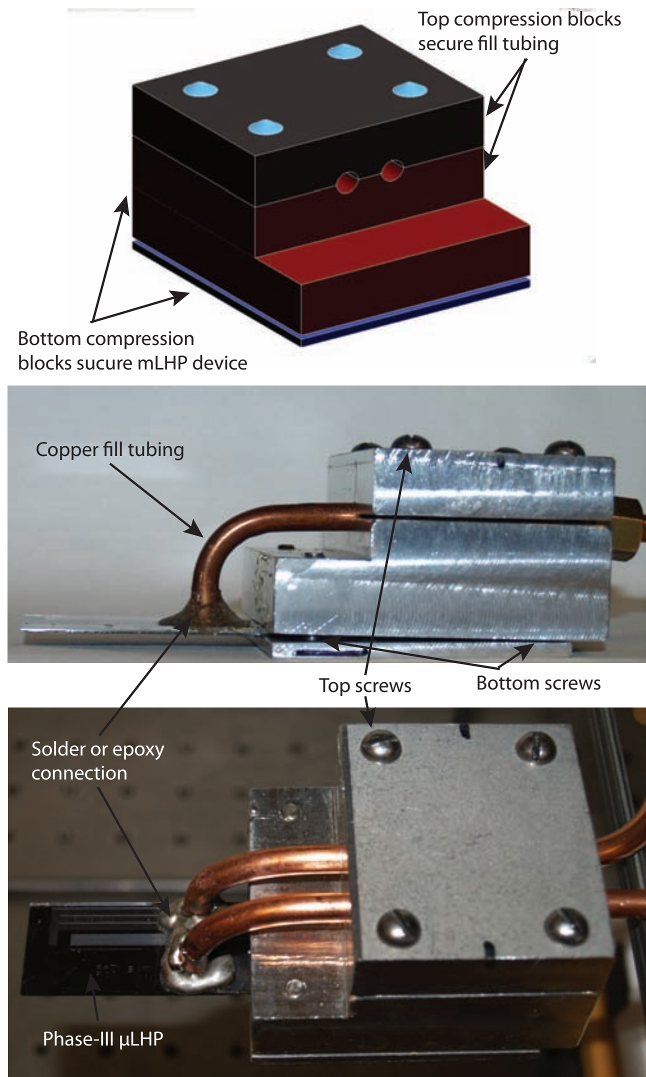

Figure 6.6: Aluminum double compression fitting assembly (DCFA) packaging (Method II): Copper tubing is mechanically placed on top of the μLHP fill holes using a machined aluminum setup. The tubing can be either epoxied or soldered onto the device. In the latter case, a thin metal film has to be deposited on the wafer.

6.3.3 Method III: Cold-Welded Plastic Package with Interference-fitted Microtubing

In Figure 6.8 is shown a packaging approach that was implemented to create compact, standalone packaged μLHP devices. Only a single plastic base is required, which can be machined according to the geometric peculiarities of a device prototype. The plastic base has machined cavities, leading to interference fitted 1/16 inch-OD

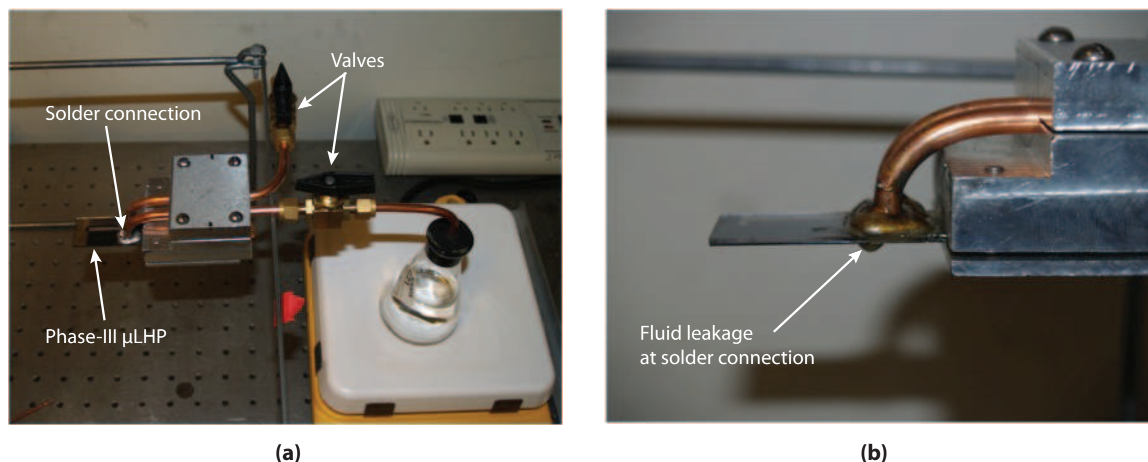

Figure 6.7: Results for the packaging method II: (a) Implementation of the μLHP filling setup using the DCFA packaging; (b) The solder connections get compromised and leak water under high pressure, indicating the need for improving tube-to-chip soldering techniques.

copper microtubing. These inlet and outlet filling cavities are meant to align with smaller fill-holes etched into the μLHP device. Separate cavities are also machined in the plastic base to provide for conductive heating of the evaporator section and convective liquid cooling of the condenser section of the μLHP device. JB-Weld epoxy paste is first spread around the cavities on the plastic base, whose surface has been roughened to improve bond strength. The μLHP device is now placed on top of the plastic base—making sure the device fill holes align with the corresponding base cavities—and is pressed slightly. Some more epoxy is applied at the device edges to improve the mechanical strength of the bond. The epoxy is allowed to cure for 24 hours at room temperature. This packaging approach is not reusable but allows for the simultaneous preparation of multiple packaged μLHP prototypes for filling and testing.

In Figure 6.9 can be seen the performance of the cold-welded plastic packaging (Method III) under the high temperatures and pressures encountered during the thermal-flux vapor purging process. The packaging showed good integrity under moderately high purge pressures, and vapor flow was observed through the device. After continuous two hours of operation, and upon a further increase in the external reservoir temperature, some water leakage was observed near the inlet filling hole (see Figure 6.9b). This area was already a weak point: the inlet cavity in the machined base was exposed around the edge of the device, and had been plugged with excess epoxy paste at this point. Additional epoxy paste was reapplied in this region and allowed to cure. But the new joint failed again, with the cured epoxy ultimately delaminating from the surface of the wafer. It seems that the temperature limit of the epoxy (400 ^oC) is severely limited by the latent heat of condensation of the incoming

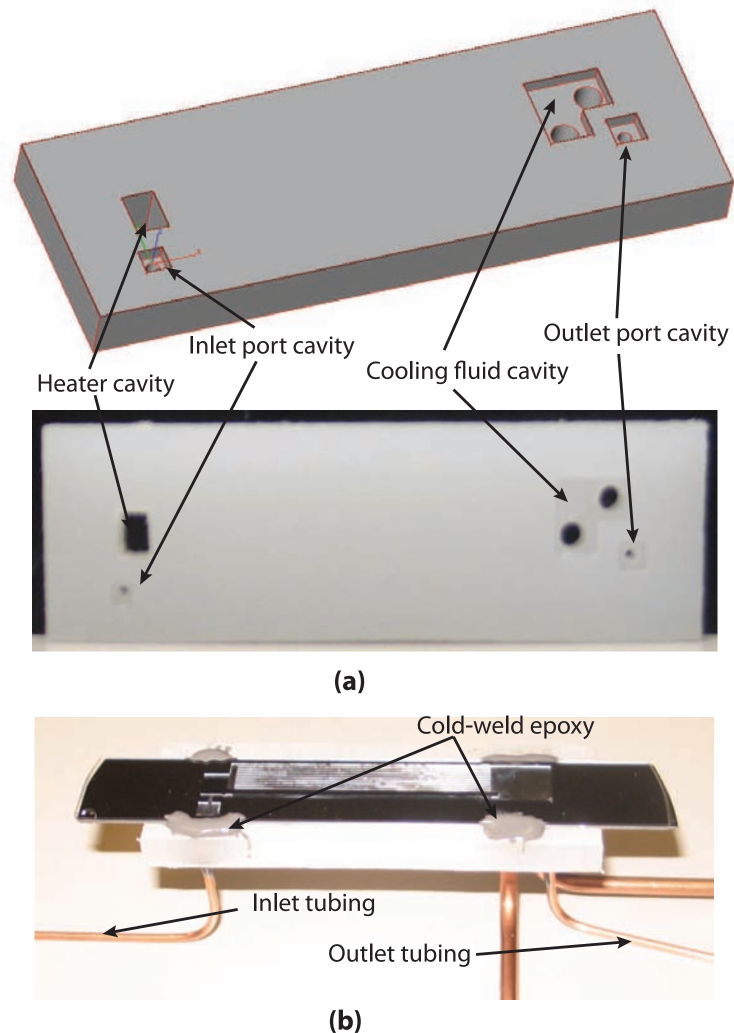

Figure 6.8: Cold-welded plastic packaging (Method III): (a) A base is machined out of plastic, with cavities that can interface with the μLHP fill holes. The cavities lead to smaller holes, which are interference-fitted with copper microtubing. (b) A cold-weld epoxy is spread around the cavities, and the μLHP device is placed on top of the plastic base, making sure the device fill holes align with the base cavities. More epoxy is used on the top to increase the mechanical strength of the package.

steam.

6.4 A Standardized Packaging Solution

Using the cumulative knowledge obtained from the preliminary packaging approaches discussed above, a standardized packaging solution was developed for the purpose of removing non-condensible gases from arbitrarily shaped μLHP devices, and

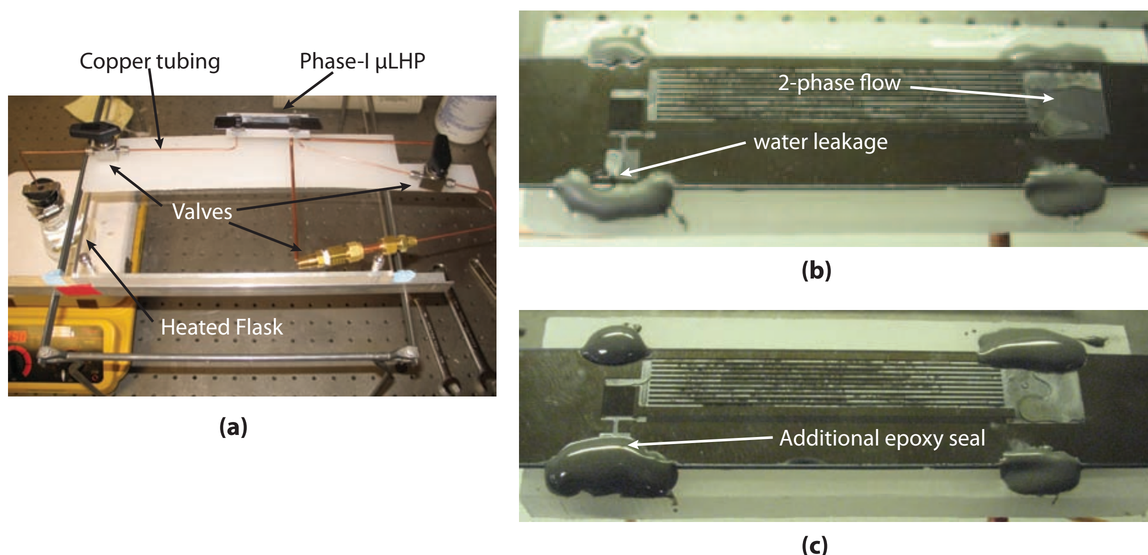

Figure 6.9: Results for the packaging method III: (a) Implementation of μLHP filling setup using the cold-welded plastic packaging; (b) At low purge pressures, two-phase flow is observed through the device without any leaking; but at higher pressures, the epoxy seal is compromised at the inlet port by the superheated steam; (c) Additional high-temperature epoxy, employed to plug the possible leak, is also found to delaminate from the wafer surface.

filling them with a degassed working fluid. The details of this packaging approach are shown in Figure 6.10. The schematic in Figure 6.10(a) shows the top view of the package as well as a cross-sectional view through the middle of the package. The objective is to establish a leak-proof connection between the μLHP device fill-holes and the copper microtubing, which supplies liquid to the device from an external fluid reservoir. For this purpose, the fill-holes in the μLHP device are first interfaced with cavities that are machined in a piece of metal or high temperature plastic (top plate). This is done by sandwiching the device between two plates, where the top plate has the cavities that align with the device fill holes. As was discussed in section 5.2.1, the placement of the fill-holes in the μLHP device is standardized to allow this one standardized package to be used for the degassing and filling of μLHP devices with different individual topologies.

A thin silicone gasket is used between the top plate and the μLHP device to avoid leakage and, additionally, to avoid fracturing the brittle silicon wafer. The plates are compressed together using two metal bolts. Two holes are drilled through the top packaging plate in order to connect the fluid cavities to the inlet and outlet copper tubing. For a package machined out of high temperature plastic, the copper tubing can be simply interference fitted into the drilled holes, by keeping the hole diameter slightly smaller than the tube outer diameter. For a package machined out of metal (soft stainless steel is best due to its strength and corrosion resistance), the copper

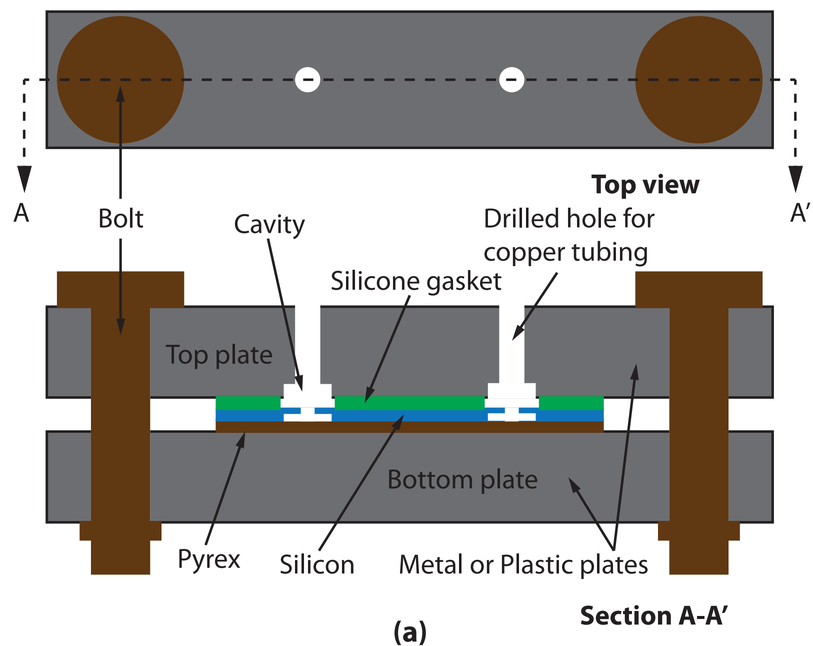

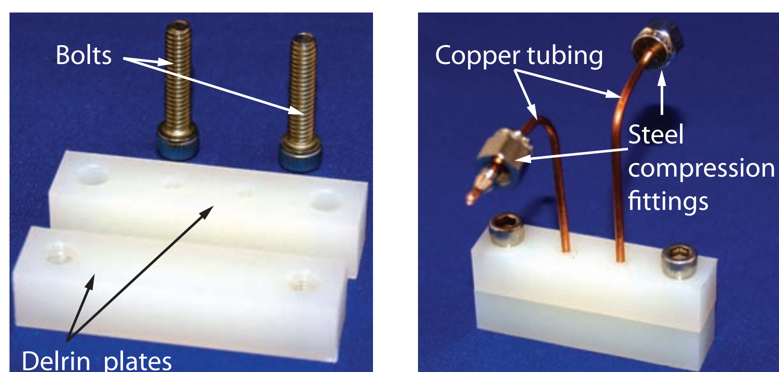

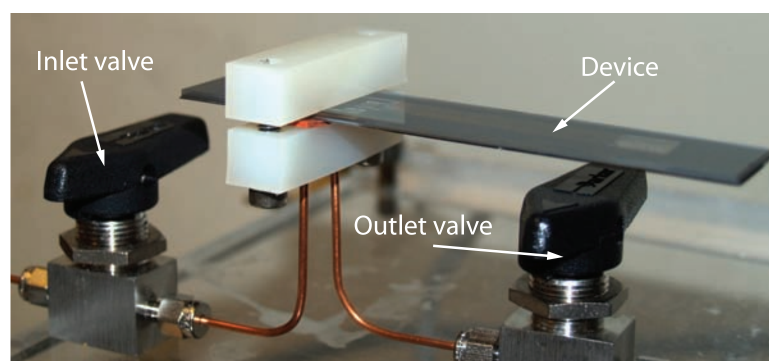

Figure 6.10: A standardized packaging solution for degassing and liquid charging of arbitrarily spaced μLHP devices: (a) A schematic of the packaging approach; (b) A picture of the different components of the package; (c) A picture of the packaged phase-II μLHP device, with inlet and outlet copper tubing connected to steel values for controlling fluid flow into and out of the device.

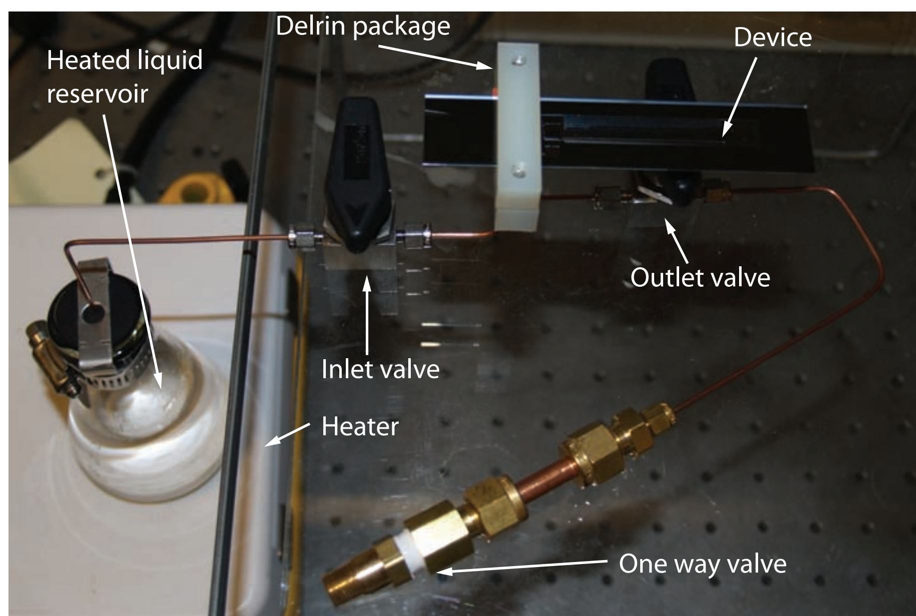

(a)

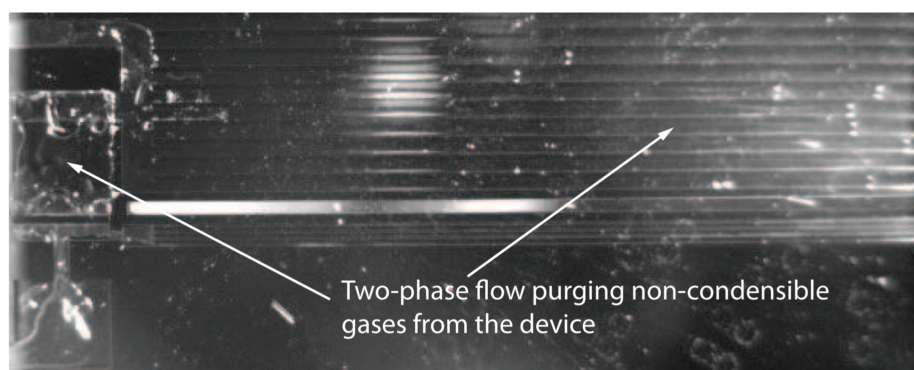

(b)

Figure 6.11: Device degassing and fluid-charging results for the standardized packaging approach: (a) A picture of the degassing and filling setup; (b) A high speed image showing the movement of two-phase fluid (water) through the device during the thermal-flux purging process.

tubing is inserted into the drilled holes and a high-temperature-compatible epoxy (JB-Weld was used here) is applied around the region where the tubing enters the holes. Note that the material used for the plates has to be high temperature-compatible to withstand the effect of superheated steam that flows through the package during the thermal flux purging and filling process. Delrin (a high temperature plastic) and steel were found to work well for this purpose.

Figure 6.10(b) shows pictures of the individual components as well as the assem-

bled packaging system machined out of Delrin. Figure 6.11(c) shows the phase-II μLHP device packaged inside this standardized packaging system. The inlet and outlet copper tubing is connected to steel ball valves. Fluid flow to and from the μLHP device can be controlled by turning these valves on and off. In this arrangement, the fluid in the copper tubing between the valves and the package forms a part of the μLHP system volume. As we will see in chapter 7, this can affect the behavior of the μLHP device during experimental testing. In the next section, we will also explore a technique that can allow for the sealing of the μLHP fill-holes, after the device has been degassed and filled with liquid using this packaging approach.

The standardized packaging approach worked very well during the device degassing and filling process. During the high temperature purging of the μLHP device by the two-phase working fluid (water), no fluid leakage was observed from any part of the package. In Figure 6.11 is shown the application of the standardized package for the μLHP degassing and filling process. Figure 6.11(a) shows the overall experimental setup. Initially, water boiled in a reservoir is circulated through the device. During this step, both the inlet and outlet steel valves are open. Note that a third one-way valve is used at the exit point of the outlet copper tubing, to prevent any intrusion of ambient air into the system. Figure 6.11(b) shows a high-speed image of the two-phase fluid flow inside the μLHP device. This flow helps to purge noncondensible gases from the device by convection. However, areas farther away from the fill-holes (such as the condenser) should also be heated slightly to purge the liquid condensed in these areas. After the purging step is complete, the outlet steel valve is closed. With the inlet valve open, fluid continues to move into the μLHP device in the form of vapor, which condenses to form liquid once it reaches the device. In this way, the μLHP device fills completely with liquid within a few seconds after the outlet valve is closed. This is no need to invert the liquid reservoir (as was done in previous filling procedures), since the thermally-induced pressure gradient helps to move the liquid from the reservoir into the device.

6.5 Hermetic Sealing of Device Prototypes

6.5.1 Noninvasive Hermetic Sealing Process

The μLHP hermetic sealing approach has to be noninvasive in order for it to be compatible with the thermal-flux filling system. *Induction heating* is one of the few available techniques that allow noninvasive localized energy transfer to the point of application.

In Figure 6.12 is shown an approach, based on induction heating, to hermetically seal degassed water inside the μLHP device after the completion of the degassing and filling process. A metal thin-film is first patterned around the device fill-holes to act as a wetting agent for molten solder (Figure 6.12(a)). A donut-shaped preformed

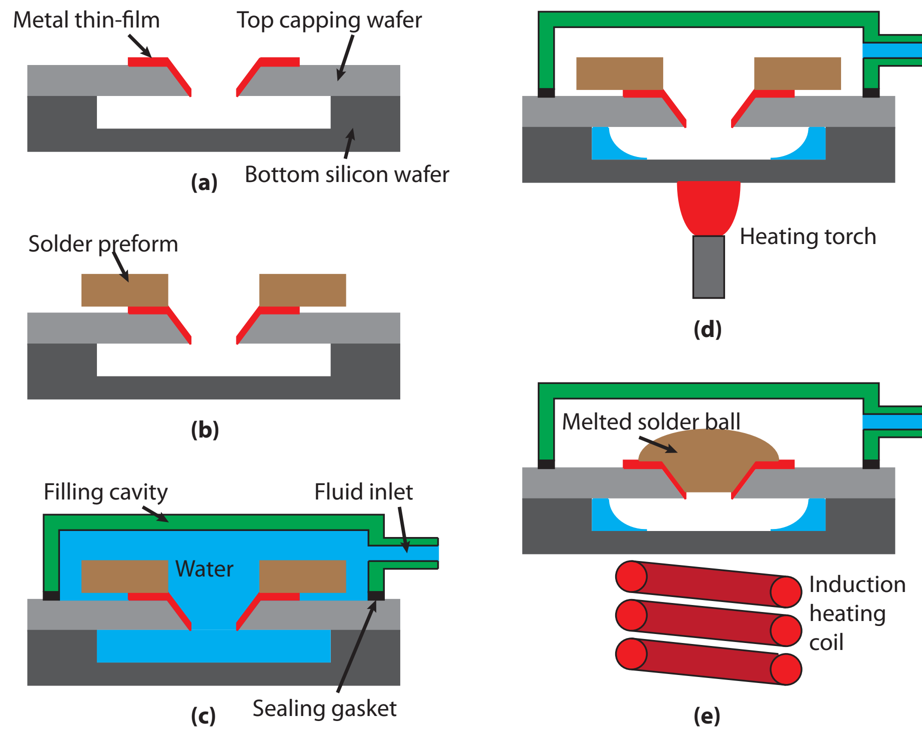

Figure 6.12: A hermetic sealing approach for sealing the μLHP device during the high-temperature degassing and fluid-filling process: (a) Pattern metal thin-film; (b) Place preformed solder ball; (c) Attach gasket-sealed filling-cavity, and degas and fill the device with water; (d) Boil off water from the vicinity of the fill-hole; (e) Inductively melt the solder to seal the hole.

solder piece is then placed around the fill-hole and heated just enough to attach it to the metal film (Figure 6.12(b)); The working concept is to provide a hole through the solder for the incoming fluid. A gasket-sealed filling-cavity, connected to the external filling setup, is placed around the fill-hole, and the device is degassed and filled with water (Figure 6.12(c)). After the filling process is complete, a heating torch is used to boil off the water from the vicinity of the fill-holes (Figure 6.12(d)). An induction heating coil, placed under the fill hole, is used to generate eddy currents inside the patterned magnetic thin-film. This heats up the adjacent solder, which melts onto the metal thin-film, thus sealing the fill-hole.

6.5.2 Experimental Verification

In order to test the inductive sealing process, 1 $mm \times 1$ mm pyramidal fill-hole samples were fabricated on a silicon wafer using the fabrication process flow shown in Figure 6.13(a).

A 2 μm thick silicon oxide layer was first deposited on both sides of the <100> silicon wafer using low pressure chemical vapor deposition (LPCVD). The top oxide

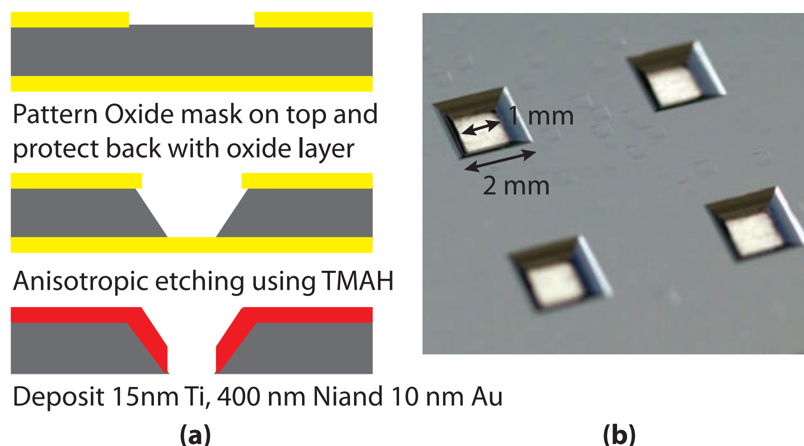

Figure 6.13: Fabrication of holes in a silicon wafer for testing the inductive-soldering approach: (a) Fabrication process flow; (b) Wet-etched holes.

was patterned using a photoresist mask and plasma dry-etching. Using this oxide layer as an etch mask, the silicon wafer was wet-etched using TMAH (Tetra methyl ammonium hydroxide), while the backside oxide protected the other side of the wafer. The following metals were then deposited using e-beam evaporation to form an adhesion layer for the solder preform: 15 nm Ti, 400 nm Ni, and 10 nm Au. Titanium provides an adhesion layer to the silicon substrate, and the magnetic properties of the thicker nickel layer allow for localized induction heating in the direct vicinity of the fill-hole. The thin gold layer provides an oxidation barrier for the nickel and readily dissolves into the solder upon bonding. In Figure 6.13(b) can be seen the fabricated fill-hole samples, which were subsequently diced for the experiments.

Induction Heating Experimental Setup

Experiments were performed to seal the fill-hole samples by inductively melting donut-shaped solder pieces. The induction heating assembly is shown in Figure 6.14(a). It consists of an internally-water-cooled hollow metal coil connected to a high voltage 11.7 MHz AC power source. The time-varying magnetic field generated inside the coil heats magnetic materials placed next to the coil by inducing eddy currents in them. The magnetic coil is placed inside a metal insulation box for protection against the high-energy fields generated by it.

Figure 6.14(b) details the method for preparing the solder-on-hole test sample. A small solder piece, manually shaped into a donut and applied with some solder flux, is placed around the fill-hole on the test sample. This sample is then placed, using a wooden holder, under the induction heating coil for heating.

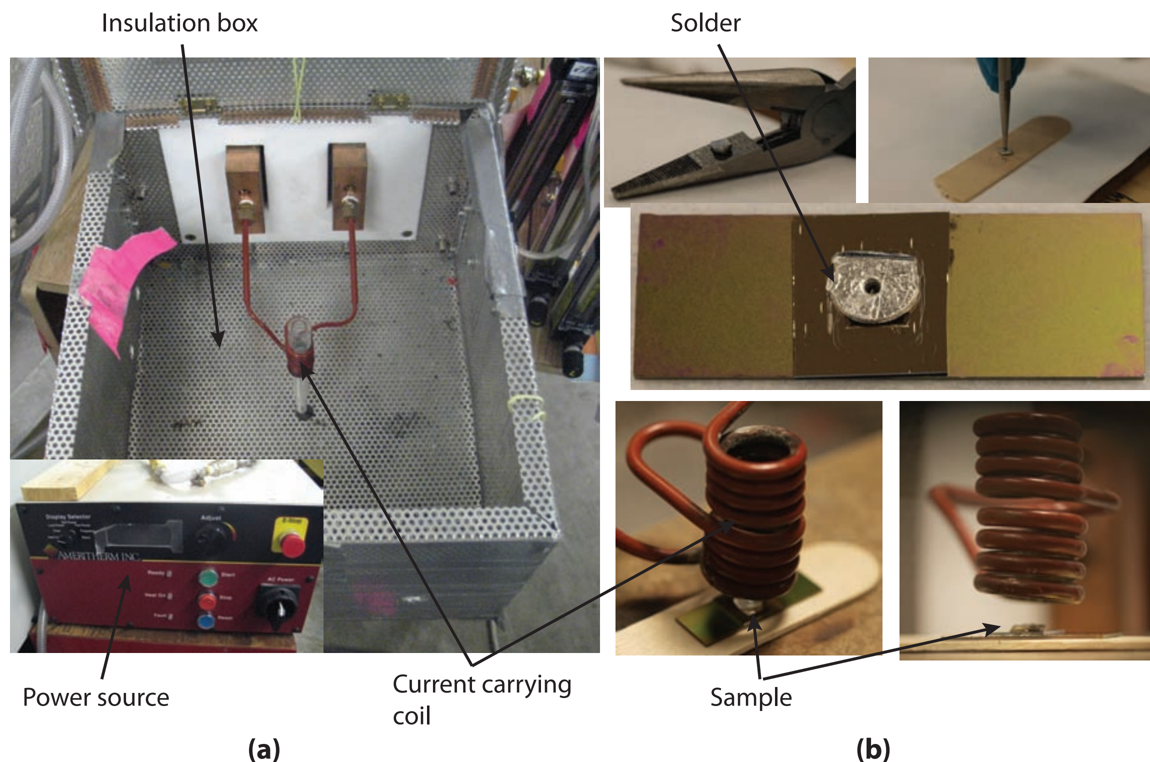

Figure 6.14: Experimental setup for implementing inductively-heated solder-sealing of holes in a silicon substrate: (a) Induction heating apparatus; (b) Solder-on-hole sample preparation.

Results

Solder-sealing experiments were conducted on a number of test samples, using different preformed solder masses and induction heating times. Figure 6.15 shows the test samples before heating and the front/back of these samples after induction heating. Also given is the mass of the solder piece used, the induction heating time, and the power setting on the induction heater for each case.

A lead-free silver bearing solder ($Sn_{96}Ag_4$), with a melting point of 221 ^oC, was employed for the experiments. The power to the induction-heating coil was kept constant at 400 W, an optimum value for melting the solder in a controlled manner. When no solder flux was used, very little spreading of the solder was observed even after a long heating time (Figure 6.15(a)). Further, the hole was not sealed and the solder ball came off the sample with a small applied force. For the rest of the cases, a water-soluble paste flux was employed. Using a solder mass of 0.06 g and a heating time of 2.9 sec, the hole was found to seal properly (Figure 6.15(b)); However, heating a similar sample (0.09 g) for just 0.4 $secs$ more resulted in the solder spreading away from the hole (Figure 6.15(c)).

A wider allowable heating time-window was obtained with the use of a larger

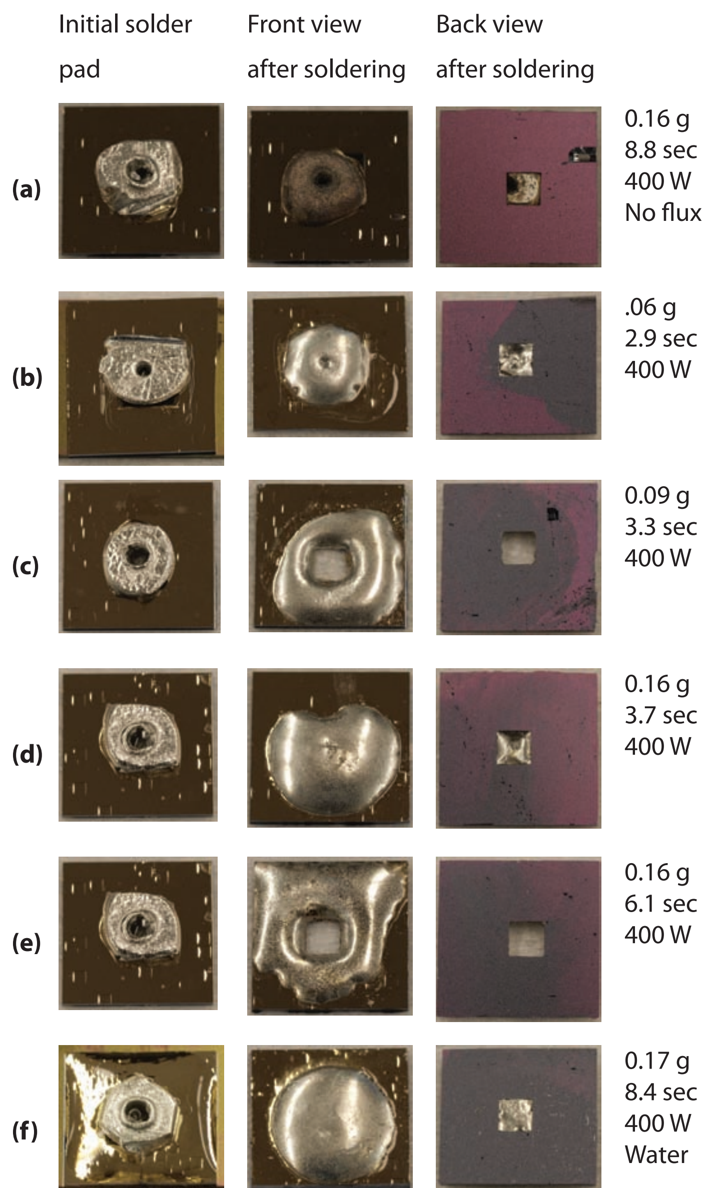

Figure 6.15: Experimental results demonstrating inductively-heated solder sealing of holes: The key parameters are the initial mass of the solder preform and the induction heating time. (a) Soldering without flux is unsuccessful; (b-c) Low solder mass can be unstable; (d-e) Larger (optimum) solder mass ensures good sealing in a wider time window; (f) Soldering in water is successful.

initial solder mass (0.16 *g*). In Figure 6.15(d), the solder was heated just long enough (3.7 *sec*) for the solder ball to form, which yielded an excellent seal. A similar sample (Figure 6.15(e)) was again heated—this time for a time (6.1 *sec*) long enough to make the solder spread away from the hole. Comparing the two heating times, we see that by using a larger solder mass, a larger heating time-window of 2.4 *sec* was achieved,

during which the solder melted but did not spread away from the hole. Induction heating of the solder was also carried out in the presence of some water on the fill-hole sample (Figure 6.15(f)). Although it took a larger heating time, successful sealing of the fill-hole was demonstrated.

Discussion

The above results verify the efficacy of the induction heating approach for sealing a μLHP device fill-hole. Under the right circumstances, the solder material melts, by absorbing heat from the magnetic thin-film, to completely cover the fill-hole. However, if we continue to heat it further, the molten solder spreads out further away from the hole, thereby leaving it exposed and unsealed. This happens because of the fact that the metal thin-film acts as a hydrophilic surface for the molten solder, and the free energy of the system is reduced as more of it is wetted.

This leads us to the conclusion that time is an important factor in this process. As soon as the solder melts, the hole in the donut-shaped solder closes very quickly due to its inherent surface tension. The fill-hole gets exposed as the meniscus of the molten solder starts traveling outwards, thereby sucking out the solder from above the hole, which does not provide a favorable wetting surface unlike the rest of the sample. Given that the meniscus travels with a finite speed, using a larger initial solder mass provides a larger solder mass above the hole, thereby increasing the time it takes for the hole to get exposed.

Sealing a wet fill-hole takes a longer time due to the fact that energy is expended in evaporating the water before the solder (with a melting point much higher than $100\ ^oC$) actually melts.

6.6 Conclusions

A two-port thermal flux method was implemented to remove non-condensible gases from a planar microscale loop heat pipe (μLHP), and to charge this device with a degassed working fluid, in order to make it operational. Due to the small device volumes involved, this method has several advantages over conventional vacuum pump based evacuation techniques. In this method, an external fluid reservoir is connected to the μLHP device, and thermally generated pressure gradients are used to purge the device with the working fluid vapor. After the purge step is complete, the entire system is sealed, and the degassed liquid inside the hermetically sealed system is thermally leaked into the device. Three different preliminary, high-temperature-compatible device packaging techniques were implemented to interface the μLHP device with the external filling setup. The first approach, using O-rings to mechanically seal the device in a plastic package, proved highly effective in hermetically sealing the device during the filling operation, and helped demonstrate the effectiveness of the thermal-

flux method. Alternative soldering and epoxy based packaging approaches were also implemented, but these were found to be quite unreliable. Building on these results, a standardized device packaging solution was developed that is capable of degassing and filling all μLHP devices irrespective of their individual design topologies.

A noninvasive induction heating-based approach was also introduced for the purpose of hermetically sealing degassed liquid inside a microfluidic electronics cooling device. Inductively-heated soldering experiments conducted on fill-hole samples demonstrated the efficacy of this approach. Using an optimum initial solder mass, inductive heating of the sample within a given time window lead to a complete sealing of the fill-hole. Successful sealing of the fill-hole in the presence of water was also demonstrated. This noninvasive sealing technique can also enable the hermetic filling of a wide range of microfluidic devices where the presence of non-condensible gases is a concern.

Chapter 7

Experimental Testing of Devices

In this chapter are the details of the experiments that were conducted on the three in-plane-wicking micro loop heat pipe (μLHP) prototypes described in chapter 5. The aim of these experiments is to characterize the behavior of the working fluid in these devices under the application of a heat flux to the device evaporator section. As per the discussion in chapter 2, the desired device functionality involves the following key behaviors:

1. When heat is applied to the device evaporator section, the liquid in the wicking structure should evaporate to form vapor.
2. The vapor formed in the evaporator should travel, via the vapor transport channels, to the condenser section, where it condenses back to liquid.
3. The liquid transport channels and the compensation chamber should be able to continuously supply liquid to the wick for evaporation.

In the following sections, we will try to find out as to what extent each of the three μLHP prototypes satisfy the above criteria. This analysis will also help us in identifying the key device components and topologies that can enable the desired two-phase flow loop.

7.1 Phase-I μLHP Prototype

Thermal experiments were conducted to study the process of evaporation and two-phase fluid flow in the phase-I μLHP device. Using the thermal flux method, the device was first degassed to remove all non-condensible gases and then filled with degassed water (see section 6.3.1). A mechanically sealed plastic packaging was used for the purpose of degassing and liquid-charging of the device. During the experiments, heat flux was applied to the evaporator section of the device, to initiate phase change in the in-plane wick. The resulting movement of the liquid

and vapor phases of the working fluid was observed and analyzed to understand the dynamics of the entire system, as well as the thermodynamical behavior of the individual components of the device.

7.1.1 Experimental Setup

In Figure 7.1 is shown the experimental setup for studying the operation characteristics of the phase-I μLHP device. Figure 7.1(a) provides the overall schematic of the setup while Figure 7.1(b)-(d) highlight the actual details of the experimental setup.

The μLHP device was filled using the thermal flux method. The external fluid reservoir, which is connected to the inlet fill-port of the μLHP using steel tubing, is also part of the two-phase fluid system. However, for the latter half of the experiment, the external fluid reservoir was disconnected from the device. The steel tubing that is connected to the outlet fill-port is plugged at the free end to keep the air out. Note that the external fluid reservoir is kept at an elevated position compared to the μLHP, to provide a gravitational pressure head that helps the water remain in the device. In the next phase of experiments, we will see that the same effect can be achieved by heating the reservoir above room temperature.

The evaporator section of the μLHP (which is only 3.8 $mm \times 4$ mm) has to be locally heated for the experiment. Since the available ceramic heater was much larger in size, a machined aluminum block was used to interface the heater with the device evaporator. Note that the heated metal block is in contact with the Pyrex wafer side (top side) of the μLHP device. Although Pyrex ($k \approx 1.10$ W/mK at 298.15 K) is a much worse thermal conductor than silicon ($k = 148$ W/mK at 300 K), still the pattern of heat flow to the evaporator would be exactly the same if the heater were to be on the silicon side. The temperature drop across the Pyrex wafer, however, would be two orders of magnitude higher than in silicon, which means the heater would be at a higher temperature for the same amount of applied heat flux. The temperature of the aluminum block (which we will call the heater temperature) is measured using a K-type thermocouple connected to a data acquisition system.

In Figure 7.1(e), we can observe the formation of vapor in the initially-liquid-filled μLHP device as a result of the heat flux supplied by the heater. Although both vapor and liquid are transparent (thus making it difficult to distinguish between the two), the shape of the liquid-vapor meniscus in channels (convex on the liquid side) provides the necessary information. Note that it is not possible to introduce a coloring dye into the working fluid, as it would be left behind in the external fluid reservoir during the boiling process undertaken for purging and filling the device. It is essential to use clean, pure, de-ionized water so that no mineral precipitation occurs in the evaporator section. Such deposits could clog the porous wick. It was also impossible to capture the flow phenomena in the entire device using a single optical camera since, while the device is quite large (~ 5.5 cm long), its individual components are quite small.

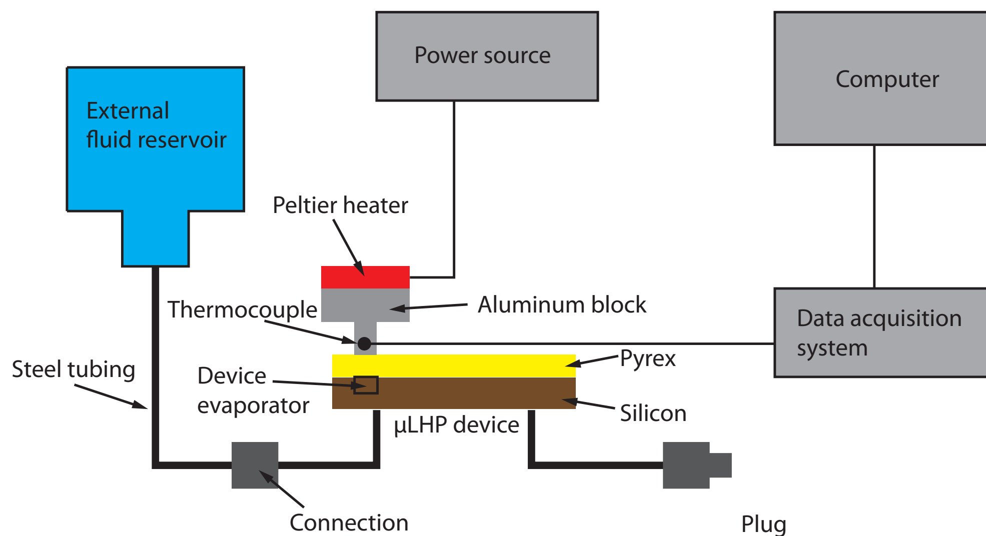

(a) A detailed schematic of the experimental setup

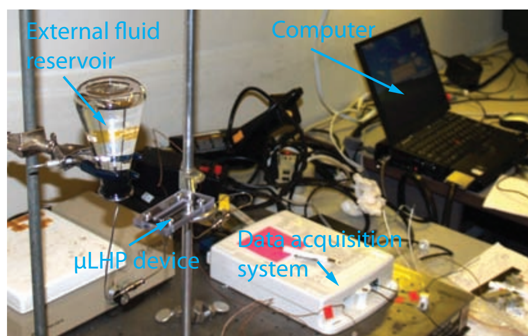

(b) Entire experimental setup

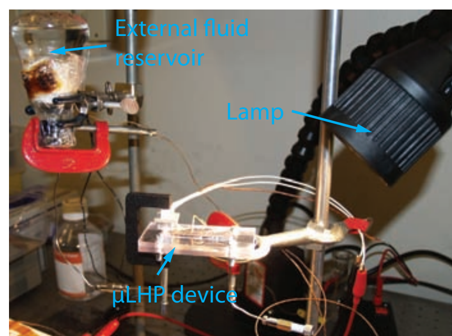

(c) Close-up view of the setup

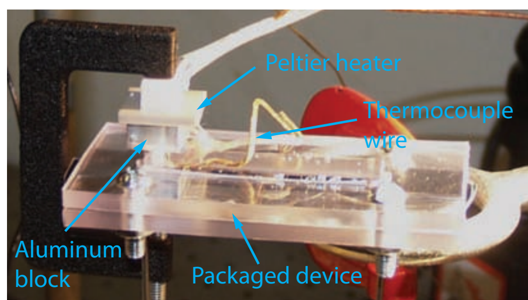

(d) Connection of heater and thermocouples to the µLHP device

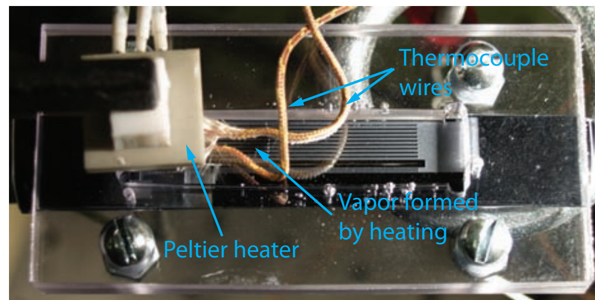

(e) Formation of vapor in the device as the heater is turned on

Figure 7.1: Experimental setup for the operational testing of the phase-I μLHP device. A ceramic heater is used to heat the evaporator section of the packaged and filled μLHP device, while thermocouples are used to track the temperature of the heater. The condenser section of the device is cooled by ambient natural convection.

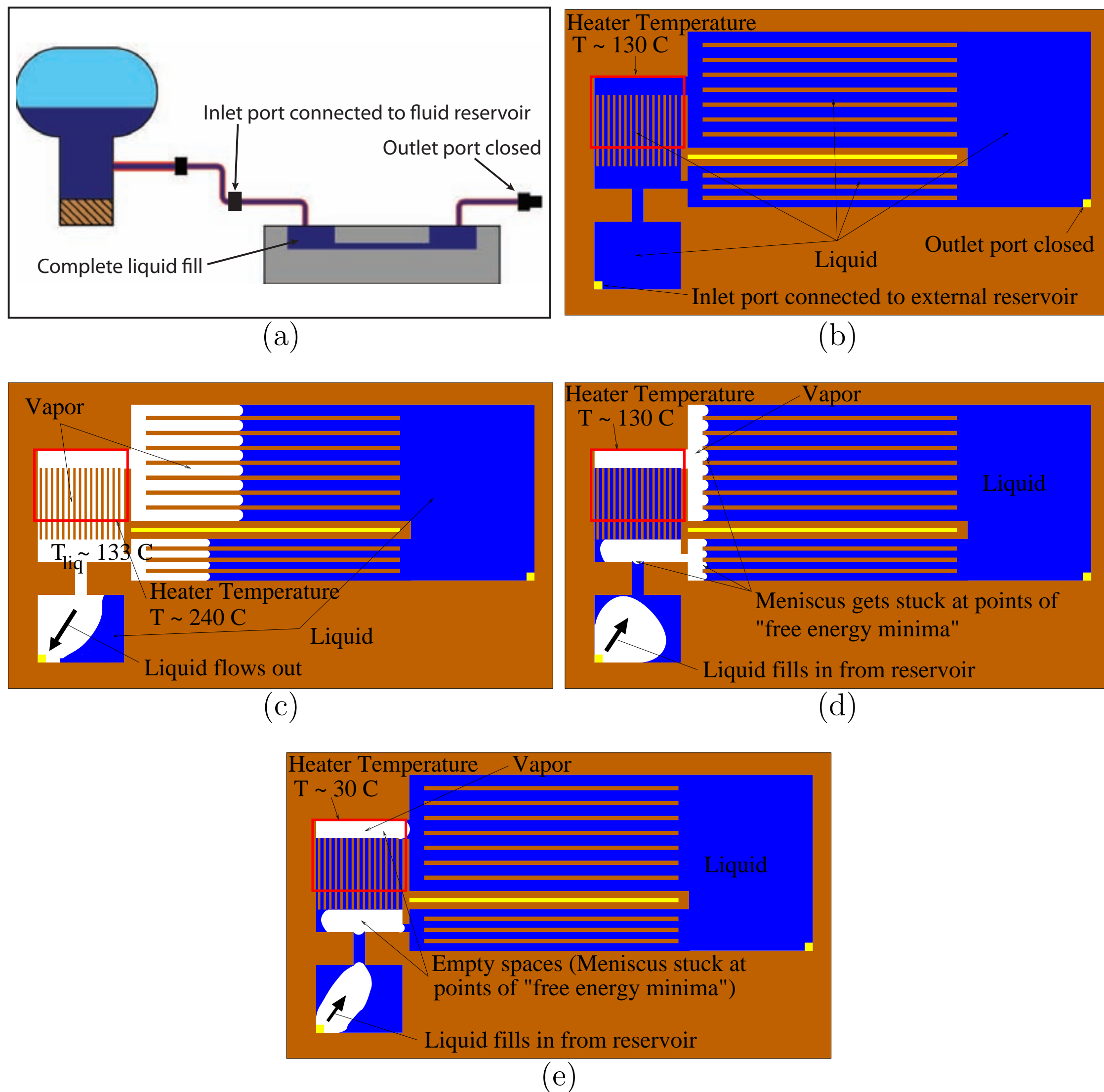

Figure 7.2: Liquid evaporation in the phase-I μLHP device connected to an external fluid reservoir (schematic representation of experimental observations): (a) Device completely filled with degassed water and connected to the external fluid reservoir via the inlet port; (b) Moderate heat-flux applied to the evaporator; (c) Larger heat-flux applied to the evaporator, expelling fluid from the device; (d) Fluid refilling the device as heater temperature is reduced; (e) Further cooling of the device.

Therefore, the distribution of liquid and vapor phases in the device during various stages of the experiment was observed visually and recorded schematically.

7.1.2 Experimental Observations

In Figure 7.2 is given a schematic representation of the device operational results obtained by heating the evaporator section of the phase-I μLHP, while its inlet fill-port

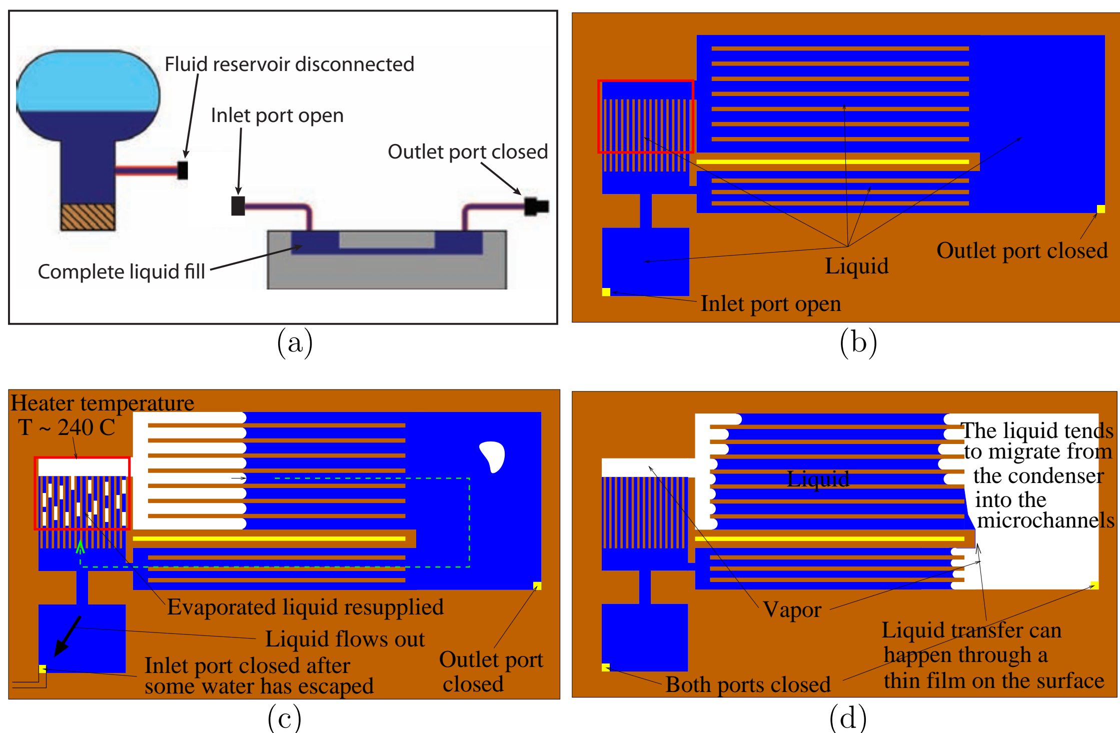

Figure 7.3: Liquid evaporation in the phase-I μLHP device disconnected from the external fluid reservoir (schematic representation of experimental observations): (a-b) External fluid reservoir disconnected from the inlet port (open to ambient) of device completely filled with degassed water; (c) Inlet port closed after partially expelling water from the device. Unsteady boiling observed in the heated evaporator; (d) Working fluid rearrangement after device has cooled to room temperature.

(and thus the compensation chamber) was connected to the external fluid reservoir. Initially, the device was completely filled with degassed water and the fluid reservoir contained a mixture of water and water vapor (Figure 7.2(a)). The device outlet fill-port was closed.

Now, power to the ceramic heater was switched on and increased gradually. It was observed that no phase change occurred in the device evaporator even when the heater temperature was increased to 130 ^oC (Figure 7.2(b)). The power to the ceramic heater was gradually increased until, at a heater temperature of approximately 240 ^oC, there was a complete dry out in the in-plane wicking structure (Figure 7.2(c)). Water in the wick, and in parts of the liquid and vapor channels adjacent to it, suddenly evaporated and the liquid in these regions was pushed out of the device, through the compensation chamber, and into the external fluid reservoir. Water remained in the condenser section as well as in parts of the liquid and vapor transport channels adjacent to it. As a result, no liquid-vapor flow loop was established in the device.

Next, the temperature of the ceramic heater was again reduced to 130 ^oC. This resulted in water from the external fluid reservoir flowing back into the device. The in-plane wick and the liquid and vapor microchannels got completely refilled with

water, but the connecting cavities were still occupied by vapor (Figure 7.2(d)). As the heater temperature was brought down close to room temperature, some more water entered the transport channels, but the evaporator cavities remained occupied with vapor (Figure 7.2(e)).

In the next phase of the experiment, the device was again filled with degassed water and subsequently the external fluid reservoir was disconnected from the device, and the outlet fill-port closed (Figure 7.2(a)-(b)). With the inlet fill-port open, the heater was turned on to expel some of the liquid from the device. Following this, the inlet fill-port was also closed. As the heater temperature was raised to 240 ^oC, extremely unsteady nucleate boiling was observed in the in-plane wick (Figure 7.2(c)). This involved the nucleation and sudden expansion of vapor bubbles in the in-plane-wick microchannels, leading to considerable back-flow fluctuations in the liquid transport microchannels. However, liquid supply to the wick, although intermittent, was maintained and no complete wick dry out was observed at any point. As the device was cooled back to room temperature, it was observed that the liquid from the condenser section moved into the vapor microchannels.

7.1.3 Analysis of Results

In the first half of the experiment (Figure 7.2), where the external fluid reservoir is connected to the μLHP device compensation chamber (Figure 7.2(a)), heating the evaporator section results in a complete dry out of the in-plane wick. Further, when the device is partially filled (Figure 7.3(c)) in the second half of the experiment (Figure 7.3), unsteady nucleate boiling is observed in the wick at a high superheat temperature. Both of these observations point to the fact that the phase-I μLHP in-plane wick design does not aid thin-film evaporation from the liquid-vapor meniscus, but only allows for nucleate boiling. This can be explained if we look at the phase-I in-plane wick design in Figure 5.1(b) of chapter 5. In this figure, we note that the 32 μm wide and 150 μm deep in-plane-wick microchannels are completely covered from the top by the capping Pyrex wafer. As a result, the liquid vapor meniscus can only form at the very end of the channels and not over the entire evaporator surface. Therefore, nucleate boiling is the only available mechanism by which phase change can occur in the wick microchannels. However, suppression of bubble nucleation and growth due to spatial confinement is a well known characteristic of narrow microchannels. Bubble growth in very narrow channels is only possible at large superheat temperatures. At these elevated temperatures, the bubbles grow very rapidly after nucleation, pushing out the surrounding liquid from the individual wick microchannels.

In the first case, where the compensation chamber provides an outlet to the external fluid reservoir (Figure 7.2(a)), the large pressure created by the nucleating bubbles pushes the liquid completely out of the wick. This happens because the vapor pressure of the partially-filled external fluid reservoir (where the liquid is at room temperature) is much lower than the vapor pressure of the superheated bubbles nucleating

in the wick. In a sense, the saturation pressure inside the μLHP device is controlled by the external fluid reservoir. Ignoring the presence of any non-condensible gases (NCGs) in the system, if the external reservoir is at room temperature (23 ^oC) then the saturation pressure inside the μLHP device should also be close to 23 ^oC. However, roughly accounting for the temperature drop across the Pyrex wafer, the liquid temperature inside the wick at the onset of nucleation (Figure 7.2(c)) was calculated to be approximately 133 ^oC. Several factors could be potentially responsible for this higher than expected value of the boiling superheat:

1. Microchannel capillary effects, which increase the saturation pressure of the liquid.
2. Suppression of bubble nucleation and growth due to spatial confinement in microchannels, which increases the required wall superheat for nucleate boiling.
3. Possible presence of NCGs in the system, which would increase the saturation pressure.
4. Error due to the imprecision of local temperature measurement.

The distribution of the liquid and vapor phases in Figure 7.2(c) is reflection of the thermodynamic state of the device. The region surrounding the heater must be at a temperature higher than the saturation temperature of the liquid in the device. The temperature drops going away from the heater—according to Fourier's law of conduction and due to thermal losses to the ambient—and should be below the saturation temperature in the liquid region. The fact that the liquid front in the transport channels moves closer to the wick with a reduction of the heater temperature (Figure 7.2(d)) is a confirmation of this argument. Note that the wick microchannels are replenished even when the heater is still at 130 ^oC (Figure 7.2(d)), which points to the substantial effect than capillary forces can have on the liquid saturation temperature. The capillary pressure gain in 32 μm wide and 150 μm deep wick microchannels is equal to

$$\Delta P_c = 2\sigma \cos\theta_c \left(\tfrac{1}{w} + \tfrac{1}{h}\right) = 101.4\ kPa \tag{7.1}$$

where

$$\sigma = 0.058\ N/m$$
$$\theta_c = 29^o$$
$$w = 32\ \mu m$$
$$h = 150\ \mu m$$

We can convert this increase in pressure to a corresponding increase in the saturation temperature of the liquid inside the wick microchannels. For an external fluid reservoir temperature of 23 ^oC, the saturation temperature of the liquid in the wick is

calculated to be approximately 100 ^oC. This would roughly match the experimental measurements if a temperature drop of 33 ^oC is assumed across the Pyrex wafer.

The experimental results in Figure 7.3 have to be analyzed slightly differently, since the external fluid reservoir is no longer connected to the μLHP device, which now acts as a constant volume closed system partially filled with liquid. Since fluid can no longer escape the device, increasing the system temperature leads to an increase in the saturation temperature of the fluid. We will see shortly as to how this affects the behavior of the flow-loop, but first note that since the device is now partially filled, vapor is present in the device even at room temperature (Figure 7.3(d)). The distribution of the liquid and vapor phases in the device at room temperature is a function of both the past history of this distribution as well as the capillary properties of the different device components. Smaller channels and cavities provide a larger surface area to volume ratio, which attracts liquids that like to wet that solid surface (hydrophilic). For example, the free energy of the system will be reduced if liquid from the condenser section (which is a large cavity) were to move into the smaller vapor microchannels (initially occupied by vapor). This is exactly what happens as the heater is switched off and the device cooled to room temperature (Figure 7.3(d)).

Now, let's return to Figure 7.3(c) and analyze why unsteady nucleate boiling is observed in the wick, as opposed to the complete wick dry out observed in Figure 7.2(c). As the heater temperature is increased, initially there should be small amounts of thin-film evaporation from the liquid-vapor menisci at the very end of the wick microchannels. However, this would be almost negligible and difficult to confirm, given the very small combined surface area of the menisci. As the heater temperature is further increased to 240 ^oC (which we previously noted is roughly equal to a wick liquid temperature of 133 ^oC), nucleate boiling is initiated in the wick. However, as soon as the vapor is generated, it increases the overall pressure of the constant-volume closed system. This results in an increase in the saturation pressure of the liquid, which suppresses further boiling and prevents a catastrophic dry out of the wick. The vapor bubbles that are generated in the wick microchannels push the liquid around them on both sides. However, since there is a large liquid inertial mass on the side of the compensation chamber and the liquid microchannels, these bubbles tend to escape to the vapor cavity attached to the vapor microchannels. This process is repeated in all the individual wick microchannels, which are essentially separate from each other. This results in an unsteady boiling process in the entire wick. Whenever an individual wick microchannel dries out due to bubble expansion, it absorbs more liquid from the liquid supply cavity connected to the compensation chamber and the liquid microchannels. The vapor diffuses to and condenses at the liquid-vapor interface in the vapor microchannels, which is at a relatively lower temperature compared to the wick.

In this way, the imbalance in the distribution of liquid and vapor phases that is created by the capillary properties of the individual μLHP components helps in the establishment of a two-phase fluid flow loop in the device. It could be argued that

the initial presence of water in the liquid supply cavity as well as the compensation chamber plays a critical role in ensuring constant liquid supply to the wick. This liquid, once present, is prevented from evaporating due to the proportional effect of the heater temperature on the liquid saturation temperature in the device.

7.2 Phase-II μLHP Prototype

The design and fabrication of the phase-II μLHP device was discussed in section 5.2. Among other things, this μLHP prototype incorporates an improved in-plane wick topology to facilitate the process of thin-film evaporation in the wicking structure. This section presents an experimental study of evaporation and two-phase fluid transport in the phase-II μLHP device. The device was first packaged and filled with a degassed working fluid following the procedure discussed in section 6.4. Some of the liquid was then thermally purged from the device, following which it was disconnected from the external fluid reservoir by closing the inlet tubing valve. The device was then thermally tested by applying heat flux to the evaporator section.

7.2.1 Experimental Setup

In Figure 7.6 is shown a schematic and picture of the experimental setup used for testing the phase-II μLHP device. The device packaging consists of the μLHP inlet and outlet fill-ports connected to 1/16-inch inlet and outlet copper tubing, respectively, using a mechanically-clamped high-temperature-plastic packaging. The copper tubes are closed at their other ends by steel ball values. The copper tubes are essentially a part of the μLHP system, since liquid in the μLHP device can flow to and from the space in the tubes. The evaporator section of the device is heated by a hot air gun that is placed right underneath the evaporator, on the silicon side of the device.

The temperature of the hot air gun can be set to a fixed value, which is maintained by an inbuilt thermostat. The thermostat periodically turns the heating element ON and OFF in order to stay close to the particular set temperature. For these experiments, the temperature of the air jet was set at 300 ^oC. This was set by trial and error to make sure that the resultant heat flux applied to the evaporator results in phase change in the wick. The actual surface temperature of the evaporator was not measured for this experiment. As we will see in the next section, there was an unexpected result of this particular approach to heat flux application. Due to the periodic ON/OFF behavior of the hot air gun thermostat, the heat flux seen by the evaporator section was also periodic.

A high speed optical camera was used to record real-time images of evaporation and liquid/vapor flow in the device. The camera was focused on the area around the evaporator, since most of the physical phenomena of interest occur in this region. Due

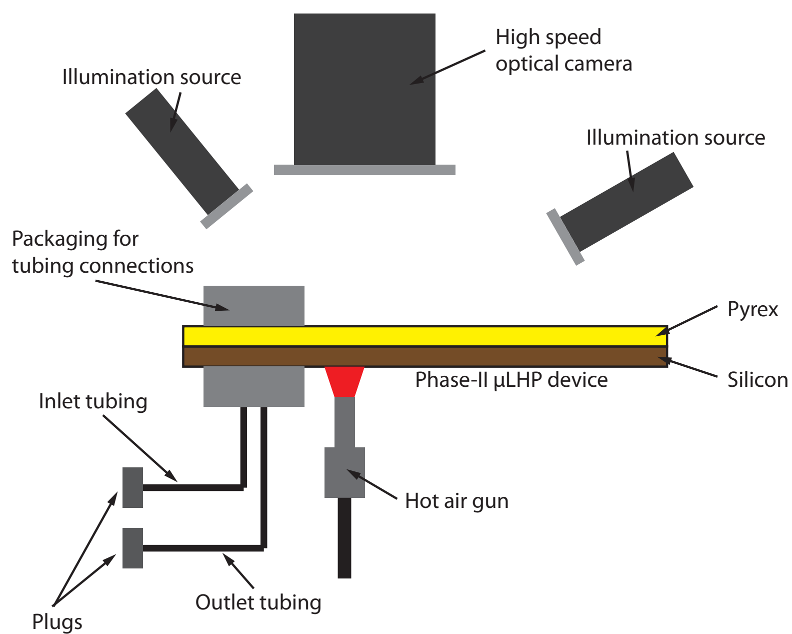

(a) Schematic of the experimental setup

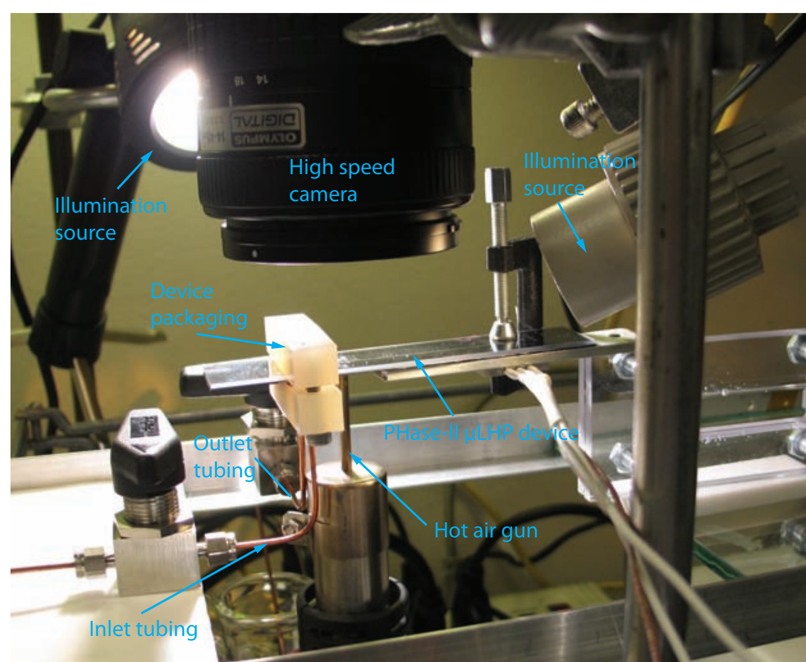

(b) Picture of the experimental setup

Figure 7.4: Experimental setup for the operational testing of the phase-II μLHP device. A hot air gun is used to heat the evaporator section of the packaged and partially filled μLHP device, while the condenser section of the device is cooled by ambient natural convection. A high speed camera is used to observe the evaporator section of the device, which is illuminated by multiple light sources.

to the very small exposure time of the camera, multiple light sources from different directions were used to illuminate the transparent Pyrex side of the μLHP.

7.2.2 Experimental Observations

Figure 7.5 shows the phase change processes that occur in the evaporator section of the partially filled phase-II μLHP device, first as the input heat flux is increased and then as it is decreased. As mentioned above, the heat flux increases when the thermostat of the hot air gun turns ON and decreases when it turns OFF.

In the first picture of the device (Figure 7.5(a)), which is taken at time $t = 0$, we can see how evaporation begins in the wick as the input flux to the evaporator is increased. Recall that in the phase-II μLHP design the silicon in-plane wick has a 200 μm deep Pyrex cavity above it (see section 5.2). First, the liquid in the Pyrex cavity evaporates due to the nucleation and growth of bubbles. Note that since the cavity is quite large, bubble nucleation and growth can happen at relatively low wall superheat temperatures. The advancing meniscus between the vapor and liquid phases in the cavity is clearly visible in Figure 7.5(a). Once the liquid layer above the wick microchannels is removed, thin-film evaporation begins from the liquid-vapor menisci that form between the liquid in the channels and the vapor in the cavity above it. Due to capillary forces, the wick microchannels continuously absorb liquid from the inlet liquid cavity, which is supplied by the compensation chamber and the liquid transport channels. There is a preexisting vapor bubble in the liquid microchannels, due to which the initial liquid supply to the wick comes exclusively from the compensation chamber.

Figure 7.5(b) shows the device at time $t = 1.56$ *sec*. The liquid in the Pyrex cavity has completely evaporated and the entire top surface of the in-plane wick is experiencing thin-film evaporation. The vapor that is being generated is pushing the liquid in the vapor microchannels back towards the condenser section. This in-turn propels the liquid in the liquid transport channels towards the wick, as is obvious from the movement of the vapor bubble initially stuck in the liquid channels. This vapor bubble finally stops at the entrance to the supply channel from the compensation chamber, and does not move even as the evaporation continues (Figure 7.5(c)). This indicates that the liquid for evaporation is now being supplied by the liquid transport channels. In fact, it can be argued that the amount of liquid evaporated is equal to the amount of the liquid displaced from the vapor microchannels. Most of the vapor formed in the evaporator is actually traveling to the outlet copper tubing and condensing back to liquid in this initially vapor-filled space. In a sense, the outlet copper tubing acts as a secondary condenser section of the μLHP.

The role of the outlet copper tubing as a secondary condenser is verified when the evaporator heat flux is decreased. In Figure 7.5(d), we can clearly see liquid from the outlet fill-port flowing into the vapor microchannels as the vapor pressure in the device falls due to a decrease in the input heat flux. At the same time, liquid from the

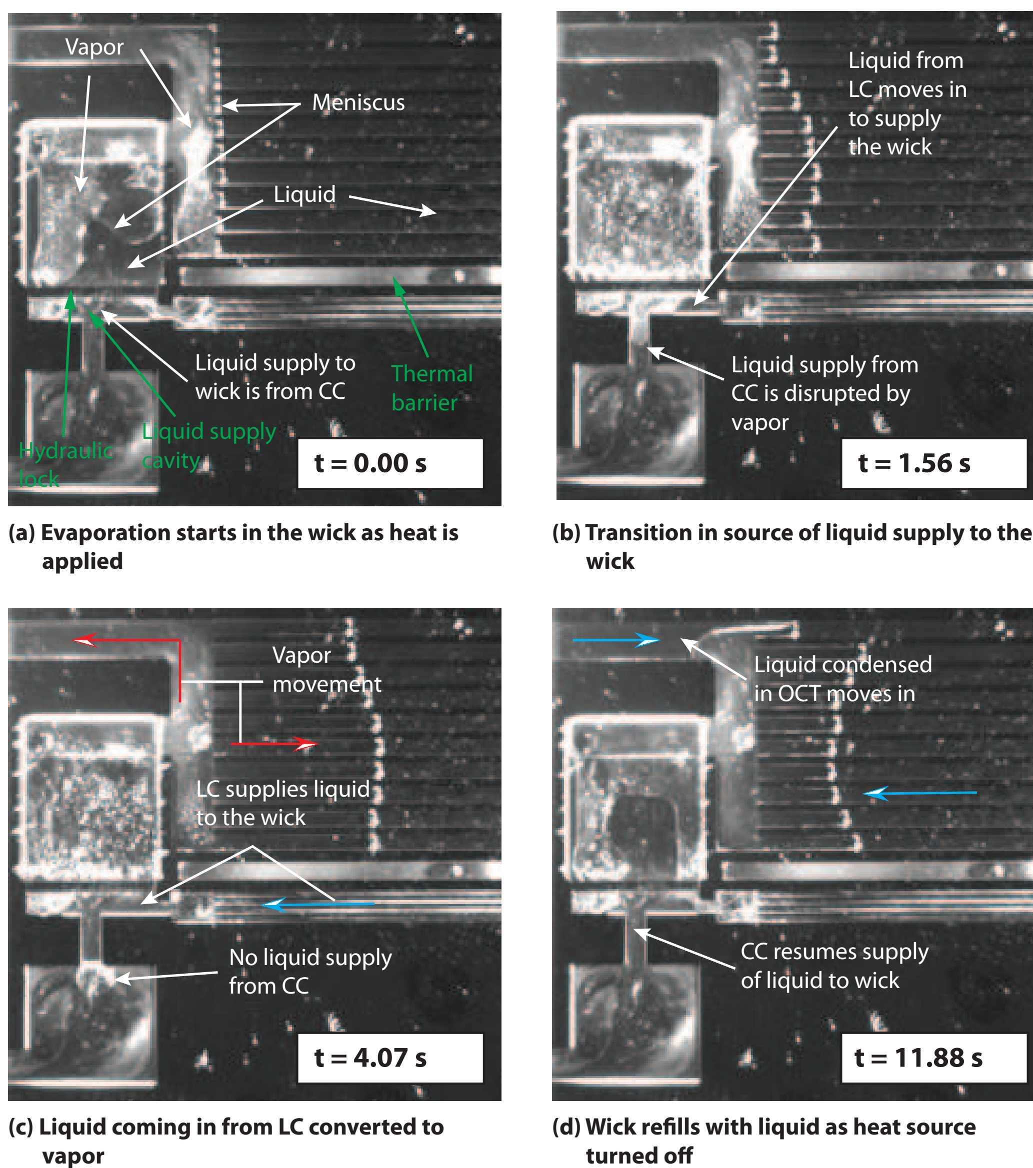

(a) Evaporation starts in the wick as heat is applied

(b) Transition in source of liquid supply to the wick

(c) Liquid coming in from LC converted to vapor

(d) Wick refills with liquid as heat source turned off

Figure 7.5: Liquid evaporation in a partially filled phase-II μLHP device. The images are taken using a high speed optical camera.

inlet copper tubing (which acts as an extension of the on-chip compensation chamber) moves in to refill the Pyrex cavity above the in-plane wick.

7.2.3 Analysis of Results

The results presented in the previous section illustrate characteristics of the startup transient behavior of a microscale loop heat pipe. They also demonstrate the efficacy of the new in-plane wick topology in implementing thin-film evaporation from the entire surface of the planar wicking structure.

This experiment could have provided better insight about the steady state operation of the μLHP if the outlet fill-port had been connected to the condenser section (as was the case in the phase-I μLHP). In the current configuration, the vapor travels to the outlet copper tubing (which acts as a secondary condenser section) instead of traveling all the way to the μLHP condenser section. An even better solution will be to seal the μLHP fill-ports directly on the surface of the wafer. This of course is the final goal of the packaging and hermetic sealing work that was presented in chapter 6. In such a hermetically sealed device, the fill-port connections will not form a large part of the overall system volume, due to which the placement of the fill-ports would not affect the behavior of the device.

However, the wick topology that is used in this particular μLHP design is successful in implementing thin-film evaporation in the evaporator section. Evaporation is seen to occur in the entire wick without any substantial vapor intrusion into the liquid supply cavity. This can be attributed to the hydraulic locking behavior of the part of the in-plane wick that is not covered by the Pyrex evaporation cavity (see Figure 7.5(a)). Further, the thermal barrier between the vapor and liquid transport microchannels seems to play a part in preventing bubble generation in the liquid transport microchannels. The liquid supply cavity plays a very interesting role in device startup. This cavity establishes a three-way connection between the wick, the compensation chamber, and the liquid transport microchannels. Any vapor that is generated in the liquid supply cavity (see Figure 7.5(b)), due to parasitic heat flow from the evaporator, is displaced into the compensation chamber as the source of liquid supply to the wick transitions from the compensation chamber to the liquid transport microchannels (see Figure 7.5(c)). This helps to avoid any blockage of liquid supply to the wick during evaporation.

7.3 Phase-III μLHP Prototype

The design and fabrication of the phase-III μLHP device was discussed in section 5.3. The primary objective behind this design was to see how much of an effect surface tension forces, which depend on the size of the microchannels and other devices cavities, have on the nature of the two-phase flow loop in a microscale loop heat

pipe. The phase-III μLHP device components were designed in order to effect a *geometric control* of the liquid-vapor meniscus. This section presents an experimental study of evaporation and two-phase fluid transport in the phase-III μLHP device. The device was degassed and filled with water following the procedure discussed in section 6.4. Some liquid was then thermally purged from the device before closing the inlet valve and disconnecting the external reservoir. Heat was then applied to the evaporator section of the partially liquid-filled device, to study the device operational characteristics.

7.3.1 Experimental Setup

In Figure 7.6 is shown the experimental setup for testing the phase-III μLHP device. It is identical to the experimental setup that was used for testing the phase-II μLHP device, as discussed in section 7.2.1.

7.3.2 Experimental Observations

Figure 7.7 shows what happens in the evaporator section and the region around it as the heat flux applied to the evaporator by the hot air gun first increases and then decreases. Similar to the phase-II μLHP, evaporation in the phase-III device starts with vapor formation in the Pyrex evaporation cavity (Figure 7.7(a)). Once the liquid in this cavity is completely removed, thin-film evaporation continues from the liquid-vapor meniscus in the in-plane-wick microchannels that lie underneath it (Figure 7.7(b)). Although the vapor generated in the wick travels into the vapor microchannels, significant intrusion of vapor into the liquid transport microchannels is also observed. The vapor also forces back the liquid in the liquid supply channel that comes from the inlet fill-port and plays the role of the compensation chamber in this particular μLHP design (Figure 7.7(b)).

As the evaporation continues, vapor intrudes into most of the liquid transport microchannels as well as the liquid supply channel coming from the inlet fill-port (Figure 7.7(c)). This is problematic, since it means that the liquid supply to the in-plane-wick microchannels has been interrupted, something which eventually leads to wick dry out. As the applied heat flux is decreased, liquid starts to refill the vapor microchannels and the in-plane wick.

7.3.3 Analysis of Results

The experimental results presented above seem to suggest that the evaporator topology employed in the phase-III μLHP has several drawbacks. Substantial amounts of vapor intrusion into the liquid transport microchannels is observed, something not seen in the case of the phase-II μLHP device. This can be attributed to a number of different factors. First, the hydraulic lock for the phase-III μLHP was a little bit

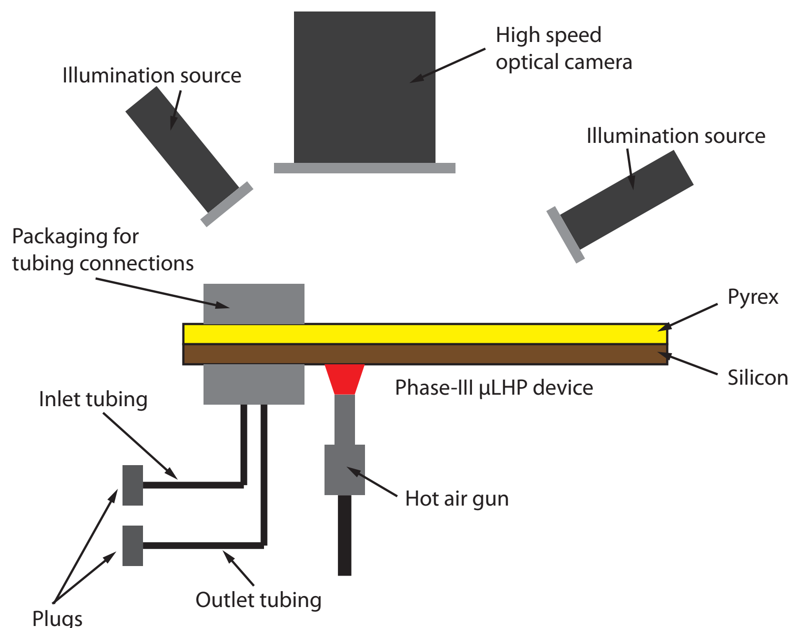

(a) Schematic of the experimental setup

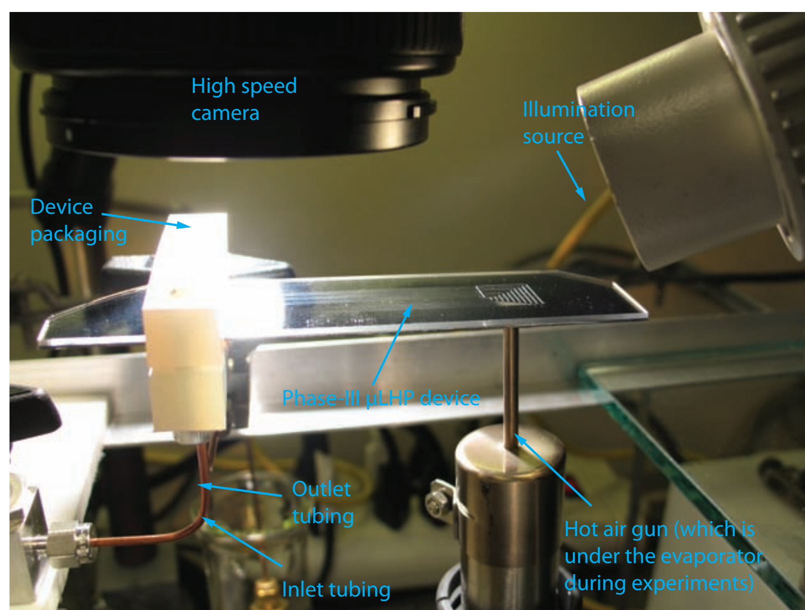

(b) Picture of the experimental setup

Figure 7.6: Experimental setup for the operational testing of the phase-III μLHP device. A hot air gun is used to heat the evaporator section of the packaged and partially filled μLHP device, while the condenser section of the device is cooled by ambient natural convection. A high speed camera is used to observe the evaporator section of the device, which is illuminated by multiple light sources.

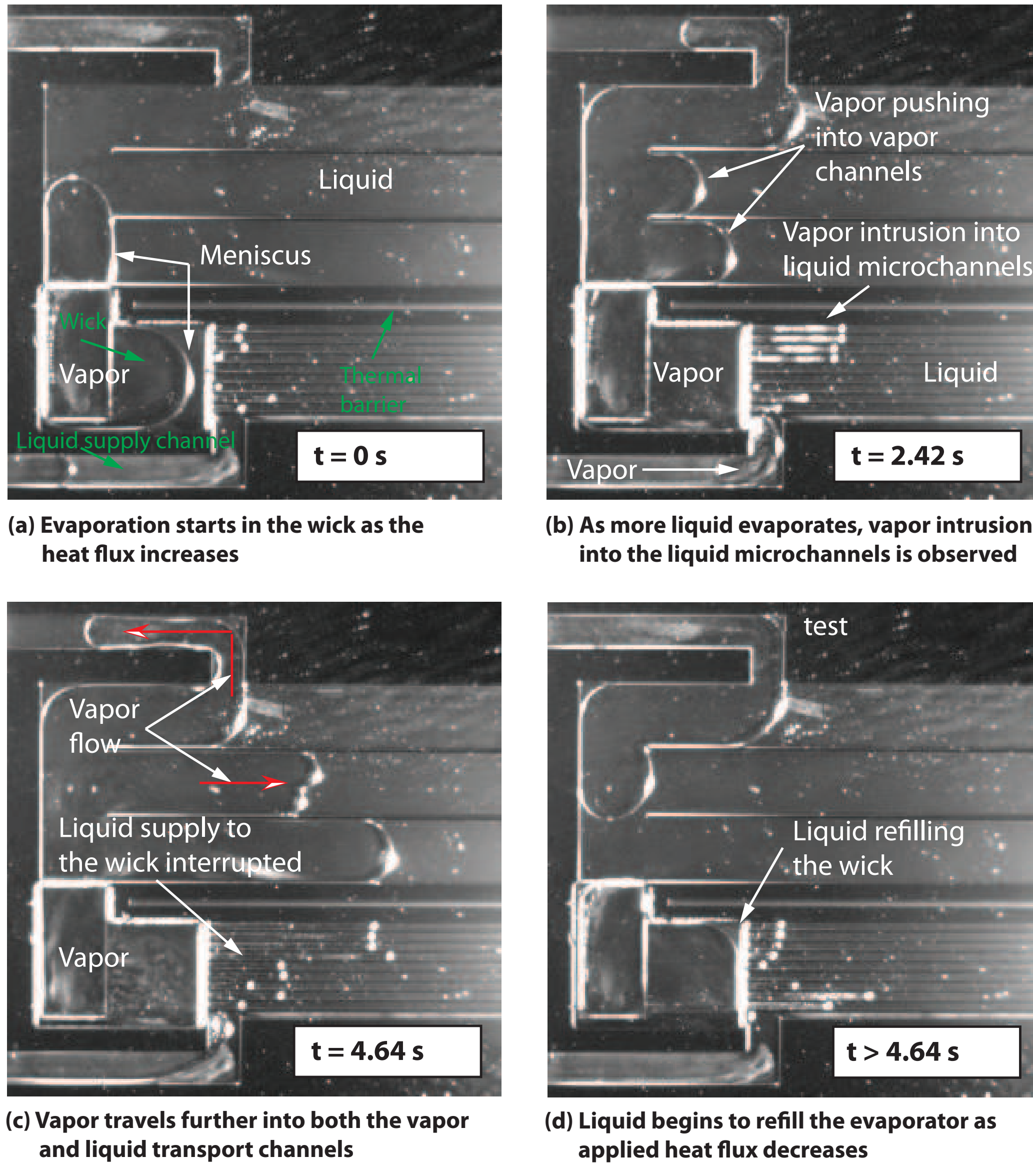

(a) Evaporation starts in the wick as the heat flux increases

(b) As more liquid evaporates, vapor intrusion into the liquid microchannels is observed

(c) Vapor travels further into both the vapor and liquid transport channels

(d) Liquid begins to refill the evaporator as applied heat flux decreases

Figure 7.7: Liquid evaporation in a partially filled phase-III μLHP device. The images are taken using a high speed optical camera.

thinner than in the case of the phase-II μLHP, which could have allowed the vapor in the Pyrex evaporation cavity to burst through into the liquid microchannels.

Second, due to the device topology in the evaporator region, the thermal barrier seems less effective in preventing parasitic heat flow from the evaporator to the liquid supply channels. In the phase-II μLHP the thermal barrier seemed to isolate the evaporator and vapor transport microchannels from the liquid transport microchannels. On the other hand, in the phase-III device the evaporator section lies on the liquid side of the thermal barrier. The parasitic heat can lead to direct bubble nucleation and vapor generation in the liquid microchannels.

The third factor responsible for vapor intrusion into the liquid transport microchannels might be the absence of the large liquid supply cavity preceding the wick, which allowed for useful interaction between the compensation chamber and the liquid transport microchannels in the case of the phase-II μLHP. Recall from section 5.3.1 that this liquid supply cavity had to be removed in the phase-III μLHP design in order to provide a monotonically decreasing channel cross-section going from the liquid transport microchannels to the in-plane-wick microchannels. The intention was to promote liquid wetting of the wick, by taking advantage of surface tension effects. However, from the above results it seems that the thermodynamic effects are just as important as those arising from surface tension. As a result, both these factors need to be considered in arriving at an optimum μLHP design topology.

Chapter 8

A Detailed Study of Phase Change and Heat Transfer in the μLHP

In this chapter, we will take a closer look at the process of phase change and heat transfer in the evaporator section of the in-plane-wicking micro loop heat pipes (μLHP). In the preceding chapter, we have seen that the phase-II μLHP design topology yields the best results from the point of view of sustained thin-film evaporation in the wicking structure. Here, a more detailed optical and thermal experimental study is performed to understand the thermodynamics of phase change in this particular μLHP design topology.

The phase-II μLHP device is degassed and filled with water, allowing the heated external reservoir to control the device saturation pressure. The evaporator section is heated, while the condenser is maintained at a fixed temperature. The objective is to observe the process of thin-film evaporation in the wicking structure, brought about the by controlled application of heat flux using a miniature ceramic heater. A high speed optical camera fitted with a microscopic lens is used for this purpose. A surface temperature profile of the μLHP, obtained using an infrared (IR) camera, is used to explain the dynamics of the two-phase fluid in the device.

8.1 Experimental Setup

In Figure 8.1 is shown a detailed schematic of the experimental setup. The inlet and outlet fill-holes of the μLHP are connected to 1/16-inch copper tubing using a steel standardized packaging (see section 6.4). The inlet copper tubing is connected to the external fluid reservoir, which contains distilled water, while the outlet copper tubing leads to the ambient using a one-way valve. Fluid flow through both the tubes can be controlled using steel ball valves. During the device purging step, both the inlet and outlet valves are kept open (see section 6.2). Once the purging is complete, the outlet valve is closed, while the inlet valve is kept open to fill the μLHP with

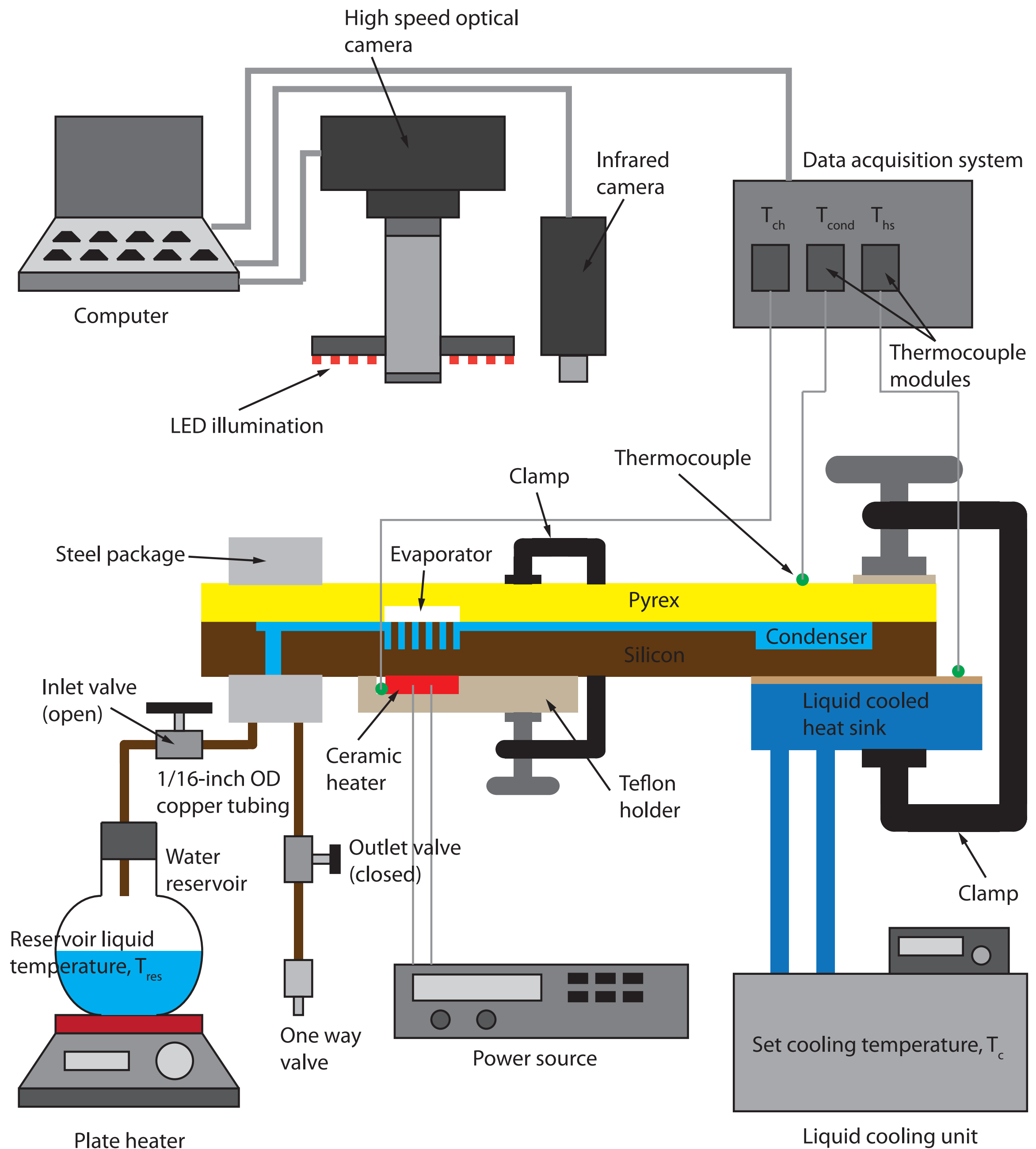

Figure 8.1: A schematic of the experimental setup for measuring evaporation characteristics of the in-plane-wicking micro loop heat pipe (μLHP). The setup can be configured to obtain either visual data using a high speed optical camera or temperature data using an infrared (IR) camera.

degassed water. Unlike in sections 7.1–7.3, the external liquid reservoir will be kept connected to the μLHP during device testing in this particular study. This will slightly modify device behavior due to the fact that with an externally-heated fluid reservoir the μLHP will actually behave like a micro capillary pumped loop. However, this should make the experimental results more repeatable by eliminating the need for partially filling the μLHP, and providing active control over the saturation pressure in the device.

Heat flux is applied to the μLHP evaporator section by placing a miniature ($5\ mm \times 5\ mm$) ceramic heater in direct contact with it on the silicon side of the device. The heater is held in place by a machined Teflon holder that is clamped to the device. The Teflon holder serves the additional purpose of preventing heat loss, due to natural convection, from the backside of the heater. The heater is powered by a high current-rated power source. The condenser section of the μLHP is clamped onto a liquid-cooled heat sink, which is provided with cold water by a liquid refrigeration unit with active temperature control. Thermocouples are used to measure the temperature of the ceramic heater (T_{ch}), the liquid cooled heat sink (T_{hs}), and the device condenser section (T_{cond}). The thermocouple data is refined by thermocouple modules on a data acquisition board that is connected to the computer.

The setup can be configured to obtain either visual data using a high speed optical camera or temperature data using an IR camera. When performing optical testing, the optical camera is connected to a long distance microscope, which is focused onto the evaporator section of the μLHP on the Pyrex side of the device (see Figure 8.2(a)). Since the camera has very short exposure times, a high-power LED light source is used to illuminate the device (Figure 8.2(b)). Figure 8.2(c) provides a close-up view of the μLHP device in the test setup. See Figure 8.2 for more exhaustive details on the experimental setup as configured for data acquisition using the high speed optical camera. Figure 8.3 shows pictures of the experimental setup when it is configured for acquiring surface temperature data of the μLHP using the IR camera. In this case, the lens of the IR camera is positioned over the middle of the device and its height is adjusted to bring the entire device in the frame of view. Figure 8.3(d) provides a close-up view of the IR camera. From Figure 8.2 and Figure 8.3, it is obvious that given the relative size of the cameras and the μLHP device, it is very difficult to obtain device optical and temperature data at the same time. Therefore, in order to enable a comparative study between the optical results and the device surface temperature profiles, identical experimental conditions were created for both the optical and thermal data acquisition setups.

Some of the experimental parameters were assigned fixed values for the entire set of experiments. The hot plate carrying the external fluid reservoir was set to a temperature of 260 ^oC (see Figure 8.4(a)). An infrared image of the glass reservoir (see Figure 8.4(b)) was used to determine the approximate values of the liquid and vapor phases of the working fluid (water) inside the reservoir. Water at the bottom of the reservoir was at a temperature of approximately 139 ^oC, while the vapor above

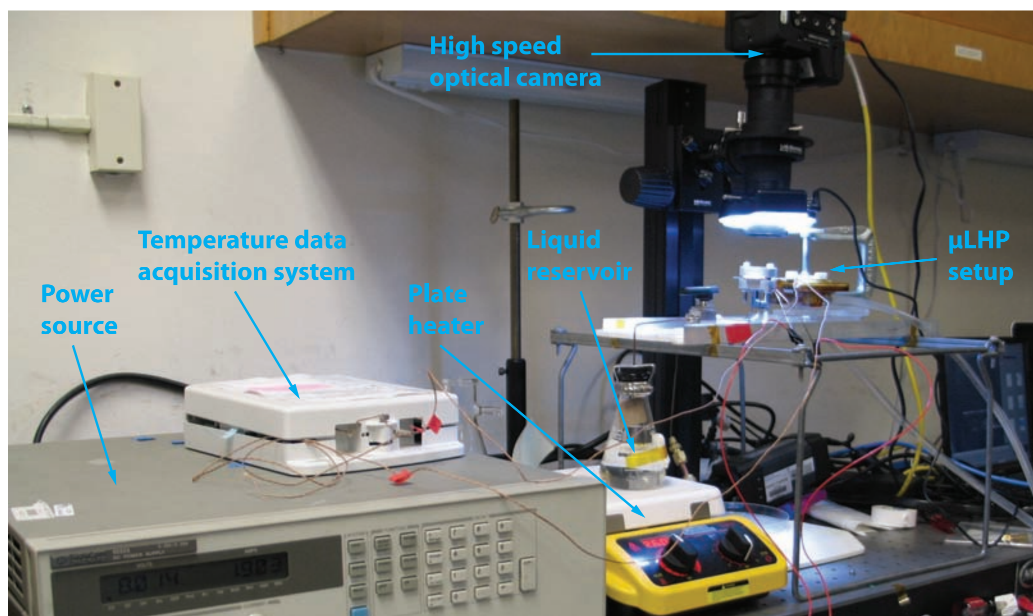

(a)

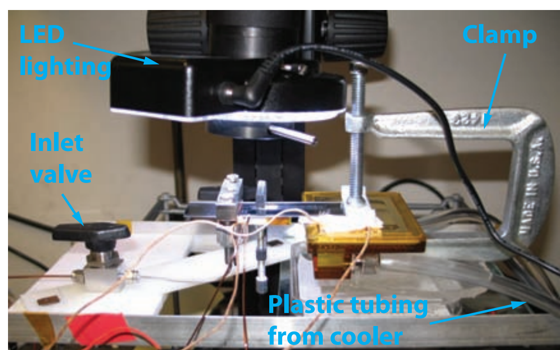

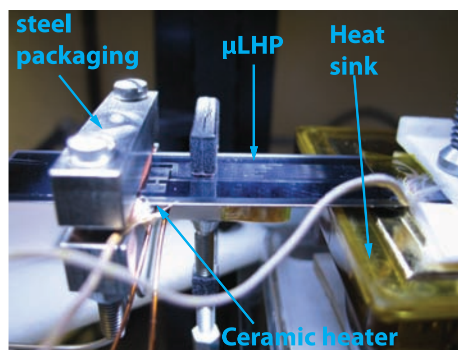

(b) (c)

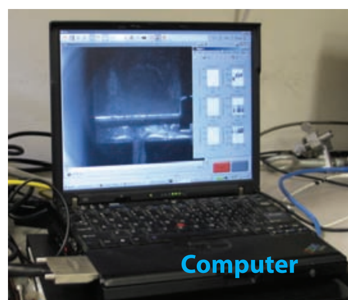

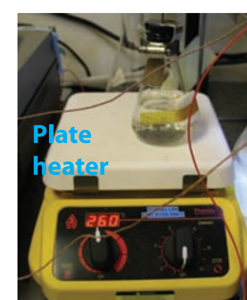

(d) (e) (f)

Figure 8.2: The experimental setup for studying evaporation in the phase-II μLHP using a high speed optical camera: (a) The overall setup; (b) The device test rig; (c) Close-up view of the device setup; (d) Computer showing image of device evaporator; (e) Liquid cooling system; (f) Heated external fluid reservoir.

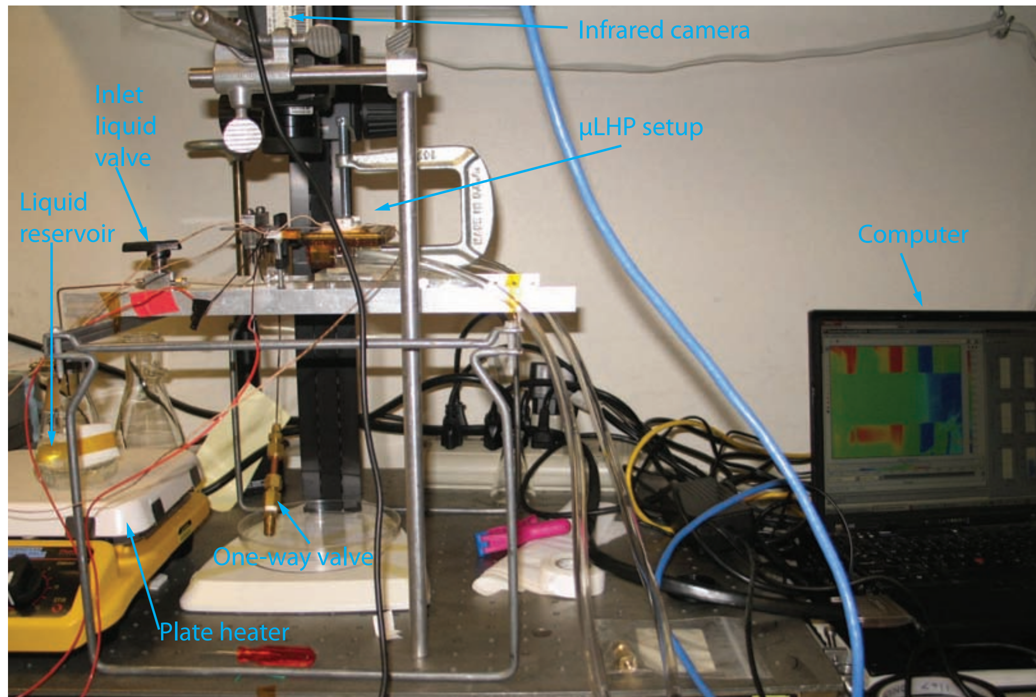

(a)

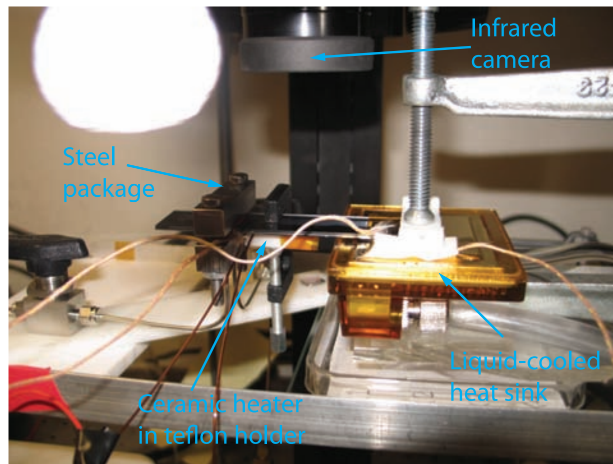

(b)

(c)

(d)

Figure 8.3: The experimental setup for studying thermal characteristics of the μLHP during evaporation in the wicking structure: (a) Overall setup; (b) The device test rig; (c) Power source and thermocouple box; (d) Infrared (IR) camera.

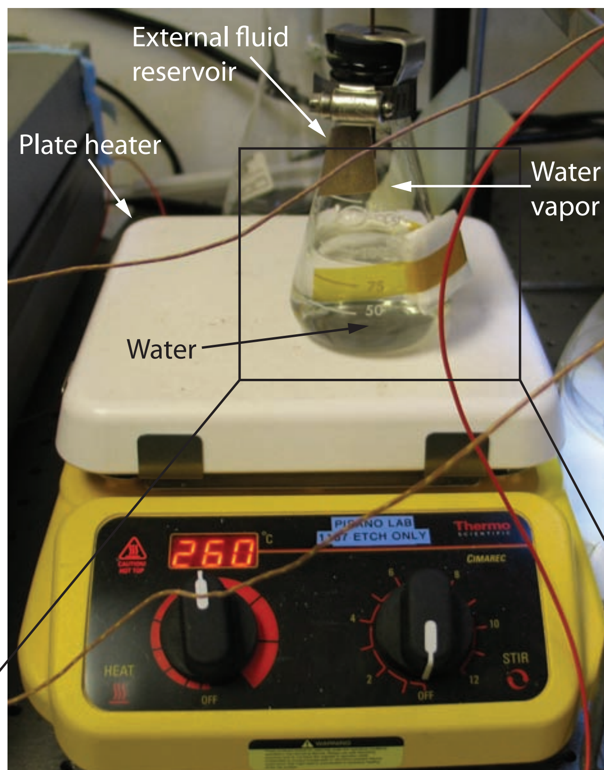

(a) Heater reservoir

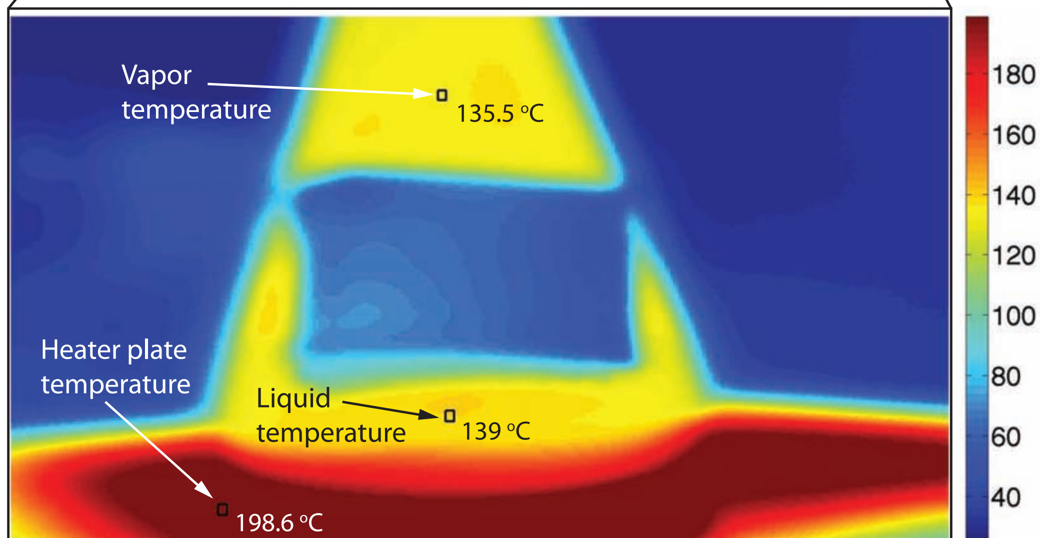

(b) Infrared image of the external fluid reservoir

Figure 8.4: Temperature of the saturated liquid-vapor system in the heated external fluid reservoir. The plate heater was set to a temperature of 260 ^oC, but the liquid and vapor temperatures in the glass flask were measured to be approximately 139 ^oC and 135.5 ^oC, respectively.

the water was at 135.5 ^oC. The temperature of the water supplied by the liquid cooling unit, T_c, was set at 10 ^oC. Thermocouple measurements indicated that the temperature at the surface of the liquid cooled heat sink, T_{hs}, remained between 13.5 ^oC and 13.9 ^oC during the experiments.

8.2 Onset of Evaporation in the Wick During Device Startup

In this experiment, a fixed amount of heat flux, sufficient for starting evaporation in the wicking structure, was applied to the evaporator of the μLHP device initially in the OFF state. A high-speed optical video of the device evaporator was recorded to understand the mechanism by which evaporation starts in the in-plane wick. It was found that applying a voltage of 7 V to the ceramic heater was sufficient for reaching full-scale evaporation in the wick within a reasonable amount of time. The power supplied to the 5 $mm \times 5$ mm heater was measured to be approximately 12.63 W, which yields an applied heat flux of approximately 51 W/cm^2.

Figure 8.5 shows the images of the evaporator section at different time instants, helping to shed some light on how evaporation starts in the wicking structure and the role of individual design components of the in-plane wick. Before the ceramic heater in contact with the evaporator section is turned on, the μLHP device is almost completely filled with water (Figure 8.5(a)). This is due to the fact that it is connected to a high temperature two-phase external fluid reservoir, and itself is being cooled by both the liquid-cooled heat sink as well as ambient air. However, we do note the presence of a residual vapor bubble in the Pyrex evaporation cavity, which most probably contains some non-condensible gases (NCGs).

At time $t = 3$ sec, the power to the ceramic heater is turned on (Figure 8.5(b)). This instantly leads to thin-film evaporation from the liquid-vapor meniscus that exists in the in-plane-wick microchannels underneath the preexisting vapor bubble in the Pyrex evaporation cavity. After an interval of about 47 seconds ($t = 50$ sec), we notice a vapor front advancing into the Pyrex evaporation cavity from the top (Figure 8.5(c)). When positioning the 5 $mm \times 5$ mm ceramic heater under the 3.8 $mm \times 4$ mm wick, it was displaced slightly upwards, away from the liquid supply cavity, on purpose. This was meant to avoid bubble generation in the liquid supply side of the wick. Due to this, the initial bubble nucleation seems to happen inside the vapor outlet cavity (see Figure 5.5 in chapter 5) near the center of the heater. The vapor bubble then expands into the rest of the Pyrex cavity. Figure 8.5(d) shows the evaporator at time $t = 61$ sec, when the vapor front has advanced further into the Pyrex cavity. At this point, we also start to witness larger amounts of thin-film evaporation from the in-plane-wick microchannels that lie under the vapor in the Pyrex cavity. The vapor formed as a result travels to the vapor transport channels and displaces the liquid in there.

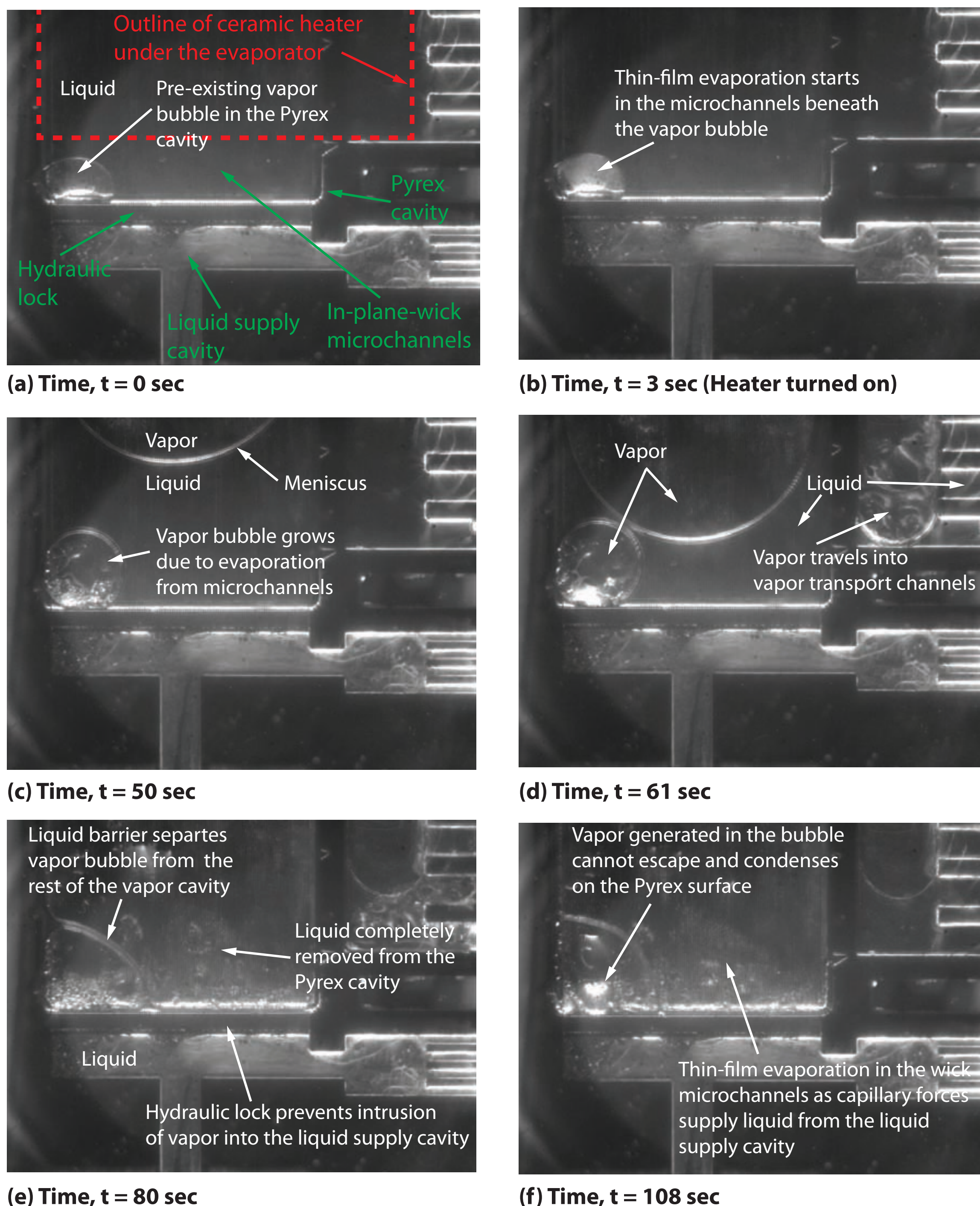

Figure 8.5: Evaporation characteristics of the μLHP in-plane wick during device startup, under an applied heat source of 12.63 W: (a) Device in OFF state; (b) Power to the ceramic heater turned on; (b-c) Vapor forms in the Pyrex evaporation cavity; (d-e) Thin-film evaporation occurs from the in-plane wick microchannels underneath the Pyrex evaporation cavity.

After about 19 seconds (t = 80 *sec*), the Pyrex evaporation cavity is completely occupied by vapor (Figure 8.5(e)). The interesting observation is that the hydraulic lock separating the Pyrex evaporation cavity from the liquid supply cavity prevents the vapor from intruding into the liquid supply. This remains the case even after 28 seconds (t = 108 *sec*), when we stop observing the device (Figure 8.5(f)). This highlights the important role played by this particular wick component in enabling a two-phase flow loop in the device. In the next section, we will see that the hydraulic lock needs to be supplemented by a thermal lock in order to keep the liquid supply free of vapor bubbles in device steady state operation. From Figure 8.5(e) and Figure 8.5(f), we can see that continuous thin-film evaporation is taking place in the in-plane-wick microchannels, which are kept wetted with liquid by the liquid supply cavity on account of their large surface tension forces.

Another interesting observation from Figure 8.5(e) and Figure 8.5(f) is the reluctance of the preexisting vapor bubble to merge with the rest of the vapor in the Pyrex evaporation cavity. A thin liquid film forms around this bubble, thereby preventing the vapor generated in the wick microchannels inside the bubble from moving out of the wick. This vapor instead condenses back to liquid on the surface of the Pyrex evaporation cavity. This bubble most probably contains some non-condensible gases (NCGs), and serves to reduce the effective area of the liquid-vapor meniscus in the wick from which evaporation can take place. Apart from blocking liquid flow in the device flow loop, this is another drawback that can be attributed to the presence of NCG bubbles inside a micro loop heat pipe.

8.3 Steady State Operation of the μLHP

Experiments were also conducted to study the steady-state operation of the phase-II μLHP at different values of the applied evaporator heat flux. The experimental setup described in section 8.1 was employed and all the experimental parameters, except the power to the ceramic heater, were kept constant during the experiment. Initially, the ceramic heater was switched off and the entire μLHP device was completely filled with water. The power supplied to the ceramic heater was then gradually increased and measurements taken using the following procedure:

1. Increase the voltage supply to the ceramic heater by 1 V.

2. After 5 minutes, record the temperatures of all the thermocouples. If undertaking an optical study using the high speed camera, record videos of the device evaporator section at various times of interest. At lower voltages, if no evaporation is observed in the device, wait for at least 5 minutes in order to allow the device to reach steady state before recording the video. If thermal measurements using the IR camera are being performed, take the IR image of the device after 5 minutes.

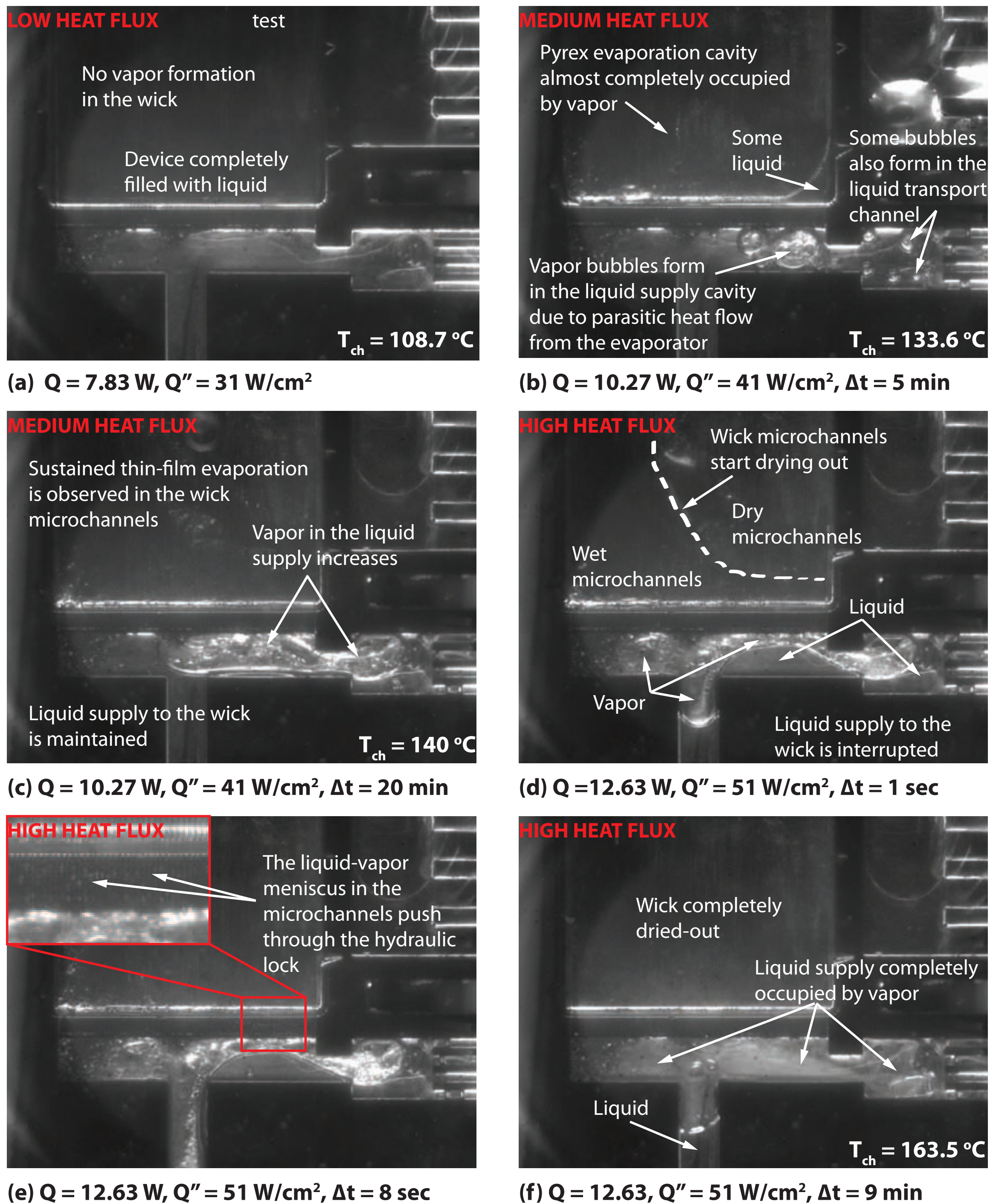

(a) Q = 7.83 W, Q" = 31 W/cm² **(b) Q = 10.27 W, Q" = 41 W/cm², Δt = 5 min**

(c) Q = 10.27 W, Q" = 41 W/cm², Δt = 20 min **(d) Q =12.63 W, Q" = 51 W/cm², Δt = 1 sec**

(e) Q = 12.63 W, Q" = 51 W/cm², Δt = 8 sec **(f) Q = 12.63, Q" = 51 W/cm², Δt = 9 min**

Figure 8.6: Effect of applied heat flux on steady-state evaporation in the in-plane wicking structure. Q is the thermal power output of the ceramic heater, Q" is the applied heat flux per unit area, and Δt is the time elapsed after the heater voltage is increased.

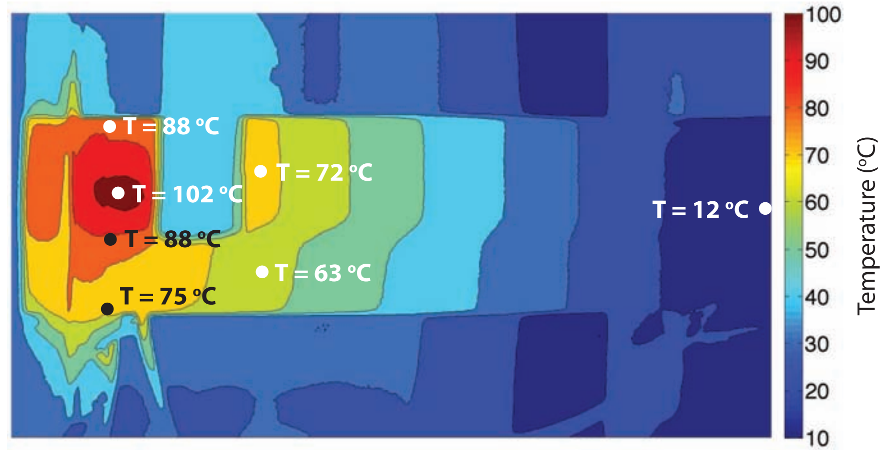

(a) Q = 7.83 W, Q″ = 31 W/cm², T_{ch} = 108.7 °C, T_{hs} = 13.8 °C

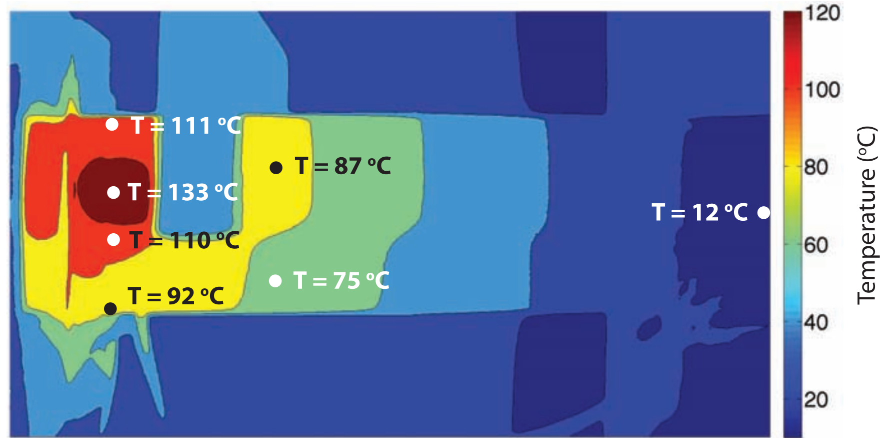

(b) Q = 10.27 W, Q″ = 41 W/cm², T_{ch} = 133.6 °C, T_{hs} = 13.9 °C

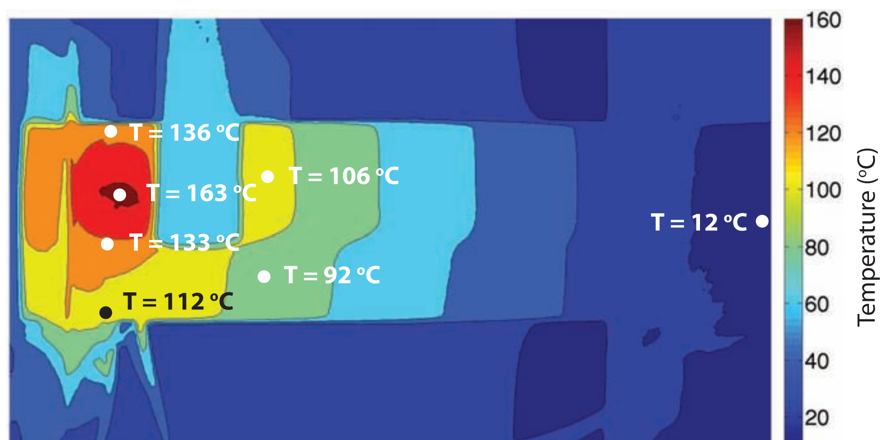

(c) Q = 12.63 W, Q″ = 51 W/cm², T_{ch} = 163.5 °C, T_{hs} = 13.9 °C

Figure 8.7: The surface temperature profile of the phase-II μLHP at different values of applied evaporator heat flux. Q is the thermal power output of the ceramic heater, Q" is the applied heat flux per unit area, T_{ch} is the temperature of the ceramic heater, and T_{hs} is the temperature of the heat sink.

3. Go back to step 1.

The procedure above was implemented twice, first for making the optical measurements and then for making the infrared measurements.

Figure 8.6 shows images of the μLHP evaporator for three different values of applied heat flux and at different time instants following an increase in voltage supply to the ceramic heater. Figure 8.7 shows surface temperature contours of the entire μLHP device at these same three values of the ceramic heater power supply. As mentioned above, the infrared thermal data was taken 5 minutes after the application of the individual heat flux. The power outputs of the ceramic heater at voltage supply values of 5 V, 6 V, and 7 V were 7.83 W, 10.27 W, and 12.63 W, respectively. Considering that the size of the ceramic heater is 5 $mm \times 5$ mm, this corresponds to applied evaporator heat fluxes of approximately 31 W/cm^2, 41 W/cm^2, and 51 W/cm^2, respectively. For the sake of simplicity, I will refer to these three values as *low heat flux*, *medium heat flux*, and *high heat flux*, respectively.

Figure 8.6(a), it is clear that no evaporation occurs in the μLHP device for the low heat flux value of 31 W/cm^2. This result can be explained by taking a look at the device surface temperature profile in Figure 8.7(a). The temperature of the ceramic heater (measured by a thermocouple) is 108.7 ^oC, while the maximum device surface temperature is 102 ^oC (in the upper half of the evaporator). In section 8.1, we saw that the temperature of the saturated vapor in the external fluid reservoir was approximately 135.5 ^oC. Since the saturation pressure inside the μLHP is controlled by this fluid reservoir, evaporation in the device will not start until this temperature is reached. From Figure 8.7(a), we can also confirm that the μLHP condenser is indeed maintained at a low temperature of 12 ^oC by the liquid-cooled heat sink.

Figure 8.6(b) shows that 5 *mins* after the medium heat flux of 41 W/cm^2 was applied, the liquid in the Pyrex evaporation cavity had almost completely evaporated. However, formation of vapor bubbles was also observed in the liquid supply cavity and to a lesser extent in the mouth of the liquid transport channels. This can be understood by analyzing the device surface temperature profile in Figure 8.7(b). We see that the maximum evaporator temperature (133 ^oC) is now almost equal to the fluid reservoir vapor temperature (135.5 ^oC). Bubble nucleation and growth has therefore led to vaporization of the liquid in the Pyrex evaporation cavity. Regarding the formation of bubbles, we saw in the previous section (Figure 8.5(f)) that during device startup, the hydraulic lock prevents the intrusion of vapor from the evaporator into the liquid supply cavity. However, it seems that over time (5 mins in this case) vapor bubbles can form in the liquid supply due to parasitic heat flow from the evaporator. The fact that the measured device surface temperature in the liquid supply cavity (see Figure 8.7(b)) is only about 110 ^oC (much less than the saturation temperature of 135.5 ^oC) supports this hypothesis. In fact, the vapor bubbles in the liquid supply cavity keep growing until approximately half of the cavity is occupied by vapor after 15 *mins* (see Figure 8.6(c)). However, liquid supply to the evaporating

thin-film menisci in the wick microchannels is maintained by liquid flowing along the walls of the cavity.

Now, let's see what happens when the high heat flux of 51 W/cm^2 is turned on. Figure 8.6(d) shows the device evaporator section 1 *sec* after the voltage supply to the ceramic heater is increased from 6 V to 7 V. We see that there is an instant outflux of water from the liquid supply cavity into the channels coming from the compensation chamber. This is obviously due to the evaporation of water in this cavity, resulting in the growth of the vapor phase. This event also cuts off the supply of liquid to the in-plane wick microchannels from both the liquid reservoir as well as the liquid transport channels. As a result, we finally see the in-plane-wick microchannels underneath the Pyrex evaporation cavity start to dry out. After about 8 seconds, we actually see the vapor pushing through the hydraulic lock into the liquid supply cavity. Looking at the evaporator after about 9 *mins* (Figure 8.6(f)), we see that the evaporator and its surrounding region is completely occupied by vapor. Even the liquid transport channels visible in the frame are devoid of any liquid. Liquid from the external fluid reservoir is trying to reach the wick, but is not allowed to do so by the large vapor pressure in the evaporator. This complete dry out of the wick can be understood by comparing the μLHP surface temperature profile in Figure 8.7(c) with the external fluid reservoir-controlled device saturation temperature of 135.5 ^oC. The maximum temperature in the evaporator is 163 ^oC, and it is also clear that almost the entire evaporator region, including part of the liquid supply cavity, is above the device saturation temperature. As a result there is no way to avoid bubble nucleation and rapid bubble growth in the wick liquid supply sources.

8.4 Discussion of Results

In the above sections, we explored both the onset of evaporation in the μLHP in-plane wick as well as the characteristics of steady state evaporation in the wick at different values of the applied heat flux.

From the first study, it is clear that both the Pyrex evaporation cavity as well as the hydraulic lock are indispensable to the proper operation of the in-plane wick design topology. The Pyrex cavity enables thin-film evaporation from the wick microchannels by allowing for the formation of a vapor domain above the liquid-filled wick microchannels. The hydraulic lock helps to maintain a continuous liquid supply to the wick by preventing vapor intrusion into the liquid supply cavity.

However, the long-term steady-state testing of the μLHP has shown that the hydraulic lock by itself is not sufficient for preventing vapor formation in the liquid supply. Even for medium heat fluxes, over time, vapor bubbles nucleate and grow in the liquid supply cavity as a result of parasitic heat flow from the evaporator section. As a result, further modifications to the topology of the evaporator section are required in order to minimize parasitic heat flows to the liquid supply cavity and

the compensation chamber.

Part IV

Closure

Chapter 9

Summary and Conclusions

This dissertation deals with the design, modeling, fabrication, and experimental testing of microscale loop heat pipes fabricated using MEMS microfabrication techniques. As discussed in chapter 1, the proposed micro-columnated loop heat pipe (μCLHP) intends to provide a localized, high-heat-flux thermal management solution for integrated cooling of a variety of modern electronic systems. This liquid phase change-based thermal transport system can absorb and carry large heat fluxes from a heat source to a heat sink, while incurring a very low temperature drop across the two. The μCLHP is designed for fabrication on silicon and Pyrex wafers, and therefore it not only has a completely planar topology but is also extremely thin. This will enable it to be deployed inside electronics that is either extremely compact or has a limitation on the allowable size in the third dimension. The μCLHP also proposes the use of a coherent porous silicon (CPS)-based vertically-wicking micro-columnated wick for providing large capillary pressures, which help to drive the flow loop, and an enhanced surface topology for better thin-film evaporation.

9.1 Summary of Device Modeling Studies

Previous efforts towards loop heat pipe miniaturization have encountered a number of problems due to the fact that the thermodynamic and phase change characteristics of these devices can be completely altered at smaller length scales. In chapter 2, a detailed thermodynamic analysis of the operational characteristics of the μCLHP device was presented. A study of the phase change diagrams of the two-phase working fluid in the device flow loop yielded three important device operational limits or requirements. The fact that favorable and adverse pressure components in the flow loop should balance each other in steady state, leads to the *capillary pumping requirement*. Parasitic heat flow from the heat source to the liquid compensation chamber results in the *motive temperature heat limit* as well as the *liquid subcooling requirement*. It was concluded that parasitic heat flow is the main hindrance to device miniaturization,

since it does not allow for a loop heat pipe wick thickness smaller than approximately 4-8 millimeters. To minimize parasitic heat flow in the MEMS-based μCLHP, where the wick thickness is smaller than 500 μm, a novel planar evaporator design topology was proposed. A finite element method (FEM)-based thermo-fluid solver was implemented to verify the performance of this evaporator topology, which employs micro-fabricated in-plane-thermal-conduction barriers and thermally-resistive fluidic connections to reduce parasitic heat flow from the evaporator to the compensation chamber. The numerical results prove that the motive temperature head and liquid subcooling limits to device operation can be avoided by substantially reducing sensible heating of the liquid coming into the compensation chamber.

Provided the μCLHP design topology ensures sufficient motive temperature head, as discussed above, the overall heat carrying capacity of the device will be determined by the capillary pumping limit. In chapter 3 was presented a design optimization study for the μCLHP using both analytical as well as numerical optimization tools. The objective was to maximize the total heat carrying capacity of the device flow loop (which depends on a number of device design parameters), subject to applicable equality and inequality constraints. The inequality constraints were derived from the capillary pumping requirement, as well as a liquid-refilling requirement that accounts for the time it takes to refill an individual dried-out wick pore. Monotonicity analysis, a pre-optimization tool, was used to simplify the problem into two individual cases depending on whether the solution is dictated by the wick refilling limit or the pressure balance limit. For the desired range of device design parameters, the pressure balance limit was found to be active and it enabled the determination of optimum values for all the design parameters except the wick pore diameter. It was found that decreasing the thickness of the wick and the length of the transport channels, and increasing the width of the transport channels increases device performance. The optimum value of the wick pore diameter was calculated by numerically solving the nonlinear equations arising out of the capillary pumping requirement. For the given model problem, the optimum value of the wick pore diameter was found to be 1.3 μm, and a total device heat carrying capacity of 135 W was predicted, which corresponds to an evaporator heat flux of 1293 W/cm^2.

Another very important aspect of μCLHP operation is the rate of thin-film evaporation in the micro-columnated wicking structure. Although an upper limit on the μCLHP heat carrying capacity can be calculated by analyzing the capillary pumping, motive temperature head, and liquid subcooling limits, the thin-film evaporation characteristics of the wicking structure can indirectly influence and even limit device performance. The rate of thin-film evaporation from the liquid-vapor meniscus in the micro-columnated wick depends on the thermodynamics of phase change processes and the behavior of the meniscus in the wick microstructures. In chapter 4 was presented a numerical model for computing the rates of thin-film evaporation from three-dimensional liquid-vapor menisci in arbitrarily-shaped wick microstructures. An energy minimizing algorithm called Surface Evolver was used to obtain the

shape of the stationary liquid-vapor meniscus in a rectangular channel, on the surface of the secondary evaporating wick of the micro-columnated wicking structure. Heat transfer and fluid flow equations were solved in the liquid domain, to simulate evaporation of the liquid from this secondary wick microchannel. A kinetic theory-based analytical model was used to assign appropriate boundary conditions to the meniscus surface, and the finite volume method (FVM) was used for the numerical solution of the governing partial differential equations. The results indicated that large evaporative heat transfer rates (4720 W/cm^2 for 5 K wall superheat) are possible from the liquid-vapor meniscus in a 100 μm wide and 50 μm deep microchannel. Further, the rate of evaporation increases with an increase in the wall superheat (8350 W/cm^2 for 10 K wall superheat) and decreases if the inlet liquid is subcooled. The predicted evaporative heat flux values might seem high, but the fact remains that in actual operation only part of the microchannels on the evaporative surface will be occupied by liquid, resulting in much lower overall evaporative heat flux. Further, this model does not account for capillary suppression effects on evaporation. This was precisely the reason why a much smaller channel ($\sim 1\ \mu m$), where capillary suppression effects will be important, was not studied. In reality, channels will need to be this small in order to provide large enough capillary forces necessary for keeping them wetted with liquid during evaporation. A 100 μm wide channel might theoretically provide high rates of evaporation, but it won't be able to attract liquid that is necessary for evaporation to take place.

9.2 Summary of Experimental Work

The latter part of the dissertation dealt with the fabrication and experimental testing of several micro loop heat pipe (μLHP) prototypes, to understand and quantify the operational characteristics of the proposed micro-columnated loop heat pipe (μCLHP). In chapter 5 were presented the detailed design and fabrication aspects of three different μLHP device prototypes. Due to the non-standard nature of coherent porous silicon (CPS) fabrication, the micro-columnated wicking structure was replaced by an in-plane wicking structure in these devices. This lead to a considerable simplification of the device fabrication process flow, while helping to retain most of the essential μCLHP design concepts. The phase-I μLHP device consists of evaporator and condenser sections connected by liquid and vapor transport channels, which are thermally isolated from each other by a conduction barrier. Two fill-holes in the device are used for purging and filling it with a degassed working fluid (water). All the device features were etched into a silicon wafer, while a Pyrex wafer was used to seal those components. The phase-II μLHP resembled the phase-I device in terms of its overall topology, but incorporated an improved in-plane wick design by introducing a Pyrex evaporation cavity above part of the in-plane wick microchannels. This helped to not just significantly increase the liquid-vapor meniscus area available for thin-film

evaporation, but also provided a hydraulic lock to prevent the vapor in the evaporator section from intruding into the liquid supply. The placement of the fill-holes was also standardized in this prototype. The phase-III μLHP device employed monotonically decreasing microchannel cross-sections in an effort to geometrically control the relative distribution of liquid and vapor phases in the device flow loop.

Chapter 6 dealt with the degassing, liquid-charging, and packaging of the fabricated μLHP devices. A novel thermal-flux degassing and fluid-filling system for ensuring the removal of non-condensible gases (NCGs) from the device working fluid was introduced. Several high temperature-compatible device packaging techniques were developed to implement this system. It was found that a standardized approach involving the use of a mechanically clamped, gasket-sealed package worked very well for the purpose of preparing liquid-filled devices that could be easily tested in a laboratory setting. A noninvasive hermetic sealing approach based on induction heating was also developed for the purpose of permanently sealing the degassed working fluid inside standalone μLHP devices. Experiments were conducted to verify the successful sealing of both dry and wet 1 mm holes in a silicon wafer using an induction heating experimental setup.

In chapter 7, each of the three μLHP device prototypes were experimentally tested by applying a heat source to their evaporator sections, in order to determine device components and topologies critical to enabling the two-phase flow loop. With its compensation chamber connected to the external fluid reservoir, a complete dry out of the wick at high wall superheat was observed in the phase-I μLHP. However, when disconnected from the reservoir and partially filled with liquid, unsteady nucleate boiling was observed in the wick, albeit again only at a high wall superheat. The results were explained by the inability of the wick to support any significant amount of thin-flm evaporation. The formation of the two-phase flow loop, as a result of nucleate boiling in the wick, was attributed to the surface tension characteristics of the individual device components. The phase-II μLHP successfully demonstrated thin-film evaporation in the improved in-plane wicking structure. A two-phase flow loop was also developed in the device, with the vapor traveling preferentially into the vapor transport channels and continuous liquid supply from the liquid transport channels. The phase-III μLHP, despite an identical improved wick design, encountered considerable vapor intrusion into the liquid transport/supply channels. This was attributed partially to the modified evaporator topology and partially to increased parasitic heat flow.

In chapter 8, a more detailed experimental study was conducted to characterize the startup and steady state evaporation characteristics of the phase-II μLHP device, under controlled application of heat flux to the evaporator. A high speed optical camera was used to observe the behavior of the two-phase fluid in the device, while an infrared (IR) camera and thermocouples were used to collect thermal data. A study on the onset of thin-film evaporation in the device evaporator revealed the critical role played by the Pyrex evaporation cavity and the hydraulic lock. Under an

applied heat flux of 51 W/cm^2, continuous thin-film evaporation was observed in the initial stages of device startup, without any apparent vapor intrusion into the liquid supply. A study of the steady-state evaporation characteristics of the device revealed that parasitic heat flow can gradually result in the formation of vapor bubbles in the liquid supply cavity, even at moderate heat flux values. Continuous operation of the flow loop was however confirmed for heat flux values as high as 41 W/cm^2. At large heat flux values, a complete dry out of the wick occurred due to disruption of liquid supply to the wick by the vapor in the liquid supply cavity.

9.3 Conclusions and Future Work

The theoretical analysis as well as the experimental results strongly suggest that the μCLHP is a promising technology for localized high-heat-flux thermal management of current and future electronics systems. Successful operation of device prototypes as thin as 1 millimeter has been demonstrated, at applied heat flux values as high as 41 W/cm^2. However, the fact that the experimental devices did not employ a vertically-wicking micro-columnated wick, or a sophisticated thermal lock to minimize parasitic heat flow from the evaporator to the liquid supply cavity, means that the heat carrying capacity of these devices can be much higher. Due to DRIE etching limitations, the in-plane wick microchannels could not be made smaller than 10 μm. However, the modeling results from chapter 3 suggest that a micro-columnated wick with an optimum wick pore size of 1.3 μm can result in device heat flux carrying capacities as high as 1293 W/cm^2 when water is used as a working fluid. Furthermore, numerical studies of thin-film evaporation from chapter 4 indicate that rates of thin-film evaporation will not limit device performance as long as the wick topologies are optimized to maximize the area of the liquid-vapor meniscus, which sustains thin-film evaporation.

Opportunities for future work exist in a number of different sub-topics that have been explored in this dissertation. The importance of reducing parasitic heat flows for improving the motive temperature head has been amply highlighted. Next generation in-plane-wicking micro loop heat pipe (μLHP) prototypes can be fabricated using the planar evaporator topology suggested in chapter 2. This approach will not require any substantial modifications to the device fabrication process flows discussed in chapter 5. Alternatively, other ways to reduce parasitic heat flow, such as the use of low thermal conductivity materials in the wick, can be explored.

The noninvasive hermetic sealing process developed in chapter 6 needs to be implemented on actual μLHP devices in order to obtain standalone hermetically-sealed device prototypes that are completely degassed and filled with water. This will not only enable a transition of the μLHP from the laboratory setting to actual field applications, but also allow for a more representative experimental testing of the device. A logical future direction would be to develop and implement a MEMS fabrication

process flow for the coherent porous silicon (CPS)-based micro-columnated wick, and integrate it with the μLHP fabrication process discussed in chapter 5.

On the numerical modeling front, the three-dimensional finite volume model for computing rates of thin-film evaporation, discussed in chapter 4, can be further improved by incorporating the effect of capillary pressure. Replacing the Surface Evolver-generated stationary meniscus with a level set-based dynamic meniscus that evolves with time can be a good doctoral dissertation topic.

Bibliography

[1] Shankar Krishnan, Suresh V. Garimella, Gregory M. Chrysler, and Ravi V. Mahajan. Towards a thermal Moore's law. *IEEE Transactions on Advanced Packaging*, 30(3):462–474, Aug 2007.

[2] Randeep Singh, Aliakbar Akbarzadeh, and Masataka Mochizuki. Thermal Potential of Flat Evaporator Miniature Loop Heat Pipes for Notebook Cooling. *IEEE Transactions on Components and Packaging Technologies*, 33(1):32–45, Mar 2010.

[3] A. Bar-Cohen, K. Geisler, and E. Rahim. Direct liquid thermal management of 3d chip stacks. In *Electronics Packaging Technology Conference, 2009. EPTC '09. 11th*, pages 119 –130, Dec 2009.

[4] F. Schindler-Saefkow, O. Wittler, D. May, and B. Michel. Thermal management in a 3d-pcb-package with water cooling. In *Electronics Systemintegration Technology Conference, 2006. 1st*, volume 1, pages 107 –110, Sep 2006.

[5] Dae-Whan Kim, E. Rahim, A. Bar-Cohen, and Bongtae Han. Direct submount cooling of high-power leds. *Components and Packaging Technologies, IEEE Transactions on*, 33(4):698 –712, Dec 2010.

[6] L. Zhang, Liu Minshan, and Dong Qiwu. Cooling devices for high power led illuminators. In *Prognostics and System Health Management Conference (PHM-Shenzhen), 2011*, pages 1–5, May 2011.

[7] Kai Zhang, D.G.W. Xiao, Xiaohua Zhang, H. Fan, Z. Gao, and M.M.F. Yuen. Thermal performance of led packages for solid state lighting with novel cooling solutions. In *Thermal, Mechanical and Multi-Physics Simulation and Experiments in Microelectronics and Microsystems (EuroSimE), 2011 12th International Conference on*, pages 1/7 –7/7, April 2011.

[8] W. Nakayama, O. Suzuki, and Y. Hara. Thermal management of electronic and electrical devices in automobile environment. In *Vehicle Power and Propulsion Conference, 2009. VPPC '09. IEEE*, pages 601–608, Sep 2009.

[9] C. Mi, Ben Li, D. Buck, and N. Ota. Advanced electro-thermal modeling of lithium-ion battery system for hybrid electric vehicle applications. In *Vehicle Power and Propulsion Conference, 2007. VPPC 2007. IEEE*, pages 107 –111, Sep 2007.

[10] D. Bharathan, A. Pesaran, A. Vlahinos, and G.-H. Kim. Improving battery design with electro-thermal modeling. In *Vehicle Power and Propulsion, 2005 IEEE Conference*, page 8, Sep 2005.

[11] Songping Mo, Zeshao Chen, and Peng Hu. Performance of a passively cooled fresnel lens concentrating photovoltaic module. In *Power and Energy Engineering Conference (APPEEC), 2011 Asia-Pacific*, pages 1–4, Mar 2011.

[12] Theodore G. van Kessel, Yves C. Martin, Robert L. Sandstrom, and Supratik Guha. Extending photovoltaic operation beyond 2000 suns using a liquid metal thermal interface with passive cooling. In *Photovoltaic Specialists Conference, 2008. PVSC '08. 33rd IEEE*, pages 1–3, May 2008.

[13] Wessel W. Wits and Tom H. J. Vaneker. Integrated Design and Manufacturing of Flat Miniature Heat Pipes Using Printed Circuit Board Technology. *IEEE Transactions on Components and Packaging Technologies*, 33(2):398–408, June 2010.

[14] K.T. Feldman Jr. and D.L. Noreen. Design of heat pipe cooled laser mirrors with an inverted meniscus evaporator wick. *AIAA Paper*, 1980.

[15] Yu.F. Maydanik. Loop heat pipes. *Applied Thermal Engineering*, 25(5-6):635 – 657, 2005.

[16] Yuming Chen, Manfred Groll, Rainer Mertz, Yu F. Maydanik, and S. V. Vershinin. Steady-state and transient performance of a miniature loop heat pipe. *International Journal of Thermal Sciences*, 45(11):1084–1090, Nov 2006.

[17] R.B. Schweickart, L. Neiswanger, and J. Ku. Verification of an analytic modeler for capillary pump loop thermal control systems. In *AIAA, 22nd Thermophysics Conference*, June 1987.

[18] A.C. Cotler, E.R. Brown, V. Dhir, and M.C. Shaw. Chip-level spray cooling of an ld-mosfet rf power amplifier. *Components and Packaging Technologies, IEEE Transactions on*, 27(2):411 – 416, June 2004.

[19] A. Langari and H. Hashemi. A cooling solution for power amplifier modules in cellular phone applications. In *Electronic Components and Technology Conference, 1999. 1999 Proceedings. 49th*, pages 316 –320, 1999.

[20] S.P. Tan, F.X. Che, Xiaowu Zhang, K.H. Teo, S. Gao, D. Pinjala, and Y.Y.G. Hoe. Thermal performance analysis of a 3d package. In *Electronics Packaging Technology Conference (EPTC), 2010 12th*, pages 72 –75, Dec 2010.

[21] S.P. Tan, K.C. Toh, J.C. Chai, D. Pinjala, and O.K.N. Khan. Thermal characterisation and liquid cooling system integration for stacked modules. In *Electronics Packaging Technology Conference, 2007. EPTC 2007. 9th*, pages 179 –183, Dec 2007.

[22] Aibin Yu, N. Khan, G. Archit, D. Pinjala, Kok Chuan Toh, V. Kripesh, Seung Wook Yoon, and J.H. Lau. Fabrication of silicon carriers with tsv electrical interconnections and embedded thermal solutions for high power 3-d package. In *Electronic Components and Technology Conference, 2008. ECTC 2008. 58th*, pages 24 –28, May 2008.

[23] Kaikai Ding, Shiwei Feng, Chunsheng Guo, Guangchen Zhang, and Chen Gao. Structure optimization of heat sink for high power led street lamp. In *Electronics and Optoelectronics (ICEOE), 2011 International Conference on*, volume 2, pages 75–78, July 2011.

[24] Ting Cheng, Xiaobing Luo, Suyi Huang, Zhiyin Gan, and Sheng Liu. Simulation on thermal characteristics of led chips for design optimization. In *Electronic Packaging Technology High Density Packaging, 2008. ICEPT-HDP 2008. International Conference on*, pages 1 –4, July 2008.

[25] Lei Liu, G.Q. Zhang, Daoguo Yang, Kailin Pan, Hong Zhong, and Fengze Hou. Thermal analysis and comparison of heat dissipation methods on high-power leds. In *Electronic Packaging Technology High Density Packaging (ICEPT-HDP), 2010 11th International Conference on*, pages 1366 –1370, Aug 2010.

[26] L. Yuan, S. Liu, Mingxiang Chen, and Xiaobing Luo. Thermal analysis of high power led array packaging with microchannel cooler. In *Electronic Packaging Technology, 2006. ICEPT '06. 7th International Conference on*, pages 1–5, Aug 2006.

[27] M. Arik, Y. Utturkar, and S. Weaver. Immersion cooling of light emitting diodes. In *Thermal and Thermomechanical Phenomena in Electronic Systems (ITherm), 2010 12th IEEE Intersociety Conference on*, pages 1–8, June 2010.

[28] Sheng Liu, Tim Lin, Xiaobing Luo, Mingxiang Chen, and Xiaoping Jiang. A microjet array cooling system for thermal management of active radars and high-brightness leds. In *Electronic Components and Technology Conference, 2006. Proceedings. 56th*, page 5, 2006.

[29] A. Shafiei and S.S. Williamson. Plug-in hybrid electric vehicle charging: Current issues and future challenges. In *Vehicle Power and Propulsion Conference (VPPC), 2010 IEEE*, pages 1–8, Sep 2010.

[30] A.A. Pesaran and M. Keyser. Thermal characteristics of selected ev and hev batteries. In *Applications and Advances, 2001. The Sixteenth Annual Battery Conference on*, pages 219 –225, 2001.

[31] B. Siegal. Solar photovoltaic cell thermal measurement issues. In *Semiconductor Thermal Measurement and Management Symposium, 2010. SEMI-THERM 2010. 26th Annual IEEE*, pages 132 –135, Feb 2010.

[32] T.J. Coutts and J.S. Ward. Thermophotovoltaic and photovoltaic conversion at high-flux densities. *Electron Devices, IEEE Transactions on*, 46(10):2145 –2153, Oct 1999.

[33] L. Montè ands and B. Bercu. A gravity independent integrated passive cooler for solar cell efficiency improvement. In *Photovoltaic Specialists Conference (PVSC), 2010 35th IEEE*, pages 3059 –3064, June 2010.

[34] D.A. Adkins. Novel method and system for monitoring cpv cell and module temperature. In *Photovoltaic Specialists Conference (PVSC), 2010 35th IEEE*, pages 1660 –1665, June 2010.

[35] W. G. Anderson, P. M. Dussinger, D. B. Sarraf, and S. Tamanna. Heat pipe cooling of concentrating photovoltaic cells. In *Photovoltaic Specialists Conference, 2008. PVSC '08. 33rd IEEE*, pages 1–6, May 2008.

[36] S. S. Anandan and V. Ramalingam. Thermal management of electronics: A review of literature. *Thermal Science*, 12(2):5–26, 2008.

[37] Ronan Grimes, Ed Walsh, and Pat Walsh. Active cooling of a mobile phone handset. *Applied Thermal Engineering*, 30(16, Sp. Iss. SI):2363–2369, Nov 2010.

[38] M.A. Ebadian and C.X. Lin. A review of high-heat-flux heat removal technologies. *Journal of Heat Transfer*, 133(11), 2011.

[39] J. P. Calame, D. Park, R. Bass, R. E. Myers, and P. N. Safier. Investigation of Hierarchically Branched-Microchannel Coolers Fabricated by Deep Reactive Ion Etching for Electronics Cooling Applications. *Journal of Heat Transfer-Transactions of the ASME*, 131(5), May 2009.

[40] E. Kermani, S. Dessiatoun, A. Shooshtari, and M.M. Ohadi. Experimental investigation of heat transfer performance of a manifold microchannel heat sink for cooling of concentrated solar cells. In *Electronic Components and Technology Conference, 2009. ECTC 2009. 59th*, pages 453 –459, May 2009.

[41] Jaeseon Lee and Issam Mudawar. Low-Temperature Two-Phase Microchannel Cooling for High-Heat-Flux Thermal Management of Defense Electronics. *IEEE Transactions on Components and Packaging Technologies*, 32(2):453–465, June 2009.

[42] Xiaobing Luo and Sheng Liu. A microjet array cooling system for thermal management of high-brightness leds. *Advanced Packaging, IEEE Transactions on*, 30(3):475 –484, Aug 2007.

[43] Gregory J. Michna, Eric A. Browne, Yoav Peles, and Michael K. Jensen. Single-Phase Microscale Jet Stagnation Point Heat Transfer. *Journal of Heat Transfer-Transactions of the ASME*, 131(11), Nov 2009.

[44] Issam Mudawar, Desikan Bharathan, Kenneth Kelly, and Sreekant Narumanchi. Two-Phase Spray Cooling of Hybrid Vehicle Electronics. *IEEE Transactions on Components and Packaging Technologies*, 32(2):501–512, June 2009.

[45] Jen-Hau Cheng, Chun-Kai Liu, Yu-Lin Chao, and Ra-Min Tain. Cooling performance of silicon-based thermoelectric device on high power led. In *Thermoelectrics, 2005. ICT 2005. 24th International Conference on*, pages 53 – 56, June 2005.

[46] C. Alaoui and Z.M. Salameh. A novel thermal management for electric and hybrid vehicles. *Vehicular Technology, IEEE Transactions on*, 54(2):468 – 476, Mar 2005.

[47] S. C. Fok, W. Shen, and F. L. Tan. Cooling of portable hand-held electronic devices using phase change materials in finned heat sinks. *International Journal of Thermal Sciences*, 49(1):109–117, Jan 2010.

[48] Charlotte Gillot, Yvan Avenas, Nathalie Cezac, Gilles Poupon, Christian Schaeffer, and Elise Fournier. Silicon heat pipes used as thermal spreaders. *IEEE Transactions on Components and Packaging Technologies*, 26(2):332 – 339, 2003.

[49] Amir Faghri. *Heat Pipe Science and Technology*. Taylor & Francis, 1st edition, 1995.

[50] J. Perkins. UK Patent No. 7059, 1836.

[51] R. Gaugler. Heat transfer device. U.S. Patent 2350348, 1944.

[52] L. Trefethen. On the surface tension pumping of liquids or a possible role of the candlewick in space exploration. G.E. Tech. Info, Serial No. 615 D114, 1962.

[53] G. M. Grover, T. P. Cotter, and G. F. Erickson. Structures of very high thermal conductance. *Journal of Applied Physics*, 35(6):1990 –1991, June 1964.

[54] G. Grover. Evaporation-condensation heat transfer device. U.S. Patent 3229759, 1966.

[55] T. P. Cotter. Theory of heat pipes. Technical Report LA-3246-MS, Los Alamos Scientific Laboratory, 1965.

[56] A. Faghri and S. Thomas. Performance characteristics of a concentric annular heat pipe - part 1. experimental prediction and analysis of the capillary limit. In *American Society of Mechanical Engineers, Heat Transfer Division, (Publication) HTD*, volume 96, pages 379 – 387, Houston, TX, USA, 1988.

[57] Yuichi Kimura, Yoshio Nakamura, Junji Sotani, and Masafumi Katsuta. Steady and transient heat transfer characteristics of flat micro heatpipe. *Furukawa Review*, (27):3 – 8, 2005.

[58] Heat pipe. USSR Inventors Certificate 449213, 1974.

[59] Yu. F. Gerasimov, Yu. F. Maidanik, G. T. Shchegolev, G. A. Filippov, L. G. Starikov, V. M. Kiseev, and Yu. E. Dolgirev. Low-temperature heat pipes with separate channels for vapor and liquid. *Journal of Engineering Physics and Thermophysics*, 28:683–685, 1975.

[60] VG Pastukhov, YF Maidanik, CV Vershinin, and MA Korukov. Miniature loop heat pipes for electronics cooling. *Applied Thermal Engineering*, 23(9):1125–1135, June 2003.

[61] Y. F. Maydanik. Evaporation chamber of a loop heat pipe. *Russian Patent 2224967*, 2004.

[62] Jon Zuo, Chanwoo Park, and David Sarraf. Hybrid loop cooling of high heat flux components. In *Collection of Technical Papers - 2nd International Energy Conversion Engineering Conference*, volume 2, pages 779–783, Providence, RI, United States, 2004.

[63] YF Maydanik, SV Vershinin, MA Korukov, and JM Ochterbeck. Miniature loop heat pipes - A promising means for cooling electronics. *IEEE Transactions on Components and Packaging Technologies*, 28(2):290–296, June 2005.

[64] M. Ghajar, J. Darabi, and N. Crews Jr. A hybrid cfd-mathematical model for simulation of a mems loop heat pipe for electronics cooling applications. *Journal of Micromechanics and Microengineering*, 15(2):313 – 321, 2005.

[65] J.T. Dickey and G.P. Peterson. Experimental and analytical investigation of a capillary pumped loop. *Journal of thermophysics and heat transfer*, 8(3):602 – 607, 1994.

[66] R.R. Riehl, H.V.R. Camargo, L. Heinen, and E. Bazzo. Experimental investigation of a capillary pumped loop towards its integration on a scientific microsatellite. In *American Society of Mechanical Engineers, Heat Transfer Division, (Publication) HTD*, volume 372, pages 101–106, New Orleans, LA, United States, 2002.

[67] E. Bazzo and R.R. Riehl. Operation characteristics of a small-scale capillary pumped loop. *Applied Thermal Engineering*, 23(6):687–705, 2003.

[68] Jeffrey Kirshberg, Dorian Liepmann, and Kirk L. Yerkes. Micro-cooler for chip-level temperature control. In *Aerospace Power Systems Conference*, SAE Technical Paper Series, Mesa, Arizona, April 1999.

[69] Jeffrey Kirshberg, Kirk L. Yerkes, and Dorian Liepmann. Demonstration of a micro-cpl based on mems fabrication technologies. In *Proceedings of the Intersociety Energy Conversion Engineering Conference*, volume 2, pages 1198 – 1204, Las Vegas, NA, USA, 2000.

[70] Jeffrey Kirshberg, Kirk Yerkes, Dave Trebotich, and Dorian Liepmann. Cooling effect of a mems based micro capillary pumped loop for chip-level temperature control. *ASME*, 2000.

[71] Dorian Liepmann. Design and fabrication of a micro-CPL for chip-level cooling. In *American Society of Mechanical Engineers, Heat Transfer Division, (Publication) HTD*, volume 369, pages 51–54, New York, NY, United States, 2001.

[72] Kirk L. Yerkes, Kenneth Pettigrew, Brian Smith, Carol Gamlen, and Dorian Liepmann. Development and testing of a planar, silicon mini-capillary pumped loop. In *Space Technology and Applications International Forum-STAIF*, pages 81–87. American Institute of Physics, 2002.

[73] D. Trebotich, J. Kirshberg, J. Teng, and D. Liepmann. Optimization of a mems based micro capillary pumped loop for chip-level temperature control. In *2001 International Conference on Modeling and Simulation of Microsystems - MSM 2001*, pages 262 – 265, Hilton Head Island, SC, United states, 2001.

[74] K. Pettigrew, J. Kirshberg, K. Yerkes, D. Trebotich, and D. Liepmann. Performance of a mems based micro capillary pumped loop for chip-level temperature control. pages 427 – 430, Interlaken, Switzerland, 2001.

[75] Laura Meyer, Samhita Dasgupta, David Shaddock, Jesse Tucker, Raymond Fillion, Peter Bronecke, Leonard Yorinks, and Philip Kraft. A silicon-carbide micro-capillary pumped loop for cooling high power devices. In *Annual IEEE Semiconductor Thermal Measurement and Management Symposium*, pages 364 – 368, San Jose, CA, United States, 2003.

[76] M. A. Chernysheva, S. V. Vershinin, and Yu. F. Maydanik. Operating temperature and distribution. of a working fluid in LHP. *International Journal of Heat and Mass Transfer*, 50(13-14):2704–2713, Jul 2007.

[77] A. Hoelke, H.T. Henderson, F.M. Gerner, and M. Kazmierczak. Analysis of the heat transfer capacity of a micromachined loop heat pipe. volume 364-3, pages 53 – 60, Nashville, TN, USA, 1999.

[78] Mohammed Hamdan, Debra Cytrynowicz, Praveen Medis, Ahmed Shuja, Frank M. Gerner, H.T. Henderson, Eric Golliher, Ken Mellott, and Chris Moore. Loop heat pipe (lhp) development by utilizing coherent porous silicon (cps) wicks. pages 457 – 465, San Diego, CA, United States, 2002.

[79] J. Pfahler, J. Harley, H. Bau, and J. Zemel. Liquid transport in micron and submicron channels. *Sensors and Actuators, A: Physical*, 22(1-3):431 – 434, 1990.

[80] S. G. Kandlikar, S. Garimella, D. Li, S. Colin, and M. R. King. *Heat Transfer and Fluid flow in Minichannels and Microchannels*. Elsevier, Kidlington, Oxford, 2006.

[81] R. K. Shah and A. L. London. *Laminar Flow Forced Convection in Ducts, Supplement 1 to Advances in Heat Transfer*. Academic Press, New York, 1978.

[82] S. Kakac, R. K. Shah, and W. Aung. *Handbook of Single-Phase Convective Heat Transfer*. John Wiley and Sons, Inc., New York, 1987.

[83] R. W. Hornbeck. Laminar flow in entrance region of pipe. *Applied Sci Research Sec A*, 13(2):1–3, 1964.

[84] John Wesley Coleman. An experimentally validated model for two-phase sudden contraction pressure drop in microchannel tube headers. *Heat Transfer Engineering*, 25(3):69 – 77, 2004.

[85] Edward W. Washburn. The dynamics of capillary flow. *Phys. Rev.*, 17(3):273–283, Mar 1921.

[86] P. Papalambros and D. J. Wilde. Global non-iterative design optimization using monotonicity analysis. *Journal of Mechanical Design*, 101(4):645–649, 1979.

[87] Pc Wayner, YK Kao, and Lv Lacroix. Interline heat-transfer coefficient of an evaporating wetting film. *International Journal of Heat and Mass Transfer*, 19(5):487–492, 1976.

[88] X. Xu and V. P. Carey. Film evaporation from a micro-grooved surface - An approximate heat transfer model and its comparison with experimental data. *Journal of Thermophysics and Heat Transfer*, 4:512–520, Oct 1990.

[89] HB Ma and GP Peterson. Temperature variation and heat transfer in triangular grooves with an evaporating film. *Journal of Thermophysics and Heat Transfer*, 11(1):90–97, Jan-Mar 1997.

[90] Hao Wang, Suresh V. Garimella, and Jayathi Y. Murthy. Characteristics of an evaporating thin film in a microchannel. *International Journal of Heat and Mass Transfer*, 50(19-20):3933–3942, Sep 2007.

[91] SJS Morris. Contact angles for evaporating liquids predicted and compared with existing experiments. *Journal of Fluid Mechanics*, 432:1–30, Apr 2001.

[92] SJS Morris. The evaporating meniscus in a channel. *Journal of Fluid Mechanics*, 494:297–317, Nov 2003.

[93] Ram Ranjan, Jayathi Y. Murthy, and Suresh V. Garimella. A microscale model for thin-film evaporation in capillary wick structures. *International Journal of Heat and Mass Transfer*, 54(1-3):169–179, Jan 2011.

[94] K. Brakke. The surface evolver. *Experimental Mathematics*, 1(2):141–165, 1992.

[95] Ram Ranjan, Jayathi Y. Murthy, and Suresh V. Garimella. Analysis of the wicking and thin-film evaporation characteristics of microstructures. *Journal of Heat Transfer*, 131(10):1 – 11, 2009.

[96] R. Marek and J. Straub. Analysis of the evaporation coefficient and the condensation coefficient of water. *International Journal of Heat and Mass Transfer*, 44(1):39 – 53, 2001.

[97] Navdeep S. Dhillon. Coherent porous silicon wick for a mems loop heat pipe. Master's thesis, University of California, Berkeley, 2012.

[98] Christopher William Hogue. *An Experimental Study of Enhanced Thermal Conductivity Utilizing Columnated Silicon Microevaporators for Convective Boiling Heat Transfer at the Microscale.* PhD thesis, University of California, Berkeley, 2011.

[99] Marc J. Madou. *Fundamentals of Mircofabrication.* CRC Press, 2nd edition.

[100] Ciprian Iliescu, Bangtao Chen, and Jianmin Miao. On the wet etching of pyrex glass. *Sensors and Actuators, A: Physical*, 143(1):154 – 161, 2008.

Appendix A

Formal Rules of Monotonicity Analysis

The 10 formal rules of monotonicity analysis as as follows:

1. Monotonicities are defined only for differentiable functions, $f(\bar{x})$, w.r.t. x_i.
2. $\frac{\partial f}{\partial x_i} > 0 \Rightarrow$ f is strictly monotonically increasing.
3. A variable, x_i, is defined as "Bounded Below by a constraint", $g_j(\bar{x}) \leq 0$, that is monotonic in x_i, if the variable achieves its minimum value at $g_j(\bar{x}) = 0$.
4. Likewise, a variable x_i is defined as "Bounded Above by a constraint", $g_j(\bar{x}) \leq 0$, that is monotonic in x_i, if the variable achieves its maximum value at $g_j(\bar{x}) = 0$.
5. An inequality constraint, $g_j(\bar{x}) \leq 0$, is defined as "active at $\bar{x}^*$" if $g_j(\bar{x}^*) = 0$. Here $\bar{x}^*$ is the optimum solution point.
6. An inequality constraint, $g_j(\bar{x}) \leq 0$, is defined as "inactive at $\bar{x}^*$" if $g_j(\bar{x}^*) < 0$.
7. An equality constraint, $h_k(\bar{x}) = 0$, is defined as "irrelevant at $\bar{x}^*$" if eliminating the constraint does not change the optimal solution.
8. If the objective function, f, is $\pm$ monotonic w.r.t. x_i, then there must exist at least one active constraint that is $\mp$ monotonic in x_i.
9. A variable, x_i, NOT EXPLICITLY represented in the objective function must either:
   (a) be contained only in inactive constraints or
   (b) be contained in two active constraints of opposite monotonicity.
10. Degenerate or unbounded problems contain violations of rules 8 and/or 9.

Appendix B

Numerical Design Optimization Program

The details of the C++ program used for solving the numerical design optimization problem in chapter 3 are given in the following sections. The program uses numerical recipes from the GNU Scientific Library (GSL) for solving the non-linear set of equations, and GNUPLOT for plotting the results.

B.1 Design Constants

```
#ifndef PARAMS_H_
#define PARAMS_H_
/* params.h -- This file gives all the
parameters used */
class params
{
public:
/* These values are specified at object
creation */
double gram, micro, centi, milli, kilo,
stokes, CtoK, dyne,
poise, atm, TP, eA, por, cA, nvc, avc,
bvc, nlc, alc, blc,
channelL, pdia, wthick, /* wwidth,
pwidth, wdepth, nwick, */
Tboil, P_condenser, Mwt, Lht, rhol,
dvis_liq, dvis_vap, T_dvis_vap,
omega_dvis_vap, vaporpress, rhov,
Cp, kl, ks, keff, surfacetension,
```

```
theta_c, Acceleration, xWickLiquid,
wickDryDepth;

/* These values are dynamically updated
and used for plotting etc. */
double Mrate, Pcap, Pwick, Pwick_liquid,
Pwick_mp, Pwick_con, Pwick_exp,
Pwick_acc, Pvapor, Pliquid, Piner;

params():
/*      Units scaling   */
gram (1.0e-3),
micro (1.0e-6),
centi (1.0e-2),
milli (1.0e-3),
kilo (1.0e3),
stokes (1.0e-4), /* convert kinematic
viscosity from
stokes to m^2/sec */
CtoK (273.15),
dyne (1.0e-5), /* to convert from dyne
to newton */
poise (0.1), /* to convert dynamic
viscosity from
poise to kg/(m sec) */
atm (101.325e3), /* convert from atm to
Pa */

/*      MLHP design parameters  */
TP (50), /* Total power in Watts */
eA (5800*micro*1800*micro), /*
evaporator area in m^2 */
por (0.349), /* porosity of the wick */
cA (8900*micro*8900*micro), /* condenser
area in m^2 */
nvc (2), /* number of vapor channels */
/* vapor channel cross section */
avc (150*micro),
bvc (2000*micro),
nlc (4), /* number of liquid channels */
/* liquid channel cross section */
alc (150*micro),
```

```
blc (150*micro),
channelL (4.6*centi), /* length of the
liquid/vapor channels */

/*      Wick Properties         */
pdia (0.8*micro), /* this is relevant
here*/
wthick (200*micro), /* wick thickness or
pore length */
//-----------------------------------------------------
//these guys are not relevant to this
Phase-d model
//wwidth (3800*micro), /* total width of
evaporator section */
//pwidth (8*micro), /* Width of a single
rectangular wick pore */
//wdepth (150*micro), /* depth of the
rectangular wick pore */
//nwick (wwidth*por/pwidth), /* Number
of pores in the wick */
//-----------------------------------------------------

/* Properties of water at the working
temperature / pressure of
100 degree C / 1 atm */
//Pboil (1.0*atm), /* assume boiling
pressure */
Tboil (100.0), /* Vapor viscosity in
microchannels
depends on this temperature (in degree
C) */
P_condenser (3.169e3), /* Condenser
pressure assuming
saturated vapor at
25 degree C
25 3.169e3
35 5.627
45 9.59
55 15.752
65 25.022
75 38.563
100 101.32e3
```

```
*/
Mwt (18.0), /* molecular weight of water
*/
Lht (2256.3 / gram), /* latent heat in
J/kg */
rhol (0.958*gram/pow(centi, 3)), /*
liquid density in SI units (kg/m3) */
dvis_liq (281.8*micro), /* dynamic
viscosity in SI units (Pa s) of water at
100 C */
dvis_vap (13.3*micro), /* dynamic
viscosity in SI units (Pa s) of vapor at
400 K (from Handbook of chemistry and
Physics) */
T_dvis_vap (400), /* temperature in K at
which dvis_vap is quoted*/
omega_dvis_vap (0.81), /* coeff. of
temperature dependence of dvis_vap
dvis_vap(T) = dvis_vap (T0) *
(T/T0)^omega_dvis_vap */
vaporpress (1*atm), /* vapor pressure in
SI units */
rhov (0.5974), /* vapor density in SI
units (8.314*1000/Mwt/(Tboil + CtoK), ~
value in thermodynamic table */
Cp (4.217*kilo), /* specific heat in
J/kg K */
kl (0.58), /* thermal conductivity of
the liquid in W/mK */
ks (130.0), /* thermal conductivity of
the solid in W/mK (input
value for silicon later) */
keff (por*kl + (1-por)*ks), /* effective
thermal conductivity
of the porous wick in W/mK */
surfacetension (58.85*dyne/centi), /*
surface tension in SI units */
theta_c (29*M_PI/180), /* contact angle
of water on SiO_2 in radians */

/* Some operational parameters which
will depend on experimental observations
```

```
*/
Acceleration (0*9.8),/* Device
Acceleration */
xWickLiquid (0.5), /* Ratio of the wick
length occupied by the liquid */
// Warning: the above value cannot be
1.0
wickDryDepth (wthick) /* refilling wick
depth */
{
}

};
#endif // PARAMS_H_
```

B.2 Program Functions

```
/* functions.c++ --
defines all the pressure drop and massflow rate functions
that will be called by main.c++ */

#include <iostream>
#include <iomanip>
#include <stdio.h>
#include <math.h>
#include <stdlib.h>

#include <gsl/gsl_math.h>

#include "functions.h"

using namespace std;

/* Fluid contraction pressure drop at
microchannel entry */
double Cpd /*contraction pressure drop*/
(void *z, double G /*mass flux*/,
double sigma_c /*contraction ratio > 1*/,
double rhol, double rhov, double x)
{
```

```
double psi_h = 1 + x*(rhol/rhov - 1);
double C_o = 1 / (0.639*pow(1-1/sigma_c,
0.5) + 1);
double Dp_c =
pow(G,2)/(2*rhol)*(pow(1/C_o-1, 2) + 1 -
1/pow(sigma_c, 2))*psi_h;
return (Dp_c);
}

/* Fluid expansion pressure drop at
microchannel exit */
double Epd /*expansion pressure drop*/
(void *z, double G, double sigma_e /*
expansion ratio < 1 */,
double rhol, double rhov, double x)
{
double psi_s = 1 +
(rhol/rhov-1)*(0.25*x*(1-x) + pow(x,2));
double Dp_e =
pow(G,2)/rhol*sigma_e*(1-sigma_e)*psi_s;
return (Dp_e);
}
/* Acceleration pressure drop due to
liquid vaporization in a microchannel */
double Apd /*acceleration pressure
drop*/
(void *z, double G, double rhol, double
rhov, double x)
{
double Dp_a = pow(G, 2) * (1/rhov -
1/rhol) * x;
return (Dp_a);
}

/* Fluid pressure drop in a rectantular
microchannel */
double Rfpd /*Rectangular fluid Pressure
Drop*/
(void *z, double mu,
double rho, double u, double L, double
a, double b)
{
```

```
double A, P, D, alpha, K, fRe, Dp;
A = a * b;
P = 2 * (a + b);
D = 4 * A / P;
if (a < b)
alpha = a / b;
else
alpha = b / a;
K = 0.0697 + 1.2197*alpha +
3.3089*pow(alpha,2) -
9.5921*pow(alpha,3)
+ 8.9089*pow(alpha,4) -
2.9959*pow(alpha,5);
fRe = 24 * (1 - 1.3553*alpha +
1.9467*pow(alpha,2) -
1.7012*pow(alpha,3)
+ 0.9564*pow(alpha,4) -
0.2537*pow(alpha,5));
Dp = (2*fRe*mu*u*L) / pow(D,2) +
K*rho*pow(u,2) / 2;
return (Dp);
}

/* Fluid pressure drop in a circular
microchannel */
double Cfpd /* Circular Fluid Pressure
Drop */
(void *z, double mu, double rho,
double u, double L, double D)
{
double K, fRe, Dp;
K = 1.28;
fRe = 16;
Dp = (2*fRe*mu*u*L) / pow(D,2) +
K*rho*pow(u,2) / 2;
return (Dp);
}

double Cmfpd /* Circular multiphase
fluid pressure drop (fully developed
only) */
(void *z, double mu_l, double mu_v,
```

```
double rhol, double rhov,
double u, double L, double D)
{
double fRe = 16;
double Dpl = (2*fRe*mu_l*u*L) / pow(D,
2);
double X2 = mu_l * rhov / (mu_v * rhol);double C = 5;
/*Both phases considered laminar*/
/* C = 21; Both phases turbulent
C = 12; Laminar liquid, turbulent vapor
C = 10; Turbulent liquid, laminar vapor
C = 5; Both phases laminar */
double phiL2 = 1 + C*(1 - exp(-319*D)) /
pow(X2, 0.5) + 1/X2;
double Dp = Dpl * phiL2;
return (Dp);
}

/* Mass flow rate of vapor in a
rectangular channel */
double Rvmf /* Rectangular vapor mass
flow */
(void *z, double mu0, double T0,
double omega, double T, double Mwt,
double L, double Pi, double Po,
double a, double b, double a1, double
a2, double a3)
{
double h, w, astar, k2, mu, R, lambdai,
lambdao, D, Kni,
Kno, Kn1i, Kn1o, II, dm;
if (a < b)
{
h = a/2;
w = b/2;
}
else
{
h = b/2;
w = a/2;
}
astar = h/w;
```

```
k2 = 16/5/sqrt(2*M_PI); /* hard sphere
gas model */
mu = mu0 * pow((T/T0), omega); /*
dynamic viscosity */
R = 8.314511 * 1000 / Mwt; /* gas
constant */
lambdai = k2*mu*sqrt(R*T)/Pi; /* mean
free path at inlet */
lambdao = k2*mu*sqrt(R*T)/Po; /* mean
free path at outlet */
D = 4*w*h / (w + h); /* hydraulic
diameter */
/* Knudsen numbers based on hydraulic
diameter */
Kni = lambdai / D;
Kno = lambdao / D;
/* Knudsen numbers based on depth
(smaller dimension) */
Kn1i = lambdai / (2*h);
Kn1o = lambdao / (2*h);
II = Pi/Po;
dm = 4*pow(h,4)*pow(Po,2) /
(astar*mu*R*T*L) * (a1/2 * (pow(II,2) -
1)
+ a2*Kn1o*(II - 1) +
a3*pow(Kn1o,2)*log(II));
return (dm);
}

/* Mass flow rate of vapor between
parallel plates */
double Pvmf /* Plate vapor mass flow */
(void *z, double mu0, double T0,
double omega, double T, double Mwt,
double L, double Pi, double Po,
        double a, double b)
{
double h, w, k2, mu, R, lambdai,
lambdao, D, Kni,
Kno, Kn1i, Kn1o, II, sigma, Sc, dm;        if (a < b)
        {
                h = a/2;
```

```
                w = b/2;
        }
        else
        {
                h = b/2;
                w = a/2;
        }
k2 = 16/5/sqrt(2*M_PI); /* hard sphere
gas model */
mu = mu0 * pow((T/T0), omega); /*
dynamic viscosity */
R = 8.314511 * 1000 / Mwt; /* gas
constant */
lambdai = k2*mu*sqrt(R*T)/Pi; /* mean
free path at inlet */
lambdao = k2*mu*sqrt(R*T)/Po; /* mean
free path at outlet */
D = 4*w*h / (w + h); /* hydraulic
diameter */
/* Knudsen numbers based on hydraulic
diameter */
        Kni = lambdai / D;
        Kno = lambdao / D;
/* Knudsen numbers based on depth
(smaller dimension) */
        Kn1i = lambdai / (2*h);
        Kn1o = lambdao / (2*h);
        II = Pi/Po;
sigma = 0.9; /* user dependent: sigma is
the fraction of the molecules
that are diffusely reflected from the
wall surface */
Sc = 5.0/6; /* for the Hard Sphere (HS)
model */
dm = 2*w*pow(h,3)*pow(Po,2) / (mu*R*T*L)
* (pow(II,2) - 1)/3 *
(1 + 12 * (2 - sigma)/sigma * Kn1o/(II +
1)
-24/(pow(k2,2)*Sc) * pow(Kn1o,2) *
log(II)/(pow(II,2) - 1));
        return (dm);
}
```

B.3 Main Solver Program

```
#include <iostream>
#include <iomanip>
#include <stdio.h>
#include <math.h>
#include <stdlib.h>

#include <gsl/gsl_vector.h>
#include <gsl/gsl_multiroots.h>
#include <gsl/gsl_math.h>

#include "params.h"
#include "functions.h"
#include "solve.h"

using namespace std;

int mlhp_f (const gsl_vector *x, void
*zz, gsl_vector *f)
{
params *z = (params *)zz;
z->Mrate = gsl_vector_get (x, 0);
z->Pvapor = gsl_vector_get (x, 1);

z->Pcap = 4 *
z->surfacetension*cos(z->theta_c) /
z->pdia;
z->Pliquid = Rfpd(z, z->dvis_liq,
z->rhol,
z->Mrate/z->rhol/z->alc/z->blc/z->nlc,
z->channelL, z->alc, z->blc);
z->Pwick_liquid = Cfpd(z, z->dvis_liq,
z->rhol,
z->Mrate/z->rhol/z->por/z->eA,z->wthick*z->xWickLiquid,z->pdia);
z->Pwick_mp = Cmfpd(z, z->dvis_liq,
z->dvis_vap, z->rhol, z->rhov,
z->Mrate/z->rhol/z->por/z->eA,
z->wthick*(1 - z->xWickLiquid),
```

```
z->pdia);
z->Pwick_con = Cpd(z, z->Mrate/z->eA,
1/z->por, z->rhol, z->rhov, 0);
z->Pwick_exp = Epd(z,
z->Mrate/z->eA/z->por, z->por, z->rhol,
z->rhov, 1);
z->Pwick_acc = Apd(z,
z->Mrate/z->eA/z->por, z->rhol, z->rhov,
1);
z->Piner = z->rhol * z->Acceleration *
z->channelL;/*inertial pressure drop */
const double Mv = z->nvc * Rvmf(z,
z->dvis_vap, z->T_dvis_vap,
z->omega_dvis_vap, z->Tboil + z->CtoK,
z->Mwt, z->channelL, z->P_condenser +
z->Pvapor, z->P_condenser, z->avc,
z->bvc,
0.28081, 2.2267, 3.6626 /*a1, a2, a3 are
chosen from page 52
corresponding to a*=0.25 and sigma = 0.9
*/);
z->Pwick = z->Pwick_liquid + z->Pwick_mp
+ z->Pwick_con + z->Pwick_exp +
z->Pwick_acc;

const double y0 = z->Pcap - z->Pliquid -
z->Pvapor - z->Pwick - z->Piner;
const double y1 = z->Mrate - Mv;

gsl_vector_set (f, 0, y0);
gsl_vector_set (f, 1, y1);

        return GSL_SUCCESS;
}

int mlhp_f_simple (const gsl_vector *x,
void *zz, gsl_vector *f)
{
params *z = (params *)zz;
z->Mrate = gsl_vector_get (x, 0);

z->Pcap = 4 *
```

```
z->surfacetension*cos(z->theta_c) /
z->pdia;
z->Pliquid = Rfpd(z, z->dvis_liq,
z->rhol,
z->Mrate/z->rhol/z->alc/z->blc/z->nlc,
z->channelL, z->alc, z->blc);
z->Pvapor = Rfpd(z, z->dvis_vap,
z->rhov,
z->Mrate/z->rhov/z->avc/z->bvc/z->nvc,
z->channelL, z->avc, z->bvc);
z->Pwick_liquid = Cfpd(z, z->dvis_liq,
z->rhol,
z->Mrate/z->rhol/z->por/z->eA,z->wthick*z->xWickLiquid,z->pdia);
z->Pwick_mp = Cmfpd(z, z->dvis_liq,
z->dvis_vap, z->rhol, z->rhov,
z->Mrate/z->rhol/z->por/z->eA,
z->wthick*(1 - z->xWickLiquid),
z->pdia);
z->Pwick_con = Cpd(z, z->Mrate/z->eA,
1/z->por, z->rhol, z->rhov, 0);
z->Pwick_exp = Epd(z,
z->Mrate/z->eA/z->por, z->por, z->rhol,
z->rhov, 1);
z->Pwick_acc = Apd(z,
z->Mrate/z->eA/z->por, z->rhol, z->rhov,
1);
z->Piner = z->rhol * z->Acceleration *
z->channelL;/*inertial pressure drop */

z->Pwick = z->Pwick_liquid + z->Pwick_mp
+ z->Pwick_con + z->Pwick_exp +
z->Pwick_acc;

const double y0 = z->Pcap - z->Pliquid -
z->Pvapor - z->Pwick - z->Piner;

gsl_vector_set (f, 0, y0);

        return GSL_SUCCESS;
}
```

```
void print_state (size_t iter,
gsl_multiroot_fsolver *s)
{
printf ("iter = %3u x = % .3e % .3e  "
"f(x) = % .3e % .3e\n",
iter,
gsl_vector_get (s->x, 0),
gsl_vector_get (s->x, 1),
gsl_vector_get (s->f, 0),
gsl_vector_get (s->f, 1));
}

int solve (params *z)
{
const gsl_multiroot_fsolver_type *T;
gsl_multiroot_fsolver *s;

int status;
size_t i, iter = 0;

const size_t n = 2;
gsl_multiroot_function f = {&mlhp_f, n,
z};

double x_init[n] = {1.0e-6, 1.0e5};
gsl_vector *x = gsl_vector_alloc (n);

T = gsl_multiroot_fsolver_hybrids;
s = gsl_multiroot_fsolver_alloc (T, n);
int should_print = 1;

gsl_vector_set (x, 0, x_init[0]);
gsl_vector_set (x, 1, x_init[1]);

gsl_multiroot_fsolver_set (s, &f, x);

//print_state (iter, s);
do
{
iter++;
status = gsl_multiroot_fsolver_iterate
```

```
(s);
//print_state (iter, s);
if (status) /* check if solver is stuck
*/
{
should_print = 0;
break;
}
status = gsl_multiroot_test_residual
(s->f, 1e-7);
}while (status == GSL_CONTINUE && iter <
1000);

//printf ("status = %s\n",
gsl_strerror(status));
//device_print_output(z, s);
printf("\nPore dia = %e \tHeat flux = %e
W/cm^2 \tstatus = %s\n", z->pdia, z->Lht
* gsl_vector_get(s->x, 0)
/ z->eA * z->centi * z->centi,
gsl_strerror(status));
if(should_print && iter < 1000)
{
should_print = 1;
z->Mrate = gsl_vector_get(s->x, 0);
}
else
should_print = 0;
gsl_multiroot_fsolver_free (s);
gsl_vector_free (x);
return (should_print);
}

int solve_simple (params *z)
{
const gsl_multiroot_fsolver_type *T;
gsl_multiroot_fsolver *s;

int status;
size_t i, iter = 0;

const size_t n = 1;
```

```
gsl_multiroot_function f =
{&mlhp_f_simple, n, z};

double x_init[n] = {1.0e-6};
gsl_vector *x = gsl_vector_alloc (n);

T = gsl_multiroot_fsolver_hybrids;
s = gsl_multiroot_fsolver_alloc (T, n);
int should_print = 1;

gsl_vector_set (x, 0, x_init[0]);

gsl_multiroot_fsolver_set (s, &f, x);

//print_state (iter, s);
do
{
iter++;
status = gsl_multiroot_fsolver_iterate
(s);
//print_state (iter, s);
if (status) /* check if solver is stuck
*/
{
should_print = 0;
break;
}
status = gsl_multiroot_test_residual
(s->f, 1e-7);
}while (status == GSL_CONTINUE && iter <
1000);

//printf ("status = %s\n",
gsl_strerror(status));
//device_print_output(z, s);
printf("\nPore dia = %e \tHeat flux = %e
W/cm^2 \tstatus = %s\n", z->pdia, z->Lht
* gsl_vector_get(s->x, 0)
/ z->eA * z->centi * z->centi,
gsl_strerror(status));
if(should_print && iter < 1000)
{
```

```
should_print = 1;
z->Mrate = gsl_vector_get(s->x, 0);
}
else
should_print = 0;
gsl_multiroot_fsolver_free (s);
gsl_vector_free (x);
return (should_print);
}
```

B.4 Solving and Plotting Program

```
#include <iostream>
#include <iomanip>
#include <stdio.h>
#include <math.h>
#include <stdlib.h>
#include <string.h>

#include <gsl/gsl_math.h>

#include "params.h"
#include "solve.h"

using namespace std;
const int LATEX_PLOT = 0;

void start_plot_latex(FILE *pipe, char*
filename, char* plotLabel)
{
fprintf(pipe, "set xlabel '[c]{Wick pore
diameter, $(\\mu m)$}'\n");
fprintf(pipe, "set ylabel '[c]{Total
heat absorbed, $Q_t$ (Watts)}'\n");
fprintf(pipe, "set size 1,1\n");
fprintf(pipe, "set key\n");
fprintf(pipe, "set term epslatex\n");
fprintf(pipe, "set out
'gsl-plots/heat/pdia_plot_refill.eps'\n");
fprintf(pipe, "plot [ ] [0:1000] '%s'
```

```
using 1:3 w lines title '[r]{Wick
refilling limit}', '%s' using 1:2 w
lines title '[r]{Wick liquid fraction,
%s}'", filename, filename , plotLabel);
//fprintf(pipe, "set out
'gsl-plots/heat/pdia_plot.eps'\n");
//fprintf(pipe, "plot [ ] [ ] '%s' using
1:2 w lines title '[r]{Wick liquid
fraction, %s}'", filename , plotLabel);
}
void start_plot(FILE *pipe, char*
filename, char* plotLabel)
{
fprintf(pipe, "set xlabel 'Wick pore
diameter (microns)'\n");
fprintf(pipe, "set ylabel 'Total heat
absorbed, Q (Watts)'\n");
fprintf(pipe, "set size 1,1\n");
fprintf(pipe, "set key\n");
fprintf(pipe, "set term x11\n");
//fprintf(pipe, "set term png\n");
//fprintf(pipe, "set out
'pdia_plot.png'\n");
fprintf(pipe, "plot [ ] [ ] '%s' using
1:3 w lines title '[r]{Wick refilling
limit}', '%s' using 1:2 w lines title
'%s'", filename, filename, plotLabel);
}
void plot(FILE *pipe, char* filename,
char* plotLabel)
{
fprintf(pipe, ", '%s' using 1:2 w lines
title '[r]{%s}'", filename, plotLabel);
}
void end_plot(FILE *pipe)
{
fprintf(pipe, "\n");
}


int main (void)
{
```

```
int cinTest;
params *z = new params;
FILE *pFile;
FILE *pipe = popen("gnuplot
-persist","w");

int plotStarted = 0;
int fileNo = 1;
char filename[30];
char plotLabel[100];
for(z->xWickLiquid = 0.95;
z->xWickLiquid >= 0.6; z->xWickLiquid -=
0.1)
{
sprintf(filename, "data-%d.dat",
fileNo);
sprintf(plotLabel, "$x_{w,liq} = %.2f$",
z->xWickLiquid);
pFile = fopen(filename, "w");
for(z->pdia = 0.1*z->micro; z->pdia
<=10*z->micro; z->pdia += 0.1*z->micro)
{

if(solve_simple(z))
fprintf(pFile, "%e \t %e \t %e \n",
z->pdia / z->micro,
z->Lht * z->Mrate,
z->Lht * z->rhol * z->surfacetension *
cos(z->theta_c) / (4 * z->dvis_liq) *
z->por * z->pdia / z->wickDryDepth *
z->eA
);
}
fileNo++;
fclose(pFile);
if(plotStarted)
plot(pipe, filename, plotLabel);
else
{
if(LATEX_PLOT)
start_plot_latex(pipe, filename,
plotLabel);
```

```
else
start_plot(pipe, filename, plotLabel); plotStarted = 1;
}
}
//fprintf(pipe, ", '%s' using 1:3 w
lines title 'Wick refilling limit'",
filename);
end_plot(pipe);
pclose(pipe);
return 0;
}
```

Appendix C

Phase Change Simulation Program

The details of the methods and the computer programs for numerically simulating evaporation from a stationary liquid-vapor meniscus (chapter 4) are provided in the following sections.

C.1 Overall Procedure

The shape of the liquid-vapor meniscus is first generated using Surface Evolver. From this program, the file is exported as an OFF file (e.g. meniscus.off). A CAD program called Blender is used to import this file and then export it as a binary STL file (e.g. meniscus.stl). Another program called Gmsh is used to open this file and then re-save it as an ASCII STL file (e.g. meniscus-ascii.stl). This geometry file is imported by OpenFOAM and meshed. The OpenFOAM solver program given below is then used to solve the numerical problem on this domain.

C.2 OpenFOAM Solver Program

OpenFOAM is a C++ library that implements the finite volume method (FVM) for numerically solving partial differential equations.

SatEvaporation.C

```
#include "fvCFD.H"
#include "singlePhaseTransportModel.H"
#include "turbulenceModel.H"


int main(int argc, char *argv[])
{
```

```
#   include "setRootCase.H"
#   include "createTime.H"
#   include "createMesh.H"
# include
"readGravitationalAcceleration.H"
#   include "createFields.H"
#   include "initContinuityErrs.H"
#   include "readTimeControls.H"
#   include "CourantNo.H"
//#   include "setInitialDeltaT.H"


Info<< "\nStarting time loop\n" << endl;
    while (runTime.loop())
    {
Info<< "Time = " << runTime.timeName()
<< nl << endl;

#       include "readTimeControls.H"
#       include "readPISOControls.H"
#       include "CourantNo.H"
#       include "setDeltaT.H"
//# include "setDeltaT_Diffusion.H"
// bool nonLinear = 0;

//do{
//# include "saveOldFields.H"
# include "TEqn.H"
#       include "UEqn.H"
//# include "TEqn.H"

        // --- PISO loop
for (int corr=0; corr<nCorr; corr++)        {
#           include "pEqn.H"
        }

        turbulence->correct();
//# include "nonLinearCourant.H"
//}while(nonLinear);

        runTime.write();
```

```
Info<< "ExecutionTime = " <<
runTime.elapsedCpuTime() << " s"
<< " ClockTime = " <<
runTime.elapsedClockTime() << " s"
            << nl << endl;
    }

    Info<< "End\n" << endl;

    return 0;
}
```

CreateFields.H

```
Info<< "Reading thermophysical
properties\n" << endl;

    Info<< "Reading field T\n" << endl;
    volScalarField T
    (
        IOobject
        (
            "T",
            runTime.timeName(),
            mesh,
            IOobject::MUST_READ,
            IOobject::AUTO_WRITE
        ),
        mesh
    );

    Info<< "Reading field p\n" << endl;
    volScalarField p
    (
        IOobject
        (
            "p",
            runTime.timeName(),
            mesh,
            IOobject::MUST_READ,
            IOobject::AUTO_WRITE
```

```
        ),
        mesh
    );

    Info<< "Reading field U\n" << endl;
    volVectorField U
    (
        IOobject
        (
            "U",
            runTime.timeName(),
            mesh,
            IOobject::MUST_READ,
            IOobject::AUTO_WRITE
        ),
        mesh
    );


    #include "createPhi.H"

#include "readTransportProperties.H"
Info<< "Creating turbulence model\n" <<
endl;
autoPtr<incompressible::turbulenceModel>
turbulence
    (
incompressible::turbulenceModel::New(U,
phi, laminarTransport)
    );

    label pRefCell = 0;
    scalar pRefValue = 0.0;
    setRefCell
    (
        p,
mesh.solutionDict().subDict("PISO"),        pRefCell,
        pRefValue
    );


// Kinematic density for buoyancy force    volScalarField rhok
```

```
    (
        IOobject
        (
            "rhok",
            runTime.timeName(),
            mesh
        ),
        1.0 - beta*(T - TRef)
    );

// FIELDS FOR THE CALCULATION OF THE
EVAPORATION SOURCE TERM
Info<< "Reading the phase change field
pc\n" << endl;
    volScalarField pc
    (
     IOobject
(
"pc",
runTime.timeName(),
mesh,
IOobject::MUST_READ,
IOobject::AUTO_WRITE
),
mesh
    );

Info<< "Calculating the Saturation
pressure in the liquid\n" << endl;
volScalarField PsatL
(
IOobject
(
"PsatL",
runTime.timeName(),
mesh
),
PrefS * exp(Mwt * h_fg / gasR * (1/TrefS
- 1/T))
);

Info<< "Calculating the evaporative mass
```

```
flux\n" << endl;
volScalarField mFlux
(
IOobject
(
"mFlux",
runTime.timeName(),
mesh
),
2 * sigmaA / (2 - sigmaA) * pow(Mwt /
(2*3.14159*gasR), 0.5) *
(PsatL/pow(T,0.5) - Pv / pow(Tv, 0.5))
);

Info<< "Calculating Phase Change source
term pcS\n" << endl;
    volScalarField pcS
    (
IOobject
(
"pcS",
runTime.timeName(),
mesh,
IOobject::READ_IF_PRESENT,
IOobject::AUTO_WRITE
),
- mFlux * pc / Rho
    );

Info<< "Calculating evaporative heat
flux at the surface\n" << endl;
    volScalarField heatFlux
    (
IOobject
(
"heatFlux",
runTime.timeName(),
mesh,
IOobject::READ_IF_PRESENT,
IOobject::AUTO_WRITE
),
mFlux * h_fg
```

```
    );
```

pEqn.H

```
{
volScalarField rUA("rUA", 1.0/UEqn.A());
surfaceScalarField rUAf("(1|A(U))",
fvc::interpolate(rUA));

    U = rUA*UEqn.H();

    surfaceScalarField phiU
    (
(fvc::interpolate(U) & mesh.Sf()) + fvc::ddtPhiCorr(rUA, U, phi)
    );

phi = phiU +
rUAf*fvc::interpolate(rhok)*(g &
mesh.Sf());

for (int nonOrth=0;
nonOrth<=nNonOrthCorr; nonOrth++)
    {
        fvScalarMatrix pEqn
        (
fvm::laplacian(rUAf, p) == fvc::div(phi)
- pcS
        );

if (corr == nCorr-1 && nonOrth ==
nNonOrthCorr)
        {
pEqn.solve(mesh.solver(p.name() +
"Final"));
        }
        else
        {
pEqn.solve(mesh.solver(p.name()));        }

        if (nonOrth == nNonOrthCorr)
```

```
        {
            phi -= pEqn.flux();
        }
    }

U += rUA*fvc::reconstruct((phi -
phiU)/rUAf);
    U.correctBoundaryConditions();

    #include "continuityErrs.H"
}
```

readTransportProperties.H

```
singlePhaseTransportModel
laminarTransport(U, phi);

// Thermal expansion coefficient [1/K]dimensionedScalar
beta(laminarTransport.lookup("beta"));

    // Reference temperature [K]
dimensionedScalar
TRef(laminarTransport.lookup("TRef"));

    // Laminar Prandtl number
dimensionedScalar
Pr(laminarTransport.lookup("Pr"));

    // Turbulent Prandtl number
dimensionedScalar
Prt(laminarTransport.lookup("Prt"));

//---------------------------------------------------------
// MODEL SPECIFIC PROPERTIES BY NAVDEEP
//
-------------------------------------------------------

// Density of the liquid (kg/m3)
dimensionedScalar
Rho(laminarTransport.lookup("Rho"));
```

```
// Accomodation coefficient for
evaporation
dimensionedScalar
sigmaA(laminarTransport.lookup("sigmaA"));

// Molecular weight of the fluid
(kg/kmol)
dimensionedScalar
Mwt(laminarTransport.lookup("Mwt"));

// Universal gas constant (J/kmol K)
dimensionedScalar
gasR(laminarTransport.lookup("gasR"));

// Reference saturation Temperature (K)
dimensionedScalar
TrefS(laminarTransport.lookup("TrefS"));

// Reference saturation Pressure (Pa)
dimensionedScalar
PrefS(laminarTransport.lookup("PrefS"));

// Latent heat of vaporization (J/kg)
dimensionedScalar
h_fg(laminarTransport.lookup("h_fg"));

// Pressure and Temperature of the
saturated vapor
dimensionedScalar
Pv(laminarTransport.lookup("Pv"));
dimensionedScalar
Tv(laminarTransport.lookup("Tv"));
```

saveOldFields.H

```
volScalarField T_old = T;
volScalarField p_old = p;
volVectorField U_old = U;
scalar deltaT_old =
runTime.deltaT().value;
scalar maxCo_old = maxCo;
```

setDeltaT Diffusion.H

```
{

    volScalarField kappaEff
    (
        "kappaEff",
turbulence->nu()/Pr +
turbulence->nut()/Prt
    );

if (adjustTimeStep)
{
scalar maxDeltaT =
min(pow(mesh.V(),2/3)/(6 * kappaEff));
runTime.setDeltaT
(
min
(
runTime.deltaT().value(),
maxDeltaT
)
);
}

}
```

TEqn.H

```
{
    volScalarField kappaEff
    (
        "kappaEff",
turbulence->nu()/Pr +
turbulence->nut()/Prt
    );

    fvScalarMatrix TEqn
    (
```

```
        fvm::ddt(T)
      + fvm::div(phi, T)
      - fvm::laplacian(kappaEff, T)
- fvm::Sp(- 2 * sigmaA / (2 - sigmaA) *
pow(Mwt / (2*3.14159*gasR), 0.5) *
((PrefS * exp(Mwt * h_fg / gasR *
(1/TrefS - 1/T)))/pow(T,0.5) - Pv /
pow(Tv, 0.5)) * pc / Rho, T)
    );

    TEqn.relax();

    TEqn.solve();

    #include "updateSource.H"

    rhok = 1.0 - beta*(T - TRef);
}
```

UEqn.H

```
    // Solve the momentum equation

    fvVectorMatrix UEqn
    (
        fvm::ddt(U)
      + fvm::div(phi, U)
      + turbulence->divDevReff(U)
    );

    UEqn.relax();

    if (momentumPredictor)
    {
        solve
        (
            UEqn
         ==
            fvc::reconstruct
            (
                (
```

```
fvc::interpolate(rhok)*(g & mesh.Sf())- fvc::snGrad(p)*mesh.magSf()
                )
            )
        );
    }
```

updateSource.H

```
PsatL = PrefS * exp(Mwt * h_fg / gasR *
(1/TrefS - 1/T));
mFlux = 2 * sigmaA / (2 - sigmaA) *
pow(Mwt / (2*3.14159*gasR), 0.5) *
(PsatL/pow(T,0.5) - Pv / pow(Tv, 0.5));
pcS = - mFlux * pc / Rho;
heatFlux = mFlux * h_fg;
```